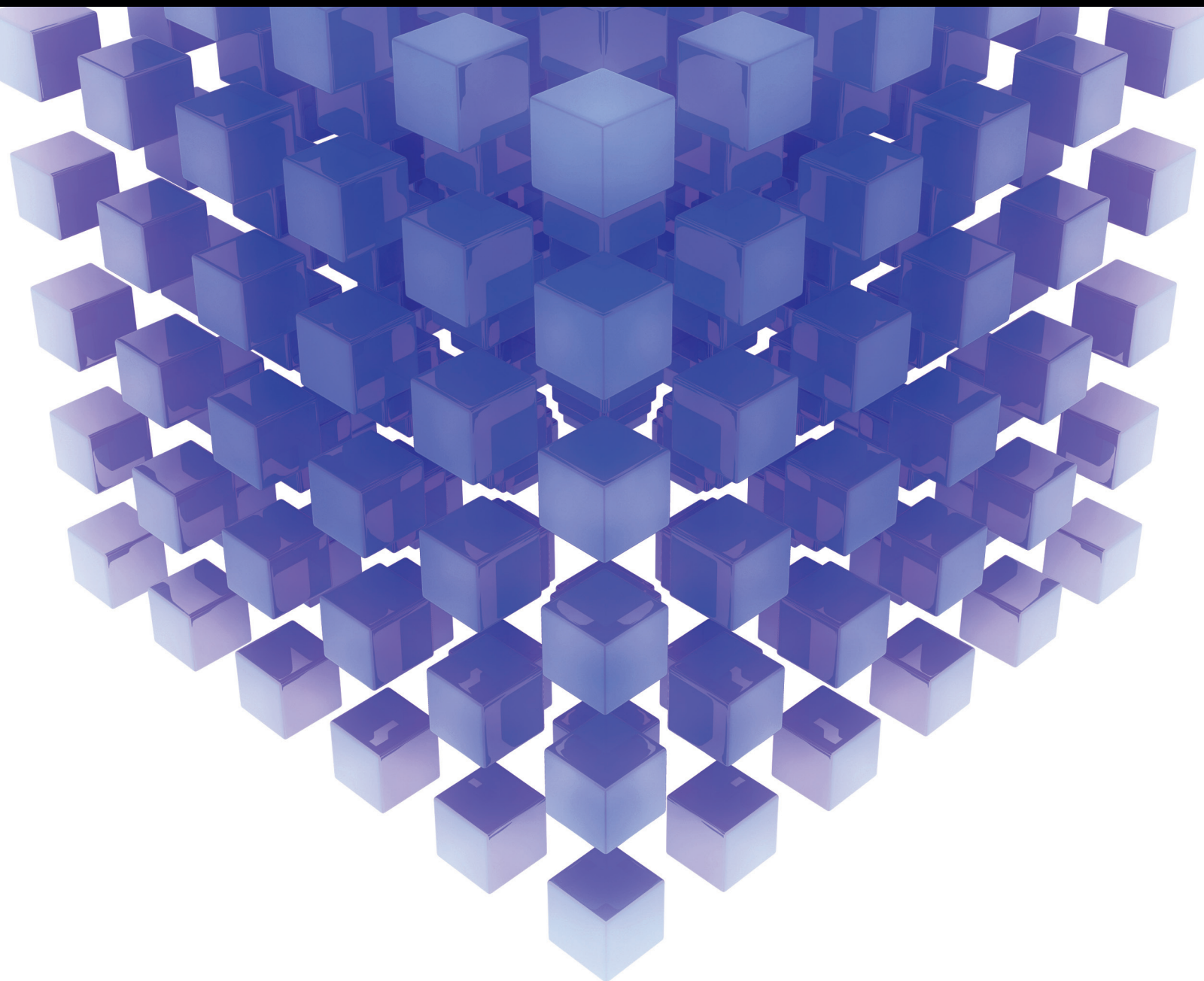


Mathematical Problems in Engineering

Applications of Methods of Numerical Linear Algebra in Engineering 2016

Guest Editors: Masoud Hajarani, Jinyun Yuan, and Ivan Kyrchei





**Applications of Methods of Numerical Linear
Algebra in Engineering 2016**

Mathematical Problems in Engineering

**Applications of Methods of Numerical Linear
Algebra in Engineering 2016**

Guest Editors: Masoud Hajarian, Jinyun Yuan, and Ivan Kyrchei



Copyright © 2016 Hindawi Publishing Corporation. All rights reserved.

This is a special issue published in “Mathematical Problems in Engineering.” All articles are open access articles distributed under the Creative Commons Attribution License, which permits unrestricted use, distribution, and reproduction in any medium, provided the original work is properly cited.

Editorial Board

- Mohamed Abd El Aziz, Egypt
Farid Abed-Meraim, France
José Ángel Acosta, Spain
Paolo Addresso, Italy
Claudia Adduce, Italy
Ramesh Agarwal, USA
Juan C. Agüero, Australia
Ricardo Aguilar-López, Mexico
Tarek Ahmed-Ali, France
Hamid Akbarzadeh, Canada
Muhammad N. Akram, Norway
Mohammad-Reza Alam, USA
Salvatore Alfonzetti, Italy
Francisco Alhama, Spain
Mohammad D. Aliyu, Canada
Juan A. Almendral, Spain
Lionel Amodeo, France
Sebastian Anita, Romania
Renata Archetti, Italy
Felice Arena, Italy
Sabri Arik, Turkey
Alessandro Arsie, USA
Eduardo Artioli, Italy
Fumihiko Ashida, Japan
Hassan Askari, Canada
Mohsen Asle Zaeem, USA
Romain Aubry, USA
Matteo Aureli, USA
Francesco Aymerich, Italy
Seungik Baek, USA
Khaled Bahlali, France
Laurent Bako, France
Stefan Balint, Romania
Alfonso Banos, Spain
Roberto Baratti, Italy
Martino Bardi, Italy
Azeddine Beghdadi, France
Denis Benasciutti, Italy
Abdel-Hakim Bendada, Canada
Ivano Benedetti, Italy
Elena Benvenuti, Italy
Jamal Berakdar, Germany
Michele Betti, Italy
Jean-Charles Beugnot, France
Simone Bianco, Italy
- Gennaro N. Bifulco, Italy
David Bigaud, France
Antonio Bilotta, Italy
Jonathan N. Blakely, USA
Paul Bogdan, USA
Alberto Borboni, Italy
Paolo Boscariol, Italy
Daniela Boso, Italy
Guillermo Botella-Juan, Spain
Abdel-Ouahab Boudraa, France
Fabio Bovenga, Italy
Francesco Braghin, Italy
Michael J. Brennan, UK
Maurizio Brocchini, Italy
Julien Bruchon, France
Michele Brun, Italy
Javier Buldú, Spain
Erik Burman, UK
Tito Busani, USA
Raquel Caballero-Águila, Spain
Pierfrancesco Cacciola, UK
Salvatore Caddemi, Italy
Jose E. Capilla, Spain
E. Javier Cara, Spain
Ana Carpio, Spain
Carmen Castillo, Spain
Inmaculada T. Castro, Spain
Gabriele Cazzulani, Italy
Luis Cea, Spain
Miguel E. Cerrolaza, Spain
M. Chadli, France
Gregory Chagnon, France
Ching-Ter Chang, Taiwan
Michael J. Chappell, UK
Kacem Chehdi, France
Peter N. Cheimets, USA
Chunlin Chen, China
Xinkai Chen, Japan
Francisco Chicano, Spain
Hung-Yuan Chung, Taiwan
Joaquim Ciurana, Spain
John D. Clayton, USA
Giuseppina Colicchio, Italy
Mario Cools, Belgium
Sara Coppola, Italy
- Jean-Pierre Corriou, France
Juan Carlos Cortés López, Spain
Carlo Cosentino, Italy
Paolo Crippa, Italy
Andrea Crivellini, Italy
Erik Cuevas, Mexico
Peter Dabnichki, Australia
Luca D'Acerno, Italy
Weizhong Dai, USA
Andrea Dall'Asta, Italy
Purushothaman Damodaran, USA
Farhang Daneshmand, Canada
Fabio De Angelis, Italy
Stefano de Miranda, Italy
Filippo de Monte, Italy
Maria do Rosário de Pinho, Portugal
Xavier Delorme, France
Frédéric Demoly, France
Luca Deseri, USA
Angelo Di Egidio, Italy
Ramón I. Diego, Spain
Yannis Dimakopoulos, Greece
Zhengtao Ding, UK
Mohamed Djemai, France
Manuel Doblaré, Spain
Alexandre B. Dolgui, France
Florent Duchaine, France
George S. Dulikravich, USA
Bogdan Dumitrescu, Romania
Horst Ecker, Austria
Ahmed El Hajjaji, France
Fouad Erchiqui, Canada
Anders Eriksson, Sweden
R. Emre Erkmen, Australia
Andrea L. Facci, Italy
Giovanni Falsone, Italy
Hua Fan, China
Yann Favennec, France
Giuseppe Fedele, Italy
Roberto Fedele, Italy
Jose R. Fernandez, Spain
Jesus M. Fernandez Oro, Spain
Eric Feulvarch, France
Simme Douwe Flapper, Netherlands
Thierry Floquet, France

Eric Florentin, France
Jose M. Framinan, Spain
Francesco Franco, Italy
Elisa Francomano, Italy
Mario L. Fravolini, Italy
Leonardo Freitas, UK
Tomonari Furukawa, USA
Mohamed Gadala, Canada
Matteo Gaeta, Italy
Mauro Gaggero, Italy
Zoran Gajic, Iraq
Erez Gal, Israel
Ugo Galvanetto, Italy
Akemi Gálvez, Spain
Rita Gamberini, Italy
Maria L. Gandarias, Spain
Arman Ganji, Canada
Xin-Lin Gao, USA
Zhong-Ke Gao, China
Giovanni Garcea, Italy
Fernando García, Spain
Jose M. Garcia-Aznar, Spain
Laura Gardini, Italy
Alessandro Gasparetto, Italy
Vincenzo Gattulli, Italy
Oleg V. Gendelman, Israel
Mergen H. Ghayesh, Australia
Agathoklis Giaralis, UK
Anna M. Gil-Lafuente, Spain
Hector Gómez, Spain
David González, Spain
Francisco Gordillo, Spain
Rama S. R. Gorla, USA
Oded Gottlieb, Israel
Nicolas Gourdain, France
Kannan Govindan, Denmark
Antoine Grall, France
Jason Gu, Canada
Federico Guarracino, Italy
José L. Guzmán, Spain
Quang Phuc Ha, Australia
Masoud Hajarian, Iran
Frédéric Hamelin, France
Zhen-Lai Han, China
Thomas Hanne, Switzerland
Xiao-Qiao He, China
Sebastian Heidenreich, Germany
Luca Heltai, Italy
Alfredo G. Hernández-Díaz, Spain
M.I. Herreros, Spain
Vincent Hilaire, France
Roland Hildebrand, Germany
Eckhard Hitzer, Japan
Jaromir Horacek, Czech Republic
Muneo Hori, Japan
András Horváth, Italy
Gordon Huang, Canada
Nicolas Hudon, Canada
Sajid Hussain, Canada
Asier Ibeas, Spain
Orest V. Iftime, Netherlands
Giacomo Innocenti, Italy
Emilio Insfran, Spain
Nazrul Islam, USA
Benoit Iung, France
Payman Jalali, Finland
Reza Jazar, Australia
Khalide Jbilou, France
Linni Jian, China
Bin Jiang, China
Zhongping Jiang, USA
Ningde Jin, China
Grand R. Joldes, Australia
Dylan F. Jones, UK
Tamas Kalmar-Nagy, Hungary
Tomasz Kapitaniak, Poland
Haranath Kar, India
Konstantinos Karamanos, Belgium
Jean-Pierre Kenne, Canada
Chaudry M. Khalique, South Africa
Do Wan Kim, Republic of Korea
Nam-Il Kim, Republic of Korea
Oleg Kirillov, Germany
Manfred Krafczyk, Germany
Frederic Kratz, France
Petr Krysl, USA
Jurgen Kurths, Germany
Kyandoghere Kyamakya, Austria
Davide La Torre, Italy
Risto Lahdelma, Finland
Hak-Keung Lam, UK
Jimmy Lauber, France
Antonino Laudani, Italy
Aime' Lay-Ekuakille, Italy
Nicolas J. Leconte, France
Marek Lefik, Poland
Yaguo Lei, China
Stefano Lenci, Italy
Roman Lewandowski, Poland
Panos Liatsis, UAE
Anatoly Lisnianski, Israel
Peide Liu, China
Peter Liu, Taiwan
Wanquan Liu, Australia
Yan-Jun Liu, China
Alessandro Lo Schiavo, Italy
Jean J. Loiseau, France
Paolo Lonetti, Italy
Sandro Longo, Italy
Sebastian López, Spain
Luis M. López-Ochoa, Spain
Vassilios C. Loukopoulos, Greece
Valentin Lychagin, Norway
Antonio Madeo, Italy
José María Maestre, Spain
Fazal M. Mahomed, South Africa
Noureddine Manamanni, France
Didier Maquin, France
Paolo Maria Mariano, Italy
Damijan Markovic, France
Benoit Marx, France
Franck Massa, France
Paolo Massioni, France
Ge'ard A. Maugin, France
Alessandro Mauro, Italy
Michael Mazilu, UK
Driss Mehdi, France
Roderick Melnik, Canada
Pasquale Memmolo, Italy
Xiangyu Meng, Canada
Jose Merodio, Spain
Alessio Merola, Italy
Luciano Mescia, Italy
Laurent Mevel, France
Yuri Vladimirovich Mikhlin, Ukraine
Aki Mikkola, Finland
Hiroyuki Mino, Japan
Pablo Mira, Spain
Vito Mocella, Italy
Roberto Montanini, Italy
Gisele Mophou, France
Rafael Morales, Spain
Marco Morandini, Italy
Simone Morganti, Italy

Philip Moser, Germany
Aziz Moukrim, France
Emiliano Mucchi, Italy
Domenico Mundo, Italy
Jose J. Muñoz, Spain
Giuseppe Muscolino, Italy
Marco Mussetta, Italy
Hakim Naceur, France
Hassane Naji, France
Keivan Navaie, UK
Dong Ngoduy, UK
Tatsushi Nishi, Japan
Xesús Nogueira, Spain
Ben T. Nohara, Japan
Mohammed Nouari, France
Mustapha Nourelfath, Canada
Sotiris K. Ntuyas, Greece
Roger Ohayon, France
Mitsuhiro Okayasu, Japan
Javier Ortega-García, Spain
Alejandro Ortega-Moñux, Spain
Naohisa Otsuka, Japan
Erika Ottaviano, Italy
Arturo Pagano, Italy
Alkis S. Paipetis, Greece
Alessandro Palmeri, UK
Anna Pandolfi, Italy
Elena Panteley, France
Achille Paolone, Italy
Xosé M. Pardo, Spain
Manuel Pastor, Spain
Pubudu N. Pathirana, Australia
Francesco Pellicano, Italy
Marcello Pellicciari, Italy
Haipeng Peng, China
Mingshu Peng, China
Zhike Peng, China
Marzio Pennisi, Italy
Matjaz Perc, Slovenia
Francesco Pesavento, Italy
Dario Piga, Italy
Antonina Pirrotta, Italy
Marco Pizzarelli, Italy
Vicent Pla, Spain
Javier Plaza, Spain
Sébastien Poncet, Canada
Jean-Christophe Ponsart, France
Mauro Pontani, Italy
Stanislav Potapenko, Canada
Sergio Preidikman, USA
Christopher Pretty, New Zealand
Carsten Proppe, Germany
Luca Pugi, Italy
Giuseppe Quaranta, Italy
Dane Quinn, USA
Vitomir Racic, Italy
Jose Ragot, France
Kumbakonam Rajagopal, USA
Gianluca Ranzi, Australia
Alain Rassineux, France
S.S. Ravindran, USA
Alessandro Reali, Italy
Oscar Reinoso, Spain
Nidhal Rezg, France
Ricardo Riaza, Spain
Gerasimos Rigatos, Greece
Eugenio Roanes-Lozano, Spain
Bruno G. M. Robert, France
José Rodellar, Spain
Rosana Rodriguez-Lopez, Spain
Ignacio Rojas, Spain
Carla Roque, Portugal
Debasish Roy, India
Gianluigi Rozza, Italy
Rubén Ruiz García, Spain
Antonio Ruiz-Cortes, Spain
Ivan D. Rukhlenko, Australia
Mazen Saad, France
Kishin Sadarangani, Spain
Mehrdad Saif, Canada
Miguel A. Salido, Spain
Roque J. Salterén, Spain
Francisco J. Salvador, Spain
Alessandro Salvini, Italy
Maura Sandri, Italy
Miguel A. F. Sanjuan, Spain
Juan F. San-Juan, Spain
Roberta Santoro, Italy
Ilmar Ferreira Santos, Denmark
José A. Sanz-Herrera, Spain
Nickolas S. Sapidis, Greece
Evangelos J. Sapountzakis, Greece
Andrey V. Savkin, Australia
Thomas Schuster, Germany
Mohammed Seaid, UK
Lotfi Senhadji, France
Joan Serra-Sagrsta, Spain
Gerardo Severino, Italy
Ruben Sevilla, UK
Leonid Shaikhet, Ukraine
Hassan M. Shanechi, USA
Bo Shen, Germany
Suzanne M. Shontz, USA
Babak Shotorban, USA
Zhan Shu, UK
Dan Simon, Greece
Luciano Simoni, Italy
Christos H. Skiadas, Greece
Michael Small, Australia
Alba Sofi, Italy
Francesco Soldovieri, Italy
Raffaele Solimene, Italy
Jussi Sopanen, Finland
Ruben Specogna, Italy
Sri Sridharan, USA
Ivanka Stamova, USA
Salvatore Strano, Italy
Yakov Strelniker, Israel
Sergey A. Suslov, Australia
Thomas Svensson, Sweden
Andrzej Swierniak, Poland
Yang Tang, Germany
Sergio Teggi, Italy
Alexander Timokha, Norway
Gisella Tomasini, Italy
Francesco Tornabene, Italy
Antonio Tornambe, Italy
Fernando Torres, Spain
Sébastien Tremblay, Canada
Irina N. Trendafilova, UK
George Tsiatas, Greece
Antonios Tsourdos, UK
Vladimir Turetsky, Israel
Mustafa Tutar, Spain
Ilhan Tuzcu, USA
Efstratios Tzirtzilakis, Greece
Filippo Ubertini, Italy
Francesco Ubertini, Italy
Hassan Ugail, UK
Giuseppe Vairo, Italy
Kuppalapalle Vajravelu, USA
Robertt A. Valente, Portugal
Pandian Vasant, Malaysia
Miguel E. Vázquez-Méndez, Spain



Josep Vehi, Spain
K. Veluvolu, Republic of Korea
Alessandro Veneziani, USA
Fons J. Verbeek, Netherlands
Franck J. Vernerey, USA
Georgios Veronis, USA
Anna Vila, Spain
Rafael Villanueva, Spain
Uchechukwu E. Vincent, UK
Mirko Viroli, Italy
Michael Vynnycky, Sweden

Shuming Wang, China
Yan-Wu Wang, China
Yongqi Wang, Germany
Roman Wendner, Austria
Desheng D. Wu, Canada
Yuqiang Wu, China
Guangming Xie, China
Xuejun Xie, China
Gen Qi Xu, China
Hang Xu, China
Joseph-Julien Yamé, France

Xing-Gang Yan, UK
Luis J. Yebra, Spain
Peng-Yeng Yin, Taiwan
Qin Yuming, China
Vittorio Zampoli, Italy
Ibrahim Zeid, USA
Huaguang Zhang, China
Qingling Zhang, China
Jian Guo Zhou, UK
Quanxin Zhu, China
Mustapha Zidi, France

Contents

Applications of Methods of Numerical Linear Algebra in Engineering 2016

Masoud Hajarian, Jinyun Yuan, and Ivan Kyrchei
Volume 2016, Article ID 4854759, 2 pages

Computing the Pseudoinverse of Specific Toeplitz Matrices Using Rank-One Updates

Predrag S. Stanimirović, Vasilios N. Katsikis, and Igor Stojanović
Volume 2016, Article ID 9065438, 16 pages

Application of the Value Optimization Model of Key Factors Based on DSEM

Chao Su and Zhiming Ren
Volume 2016, Article ID 3240720, 12 pages

Application of the Least Squares Method in Axisymmetric Biharmonic Problems

Vasyl Chekurin and Lesya Postolaki
Volume 2016, Article ID 3457649, 9 pages

Explicit Determinantal Representation Formulas of W -Weighted Drazin Inverse Solutions of Some Matrix Equations over the Quaternion Skew Field

Ivan I. Kyrchei
Volume 2016, Article ID 8673809, 13 pages

A General Solution to Least Squares Problems with Box Constraints and Its Applications

Yueyang Teng, Shouliang Qi, Dayu Xiao, Lisheng Xu, Jianhua Li, and Yan Kang
Volume 2016, Article ID 3934872, 11 pages

A Novel Control Strategy of DFIG Based on the Optimization of Transfer Trajectory at Operation Points in the Islanded Power System

Zengqiang Mi, Liqing Liu, He Yuan, Ping Du, and Yuliang Wan
Volume 2016, Article ID 3925879, 10 pages

A Joint Scheduling Optimization Model for Wind Power and Energy Storage Systems considering Carbon Emissions Trading and Demand Response

Yin Aiwei, Xu Congwei, and Ju Liwei
Volume 2016, Article ID 4070251, 10 pages

Parallelization of Eigenvalue-Based Dimensional Reductions via Homotopy Continuation

Size Bi, Xiaoyu Han, Jing Tian, Xiao Liang, Yang Wang, and Tinglei Huang
Volume 2016, Article ID 5815429, 9 pages

Editorial

Applications of Methods of Numerical Linear Algebra in Engineering 2016

Masoud Hajarian,¹ Jinyun Yuan,² and Ivan Kyrchei³

¹Shahid Beheshti University, General Campus, Evin, Tehran 19839-63113, Iran

²Centro Politécnico, Universidade Federal do Paraná, 81531-980 Curitiba, PR, Brazil

³National Academy of Sciences of Ukraine, Kiev, 3b Naukova Street, Lviv 79060, Ukraine

Correspondence should be addressed to Masoud Hajarian; m_hajarian@sbu.ac.ir

Received 13 July 2016; Accepted 13 July 2016

Copyright © 2016 Masoud Hajarian et al. This is an open access article distributed under the Creative Commons Attribution License, which permits unrestricted use, distribution, and reproduction in any medium, provided the original work is properly cited.

Methods of numerical linear algebra are concerned with the theory and practical aspects of computing solutions of mathematical problems in engineering such as image and signal processing, telecommunication, data mining, computational finance, bioinformatics, optimization, and partial differential equations. In recent years, applications of methods of numerical linear algebra in engineering have received a lot of attention and a large number of papers have proposed several methods for solving engineering problems. This special issue is devoted to publishing the latest and significant methods of numerical linear algebra for computing solutions of engineering problems.

We received thirty-two papers in the interdisciplinary research fields. This special issue includes eight high quality peer-reviewed articles.

In the following, we briefly review each of the papers that are published.

(1) In the paper entitled “Application of the Least Squares Method in Axisymmetric Biharmonic Problems” V. Chekurin and L. Postolaki develop an approach for solving the axisymmetric biharmonic boundary value problems for semi-infinite cylindrical domain.

(2) In the paper entitled “Explicit Determinantal Representation Formulas of W -Weighted Drazin Inverse Solutions of Some Matrix Equations over the Quaternion Skew Field” I. I. Kyrchei obtains explicit formulas for determinantal representations of the W -weighted Drazin inverse solutions (analog of Cramer’s rule) of the quaternion matrix equations.

(3) In the paper entitled “A General Solution to Least Squares Problems with Box Constraints and Its Applications”

Y. Teng et al. introduce a flexible solution to the box-constrained least squares problems. This solution is applicable to many existing problems, such as nonnegative matrix factorization, support vector machine, signal deconvolution, and computed tomography reconstruction.

(4) In the paper entitled “A Novel Control Strategy of DFIG Based on the Optimization of Transfer Trajectory at Operation Points in the Islanded Power System” Z. Mi et al. propose a novel control strategy based on the optimization of transfer trajectory at operation points for DFIG.

(5) In the paper entitled “A Joint Scheduling Optimization Model for Wind Power and Energy Storage Systems considering Carbon Emissions Trading and Demand Response” Y. Aiwei et al. introduce energy storage systems (ESSs) and demand response (DR) to the traditional scheduling model of wind power and thermal power with carbon emission trading (CET).

(6) In the paper entitled “Parallelization of Eigenvalue-Based Dimensional Reductions via Homotopy Continuation” S. Bi et al. investigate a homotopy-based method for embedding with hundreds of thousands of data items which yields a parallel algorithm suitable for running on a distributed system.

(7) In the paper entitled “Application of the Value Optimization Model of Key Factors Based on DSEM” C. Su and Z. Ren establish a value optimization model of key factors to control the simulation accuracy and computational efficiency of the soil-structure interaction.

(8) In the paper entitled “Computing the Pseudoinverse of Specific Toeplitz Matrices Using Rank-One Updates” P.

S. Stanimirović et al. present application of the pure rank-one update algorithm as well as a combination of rank-one updates and the Sherman-Morrison formula in computing the Moore-Penrose inverse of the particular Toeplitz matrix.

Acknowledgments

The editors of this special issue would like to express their gratitude to the authors who have submitted manuscripts for consideration. They also thank the many individuals who served as referees of the submitted manuscripts.

Masoud Hajarian

Jinyun Yuan

Ivan Kyrchei

Research Article

Computing the Pseudoinverse of Specific Toeplitz Matrices Using Rank-One Updates

Predrag S. Stanimirović,¹ Vasilios N. Katsikis,² and Igor Stojanović³

¹University of Niš, Faculty of Sciences and Mathematics, Višegradska 33, 18000 Niš, Serbia

²Department of Economics, Division of Mathematics and Informatics, National and Kapodistrian University of Athens, Sofokleous 1 Street, 10559 Athens, Greece

³Faculty of Computer Science, Goce Delčev University, Goce Delčev 89, 2000 Štip, Macedonia

Correspondence should be addressed to Predrag S. Stanimirović; pecko@pmf.ni.ac.rs

Received 29 February 2016; Accepted 3 July 2016

Academic Editor: Masoud Hajarian

Copyright © 2016 Predrag S. Stanimirović et al. This is an open access article distributed under the Creative Commons Attribution License, which permits unrestricted use, distribution, and reproduction in any medium, provided the original work is properly cited.

Application of the pure rank-one update algorithm as well as a combination of rank-one updates and the Sherman-Morrison formula in computing the Moore-Penrose inverse of the particular Toeplitz matrix is investigated in the present paper. Such Toeplitz matrices appear in the image restoration process and in many scientific areas that use the convolution. Four different approaches are developed, implemented, and tested on a number of numerical experiments.

1. Introduction

Let $\mathbb{C}^{m \times n}$ and $\mathbb{C}_r^{m \times n}$ denote the set of all complex $m \times n$ matrices and the set of all complex $m \times n$ matrices of rank r , respectively. The identity matrix of an appropriate order is denoted by I . The conjugate transpose, the range, the rank, and the null space of $A \in \mathbb{C}^{m \times n}$ are denoted by A^* , $\mathcal{R}(A)$, $\text{rank}(A)$, and $\mathcal{N}(A)$, respectively.

Representation and computation of various generalized inverses are closely related to the following Penrose equations:

$$\begin{aligned} AXA &= A, \\ XAX &= X, \\ (AX)^* &= AX, \\ (XA)^* &= XA. \end{aligned} \tag{1}$$

The set of all matrices obeying the conditions contained in a subset $\mathcal{S} \subseteq \{1, 2, 3, 4\}$ is denoted by $A\{\mathcal{S}\}$. Any matrix from $A\{\mathcal{S}\}$ is called \mathcal{S} -inverse of A and is denoted by $A^{(\mathcal{S})}$.

By $A\{\mathcal{S}\}_s$, we denote the set of all \mathcal{S} -inverses of A with rank s . For any matrix A there exists a single element in the set $A\{1, 2, 3, 4\}$, called the Moore-Penrose inverse of A and denoted by A^\dagger .

A rank-one modification of a matrix $A \in \mathbb{C}^{m \times n}$ is the matrix $M = A + bc^*$, which is created from A and two vectors $b \in \mathbb{C}^m$ and $c \in \mathbb{C}^n$. The Sherman-Morrison formula (S-M shortly) gives the basic relationship between the inverses M^{-1} and A^{-1} (for more details see, e.g., [1]):

$$M^{-1} = A^{-1} - \frac{1}{1 + c^* A^{-1} b} A^{-1} b c^* A^{-1}. \tag{2}$$

The identity (2) provides a numerically efficient way to compute the inverse M^{-1} of the rank-one update M . The S-M formula is important in many different fields of numerical computation; see for example [2–7].

On the other hand, Toeplitz matrices arise in a number of various theoretical investigations and applications. A number of iterative processes for finding generalized inverses of an arbitrary Toeplitz matrix by modifying Newton's method have been developed so far. The main results were stated in

[8–13]. Adaptations of the iterative processes to the Toeplitz structure are based on the usage of the displacement operator as well as the concept of displacement representation and ε -displacement rank of matrices.

A variety of methods for computing the Moore-Penrose inverse of a rank-one modified matrix have been developed so far. Main results were derived in [14–18]. Relationships between various generalized inverses of an arbitrary matrix and corresponding generalized inverses of its rank-one modifications were investigated in [19]. The leading idea in [15, 16] was successive computation of the symmetric rank-one (SRI) updates $(A_{i-1} + a_i a_i^*)^\dagger$ of a given matrix A , where a_i^* denotes the i th row of A and $A_{i-1} = \sum_{j=1}^{i-1} a_j a_j^*$. The authors of the paper [15] introduced a computational procedure for the Moore-Penrose inverse of a symmetric rank-one perturbed matrix. Using this method, the authors of [16] proposed a finite method for computing the minimum-norm least-squares solution of the linear system $Ax = b$.

The results derived in [20] reveal that both the SRI updates techniques and the S-M recursive rule are useful tools in the computation of various matrix products involving the Moore-Penrose inverse of certain symmetric matrices. Particularly, the algorithms introduced in [20] are numerically efficient in computation of $\{2, 4\}$ and $\{2, 3\}$ inverses.

In the present paper, we investigate the possibilities to apply the SRI update procedure and the S-M formula in the computation of the Moore-Penrose inverse of specific Toeplitz matrices that appear in the image restoration process. Our main motivation arises from the convenience to apply the SRI update and the S-M procedure in removing the blur which is always present in digital images. Firstly, both the SRI update and the S-M formula are based on the usage of columns (or rows) of the input matrix. On the other hand, the matrices which appear in the mathematical model of blur in computer-generated images possess very specific structure which can be used to accelerate SRI and S-M procedures. Namely, entries in Toeplitz matrices are constant along main diagonal parallels and, moreover, possess a significant proportion of zero elements.

The paper is organized as follows. Some basic notations and necessary facts are restated in Section 2. Also, some additional motivation is presented in the same section. Usage of the pure SRI update algorithm, proposed in [15], in the computation of the Moore-Penrose inverse of a kind of Toeplitz matrices is considered in Section 3. A hybrid combination of the SRI and the S-M recursive rules is defined in Section 4. An improvement of the SRI procedure, which is derived on the basis of the specific structure of the underlying Toeplitz matrix, is presented in the same section. An application of introduced methods in image restoration is presented in Section 5.

2. Preliminaries and Motivation

Toeplitz matrices or diagonally constant matrices are matrices having constant diagonal entries. Toeplitz matrices which are applicable in the image restoration process contain ℓ nonzero main diagonal parallels above the main diagonal,

where ℓ defines the blurring process. In what follows, let us consider the Toeplitz matrix of such form:

$$H = \begin{bmatrix} t_1 & t_2 & t_3 & \cdots & t_\ell & 0 & 0 & 0 & 0 & 0 & 0 & 0 \\ 0 & t_1 & t_2 & t_3 & \cdots & t_\ell & 0 & 0 & 0 & 0 & 0 & 0 \\ \vdots & \ddots & \ddots & \ddots & \ddots & \vdots & \ddots & \ddots & \ddots & \ddots & \vdots & \vdots \\ 0 & 0 & 0 & t_1 & t_2 & t_3 & \cdots & t_\ell & 0 & 0 & 0 & 0 \\ 0 & 0 & 0 & 0 & t_1 & t_2 & t_3 & \cdots & t_\ell & 0 & 0 & 0 \\ 0 & 0 & 0 & 0 & 0 & t_1 & t_2 & t_3 & \cdots & t_\ell & 0 & 0 \\ \vdots & \ddots & t_3 & \vdots & \ddots & \vdots \\ 0 & 0 & 0 & 0 & 0 & 0 & 0 & 0 & t_1 & t_2 & t_3 & \cdots & t_\ell \end{bmatrix}. \quad (3)$$

The assumption $t_1 \neq 0$ is active.

To clarify notation, Toeplitz matrices of the general form (3) will be denoted shortly by

$$\text{Tpl}(\{t_1\}, \{t_1, \dots, t_\ell\}). \quad (4)$$

We investigate the use of the SRI update method, as described in [15, Algorithm 2], during the numerical computation of the Moore-Penrose inverse of Toeplitz matrices satisfying the $\text{Tpl}(\{t_1\}, \{t_1, \dots, t_\ell\})$ pattern. Also, we examine different improvements of the original method. The improvements are based on appropriate adaptations of the SRI method and the S-M formula to the characteristic structure of underlying matrices of type $\text{Tpl}(\{t_1\}, \{t_1, \dots, t_\ell\})$. The method of SRI updates is based on the expression which computes the Moore-Penrose inverse of the first k columns of the initial matrix A using the Moore-Penrose inverse of its first $k - 1$ columns. In detail, the SRI method from [15] starts from the well-known representation $A^\dagger = (A^* A)^\dagger A^*$ of the Moore-Penrose. If the i th row of A is denoted by a_i^* , then

$$A^* A = \sum_{i=1}^m a_i a_i^*. \quad (5)$$

Chen and Ji in [15] defined the matrix sequences A_k and X_k , as

$$\begin{aligned} A_0 &= \mathbb{O} \in \mathbb{C}^{n \times n}, \\ A_k &= \sum_{i=1}^k a_i a_i^*, \quad k = 1, \dots, m, \\ X_k &= A_k^\dagger A^*, \quad k = 1, \dots, m. \end{aligned} \quad (6)$$

Clearly, $A_k = A_{k-1} + a_k a_k^*$ is the rank-one modification of A_{k-1} and

$$X_m = A_m^\dagger A^* = \left(\sum_{i=1}^m a_i a_i^* \right)^\dagger A^* = A^\dagger. \quad (7)$$

Recall that the Moore-Penrose inverse of a general rank-one modified matrix $M = A + bc^*$, where A is an arbitrary

TABLE I: Comparison of the rank-one updates method and the BP method.

Method	Sizes n, ℓ, s	CPU time	r_1	r_2	r_3	r_4
BP	50, 15, 10	0.0025	$2.0011e - 15$	$2.0385e - 14$	$3.773e - 15$	$1.6463e - 14$
SRI	50, 15, 10	0.0490	$2.2762e - 14$	$5.5984e - 13$	$1.2594e - 14$	$4.0623e - 13$
BP	50, 20, 10	0.0028	$6.9626e - 16$	$2.8774e - 14$	$3.4226e - 15$	$2.7706e - 14$
SRI	50, 20, 10	0.0364	$6.16e - 14$	$2.0705e - 12$	$1.3341e - 14$	$1.3718e - 12$
BP	50, 15, 500	0.0029	$8.0717e - 16$	$1.6354e - 14$	$3.7149e - 15$	$7.0839e - 15$
SRI	50, 15, 500	0.0501	$1.9666e - 14$	$4.8611e - 13$	$8.979e - 15$	$3.5898e - 13$
BP	50, 20, 500	0.0016	$6.8218e - 16$	$2.1407e - 14$	$3.2663e - 15$	$6.0107e - 15$
SRI	50, 20, 500	0.0362	$2.0844e - 14$	$5.3265e - 13$	$7.9594e - 15$	$4.1980e - 13$
BP	250, 15, 500	0.0059	$3.4724e - 15$	$2.3693e - 13$	$1.5467e - 14$	$7.4894e - 14$
SRI	250, 15, 500	23.9762	$7.81e - 12$	$3.6574e - 11$	$1.2707e - 13$	$2.2523e - 11$
BP	400, 20, 500	0.0135	$4.731e - 15$	$3.7769e - 13$	$2.6494e - 14$	$9.909e - 14$
SRI	400, 20, 500	320.0578	$3.8409e - 11$	$1.4246e - 10$	$2.2311e - 13$	$8.0923e - 11$

matrix and b, c are arbitrary vectors, is obtained in [14, Theorem 3.1.3]. The general theorem from [14] suggests six different cases that one has to follow in order to establish a relation between M^\dagger and A^\dagger . In [15], the authors proved that the real number $\beta_l = 1 + a_l^* A_{l-1}^\dagger a_l$, corresponding to the term $1 + c^* A^{-1} b$ in (2), satisfies $\beta_l \geq 1$. Later using this result in conjunction with the fact that A_l is a positive semidefinite matrix, the six cases of Theorem 3.1.3 from [14] can be reduced to the two-case problem. This reduction simplifies the SRI updates formulas.

Let us denote the first k columns of H by

$$H^{(k)} = [h^1 | \dots | h^k]. \quad (8)$$

Also, the last $n - k$ columns of H are denoted by ${}^{(k+1)}H^{(n)}$. Then the matrix H is given in the block form

$$\begin{aligned} H &= [H^{(m)} | {}^{(m+1)}H^{(n)}] \in \mathbb{C}^{m \times n}, \\ n &= m + \ell - 1, \quad \ell \geq 1, \\ H^{(m)} &\in \mathbb{C}^{m \times m}, \\ {}^{(m+1)}H^{(n)} &\in \mathbb{C}^{m \times (n-m)}, \end{aligned} \quad (9)$$

where the square block

$$H^{(m)} = \begin{bmatrix} t_1 & t_2 & t_3 & \dots & t_\ell & 0 & 0 & 0 \\ 0 & t_1 & t_2 & t_3 & \dots & t_\ell & 0 & 0 \\ \vdots & \vdots & \ddots & \ddots & \ddots & \vdots & \ddots & \vdots \\ 0 & 0 & 0 & t_1 & t_2 & t_3 & \dots & t_\ell \\ 0 & 0 & 0 & 0 & t_1 & t_2 & t_3 & \dots \\ 0 & 0 & 0 & 0 & 0 & t_1 & t_2 & t_3 \\ \vdots & \ddots & \ddots & \ddots & \ddots & \ddots & \ddots & \vdots \\ 0 & 0 & 0 & 0 & 0 & 0 & \dots & t_1 \end{bmatrix} \quad (10)$$

is the nonsingular band Toeplitz matrix and

$${}^{(m+1)}H^{(n)} = \begin{bmatrix} 0 & \dots & 0 & 0 \\ \vdots & \ddots & \ddots & \ddots \\ t_\ell & \dots & 0 & 0 \\ \dots & t_\ell & 0 & 0 \\ \vdots & \dots & \ddots & \vdots \\ t_2 & t_3 & \dots & t_\ell \end{bmatrix} \quad (11)$$

collects the last $n - m$ columns of H .

An application of Greville's partitioning method from [21] and the block partitioning method (BP method, shortly) from [22] in computing the Moore-Penrose inverse of the matrix H is presented in [23]. According to Algorithms 1 and 2 and Lemma 3 from [23], it is clear that the specific structure of matrix H enables computation H^\dagger simply by computing the inverse of the nonsingular block $H^{(m)}$.

In this paper, we investigate some alternative methods for computing H^\dagger using the SRI updates and the S-M formula. Our intention is to decrease computational complexity as much as possible using a specific structure of Toeplitz matrices of the general form $\text{Tpl}(\{t_1\}, \{t_1, \dots, t_\ell\})$.

3. Computing the Pseudoinverse of a Toeplitz Matrix by Rank-One Updates

Our first attempt consists in applying the unmodified SRI method from [15] in order to compute the pseudoinverse of the matrix H that belongs to the class $\text{Tpl}(\{t_1\}, \{t_1, \dots, t_\ell\})$. Obtained results are compared with corresponding results derived by applying Algorithm 2 from [23] (the BP method). The results of this comparison are presented in Table 1, where n, ℓ , and s are the parameters which define the Gaussian blur modeled by the Toeplitz matrix H . In the rest of the paper, it is assumed that the matrix H is of the order $m \times n$, where $n = m + \ell - 1$ and $\ell \geq 1$ represents the width of the blurring function.

TABLE 2: Comparison of the combination of AlgSRI and AlgBP methods and the block partitioning method.

Method	Sizes n, ℓ, s	CPU time	r_1	r_2	r_3	r_4
BP	50, 15, 10	0.0037	$2.0011e - 15$	$2.0385e - 14$	$3.773e - 15$	$1.6463e - 14$
HSRI + BP	50, 15, 10	0.0592	$2.6951e - 14$	$2.9305e - 13$	$1.3171e - 13$	$4.0769e - 14$
BP	50, 20, 10	$3.4243e - 04$	$6.9626e - 16$	$2.8774e - 14$	$3.4226e - 15$	$2.7706e - 14$
HSRI + BP	50, 20, 10	0.0305	$5.3084e - 14$	$4.1354e - 13$	$3.1072e - 13$	$9.9898e - 14$
BP	50, 15, 500	0.0019	$8.0717e - 16$	$1.6354e - 14$	$3.7149e - 15$	$7.0839e - 15$
HSRI + BP	50, 15, 500	0.0411	$2.1453e - 14$	$2.2518e - 13$	$7.0401e - 14$	$3.2624e - 14$
BP	50, 20, 500	$3.2256e - 04$	$6.8218e - 16$	$2.1407e - 14$	$3.2663e - 15$	$6.0107e - 15$
HSRI + BP	50, 20, 500	0.0288	$6.029e - 15$	$1.3385e - 13$	$2.6565e - 14$	$1.3927e - 14$
BP	250, 15, 500	0.0048	$3.4724e - 15$	$2.3693e - 13$	$1.5467e - 14$	$7.4894e - 14$
HSRI + BP	250, 15, 500	21.9978	$1.8868e - 12$	$3.4807e - 10$	$1.154e - 11$	$4.0825e - 12$
BP	400, 20, 500	0.0132	$4.731e - 15$	$3.7769e - 13$	$2.6494e - 14$	$9.909e - 14$
HSRI + BP	400, 20, 500	306.1949	$7.3251e - 12$	$2.7048e - 09$	$6.4634e - 11$	$2.0001e - 11$

If an approximation of H^\dagger is denoted by X , then the residual norms are denoted by

$$\begin{aligned}
r_1 &= \|HXH - H\|_2, \\
r_2 &= \|HXH - X\|_2, \\
r_3 &= \|(HX)^* - HX\|_2, \\
r_4 &= \|(XH)^* - XH\|_2.
\end{aligned} \tag{12}$$

For the sake of simplicity, let us denote Algorithm 2 from [15] by SRI and Algorithm 2 from [23] by BP.

From Table 1, it is observable that the SRI method is marginally efficient in terms of accuracy, but it is time consuming, especially for larger dimensions. There is a theoretical explanation for these results. The number of multiplications and divisions included in the SRI algorithm is about $O(m^2n + mn)$ in the case $m < n$ and $O(n^2m + mn)$ in the case $n < m$. Therefore, as it is stated in [15], the rank-one updates algorithm works efficiently in cases where it holds $m \ll n$ or $m \gg n$. In our case, $n = m + \ell - 1$, where $\ell \geq 1$ represents the width of the blurring process. Since, in the general case, ℓ is a relatively small integer, the conditions $m < n$ and $m \approx n$ are satisfied. This fact causes relative inefficiency of the SRI method.

Our second attempt is to apply Algorithm SRI to the matrix $H^{[m]}$, from (10), in order to generate its inverse. Then the Moore-Penrose inverse of H comes from the block partitioning method (called BP), as it was described in [23]. This approach is shortly denoted by HSRI + BP.

It is observable from Table 2 that the method HSRI + BP is marginally efficient in terms of accuracy, but it is time consuming; see, for example, the case $n = 400$.

From the previous analysis of data included in Tables 1 and 2, we conclude that both algorithms SRI and HSRI + BP are not efficient approaches for computing H^\dagger with respect to the BP method in terms of computational speed, especially for large matrices. But both approaches show marginal efficiency in terms of the accuracy.

4. A Combination of SRI Updates and S-M Formula

Two additional algorithms are defined in the current section. The first one uses the SRI updates to compute the matrix $H_m = H^{[m]}(H^{[m]})^*$ in the first step and the S-M formula to compute H_m^\dagger in the subsequent step. The second algorithm replaces the usage of the SRI updates from the first step by a direct construction of the matrix H_m . The matrix H_m can be generated efficiently in view of the specific structure of the input matrix H .

4.1. SRI Updates in Conjunction with the S-M Formula. As usual, the i th column of H is denoted by h^i . Then, since H is of full row rank, it is advantageous to define a proper SRI recursive computational method for generating the Moore-Penrose inverse of H on the basis of the relation

$$H^\dagger = H^* (HH^*)^{-1} = H^* \left(\sum_{i=1}^n h^i (h^i)^* \right)^{-1}. \tag{13}$$

For that purpose, it is necessary to define the matrix sequence

$$\begin{aligned}
H_0 &= \mathbb{O} \in \mathbb{C}^{m \times m}, \\
H_k &= \sum_{i=1}^k h^i (h^i)^* = H_{k-1} + h^k (h^k)^*, \quad k = 1, \dots, n.
\end{aligned} \tag{14}$$

Lemma 1 reveals some of basic properties of the sequence H_k . Following the notation from [20], the notation $h^k \in \mathcal{L}(h^1, \dots, h^{k-1})$ means that a column h^k is linearly dependent on the previous columns h^1, \dots, h^{k-1} and $h^k \notin \mathcal{L}(h^1, \dots, h^{k-1})$ indicates that h^k is linearly independent of h^1, \dots, h^{k-1} .

Lemma 1. *The following statements are valid:*

- (i) $h^k \notin \mathcal{L}(h^1, \dots, h^{k-1})$, for each $1 < k \leq n$.
- (ii) $\text{rank}(H_k) = \text{rank}(H_{k-1}) + 1$, for each $1 < k \leq n$.

(iii) $\text{rank}(H_k) < m$, for each $1 \leq k < m$, and $\text{rank}(H_k) = \text{rank}(H_{k-1}) = m$, for each $k = m + 1, \dots, n$.

(iv) The following concluding relation is valid:

$$H^* H_n^{-1} = H^\dagger. \quad (15)$$

Proof. (i) This part of the proof is implied by the fact that the columns of H are linearly independent.

(ii) According to the part (i), immediately follows $\text{rank}(H^{[k]}) = \text{rank}(H^{[k-1]}) + 1$, for each $1 < k \leq n$. Later, it is easy to verify

$$\begin{aligned} H_k &= \sum_{i=1}^k h^i (h^i)^* = \left[h^1 \mid \dots \mid h^k \right] \begin{bmatrix} (h^1)^* \\ \vdots \\ (h^k)^* \end{bmatrix} \\ &= H^{[k]} (H^{[k]})^*, \end{aligned} \quad (16)$$

which implies

$$\begin{aligned} \text{rank}(H_k) &= \text{rank}(H^{[k]}) = \text{rank}(H^{[k-1]}) + 1 \\ &= \text{rank}(H^{[k-1]} (H^{[k-1]})^*) + 1 \\ &= \text{rank}(H_{k-1}) + 1. \end{aligned} \quad (17)$$

(iii) This part of the proof can be verified by using (i) and (ii), together with the fact that H_k are all $m \times m$ matrices, for each $k = 1, \dots, n$.

(iv) According to part (iii), matrices H_k , $m \leq k \leq n$, are invertible. Since

$$H_n = H^{[n]} (H^{[n]})^* = HH^* \quad (18)$$

is invertible, then it holds

$$H^* H_n^{-1} = H^* (HH^*)^{-1} = H^\dagger, \quad (19)$$

which completes the proof. \square

Remark 2. According to Lemma 1 the matrices H_k are of the order $m \times m$ and it holds $\text{rank}(H_k) < m$, for each $1 \leq k < m$, while $\text{rank}(H_k) = \text{rank}(H_{k-1}) = m$, for each $k = m + 1, \dots, n$. Since $\text{rank}(H_n) = \text{rank}(HH^*) = m$, the invertibility of H_n is guaranteed, so that we are able to apply the S-M formula which relates H_k^{-1} with H_{k-1}^{-1} , for each $k = m + 1, \dots, n$.

According to Lemma 1, matrices H_k , $m \leq k \leq n$, are invertible. Therefore, it is possible to define the following matrix sequence:

$$X_k = H^* H_k^{-1}, \quad k = m, \dots, n. \quad (20)$$

Identity (15) immediately implies $X_n = H^\dagger$.

Lemma 3. It holds $1 + (h^k)^* H_{k-1}^{-1} h^k \geq 1$, for each $k = m + 1, \dots, n$.

Proof. The proof of lemma follows from the fact that H_{k-1} is regular, for each $k = m + 1, \dots, n$. \square

Now, we turn our attention to (20). Since the matrices H_{k-1} , $k = m + 1, \dots, n$ are regular, it is possible to find a relation between $H_k^{-1} = (H_{k-1} + h^k (h^k)^*)^{-1}$ and H_{k-1}^{-1} by applying the Sherman-Morrison formula (2). This relation is given in Proposition 4.

Proposition 4. Let the matrix H be defined as in (3). Assume that the matrix sequence H_k is defined in (14). The inverse of H_k is equal to

$$\begin{aligned} H_k^{-1} &= \left(H_{k-1} + h^k (h^k)^* \right)^{-1} \\ &= H_{k-1}^{-1} \\ &\quad - \left(1 + (h^k)^* H_{k-1}^{-1} h^k \right)^{-1} H_{k-1}^{-1} h^k (h^k)^* H_{k-1}^{-1}, \end{aligned} \quad (21)$$

for each $k = m + 1, \dots, n$.

In order to present the finite recursive algorithm for computing the Moore-Penrose inverse of H with the help of the actual SRI update formulas (20) and (21), we first define $H_0 = \mathbb{O} \in \mathbb{C}^{m \times m}$. For each $k = 1, \dots, m$, it is necessary to compute $H_k = H_{k-1} + h^k (h^k)^*$. This requires calculated values of the vectors $y_{m,t} = H_m^{-1} h^t \in \mathbb{C}^m$, $t = 1, \dots, n$ and the matrix $X_m = H^* H_m^{-1}$.

Theorem 5. Let the matrix H be defined as in (3), the matrix sequence H_k defined in (14), and the matrix sequence X_k defined in (20). Then the following recursive relations are true:

$$y_{k,t} = y_{k-1,t} - \frac{y_{k-1,k} (h^k)^* y_{k-1,t}}{1 + (h^k)^* y_{k-1,k}} \quad (22)$$

$$= \left(I_m - \frac{y_{k-1,k} (h^k)^*}{1 + (h^k)^* y_{k-1,k}} \right) \cdot y_{k-1,t},$$

$$X_k = X_{k-1} - \frac{H^* y_{k-1,k} (y_{k-1,k})^*}{1 + (h^k)^* y_{k-1,k}}. \quad (23)$$

Proof. Note that from $y_{l,t} = H_l^{-1} h^t$ it follows that $(y_{l,t})^* = (H_l^{-1} h^t)^* = (h^t)^* H_l^{-1}$. Based on the use of (21), the recursive sequences $y_{k,t}$ are defined for $k = m + 1, \dots, n$ as in the following:

$$\begin{aligned} y_{k,t} &= H_k^{-1} h^t = \left(H_{k-1} + h^k (h^k)^* \right)^{-1} h^t = \left(H_{k-1}^{-1} \right. \\ &\quad \left. - \left(1 + (h^k)^* H_{k-1}^{-1} h^k \right)^{-1} H_{k-1}^{-1} h^k (h^k)^* H_{k-1}^{-1} \right) h^t \\ &= H_{k-1}^{-1} h^t - \frac{H_{k-1}^{-1} h^k (h^k)^* H_{k-1}^{-1} h^t}{1 + (h^k)^* H_{k-1}^{-1} h^k}, \quad t = 1, \dots, n. \end{aligned} \quad (24)$$

Then the statement (22) can be easily verified using (24).

Also, matrices X_k , $k = m + 1, \dots, n$ are defined as

$$\begin{aligned}
 X_k &= H^* H_k^{-1} = H^* \left(H_{k-1}^{-1} \right. \\
 &\quad \left. - \left(1 + (h^k)^* H_{k-1}^{-1} h_k \right)^{-1} H_{k-1}^{-1} h^k (h^k)^* H_{k-1}^{-1} \right) \\
 &= H^* H_{k-1}^{-1} \\
 &\quad - H^* \left(\left(1 + (h^k)^* H_{k-1}^{-1} h^k \right)^{-1} G_{k-1}^{-1} h^k (h^k)^* H_{k-1}^{-1} \right) \\
 &= X_{k-1} - \frac{H^* H_{k-1}^{-1} h^k (h^k)^* H_{k-1}^{-1}}{1 + (h^k)^* H_{k-1}^{-1} h^k}.
 \end{aligned} \tag{25}$$

So, (23) holds. \square

According to Theorem 5, we present Algorithm 1 for computing the Moore-Penrose inverse of the Toeplitz matrix H . The algorithm is based on the SRI modifications to compute H_m and subsequently the S-M formula to compute H^\dagger . For this purpose, we use the abbreviation HSRI + S-M to denote Algorithm 1.

A *Matlab* implementation of Algorithm 1 is placed in Appendix.

4.2. An Improvement of the Hybrid Combination in Algorithm 1. By taking into account the fact that the Toeplitz matrix H has a specific structure, the matrix H_m can be generated in an efficient way. In this way, an improvement of step (1) of Algorithm 1 is introduced. The effectiveness of this method will be justified in the numerical experiments presented in Section 4.3.

According to the proper structure of the matrix H and step (1) of Algorithm 1, the general structure of the matrix H_m is defined as

$$H_m = \left[\begin{array}{cccccc|cccc}
 \sum_{i=1}^{\ell} t_i^2 & \sum_{i=1}^{\ell-1} t_i t_{i+1} & \sum_{i=1}^{\ell-2} t_i t_{i+2} & \cdots & \cdots & t_1 t_\ell & 0 & 0 & \cdots & \cdots & 0 \\
 \sum_{i=1}^{\ell-1} t_i t_{i+1} & \sum_{i=1}^{\ell} t_i^2 & \sum_{i=1}^{\ell-1} t_i t_{i+1} & \ddots & \ddots & \ddots & t_1 t_\ell & 0 & \ddots & \ddots & 0 \\
 \sum_{i=1}^{\ell-2} t_i t_{i+2} & \sum_{i=1}^{\ell-1} t_i t_{i+1} & \sum_{i=1}^{\ell} t_i^2 & \sum_{i=1}^{\ell-1} t_i t_{i+1} & \ddots & \ddots & \ddots & t_1 t_\ell & \ddots & \ddots & 0 \\
 \vdots & \ddots & \vdots \\
 \vdots & \ddots & \ddots & \ddots & \sum_{i=1}^{\ell} t_i^2 & \ddots & \ddots & \ddots & \ddots & \ddots & 0 \\
 \vdots & \ddots & \ddots & \ddots & \ddots & \sum_{i=1}^{\ell} t_i^2 & \ddots & \ddots & \ddots & \ddots & t_1 t_\ell \\
 \hline
 \vdots & \ddots & \ddots & \ddots & \ddots & \ddots & \sum_{i=1}^{\ell-1} t_i^2 & \ddots & \ddots & \ddots & t_1 t_{\ell-1} \\
 \vdots & \ddots & \vdots \\
 \vdots & \ddots & \sum_{i=1}^2 t_i t_{i+1} & \ddots & \vdots \\
 \vdots & \ddots & \sum_{i=1}^2 t_i t_{i+1} & \sum_{i=1}^2 t_i^2 & t_1 t_2 \\
 0 & \cdots & \cdots & \cdots & 0 & t_1 t_\ell & \cdots & \cdots & \cdots & t_1 t_2 & t_1^2
 \end{array} \right] \tag{26}$$

Let $w = (w_1, \dots, w_n)$ be one-dimensional vector; then the symmetric Toeplitz matrix generated by w is denoted by $\text{Toeplitz}(w)$:

$$\text{Toeplitz}(w) = \begin{bmatrix} w_1 & w_2 & w_3 & \cdots & w_n \\ w_2 & w_1 & w_2 & \cdots & w_{n-1} \\ \vdots & \ddots & \ddots & \ddots & \vdots \\ w_{n-1} & \cdots & \cdots & w_1 & w_2 \\ w_n & \cdots & \cdots & w_2 & w_1 \end{bmatrix}. \tag{27}$$

Also, for two appropriate vectors u, v , we denote by $F = \text{Hankel}(u, v)$ the (symmetric) Hankel matrix whose first column is u and whose last row is v .

Theorem 6. *The matrix H_m can be expressed as the difference of a specific banded symmetric Toeplitz matrix and a partitioned matrix of the form*

$$\left[\begin{array}{c|c} \mathbb{O}_{m-\ell+1} & \mathbb{O}_{(m-\ell+1) \times (\ell-1)} \\ \hline \mathbb{O}_{(\ell-1) \times (m-\ell+1)} & F_{\ell-1} \end{array} \right], \tag{28}$$

where the block $F_{\ell-1}$ is defined by $F_{\ell-1} = F^2$, for an appropriate Hankel matrix F .

Require: Start with $H \in \mathbb{C}^{m \times n}$ and $n > m$. Let h^i be the i th column of H , for $i = 1, \dots, n$, $H_0 = \mathbb{O} \in \mathbb{C}^{m \times m}$.

- (1) (SR1 Step) For $k = 1, \dots, m$, compute $H_k = H_{k-1} + h^k(h^k)^*$.
- (2) Set $y_{m,t} = H_m^{-1}h^t \in \mathbb{C}^m$ for all $t = 1, \dots, n$ and $X_m = H^*H_m^{-1}$.
- (3) (S-M Step) Compute $y_{l,t}$ and X_l by using (22) and (23), respectively for all $l = m + 1, \dots, n$.
- (4) Output $H^\dagger = X_n$.

 ALGORITHM 1: Computing the Moore-Penrose inverse of the Toeplitz matrix H .

Proof. Let u and v be vectors defined by

$$u = (t_\ell \ t_{\ell-1} \ \cdots \ t_2), \quad (29)$$

$$v = \left(\underbrace{0 \ \cdots \ 0}_{\ell-2} \ t_\ell \right), \quad (30)$$

respectively. Then we define the following matrices:

$$E = \text{Toeplitz} \left(\left(\sum_{i=1}^{\ell} t_i^2 \quad \sum_{i=1}^{\ell-1} t_i t_{i+1} \quad \sum_{i=1}^{\ell-2} t_i t_{i+2} \quad \cdots \quad t_1 t_\ell \quad \underbrace{0 \ \cdots \ 0}_{m-\ell} \right) \right), \quad (31)$$

$$F = \text{Hankel}(v, u),$$

$$L = \left[\begin{array}{c|c} \mathbb{O}_{m-\ell+1} & \mathbb{O}_{(m-\ell+1) \times (\ell-1)} \\ \hline \mathbb{O}_{(\ell-1) \times (m-\ell+1)} & F_{\ell-1} \end{array} \right], \quad F_{\ell-1} = F^2.$$

A simple verification shows that $H_m = E - L$. \square

Next we present an example, in low dimensions, in order to illustrate Theorem 6.

Example 7. Consider the Toeplitz matrix $H \in \mathbb{C}^{m \times n}$, defined in (3) for $m = 5$, $\ell = 3$, and $n = m + \ell - 1 = 7$:

$$H = [H^{[5]} \mid \{6\}H^{[7]}] = \left[\begin{array}{ccccc|cc} t_1 & t_2 & t_3 & 0 & 0 & 0 & 0 \\ 0 & t_1 & t_2 & t_3 & 0 & 0 & 0 \\ 0 & 0 & t_1 & t_2 & t_3 & 0 & 0 \\ 0 & 0 & 0 & t_1 & t_2 & t_3 & 0 \\ 0 & 0 & 0 & 0 & t_1 & t_2 & t_3 \end{array} \right]. \quad (32)$$

According to (14),

$$H_m = H_5 = H^{[5]} (H^{[5]})^* = \left[\begin{array}{ccccc} t_1^2 + t_2^2 + t_3^2 & t_1 t_2 + t_2 t_3 & t_1 t_3 & 0 & 0 \\ t_1 t_2 + t_2 t_3 & t_1^2 + t_2^2 + t_3^2 & t_1 t_2 + t_2 t_3 & t_1 t_3 & 0 \\ t_1 t_3 & t_1 t_2 + t_2 t_3 & t_1^2 + t_2^2 + t_3^2 & t_1 t_2 + t_2 t_3 & t_1 t_3 \\ 0 & t_1 t_3 & t_1 t_2 + t_2 t_3 & t_1^2 + t_2^2 & t_1 t_2 \\ 0 & 0 & t_1 t_3 & t_1 t_2 & t_1^2 \end{array} \right]. \quad (33)$$

We exploit the matrix

$$E = \text{Toeplitz} \left(\left(\sum_{i=1}^3 t_i^2 \quad \sum_{i=1}^2 t_i t_{i+1} \quad t_1 t_3 \quad 0 \quad 0 \right) \right) = \left[\begin{array}{ccccc} t_1^2 + t_2^2 + t_3^2 & t_1 t_2 + t_2 t_3 & t_1 t_3 & 0 & 0 \\ t_1 t_2 + t_2 t_3 & t_1^2 + t_2^2 + t_3^2 & t_1 t_2 + t_2 t_3 & t_1 t_3 & 0 \\ t_1 t_3 & t_1 t_2 + t_2 t_3 & t_1^2 + t_2^2 + t_3^2 & t_1 t_2 + t_2 t_3 & t_1 t_3 \\ 0 & t_1 t_3 & t_1 t_2 + t_2 t_3 & t_1^2 + t_2^2 + t_3^2 & t_1 t_2 + t_2 t_3 \\ 0 & 0 & t_1 t_3 & t_1 t_2 + t_2 t_3 & t_1^2 + t_2^2 + t_3^2 \end{array} \right]. \quad (34)$$

Let $u = (t_3 \ t_2)$ and $v = (0 \ t_3)$; then

$$F = \text{Hankel}(v, u) = \begin{bmatrix} 0 & t_3 \\ t_3 & t_2 \end{bmatrix}, \quad (35)$$

$$F^2 = \begin{bmatrix} t_3^2 & t_2 t_3 \\ t_2 t_3 & t_2^2 + t_3^2 \end{bmatrix}.$$

Finally, it is necessary to construct the matrix

$$L = \left[\begin{array}{cc|cc} \mathbb{O}_3 & \mathbb{O}_{3 \times 2} & & \\ \hline \mathbb{O}_{2 \times 3} & F^2 & & \end{array} \right] = \left[\begin{array}{ccc|cc} 0 & 0 & 0 & 0 & 0 \\ 0 & 0 & 0 & 0 & 0 \\ 0 & 0 & 0 & 0 & 0 \\ \hline 0 & 0 & 0 & t_3^2 & t_2 t_3 \\ 0 & 0 & 0 & t_2 t_3 & t_2^2 + t_3^2 \end{array} \right]. \quad (36)$$

It is easy to see that $H_5 = E - L$.

According to Theorem 6 we present the following improved version of Algorithm 1, called Algorithm 2. A *Matlab* implementation of Algorithm 2 is placed in Appendix. It is appropriate to use the term IHSRI to denote the improvement of the HSRI step of Algorithm 1 and IHSRI + S-M to denote Algorithm 2.

Note that proposed Algorithms 1 and 2 are not using directly, at any step, the Sherman-Morrison formula to compute the inverse of some matrix. In Section 4.4, we provide more information regarding this situation.

4.3. Numerical Experiments. In this subsection we analyze numerical data arising during the computation of the Moore-Penrose inverse of the Toeplitz matrix H by applying a *Matlab* implementation of Algorithms 1 and 2. In order to test the time efficiency as well as the accuracy of considered methods, we enrich our collection of matrices used in Tables

Require: Start with $H \in \mathbb{C}^{m \times n}$, $n > m$. Let h^i be the i th column of H , for $i = 1, \dots, n$.
 (1) (Improved HSR1 Step) Define E and L as in Theorem 6. Then, set $H_m = E - L$.
 (2) Set $y_{m,t} = H_m^{-1} h^t \in \mathbb{C}^m$ for all $t = 1, \dots, n$ and $X_m = H^* H_m^{-1}$.
 (3) (S-M Step) Compute $y_{l,t}$ and X_l by using (22) and (23), respectively for all $l = m + 1, \dots, n$.
 (4) Output $H^\dagger = X_n$.

ALGORITHM 2: Computing the Moore-Penrose inverse of the Toeplitz matrix H .

TABLE 3: Comparison of Algorithm 1 (HSR1 + S-M), Algorithm 2 (IHSR1 + S-M), and BP.

Method	Sizes n, ℓ, s	CPU time	r_1	r_2	r_3	r_4
HSR1 + S-M	50, 15, 10	0.0054	$1.6449e - 14$	$2.5845e - 12$	$3.5344e - 13$	$1.9362e - 14$
IHSR1 + S-M	50, 15, 10	0.0035	$2.0486e - 14$	$2.7318e - 12$	$5.4426e - 13$	$2.3222e - 14$
BP	50, 15, 10	0.0018	$2.0011e - 15$	$2.0385e - 14$	$3.773e - 15$	$1.6463e - 14$
HSR1 + S-M	50, 20, 10	0.0040	$1.8748e - 14$	$8.8674e - 13$	$2.2185e - 13$	$1.5379e - 14$
IHSR1 + S-M	50, 20, 10	0.0032	$9.4733e - 15$	$8.9539e - 13$	$1.9076e - 13$	$1.4775e - 14$
BP	50, 20, 10	0.0027	$9.2684e - 16$	$1.6646e - 14$	$3.2679e - 15$	$5.8648e - 15$
HSR1 + S-M	50, 20, 500	0.0053	$1.2862e - 14$	$9.6327e - 13$	$1.2288e - 13$	$1.4447e - 14$
IHSR1 + S-M	50, 20, 500	0.0044	$8.6971e - 15$	$1.5068e - 12$	$2.2331e - 13$	$1.5216e - 14$
BP	50, 20, 500	0.0022	$6.8218e - 16$	$2.1407e - 14$	$3.2663e - 15$	$6.0107e - 15$
HSR1 + S-M	250, 15, 500	0.0482	$2.5535e - 13$	$3.7054e - 11$	$4.7471e - 12$	$2.5608e - 13$
IHSR1 + S-M	250, 15, 500	0.0195	$2.209e - 13$	$3.7065e - 11$	$5.5401e - 12$	$2.4239e - 13$
BP	250, 15, 500	0.0032	$3.4724e - 15$	$2.3693e - 13$	$1.5467e - 14$	$7.4894e - 14$
HSR1 + S-M	400, 20, 500	0.3234	$4.5138e - 13$	$6.0769e - 10$	$1.4669e - 11$	$5.5243e - 13$
IHSR1 + S-M	400, 20, 500	0.1466	$5.881e - 13$	$6.0878e - 10$	$1.5866e - 11$	$5.3143e - 13$
BP	400, 20, 500	0.0116	$6.5483e - 15$	$6.052e - 13$	$3.0382e - 14$	$1.3117e - 13$
HSR1 + S-M	1200, 20, 500	11.0062	$3.0653e - 12$	$1.7107e - 08$	$1.4049e - 10$	$3.2612e - 12$
IHSR1 + S-M	1200, 20, 500	2.3018	$3.5064e - 12$	$1.711e - 08$	$1.3136e - 10$	$3.1795e - 12$
BP	1200, 20, 500	0.1049	$1.2805e - 14$	$3.179e - 12$	$8.9833e - 14$	$2.3321e - 13$
HSR1 + S-M	1500, 20, 500	21.7539	$4.3812e - 12$	$3.2457e - 08$	$2.2848e - 10$	$4.2712e - 12$
IHSR1 + S-M	1500, 20, 500	3.7358	$4.2345e - 12$	$3.2456e - 08$	$2.0156e - 10$	$4.2919e - 12$
BP	1500, 20, 500	0.1886	$1.3786e - 14$	$4.0422e - 12$	$1.1081e - 13$	$3.0133e - 13$
HSR1 + S-M	2000, 50, 500	74.5230	$5.5113e - 12$	$4.6497e - 08$	$5.1185e - 10$	$6.7183e - 12$
IHSR1 + S-M	2000, 50, 500	30.8622	$5.3682e - 12$	$4.6504e - 08$	$5.4329e - 10$	$6.6102e - 12$
BP	2000, 50, 500	0.4038	$1.8118e - 14$	$6.5462e - 12$	$1.408e - 13$	$3.6715e - 13$

1 and 2 with larger matrices. In order to complete our numerical study, we also compare the results derived by applying Algorithm 2 from [23] (Algorithm BP). A comparison of Algorithms 1 and 2 and BP is presented in Table 3.

From Table 3, it is observable that the level of improvement in CPU time that can be achieved by using Algorithm 2 instead of Algorithm 1 is significant. Also, it is clear that the accuracy of both algorithms is almost the same. Clearly, the BP method requires minimal CPU time.

4.4. Rounding Error Analysis. The starting motivation of this subsection is the following basic problem: approximation error grows with repeated use of the S-M formula. As a consequence, computations which involve the S-M rule become unstable. For this purpose, it is interesting to investigate the

error curves corresponding to the four Penrose equations during the iterations included in step (3) of Algorithm 2. Nevertheless, it is important to note that the proposed Algorithm 2 does not use in each step the S-M rule. Of course, Theorem 5 is in the heart of Algorithm 2 but also it is clear that the poor stability of the S-M formula has no serious influence on the stability of proposed algorithms.

So, in this subsection, we shall present error estimations regarding Algorithm 2. That is, we record and investigate the residual matrix norms r_1, r_2, r_3 , and r_4 , corresponding to the four Penrose equations during the execution of step (3) of Algorithm 2. The results are presented in Figures 1, 2, and 3 for the cases: (a) $n = 1200, l = 20$, and $s = 500$, (b) $n = 1500, l = 20$, and $s = 500$, and (c) $n = 2000, l = 20$, and $s = 500$, respectively. The choice of these matrices from Table 3 is random.

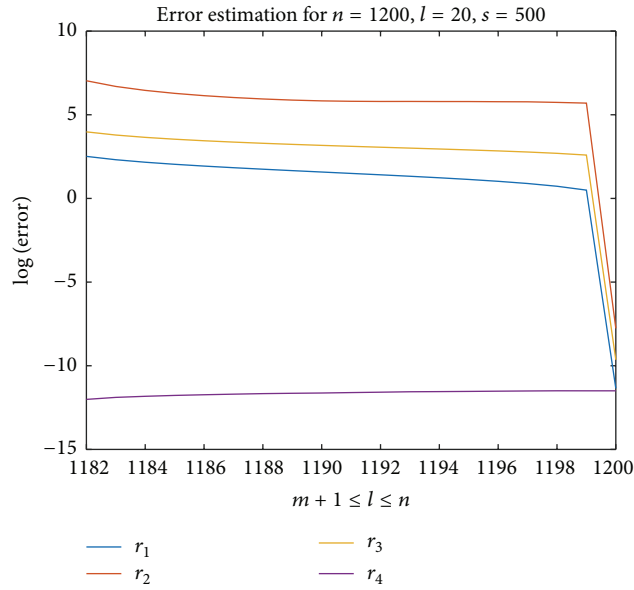


FIGURE 1: Errors recorded for $n = 1200$, $l = 20$, and $m = 500$ while the loop of step (3) is iterating.

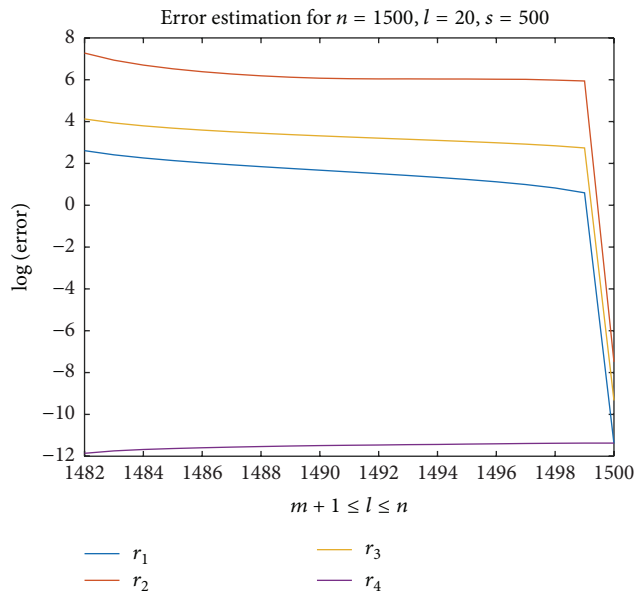


FIGURE 2: Errors recorded for $n = 1500$, $l = 20$, and $m = 500$ while the loop of step (3) is iterating.

The purple line in each of Figures 1–3 corresponds to the values of the matrix norm $\|(X_l H)^* - X_l H\|_2$, $l = m + 1, \dots, n$. Since $X_l = H^* H_l^{-1}$ and the matrix H_l is symmetric, the matrix $X_l H$ is symmetric. For this reason, the graph corresponding to these values is almost a constant line.

The stable convergence is observable from each of these figures. Also, it is possible to notice very fast convergence in the terminal phase of the convergence as well as a relatively slower convergence in the middle of the recurrent process. This fact is understandable if one takes into account that it is necessary to take into consideration all the columns of the

input matrix in order to get the complete information on the pseudoinverse.

5. Application in Image Restoration

Several image restoration examples are presented in this subsection. Experiments are done using Matlab programming package on an Intel(R) Core(TM) i5-2540M CPU @ 2.6 GHz 64-bit system with 8 GB RAM memory.

Numerical results corresponding to the Moore-Penrose inverse are derived using Algorithm 2. Results are derived using $n = 1200$ and $s = 100$ and different values of ℓ . Suppose

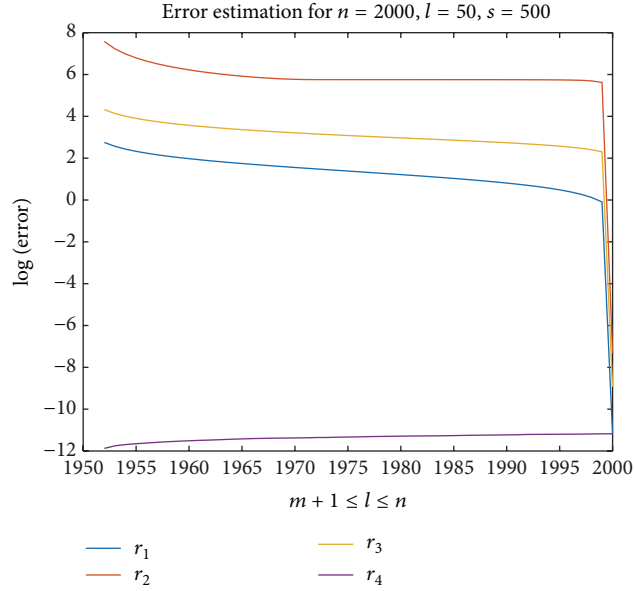


FIGURE 3: Errors recorded for $n = 2000, l = 50$, and $m = 500$ while the loop of step (3) is iterating.

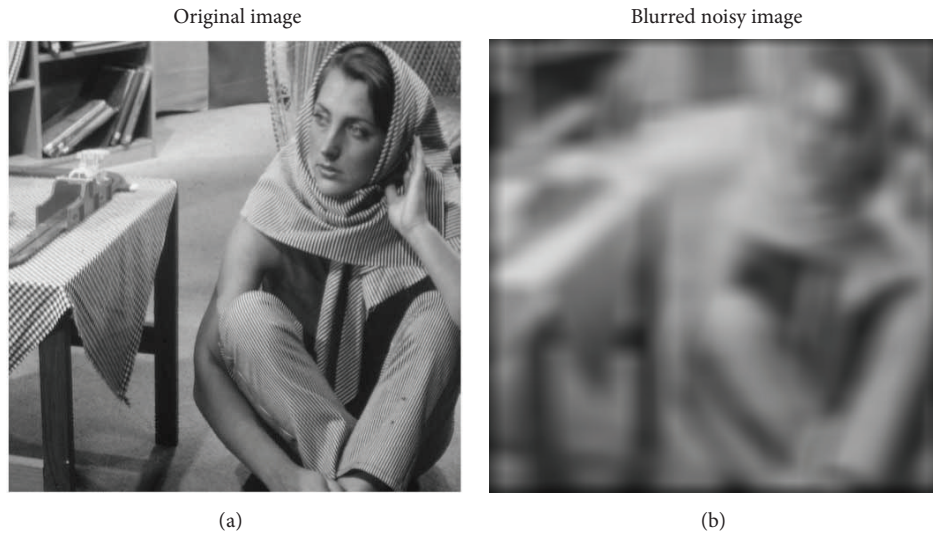


FIGURE 4: (a) Image of Barbara. (b) Blurred noisy image of Barbara.

that the matrix $F \in \mathbb{R}^{r \times m}$ corresponds to the original image and $G \in \mathbb{R}^{r \times m}$ is the matrix corresponding to the degraded image.

The model of the nonuniform blurring is the same as in [23] and assumes that the blurring of columns in the image is independent with respect to the blurring of its rows. Therefore, the relations between the original and the blurred image are expressed by the matrix equation

$$G = H_C F H_R^T, \quad (37)$$

$$G \in \mathbb{R}^{r \times m}, H_C \in \mathbb{R}^{r \times n}, F \in \mathbb{R}^{n \times t}, H_R \in \mathbb{R}^{m \times t},$$

where $n = r + \ell_c - 1$, $t = m + \ell_r - 1$, ℓ_c is length of the vertical blurring, and ℓ_r is length of the horizontal blurring

(in pixels). Following the approach used in [23], the Moore-Penrose inverse approach is used to restore the blurred image G , which produces the next approximation of F :

$$\tilde{F} = H_C^\dagger G (H_R^\dagger)^T. \quad (38)$$

The algorithm for computing the Moore-Penrose inverse of the blurring matrix used in [24, 25] is based on the method for computing the Moore-Penrose inverse of a full rank matrix, introduced in [26, 27]. In our case, we use Algorithm 2.

The first approach is based on the usage of the pure SRI update algorithm, proposed in [15]. The second approach starts with the SRI update algorithm and, after its completion, continues with the BP method. The third approach is a hybrid combination which comprises the SRI updates in the first

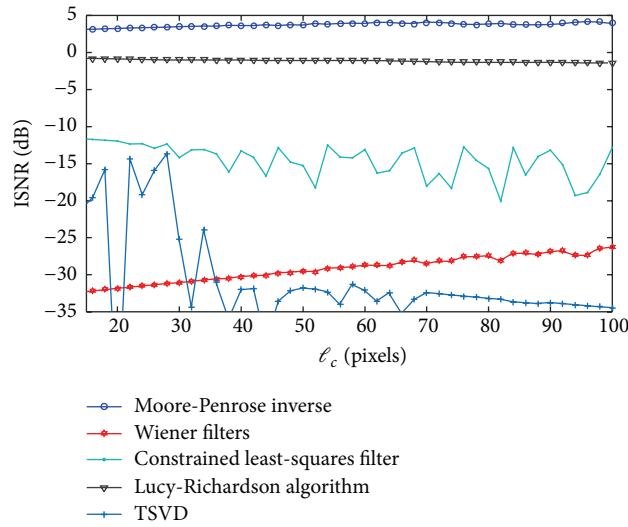


FIGURE 5: ISNR versus ℓ_c for the removal of Gaussian white noise with zero mean and variance 0.05 and Gaussian blur ($\ell_r = 35, s = \ell_r/2$, and $s = \ell_c/2$) for Barbara image.

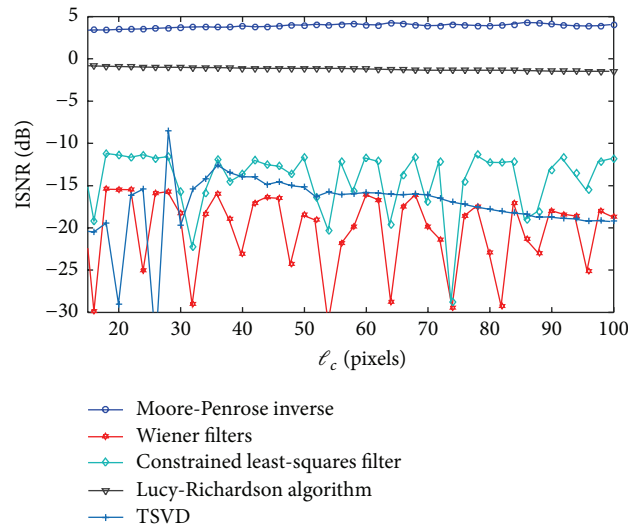


FIGURE 6: ISNR versus ℓ_c for the removal of Gaussian white noise with zero mean and variance 0.05 and Gaussian blur ($\ell_r = 35$, and $s = 100$) for Barbara image.

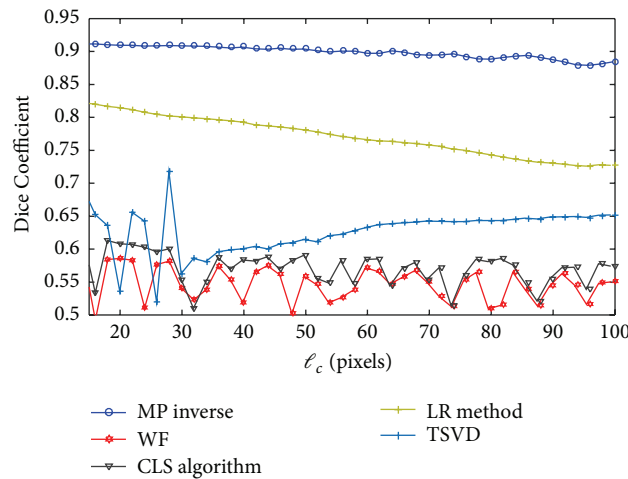


FIGURE 7: DC versus ℓ_c for the removal of Gaussian white noise with zero mean and variance 0.05 and Gaussian blur ($\ell_r = 35$, and $s = 100$) for Barbara image.



FIGURE 8: (a) Moore-Penrose restored image. (b) Lucy-Richardson restored image.

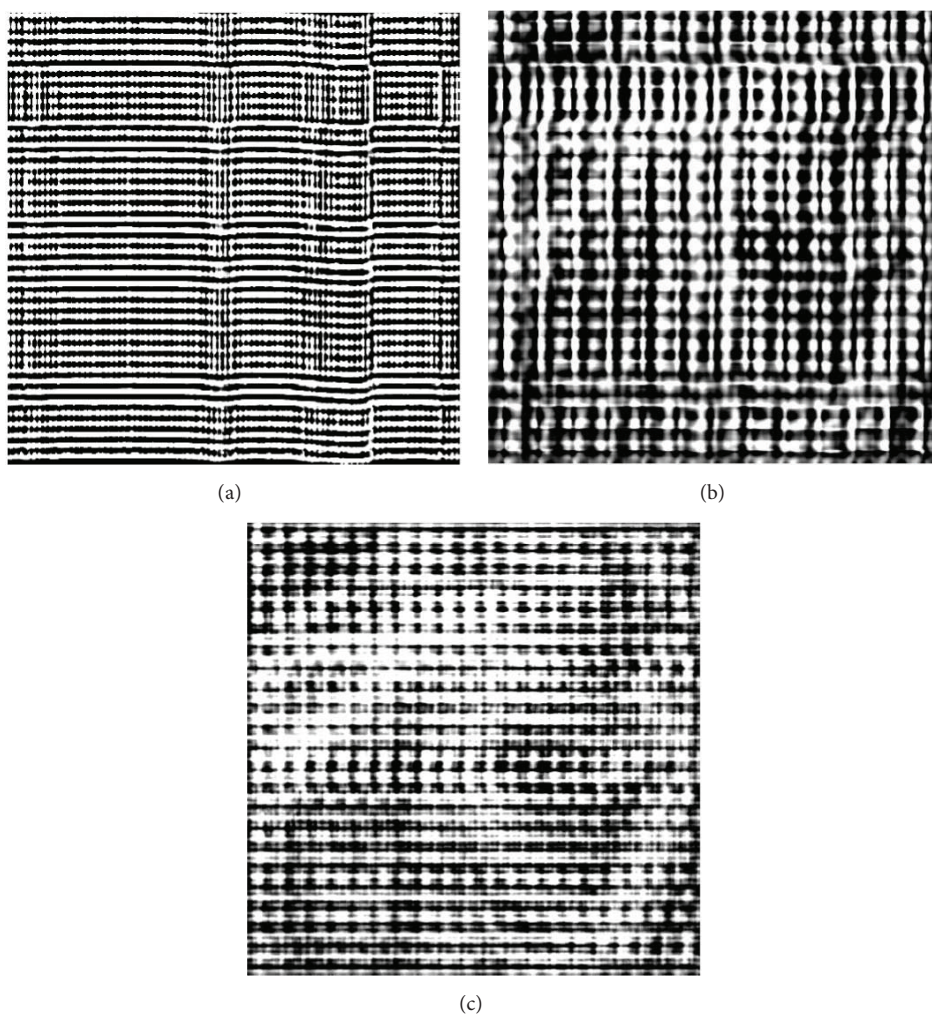


FIGURE 9: (a) Wiener filter restored image, (b) constrained least-squares filter restored image, and (c) truncated singular value decomposition restored image.

```

function alg41 = alg41(A)
%*****%
% General Information.           %
%*****%
% Synopsis:
% alg41 = alg41(A)
% Input:
% A = the initial matrix of interest.
% Output:
% alg41 = mp-inverse by using rank-one updates and the Sherman-Morrison formula.
% This function follows Algorithm 1.
% The correct performance of alg41b requires the presence of yltXl function.

Astar = A';
[m,n] = size(A);
GO = zeros(m,m);
if m > 1
    for i = 1:m-1
        Gkout = GO+A(:,i)*Astar(i,:);
        GO = Gkout;
    end

    Gm = Gkout+A(:,m)*Astar(m,:);
else
    Gm = GO;
end

Gkout = Gm;
Y02 = Gkout\A;
X02 = Y02';

for l = m+1:n-1
    [yltout,Xlout] = yltXl(Y02,X02,Astar,l,m,n);
    Y02 = yltout;
    X02 = Xlout;
end
alg41 = X02 - Astar*Y02(:,n)*Y02(:,n)'/(1+Astar(n,:)*Y02(:,n));

```

ALGORITHM 3

step and the S-M formula in the second phase (Algorithm 1). The fourth approach is based on the improvement of the SRI update step method of Algorithm 1, which leads to Algorithm 2 with the best performances. The improvement is achieved using the specific structure of the underlying Toeplitz matrix.

The most popular algorithm for image restoration based on the matrix pseudoinverse is developed using the singular value decomposition (SVD) [28]. But, the SVD is sensitive to singular values very close to zero. For this purpose, it is common approach to leave out small singular values, corresponding to high-frequency components. The resulting method is known as the truncated SVD (or TSVD shortly) [28]. On the other hand, the methods proposed in the present paper are based on different approach and do not require any kind of the regularization. In order to verify the applicability of the proposed method in the image restoration, we present

a comparison of results generated by the TSVD and the rank-one updates.

Parameters of Barbara image degradation are $\ell_r = 39$, $\ell_c = 25$, $s = \ell_r/2$, and $s = \ell_c/2$ and salt pepper noise with the noise density of 0.05 is assumed. The original and damaged image are presented in Figure 4.

Comparison with the state-of-the-art methods in image processing is presented. Many of them are constrained least-squares filter (CLS); Wiener filter (WF); Lucy-Richardson algorithm (LR); and truncated singular value decomposition (TSVD) [28]. Improvements in signal-to-noise ratio (ISNR) and Dice Coefficient (DC) are considered.

Results corresponding to ISNR values are presented in Figures 5 and 6.

Values corresponding to Dice Coefficient (DC) [29, 30] are presented in Figure 7.

Restored images are presented in Figures 8 and 9.

```

function alg42 = alg42(A,ll)
%*****%
% General Information.      %
%*****%
% Synopsis:
% alg42 = alg42(A)
% Input:
% A = the mxn initial matrix of interest.
% ll=n-m+1
% Output:
% alg42 = improvement of Algorithm 1 according to Theorem 6.
% This function follows Algorithm 2.
% The correct performance of alg42 requires the presence of yltX1 function.

Astar = A';
[m,n] = size(A);

f = A(1,1:ll);
E0 = zeros(1,m);
product = f'*f;

for i = 1:ll
    E0(1,i) = sum(diag(product,i-1));
end
E1=E0;
E = toeplitz(E1);

G0=zeros(ll-1);
Gnew = hankel([zeros(1,ll-2) f(end)], flip(f(1,2:end)));
for i = 1:ll-1
    Gkoutnew = G0+Gnew(:,i)*Gnew(i,:);
    G0=Gkoutnew;
end

Gmnew = G0;
fullmatrix = [zeros(m-ll+1) zeros(m-ll+1,ll-1);zeros(ll-1,m-ll+1) Gmnew];
Gkout = E-fullmatrix;
Y02 = Gkout\A;
X02 = Y02';

for l = m+1:n-1
    [yltout,Xlout] = yltX1(Y02,X02,Astar,l,m,n);
    Y02 = ylout;
    X02 = Xlout;
end

alg42 = X02 - Astar*Y02(:,n)*Y02(:,n)'/(1+Astar(n,:)*Y02(:,n));

```

ALGORITHM 4

6. Conclusion

The present paper investigates the application of the SRI updates procedure and S-M formula in computation of the Moore-Penrose inverse of specific Toeplitz matrices that appear in the image restoration process.

The first approach is based on the usage of the pure SRI update algorithm, proposed in [15]. The second approach starts with the SRI update algorithm and, after its completion, continues with the BP method. The third approach is a hybrid

combination which comprises the SRI updates in the first step and the S-M formula in the second phase (Algorithm 1). The fourth approach is based on the improvement of the SRI update step method of Algorithm 1, which leads to Algorithm 2 with the best performances. The improvement is achieved using the specific structure of the underlying Toeplitz matrix.

An application of Algorithm 2 in image restoration is considered. In this case, a comparison with the modified BP method from [23] is presented.

```

function [yltout,Xlout] = yltX1(Y0,X0,G,l,m,n)
d = n-1;
Y0l = Y0(:,1);
g = 1+G(1,:)*Y0l;
g1 = Y0l*G(1,:);
multiplier = eye(m)-g1/g;
Y0lherm = Y0l*Y0l';
Xl = X0 - G*Y0lherm/g;
Xlout = Xl;

ylt = zeros(m,n);
for i = 1:d
    t = l+i;
    ylt(:,t) = multiplier*Y0(:,t);
yltout = ylt;
end

```

ALGORITHM 5

Appendix

The *Matlab* implementation of Algorithm 1 is given in Algorithm 3 under the function alg41. Note that the correct performance of the function alg41 requires the presence of yltX1 function for computing the sequences $y_{k,t}$ and X_k .

The *Matlab* implementation of Algorithm 2 is given in Algorithm 4 under the function alg42. Note that the correct performance of alg42 requires the presence of yltX1 function for computing the sequences $y_{k,t}$ and X_k .

The yltX1 Function. See Algorithm 5.

Competing Interests

The authors declare that there is no conflict of interests regarding the publication of this paper.

Acknowledgments

Predrag S. Stanimirović gratefully acknowledges support from the Research Project 174013 of the Serbian Ministry of Science. Vasilios N. Katsikis gratefully acknowledges that this work was carried out at the Department of Economics, University of Athens, Greece, and supported by Special Account Research Grant 11698. Predrag S. Stanimirović and Igor Stojanović gratefully acknowledge support from the Project “Applying Direct Methods for Digital Image Restoring” of the Goce Delčev University.

References

- [1] D. K. Faddeev and V. N. Faddeeva, *Computational Methods of Linear Algebra*, W.H. Freeman, San Francisco, Calif, USA, 1963.
- [2] C. G. Broyden, “A class of methods for solving nonlinear simultaneous equations,” *Mathematics of Computation*, vol. 19, pp. 577–593, 1965.
- [3] R. Bru, J. Cerdán, J. Marín, and J. Mas, “Preconditioning sparse nonsymmetric linear systems with the Sherman-Morrison formula,” *SIAM Journal on Scientific Computing*, vol. 25, no. 2, pp. 701–715, 2003.
- [4] A. S. Householder, *The Theory of Matrices in Numerical Analysis*, Blaisdell Publishing, New York, NY, USA, 1964.
- [5] P. Maponi, “The solution of linear systems by using the Sherman-Morrison formula,” *Linear Algebra and its Applications*, vol. 420, no. 2-3, pp. 276–294, 2007.
- [6] K. Moriya, L. Zhang, and T. Nodera, “An approximate matrix inversion procedure by parallelization of the Sherman-Morrison formula,” *The ANZIAM Journal*, vol. 51, no. 1, pp. 1–9, 2009.
- [7] E. D. Nino-Ruiz, A. Sandu, and J. Anderson, “An efficient implementation of the ensemble Kalman filter based on an iterative Sherman-Morrison formula,” *Statistics and Computing*, vol. 25, no. 3, pp. 561–577, 2015.
- [8] D. Bini and B. Meini, “Approximate displacement rank and applications,” in *Structured Matrices in Mathematics, Computer Science and Engineering II*, V. Olshevsky, Ed., vol. 281 of *Contemporary Mathematics*, pp. 215–232, American Mathematical Society, Rhode Island, RI, USA, 2001.
- [9] D. A. Bini, G. Codevico, and M. Van Barel, “Solving Toeplitz least squares problems by means of Newton’s iteration,” *Numerical Algorithms*, vol. 33, no. 1–4, pp. 93–103, 2003.
- [10] J.-F. Cai, M. K. Ng, and Y.-M. Wei, “Modified Newton’s algorithm for computing the group inverses of singular Toeplitz matrices,” *Journal of Computational Mathematics*, vol. 24, no. 5, pp. 647–656, 2006.
- [11] M. Miladinović, S. Miljković, and P. Stanimirović, “Modified SMS method for computing outer inverses of Toeplitz matrices,” *Applied Mathematics and Computation*, vol. 218, no. 7, pp. 3131–3143, 2011.
- [12] W. R. Trench, “An algorithm for the inversion of finite Toeplitz matrices,” *SIAM: SIAM Journal on Applied Mathematics*, vol. 12, no. 3, pp. 515–522, 1964.
- [13] Y. Wei, J. Cai, and M. K. Ng, “Computing Moore-Penrose inverses of Toeplitz matrices by Newton’s iteration,” *Mathematical and Computer Modelling*, vol. 40, no. 1-2, pp. 181–191, 2004.
- [14] S. L. Campbell and C. D. Meyer, *Generalized Inverses of Linear Transformations*, Pitman, London, UK, 1979.
- [15] X. Chen and J. Ji, “Computing the Moore-Penrose inverse of a matrix through symmetric rank-one updates,” *American Journal of Computational Mathematics*, vol. 1, no. 3, pp. 147–151, 2011.
- [16] X. Chen and J. Ji, “The minimum-norm least-squares solution of a linear system and symmetric rank-one updates,” *Electronic Journal of Linear Algebra*, vol. 22, pp. 480–489, 2011.
- [17] X. Chen, “The generalized inverses of perturbed matrices,” *International Journal of Computer Mathematics*, vol. 41, no. 3-4, pp. 223–236, 1992.
- [18] C. D. Meyer Jr., “Generalized inversion of modified matrices,” *SIAM Journal on Applied Mathematics*, vol. 24, pp. 315–323, 1973.
- [19] J. K. Baksalary and O. M. Baksalary, “Relationships between generalized inverses of a matrix and generalized inverses of its rank-one-modifications,” *Linear Algebra and Its Applications*, vol. 388, pp. 31–44, 2004.
- [20] P. S. Stanimirović, V. N. Katsikis, and D. Pappas, “Computing 2,4 and 2,3-inverses by using the Sherman-Morrison formula,” *Applied Mathematics and Computation*, vol. 273, pp. 584–603, 2016.

- [21] T. N. E. Grevile, "Some applications of the pseudo-inverse of matrix," *SIAM Review*, vol. 3, pp. 15–22, 1960.
- [22] F. E. Udvardia and R. E. Kalaba, "General forms for the recursive determination of generalized inverses: unified approach," *Journal of Optimization Theory and Applications*, vol. 101, no. 3, pp. 509–521, 1999.
- [23] P. S. Stanimirović, M. Miladinović, I. Stojanović, and S. Miljković, "Application of the partitioning method to specific Toeplitz matrices," *International Journal of Applied Mathematics and Computer Science*, vol. 23, no. 4, pp. 809–821, 2013.
- [24] S. Chountasis, V. N. Katsikis, and D. Pappas, "Applications of the Moore-Penrose inverse in digital image restoration," *Mathematical Problems in Engineering*, vol. 2009, Article ID 170724, 12 pages, 2009.
- [25] S. Chountasis, V. N. Katsikis, and D. Pappas, "Digital image reconstruction in the spectral domain utilizing the Moore-Penrose inverse," *Mathematical Problems in Engineering*, vol. 2010, Article ID 750352, 14 pages, 2010.
- [26] S. Karanasios and D. Pappas, "Generalized inverses and special type operator algebras," *Facta Universitatis, Series: Mathematics and Informatics*, vol. 21, pp. 41–48, 2006.
- [27] V. N. Katsikis and V. D. Pappas, "Fast computing of the Moore-Penrose inverse matrix," *Electronic Journal of Linear Algebra*, vol. 17, pp. 637–650, 2008.
- [28] P. C. Hansen, J. G. Nagy, and D. P. O'Leary, *Deblurring Images: Matrices, Spectra, and Filtering*, SIAM, Philadelphia, Pa, USA, 2006.
- [29] R. C. Craddock, G. A. James, P. E. Holtzheimer III, X. P. Hu, and H. S. Mayberg, "A whole brain fMRI atlas generated via spatially constrained spectral clustering," *Human Brain Mapping*, vol. 33, no. 8, pp. 1914–1928, 2012.
- [30] L. R. Dice, "Measures of the amount of ecologic association between species," *Ecology*, vol. 26, no. 3, pp. 297–302, 1945.

Research Article

Application of the Value Optimization Model of Key Factors Based on DSEM

Chao Su and Zhiming Ren

College of Water Conservancy and Hydropower Engineering, Hohai University, Nanjing 210098, China

Correspondence should be addressed to Zhiming Ren; renzhiming1101@outlook.com

Received 14 March 2016; Accepted 7 June 2016

Academic Editor: Ivan Kyrchei

Copyright © 2016 C. Su and Z. Ren. This is an open access article distributed under the Creative Commons Attribution License, which permits unrestricted use, distribution, and reproduction in any medium, provided the original work is properly cited.

The key factors of the damping solvent extraction method (DSEM) for the analysis of the unbounded medium are the size of bounded domain, the artificial damping ratio, and the finite element mesh density. To control the simulation accuracy and computational efficiency of the soil-structure interaction, this study establishes a value optimization model of key factors that is composed of the design variables, the objective function, and the constraint function system. Then the optimum solutions of key factors are obtained by the optimization model. According to some comparisons of the results provided by the different initial conditions, the value optimization model of key factors is feasible to govern the simulation accuracy and computational efficiency and to analyze the practical unbounded medium-structure interaction.

1. Introduction

The rationality of numerical simulation in seismic loads plays an important role in the dynamic response analysis of the soil-structure interaction. With the development of science and technology, the research and application into the soil-structure interaction are of interest to those in the engineering profession and academia. Moreover, many researches on the unbounded media-structure interaction improve the rationality and accuracy of the foundations in frequency and time domains.

The methods for analyzing the soil-structure interaction are currently the artificial boundary method, the boundary element method, and the damping solvent extraction method. The artificial boundary method [1, 2] intercepts the bounded domain and increases the energy transfer system at the outer boundary (such as by a damper or spring-damper). But this method is not appropriate for analyzing an irregular foundation. The boundary element method [3] proposes the principle of wave amplitude attenuation of various frequencies far afield and makes a transformation into the time domain. Likewise, this method has a low computational efficiency and does not analyze a complicated unbounded media. However, through introducing and extracting the

artificial damping ratio of the bounded medium, the damping solvent extraction method [4, 5] is appropriate for the simulation of the various foundations. Meanwhile, the DSEM implements the mutual conversion in the frequency-time domain and eliminates the convolution operation in the time domain.

Since the DSEM was first presented by Wolf and Song in 1994, some researches have presented gradually the perfect basis theory, the improved computational procedure, and the evaluation of key factors of the soil-structure interaction. In the computational algorithm, a series of calculation procedures had been suggested to improve the accuracy, such as the acceleration input stagger method [6], the precise step-by-step time integration scheme [7], and the subregional explicit implicit recursive method [8, 9]. In its practical application, the DSEM was applied to analyze the soil-structure interaction with fractional order [10], the nonlinear overload of the unbounded medium-arch dam [11], the impact of pile driving vibration on seawall [12], and fluid-structure dynamic interaction [13]. In the evaluation of key factors, the causes of the error of the DSEM had been analyzed and described in detail in [14–16]. Simultaneously, the key factors estimated in [17–19] have a great influence on the accuracy of the soil-structure interaction.

The size of bounded domain and the finite element mesh density were randomly assigned and the artificial damping ratio was limited in a specified scope, so the key influence factors of the DSEM were roughly analyzed both in the analysis and in the application. To meet the requirements of practical engineering and get the optimum solution of key factors, this study analyzes the dimensionless dynamic stiffness coefficients of various mediums and proposes the value optimization model of key factors. The initial conditions of the optimization model are the maximum of the difference function of the dynamic stiffness coefficient, the wave amplitude attenuation, and the maximum finite element number. Numerical verification demonstrates that the value optimization model of key factors can regulate the simulation accuracy and computational efficiency and analyze the practical infinite foundation-structure interaction.

2. Damping Solvent Extraction Method

The damping solvent extraction method is simply reviewed in this chapter. A bounded domain of the infinite media adjacent to the soil-structure interface is discretized with a finite element meshes shown in Figure 1.

2.1. Implementation in the Frequency Domain. The procedure of the DSEM consists of the following steps for each frequency, which calculate the dynamic stiffness coefficients of the unbounded medium.

Step 1. In the selected bounded domain idealized as an assemblage of the finite elements, the artificial damping ratio in the domain and the viscous dashpots at the outer boundary serve to attenuate the vibration amplitudes of the outgoing wave and reflected wave. The coefficients of the viscous dashpots per unit surface area at the outer boundary are ρc_s^* in the perpendicular direction and ρc_p^* in the tangential direction. The shear-wave velocity and the dilatation-wave velocity are affected by the factor $1 + 2i\zeta$. Consider

$$c_s^* = c_s \sqrt{1 + 2i\zeta}, \quad (1a)$$

$$c_p^* = c_p \sqrt{1 + 2i\zeta},$$

$$G^* = G(1 + 2i\zeta), \quad (1b)$$

$$a_0^* = a_0 \sqrt{1 + 2i\zeta},$$

where G and a_0 are the shear modulus and dimensionless frequency, respectively.

Step 2. Eliminating all degrees of freedom, which are located in the medium except the interface, the dynamic stiffness condensed matrix of the bounded medium, $\tilde{S}^f(\omega)$, is transformed from the dynamic stiffness matrix $S^f(\omega)$. The dynamic stiffness matrix of the damped bounded foundation is expressed as follows:

$$S^f(\omega) = G^* S^f(a_0^*) = G^* \left(-a_0^{*2} \bar{M}^f + ia_0^* \bar{C}^f + \bar{K}^f \right), \quad (2)$$

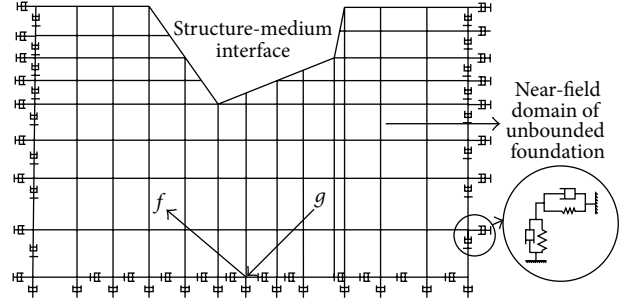


FIGURE 1: Finite element mesh of bounded domain adjacent to structure.

where \bar{M}^f , \bar{C}^f , and \bar{K}^f are the dimensionless stiffness, damping, and mass matrices.

Step 3. Since the dynamic stiffness coefficient is derived with ω and the dynamic stiffness condensed matrix of the bounded medium, $\tilde{S}^f(\omega)$, convert to the dynamic stiffness condensed matrix of the unbounded media, $\tilde{S}^\infty(\omega)$, the dimensionless dynamic stiffness condensed matrix, $\tilde{S}^\infty(a_0^*)$, is written as follows:

$$\begin{aligned} \tilde{S}^\infty(a_0^*) &= \tilde{S}^f(a_0^*), \\ \tilde{S}^\infty(a_0^*)_{,a_0^*} &= \tilde{S}^f(a_0^*)_{,a_0^*}. \end{aligned} \quad (3)$$

Taking the first-order Taylor expansion of $\tilde{S}^\infty(a_0^*)$, the dynamic stiffness matrix of the undamped unbounded medium is equal to

$$\tilde{S}^\infty(a_0) = \tilde{S}^\infty(a_0^*) + \tilde{S}^\infty(a_0^*)_{,a_0^*} (a_0 - a_0^*). \quad (4)$$

2.2. Implementation in the Time Domain. The medium-structure interaction force is obtained by the DSEM in the time domain, so the motion equation of the damped bounded medium takes the form

$$\begin{aligned} \begin{bmatrix} M_{mm} & 0 \\ 0 & M_{mm} \end{bmatrix} \begin{Bmatrix} \ddot{u}_m \\ \ddot{u}_b \end{Bmatrix} + \begin{bmatrix} C_{mm} & C_{mb} \\ C_{bm} & C_{bb}^f \end{bmatrix} \begin{Bmatrix} \dot{u}_m \\ \dot{u}_b \end{Bmatrix} \\ + \begin{bmatrix} M_{mm} & M_{mb} \\ M_{bm} & M_{bb} \end{bmatrix} \begin{Bmatrix} u_m \\ u_b \end{Bmatrix} = \begin{Bmatrix} 0 \\ R_b(t) \end{Bmatrix} \end{aligned} \quad (5)$$

with

$$\begin{aligned} [K] &= [\bar{K}] + \zeta^2 [\bar{M}], \\ [C] &= [\bar{C}] + 2\zeta [\bar{M}], \\ [M] &= [\bar{M}], \end{aligned} \quad (6)$$

where $[\bar{M}]$, $[\bar{C}]$, and $[\bar{K}]$ are the mass, damping, and stiffness matrices, respectively, and $\{R_b\}$ is the interaction force at the soil-structure interface. The subscript b denotes the nodes of the bounded medium at the soil-structure interface and m

denotes the remaining nodes. Furthermore, the interaction force of the soil-structure was written in [19]:

$$R_b(t) = M_{bb}\ddot{u}_b + (K_{bb} - \zeta C_{bb})u_b + K_{bm}u_m + \zeta K_{bb}v_m, \quad (7)$$

where \ddot{u}_b , \dot{u}_b , and u_b are the displacement, velocity, and acceleration vectors and the unknown u_m and v_m vectors are provided by the following equations:

$$\begin{aligned} M_{mm}\ddot{u}_m + C_{mm}\dot{u}_m + K_{mm}u_m &= -K_{mb}u_b - C_{mb}\dot{u}_b, \\ M_{mm}\dot{v}_m + C_{mm}v_m + K_{mm}v_m & \\ &= 2M_{mm}\dot{u}_m + C_{mm}u_m + C_{mb}u_b. \end{aligned} \quad (8)$$

3. Constraint Function

The constraint functions regarded as the essential components are crucial if one wishes to solve the optimization model. Therefore, the references and analysis of the constraint functions are described in detail in this chapter.

3.1. Constraint Function of Artificial Damping Ratio. The dynamic stiffness coefficient $S^\infty(a_0)$ and the dimensionless dynamic stiffness coefficient $\bar{S}^\infty(a_0)$ of the undamped unbounded medium are, respectively, given by

$$S^\infty(a_0) = K^\infty(k(a_0) + ia_0c(a_0)), \quad (9)$$

$$\bar{S}^\infty(a_0) = \frac{S^\infty(a_0)}{K^\infty} = \sqrt{1 - a_0^2} = k(a_0) + ia_0c(a_0). \quad (10)$$

$$\text{If } a_0 \leq 1, k(a_0) = \sqrt{1 - a_0^2} \text{ and } c(a_0) = 0.$$

$$\text{If } a_0 > 1, k(a_0) = 0 \text{ and } c(a_0) = \sqrt{1 - (1/a_0^2)}.$$

On the basis of the plural damping coefficient correspondence principle, the dimensionless dynamic stiffness coefficient of the damped unbounded medium is deduced as

$$\bar{S}^\infty(a_0^*) = \sqrt{1 - (a_0^*)^2} \quad (11)$$

with

$$a_0^* = \frac{(\omega - i\zeta)b}{c_1} = a_0 - i\bar{\zeta}, \quad (12)$$

where a_0^* and a_0 are the dimensionless frequencies of the damped and undamped bounded medium.

The dimensionless dynamic stiffness of the damped bounded medium is determined by the size of the bounded domain, l/b , and the artificial damping ratio $\bar{\zeta}$:

$$\bar{S}(a_0^*) = \sqrt{1 - (a_0^*)^2} \frac{1 - c_1/c_2}{1 + c_1/c_2}, \quad (13)$$

where c_1 and c_2 are the vibration amplitudes of the incoming wave and outgoing wave.

The dynamic stiffness coefficient of the undamped unbounded medium is calculated by taking the first-order Taylor expansion to eliminate the artificial damping ratio:

$$\bar{S}^\infty(a_0) = \bar{S}(a_0^*) + \bar{S}'(a_0^*)_{a_0^*} (a_0 - a_0^*). \quad (14)$$

TABLE 1: Values of bounded domain size and artificial damping ratio.

Case	C1	C2	C3	C4	C5	C6	C7	C8
l/b	3	3	3	3	1	3	5	7
$\bar{\zeta}$	0.01	0.1	0.5	1	0.3	0.3	0.3	0.3

The various values of the size of the bounded medium and the artificial damping ratio listed in Table 1 are used to analyze the dynamic stiffness coefficients of the undamped unbounded, damped unbounded, damped bounded, and simulating undamped unbounded medium.

When the dynamic stiffness coefficient of the undamped unbounded medium is regarded as the accurate solution, the dynamic stiffness coefficients determined by ($l/b = 3$, $\bar{\zeta} = 0.2$) shown in Figure 2 indicate that (1) the larger artificial damping ratio increases the difference between the dynamic stiffness coefficient of the undamped and damped unbounded medium; (2) the larger size of the bounded medium reduces the amplitude of the dynamic stiffness coefficient of the damped unbounded medium; (3) the smaller artificial damping ratio and the larger size of the bounded medium lead to the more accurate dynamic stiffness coefficient of the undamped unbounded medium. Therefore, the constraint function of artificial damping ratio is the difference function between the dimensionless dynamic stiffness coefficient of the undamped and damped unbounded medium.

3.2. Constraint Function of Size of the Bounded Medium.

Suppose that the artificial damping ratio $\bar{\zeta} = \zeta(b/c_s)$ is zero and the size of bounded medium is l/b ; $e^{-i\omega l/c_s}$ is the phase angle caused by radiating the shear wave from the interface to the outer boundary of the undamped bounded domain. If the artificial damping ratio is nonzero, the frequency ω is replaced by $\omega - i\zeta$ and the phase angle is replaced by $e^{-\zeta l/c_1} \cdot e^{-i\omega l/c_1}$. Thus, $e^{-\zeta l/c_1}$ is the attenuation of the wave amplitude in the damped bounded domain.

Due to the addition of the artificial damping ratio into the bounded medium, the wave is reflected by the outer boundary and radiated to the interface. The wave amplitude attenuation function of the initial displacement wave excited at the interface is written as

$$\phi\left(\zeta, \frac{l}{b}\right) = \exp\left(-2\zeta \frac{l}{b} \frac{1}{c_1}\right) = \exp\left(-2\bar{\zeta} \frac{l}{c_1}\right). \quad (15)$$

If the wave amplitude attenuation at the interface is known, the constraint function of the size of bounded medium is transformed from function (15). Consider

$$\frac{l}{b} = -\frac{\ln(\phi_0)}{2\bar{\zeta}}. \quad (16)$$

3.3. Constraint Function of Finite Element Mesh Density. In the finite element discretization of the bounded medium, the finite element mesh of only one row, denoted as the ‘‘base row,’’ is merely required. S_r denotes the dynamic stiffness matrix of one row of the finite element mesh with length

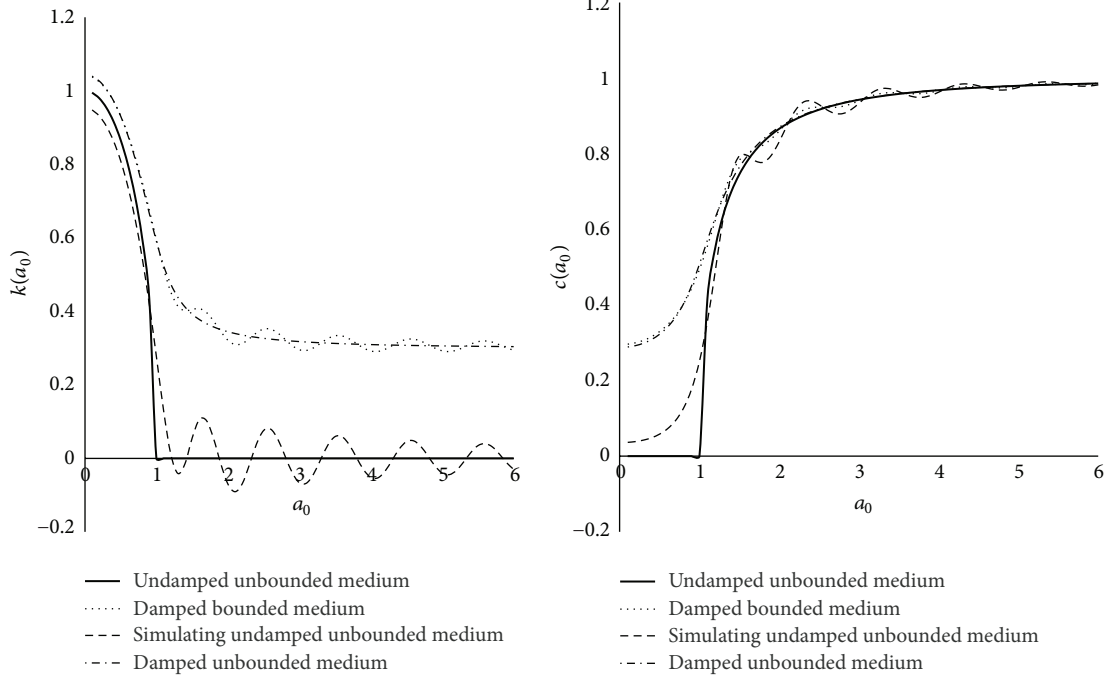


FIGURE 2: Dimensionless dynamic stiffness coefficients of $l/b = 3, \bar{\zeta} = 0.2$.

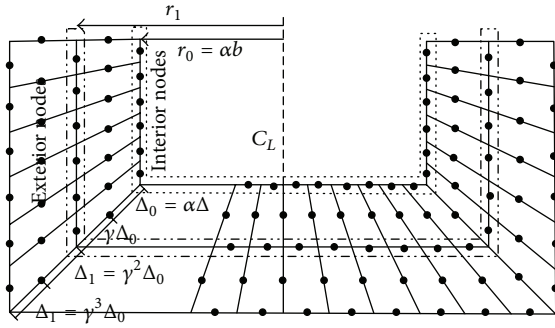


FIGURE 3: First row of finite element mesh.

r (Figure 3). The same is true for the condensed matrix obtained by eliminating all degrees of freedom except those related to interior nodes:

$$\begin{aligned} S_{\alpha b}(\omega) &= S_b(\alpha\omega), \\ \tilde{S}_{\alpha b}(\omega) &= \tilde{S}_b(\alpha\omega). \end{aligned} \quad (17)$$

The formula relates \tilde{S}_{r_1} for exterior nodes to the corresponding matrix of interior nodes \tilde{S}_{r_0} :

$$\tilde{S}_{r_1}(\omega) = \tilde{S}_{r_0}(\kappa\omega), \quad (18)$$

in which $\kappa = r_1/r_0 = \gamma^2$.

The dashpots are assigned at the exterior nodes of the base row. Both $\tilde{S}_{r_0}(\gamma^{2n-2}\omega)$ and $\tilde{S}_{r_1}(\gamma^{2n-4}\omega)$ are calculated by (18). After removing the dashpots, either $\tilde{S}_{r_0}(\gamma^{2n-2}\omega)$ or $\tilde{S}_{r_1}(\gamma^{2n-4}\omega)$ is assembled at the exterior nodes of the base row

for frequency $\gamma^{2n-4}\omega$. $\tilde{S}_{r_0}(\gamma^{2n-4}\omega)$ is calculated by condensing again into the dynamic stiffness matrix for interior nodes. $\tilde{S}^f(\omega)$ is obtained by repeating the last process $n-2$ and the proportionality factor γ must satisfy

$$\frac{r_0 + 1/\sqrt{2}(\Delta + \gamma\Delta)}{r_0} = \gamma^2. \quad (19)$$

4. Value Optimization Model of Key Factors

A value optimization model of key factors is proposed to control the simulation accuracy and computational efficiency of the infinite soil-structure interaction. Then the optimum solutions of key factors of the DSEM are obtained by the value optimization.

4.1. Design Variable. Because the optimum values of key factors are provided by solving the value optimization model, the design variables of optimization model include the size of the bounded medium, the artificial damping ratio, the mesh size of finite element, and the proportionality factor.

4.2. Objective Function. The relationship between the size of bounded medium and the finite element mesh density is expressed as

$$\frac{l}{b} = \frac{\sqrt{2} \Delta}{2} \frac{1 - \gamma^{2n}}{b(1 - \gamma)}. \quad (20)$$

Substituting (19) into (20), the objective function is transformed from (20).

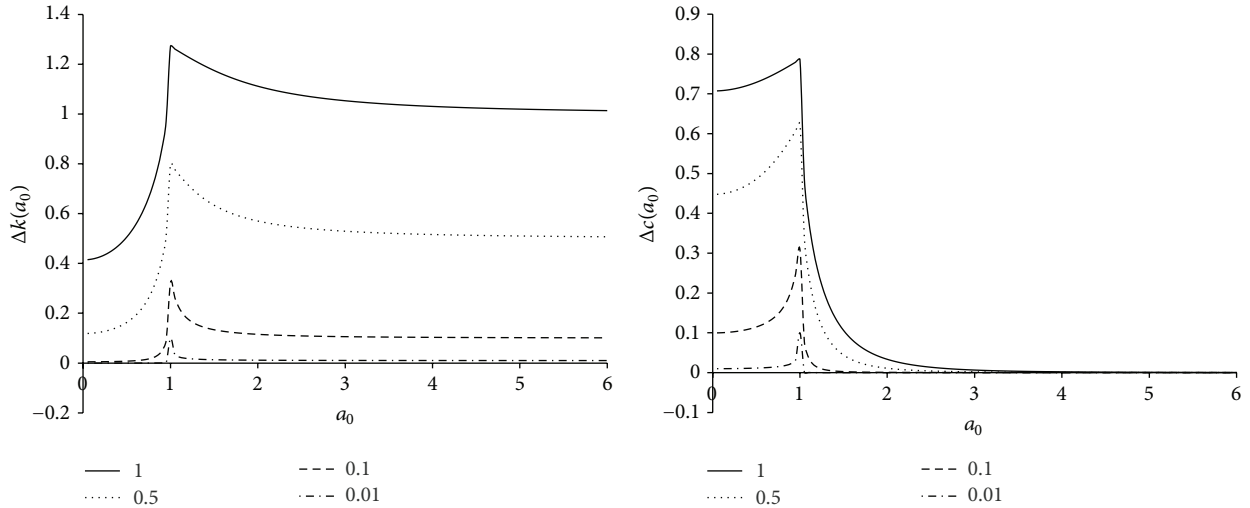


FIGURE 4: Difference function of dimensionless dynamic stiffness coefficients.

4.3. Constraint Function. The constraint function system is composed of the constraint functions of the size of the bounded medium, the artificial damping ratio, and the finite element mesh density as described in Section 2.

The difference function between the dimensionless dynamic stiffness coefficient of the damped and undamped unbounded foundation is expressed as follows:

$$\begin{aligned} \Delta S(a_0) &= \bar{S}^{\infty}(a_0^*) - \bar{S}^{\infty}(a_0) \\ &= \sqrt{1 - (a_0^*)^2} - \sqrt{1 - (a_0)^2}. \end{aligned} \quad (21)$$

The results shown in Figure 4 indicate that the smaller artificial damping ratio results in the smaller difference of the dynamic stiffness coefficient and the maximum of the difference function is calculated at the point given by $a_0 = 1$ ($\text{Max } S = \Delta S(1)$).

Taking the accuracy and computational cost of the soil-structure interaction into account, the initial conditions of the optimization model consist of the maximum of the difference function of the dynamic stiffness coefficient, the wave amplitude attenuation, and the maximum finite element number in the bounded medium. Therefore, the value optimization model of key factors based on the DSEM is expressed as follows:

(1) Initial conditions: $\text{Max } S$, ϕ_0 , $\text{Max } N$.

(2) Design variables: $\bar{\zeta}$, l/b , Δ/b , γ .

(3) Objective function:

$$\gamma = \exp\left(\frac{1}{2n} \ln\left(\frac{l}{b} - 1\right)\right). \quad (22)$$

(4) Constraint functions:

$$\text{abs}(\Delta S(1, \bar{\zeta})) \leq \text{Max } S = \Delta S(1),$$

$$\frac{l}{b} = -\frac{\ln(\phi_0)}{2\bar{\zeta}}, \quad (23)$$

$$1 + \frac{1}{\sqrt{2b}(\Delta + \gamma\Delta)} = \gamma^2,$$

$$n \leq \text{Max } N.$$

5. Numerical Verification

5.1. Verification in the Frequency Domain

5.1.1. Problem Chosen. A cross section shown in Figure 5 is the intercepted plane of a rectangular rigid strip foundation of width $2b$ and depth b embedded in a homogeneous half plane with shear modulus G , Poisson ratio ν , and artificial damping ratio ζ . The DOFs, vertical (V), horizontal (H), and rocking (R), describe the plane motion of the foundation. The procedure analyzes the dynamic stiffness matrix, $S^{\infty}(a_0)$, of the rigid strip on the damped unbounded medium in the frequency domain.

Let P_n and Δ_n , $n \in (V, H, R)$, respectively, denote the amplitudes of the harmonic force and displacement; the vectors are related by the dynamic stiffness matrix:

$$\begin{bmatrix} P_V \\ P_H \\ \frac{P_R}{b} \end{bmatrix} = \bar{S}^{\infty}(a_0) \begin{bmatrix} \Delta_V \\ \Delta_H \\ b\Delta_R \end{bmatrix} \quad (24)$$

$$= \begin{bmatrix} S_{VV}(a_0) & 0 & 0 \\ 0 & S_{HH}(a_0) & S_{HR}(a_0) \\ 0 & S_{RH}(a_0) & S_{RR}(a_0) \end{bmatrix} \begin{bmatrix} \Delta_V \\ \Delta_H \\ b\Delta_R \end{bmatrix}.$$

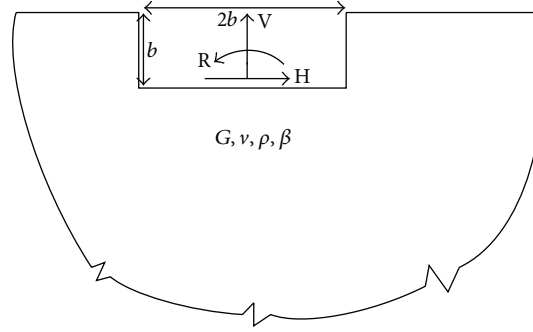


FIGURE 5: Cross section of a strip foundation embedded in a homogeneous half plane.

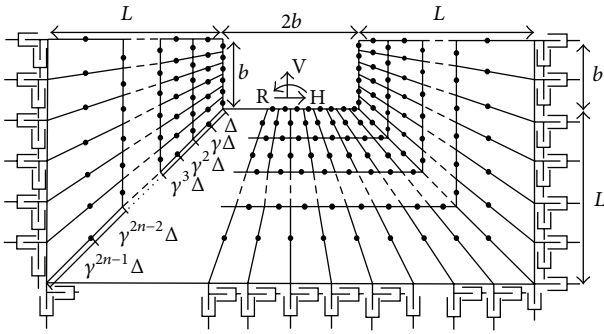


FIGURE 6: Finite element mesh of bounded medium.

The dynamic stiffness coefficients of the bounded medium are decomposed into the spring coefficient $k(a_0)$ and the damping coefficient $c(a_0)$:

$$S_{jj}(a_0) = \frac{1}{G} (k_{jj}(a_0) + ia_0 c_{jj}(a_0)) \quad j \in \{V, H, R\}. \quad (25)$$

5.1.2. Numerical Evaluation. The discretization of the finite element mesh is shown in Figure 6, in which the eight-node isoparametric finite element is employed. The finer mesh is utilized near the strip foundation and it becomes coarser away from that with a proportionality factor γ . The material constants of the foundation are Poisson ratio $\nu = 0.25$ and natural damping ratio $\beta = 0.05$. The various initial conditions of the value optimization model and the corresponding optimum solutions of key factors are listed in Table 2. The dynamic stiffness coefficient solved by case C1 is seen as the accurate soil-structure interaction.

As the wave amplitude attenuation and the maximum finite element number in the bounded medium are held constant, the maximum of the difference function of the dynamic stiffness coefficient is a variable value. According to the comparison of the dynamic stiffness coefficient of cases C1, C2, C3, C4, and C5 shown in Figure 7, the smaller maximum of the difference function of the dynamic stiffness coefficient promotes the accuracy of the dimensionless dynamic stiffness coefficient of the unbounded medium.

As the maximum of the difference function of the dynamic stiffness coefficient and the maximum finite element number in the bounded medium remain unchangeable, the

wave amplitude attenuation is a variable value. According to the comparison of the dynamic stiffness coefficient of cases C1, C6, C7, C8, and C9 shown in Figure 8, the larger wave amplitude attenuation improves the accuracy of the dimensionless dynamic stiffness coefficient of the unbounded medium.

As the maximum of the difference function of the dynamic stiffness coefficient and the wave amplitude attenuation are changeless, the maximum finite element number in the bounded medium is a variable value. According to the comparison of the dynamic stiffness coefficient of cases C1, C10, C11, C12, and C13 shown in Figure 9, the larger maximum finite element number reduces the computational efficiency but enhances the simulation precision of the dimensionless dynamic stiffness coefficient of the unbounded medium.

5.2. Verification in the Time Domain. A transient horizontal displacement is excited at the interface of the discretization of the finite element shown in Figure 10 to test the feasibility of the value optimization model of key factors in the time domain. The material constants of the medium are shear modular $G = 0.32$ GPa, Poisson's ratio $\nu = 0.25$, a density of $\rho = 2000$ kg/m³, shear-wave velocity $c_s = 400$ m/s, dilatational wave velocity $c_p = 693$ m/s, and time step $\Delta t = 0.001$ s.

The transient excitation is a prescribed horizontal displacement at the center of the rigid base (with zero values for the vertical and rocking motions)

$$u_b(t) = \begin{cases} \frac{u_0}{2} \left[1 - \cos\left(2\pi\frac{t}{T}\right) \right] & 0 \leq t \leq 2T \\ 0 & t > 2T \end{cases} \quad (26)$$

with period $T = 8b/c_s$.

The initial conditions and the optimum solutions by the value optimization listed in Table 3 are realized by the damping solvent extraction method. The interaction force based on the case A1 is regarded as the exact interaction force of the foundation-structure.

Since the maximum finite element number in the bounded medium remains unchanged, the computational efficiency of the unbounded foundation-structure interaction is fixed. The interaction force shown in Figure 11 is calculated by the various initial conditions of the value optimization

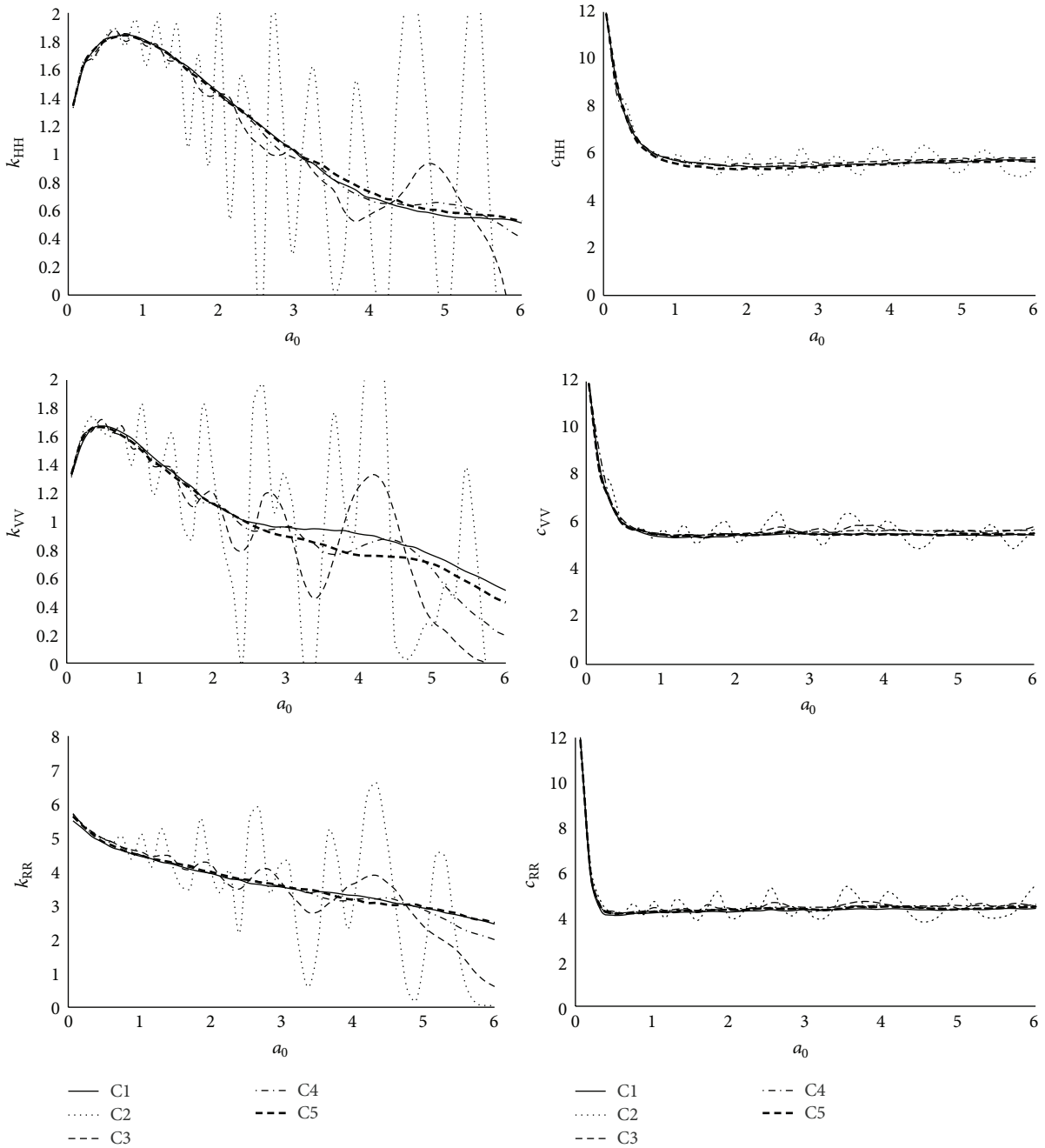


FIGURE 7: Effect of maximum of difference function of dynamic stiffness coefficient on dynamic stiffness coefficient.

model of key factors. When the maximum value of the difference function of the dynamic stiffness coefficients is a variable value (such as in cases A1, A2, A3, and A4), the larger wave amplitude attenuation improves the precision of the interaction force; nevertheless, the over-large attenuation has a negligible effect. When the wave amplitude attenuation is changeless (such as in cases A1, A3, A5, and A6), the smaller maximum of the difference function of the dynamic stiffness coefficient increases the accuracy of the soil-structure interaction force.

In summary, the implementation of the unbounded medium-structure interaction in the time-frequency domain illustrates that the alterable initial conditions of the value optimization model of key factors can improve the simulation accuracy and computational efficiency of the interaction, which are made up with the smaller maximum finite element number, the larger wave amplitude attenuation, and the smaller maximum of the difference function between the dimensionless dynamic stiffness coefficients of the damped and undamped unbounded foundation.

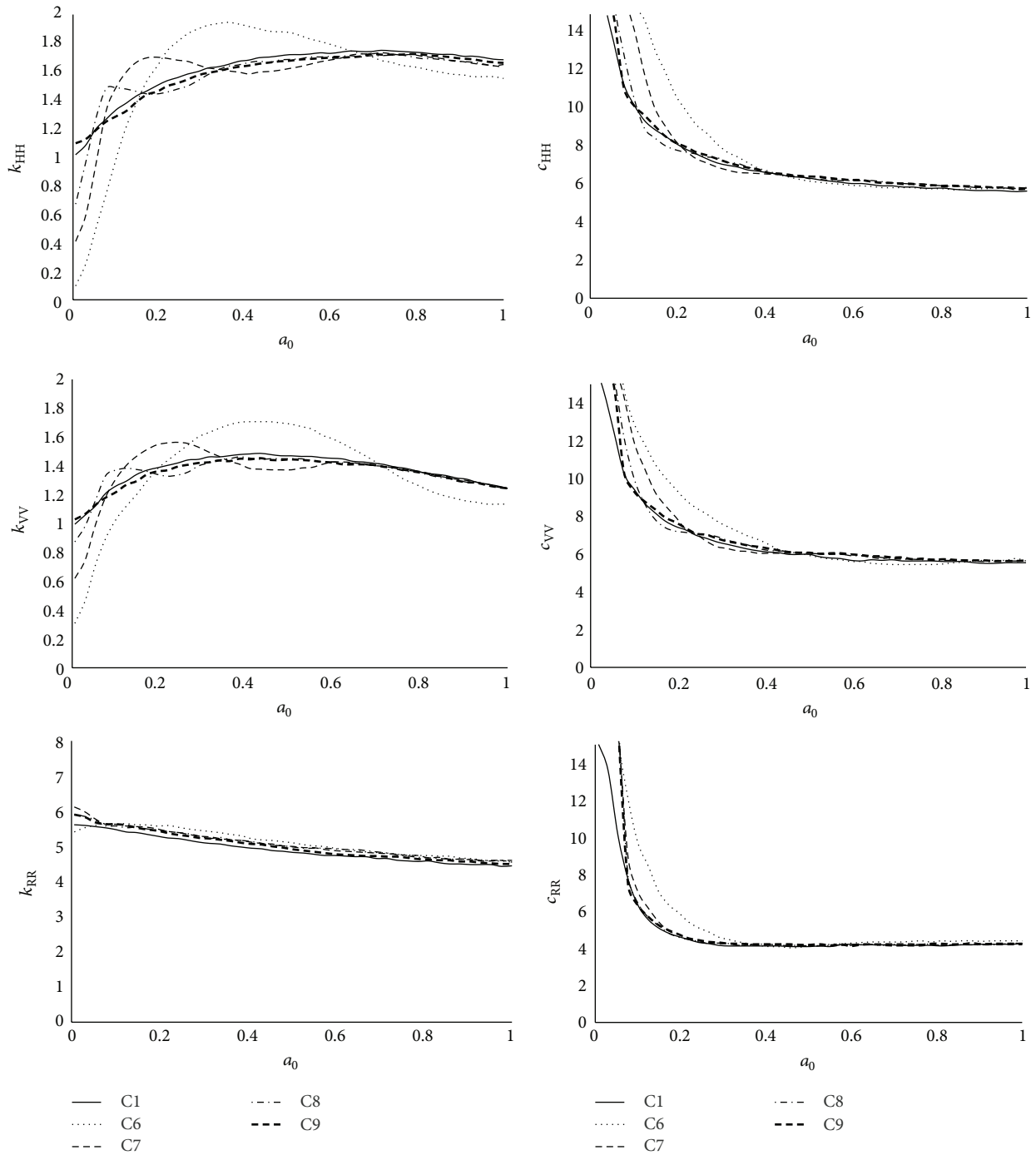


FIGURE 8: Effect of wave amplitude attenuation on dynamic stiffness coefficient.

6. Application

To demonstrate the adaptation of the value optimization model of key factors in practical engineering, the rock foundation-gravity dam shown in Figure 12 is applied to analyze the dynamic response of the dam to harmonic ground motion. The geometric properties of the gravity dam are the height, 132 m, and the width, which is 14 m at the crest and 110 m at the bottom. Taking the cross section of the

medium-dam as an example, the dynamic response analysis of the gravity dam is calculated as a plane-strain problem. The material parameters of the gravity dam are Young's modulus of 20 GPa, Poisson's ratio of 0.18, and a density of 2600 kg/m^3 . The material parameters of the rock foundation are Young's modulus of 2.4 GPa, Poisson's ratio of 0.333, a density of 2100 kg/m^3 , and the characteristic length of 40 m. The constants of the displacement input harmonic wave are the amplitude, 0.2 m, and the cycle, 0.4 s. Meanwhile, the

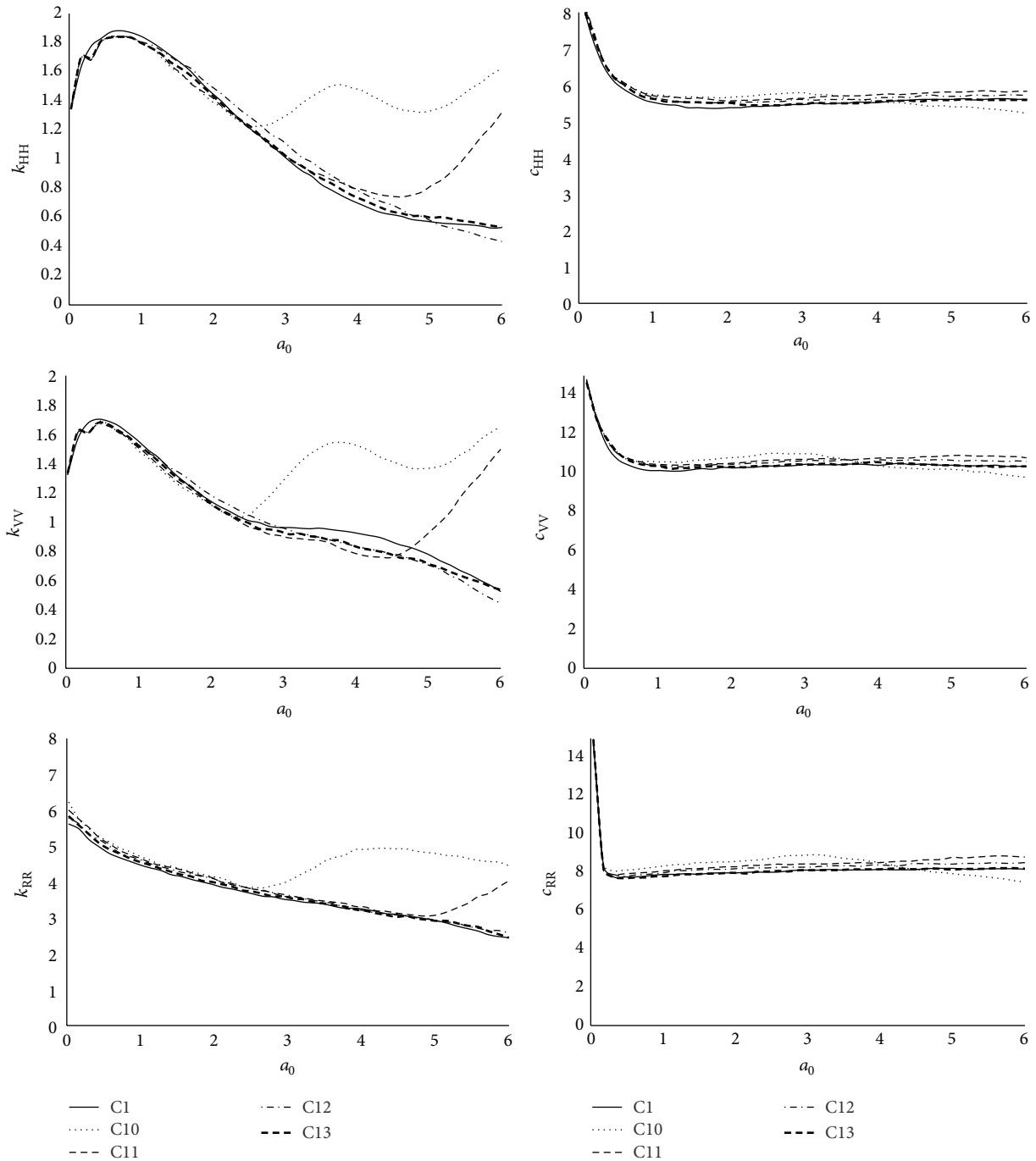


FIGURE 9: Effect of maximum finite element number on dynamic stiffness coefficient.

various initial conditions of the value optimization model of key factors based on the DSEM are implemented to analyze the dynamic response of the gravity dam.

The displacement function of the dam at the crest shown in Figure 13 indicates that the simulation precision and computational efficient of the displacement response of the gravity dam can be enhanced by reducing the maximum of the difference function of the dynamic stiffness coefficient and raising the wave amplitude attenuation at the interface and the maximum of finite element number in the bounded medium.

7. Conclusion

Considering the simulation accuracy and computational efficiency of the soil-structure interaction, this study's aim was to establish the value optimization model of key factors (such as the artificial damping ratio, the size of the bounded medium, and the finite element mesh density). From the impact assessment of the key factors on the dimensionless dynamic stiffness coefficient and the analysis of the interrelation among the key factors, the value optimization model of

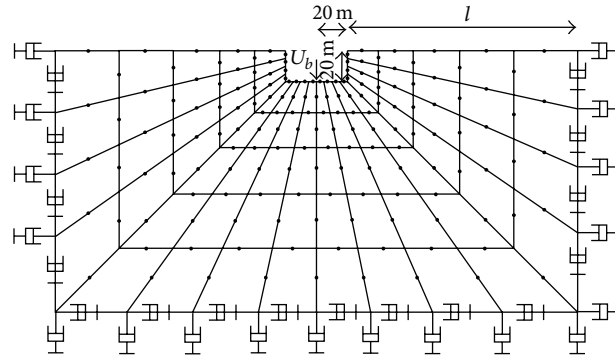


FIGURE 10: Finite element mesh of bounded media.

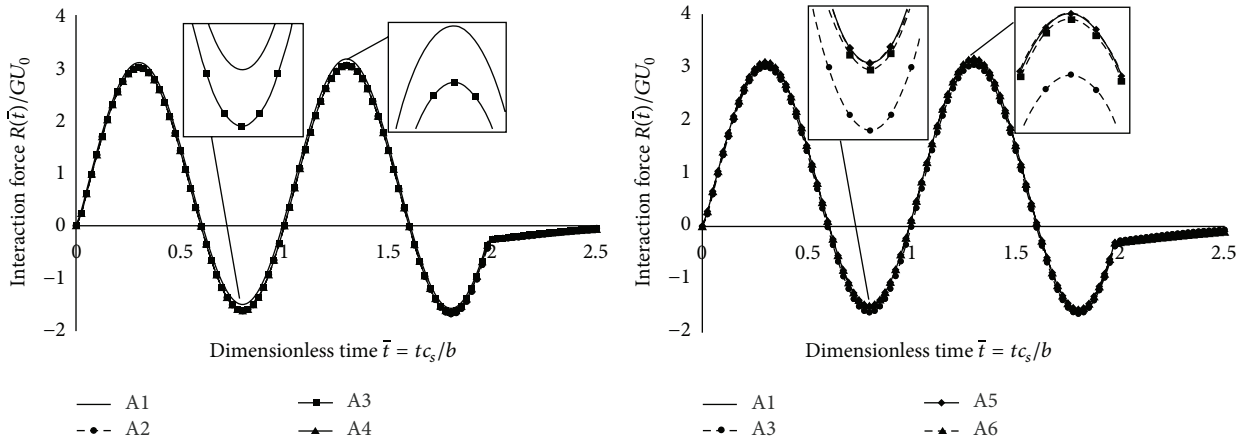


FIGURE 11: Time history of horizontal interaction force varying maximum of difference function of dynamic stiffness coefficient and wave amplitude attenuation.

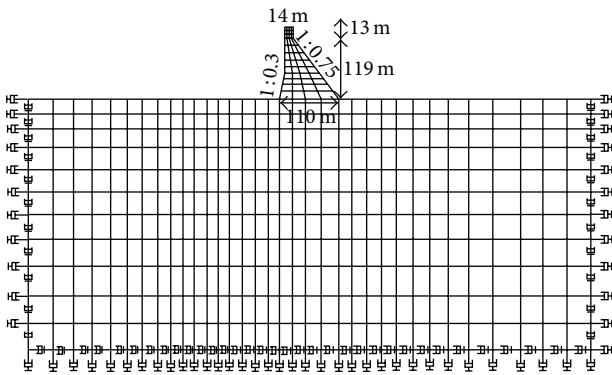


FIGURE 12: Finite element mesh of the gravity dam-bounded medium.

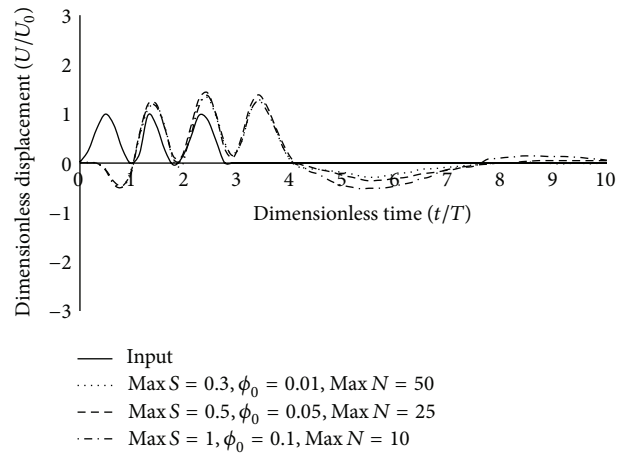


FIGURE 13: Dynamic magnification of crest displacements under seismic excitation $T = 0.4$ s.

key factors based on the DSEM was proposed. In additions, the initial conditions of the value optimization model were composed of the wave amplitude attenuation, the maximum finite element number, and the maximum of the difference function between the dimensionless dynamic stiffness coefficient of the undamped and damped unbounded medium.

The implementations of the dimensionless dynamic stiffness coefficient and the interaction force demonstrated that the value optimization model of key factors was capable

of controlling the simulation accuracy and computational efficiency of the unbounded medium-structure interaction in the frequency and time domain. Finally, the displacement history function at the crest of the gravity dam on the rock foundation indicated that the value optimization model of key

TABLE 2: Characteristics of the finite element discretization of bounded medium.

Case	Initial condition				Optimal value of key factor			
	Max S	ϕ_0	Max N	$\bar{\zeta}$	l/b	n	Δ/b	γ
C1	0.32	0	2000	0.05	3000	2000	0.0028	1.002
C2	1.12	$1.00E-04$	25	0.6	7.68	25	0.062	1.044
C3	0.9	$1.00E-04$	25	0.4	11.51	25	0.074	1.052
C4	0.64	$1.00E-04$	25	0.2	23.03	25	0.094	1.066
C5	0.32	$1.00E-04$	25	0.1	46.06	25	0.114	1.080
C6	1.12	$1.00E-04$	25	0.6	7.68	25	0.062	1.044
C7	1.12	$1.00E-06$	25	0.6	11.51	25	0.074	1.052
C8	1.12	$1.00E-13$	25	0.6	24.95	25	0.096	1.068
C9	1.12	$1.00E-48$	25	0.6	46.06	25	0.114	1.095
C10	1.12	$1.00E-13$	6	0.6	23.03	6	0.429	1.304
C11	1.12	$1.00E-13$	12	0.6	23.03	12	0.201	1.142
C12	1.12	$1.00E-13$	18	0.6	23.03	18	0.131	1.093
C13	1.12	$1.00E-13$	25	0.6	23.03	25	0.094	1.066

TABLE 3: Various initial conditions and the optimum values of key factors.

Case	(Max S , ϕ_0 , Max N)	$(l/b, \bar{\zeta}, n, \Delta/b, \gamma)_{\text{opt}}$
A1	(0.1, 0, 2000)	(3000, 0.05, 2000, 0.0028, 1.002)
A2	(1, 0.1, 25)	(2.4, 0.48, 25, 0.035, 1.025)
A3	(1, 0.05, 25)	(3.2, 0.48, 25, 0.044, 1.031)
A4	(1, 0.01, 25)	(4.8, 0.48, 25, 0.051, 1.036)
A5	(0.5, 0.05, 25)	(12.4, 0.12, 25, 0.075, 1.053)
A6	(0.3, 0.05, 25)	(37.4, 0.04, 25, 0.107, 1.076)

factors based on the DSEM was appropriate for analyzing the interaction of the practical unbounded medium-structure.

Competing Interests

The authors declare that there is no conflict of interests regarding the publication of this paper.

Acknowledgments

This work was supported by National Natural Science Foundation of China (51279053).

References

- [1] J. Lysmer and G. Waas, "Shear waves in plane infinite structures," *Journal of the Engineering Mechanics Division*, vol. 98, no. 1, pp. 85–105, 1972.
- [2] Z. P. Liao and H. L. Wong, "A transmitting boundary for the numerical simulation of elastic wave propagation," *International Journal of Soil Dynamics and Earthquake Engineering*, vol. 3, no. 4, pp. 174–183, 1984.
- [3] S. Chongmin and Z. Chuhan, "A dynamic boundary element method for earthquake resistant analysis of dams," *Earthquake Engineering & Engineering Vibration*, vol. 8, no. 4, pp. 14–25, 1988.
- [4] C. Song and J. P. Wolf, "Dynamic stiffness of unbounded medium based on damping-solvent extraction," *Earthquake Engineering & Structural Dynamics*, vol. 23, no. 2, pp. 169–181, 1994.
- [5] J. P. Wolf and C. Song, *Finite-Element Modeling of Unbounded Media*, John Wiley & Sons, Chichester, UK, 1996.
- [6] J. Chen, J. Li, and J. Zhou, "Seismic analysis of large 3-D underground caverns based on high performance recursive method," *International Journal of Solids and Structures*, vol. 41, no. 11-12, pp. 3081–3094, 2004.
- [7] J.-B. Li, J.-Y. Chen, and G. Lin, "Finite element damping-extraction method for dynamic interaction time domain analysis of non-homogeneous unbounded rock," *Chinese Journal of Geotechnical Engineering*, vol. 26, no. 2, pp. 263–267, 2004.
- [8] J.-Y. Chen, J. Li, and J.-B. Li, "A refined sub-regional reciprocal method in time domain and its application in dynamic interaction analysis," in *Proceedings of the 13th World Conference on Earthquake Engineering*, Vancouver, Canada, August 2004.
- [9] J. B. Li, J. Yang, and G. Lin, "A stepwise damping-solvent extraction method for large-scale dynamic soil-structure interaction analysis in time domain," *International Journal for Numerical and Analytical Methods in Geomechanics*, vol. 32, no. 4, pp. 415–436, 2008.
- [10] Y. Chen, X. Wang, and X. Zhou, "Time domain damping-extraction method for interaction of unbounded media with fractional-order," *Chinese Journal of Rock Mechanics and Engineering*, vol. 28, supplement 2, pp. 3666–3672, 2009.
- [11] H. Zhong, G. Lin, J. Li, and J. Chen, "An efficient time-domain damping solvent extraction algorithm and its application to arch dam-foundation interaction analysis," *Communications in Numerical Methods in Engineering with Biomedical Applications*, vol. 24, no. 9, pp. 727–748, 2008.
- [12] Y.-H. Chen, X.-Q. Wang, X.-D. Zhou, and Y.-D. Gui, "Determination of impact of pile driving vibration on seawall by infinite foundation method," *Journal of Hydraulic Engineering*, vol. 42, no. 2, pp. 226–231, 2011.
- [13] M. A. Xiuping, *The DSE Method in Time-Domain of Dynamic Interaction Analysis*, Dalian University of Technology, Dalian, China, 2006.

- [14] Y. Xunqiang, L. Jianbo, W. Chenglin, and L. Gao, "ANSYS implementation of damping solvent stepwise extraction method for nonlinear seismic analysis of large 3-D structures," *Soil Dynamics and Earthquake Engineering*, vol. 44, pp. 139–152, 2013.
- [15] E. A. Kausel, "Complex frequencies in elastodynamics, with application to the damping-solvent extraction method," *Journal of Engineering Mechanics*, vol. 136, no. 5, pp. 641–652, 2010.
- [16] H.-P. Ding and Z.-P. Liao, "Improvement of dynamic stiffness calculation based on damping-solvent extraction method," *Earthquake Engineering & Engineering Vibration*, vol. 21, no. 2, pp. 13–18, 2001.
- [17] M. R. Hajiabadi and V. Lotfi, "An effective approach for utilizing damping solvent extraction method in frequency domain," *Soil Dynamics & Earthquake Engineering*, vol. 38, pp. 46–57, 2012.
- [18] U. Basu and A. K. Chopra, "Numerical evaluation of the damping-solvent extraction method in the frequency domain," *Earthquake Engineering & Structural Dynamics*, vol. 31, no. 6, pp. 1231–1250, 2002.
- [19] Y. Xun-Qiang, *Improvement and Engineering Application of Structure-Foundation Dynamic Interaction Model*, Dalian University of Technology, 2013.

Research Article

Application of the Least Squares Method in Axisymmetric Biharmonic Problems

Vasyl Chekurin and Lesya Postolaki

*Pidstryhach Institute for Applied Problems of Mechanics and Mathematics of National Academy of Sciences of Ukraine,
3-b Naukova Street, Lviv 79060, Ukraine*

Correspondence should be addressed to Vasyl Chekurin; v.chekurin@gmail.com

Received 29 March 2016; Revised 29 May 2016; Accepted 2 June 2016

Academic Editor: Masoud Hajarian

Copyright © 2016 V. Chekurin and L. Postolaki. This is an open access article distributed under the Creative Commons Attribution License, which permits unrestricted use, distribution, and reproduction in any medium, provided the original work is properly cited.

An approach for solving of the axisymmetric biharmonic boundary value problems for semi-infinite cylindrical domain was developed in the paper. On the lateral surface of the domain homogeneous Neumann boundary conditions are prescribed. On the remaining part of the domain's boundary four different biharmonic boundary pieces of data are considered. To solve the formulated biharmonic problems the method of least squares on the boundary combined with the method of homogeneous solutions was used. That enabled reducing the problems to infinite systems of linear algebraic equations which can be solved with the use of reduction method. Convergence of the solution obtained with developed approach was studied numerically on some characteristic examples. The developed approach can be used particularly to solve axisymmetric elasticity problems for cylindrical bodies, the heights of which are equal to or exceed their diameters, when on their lateral surface normal and tangential tractions are prescribed and on the cylinder's end faces various types of boundary conditions in stresses in displacements or mixed ones are given.

1. Introduction

Many practically important problems bring the biharmonic equation

$$\begin{aligned}\Delta^2 w &= 0, \\ w &= w(x), \quad x \in S \subset R^2\end{aligned}\quad (1)$$

considering in 2D domains S with Lipschitz-continuous boundary ∂S .

Here Δ is Laplace differential operator: $\Delta = \nabla \cdot \nabla$, where ∇ stands for the gradient operator in R^2 and the dot (\cdot) denotes scalar product. Function w is considered as four-time differentiable one in S .

The classical formulations of biharmonic problems distinguish the Dirichlet and Neumann boundary value problems. Two kinds of Dirichlet problems are usually considered for biharmonic equation (1). In the problem of the first and

second kinds the biharmonic functions should be subordinated to boundary conditions (2) and (3) correspondingly [1]:

$$\begin{aligned}w|_{x \in \partial S} &= f_0(x), \\ \frac{\partial w}{\partial \nu} \Big|_{x \in \partial S} &= f_1(x),\end{aligned}\quad (2)$$
$$x \in \partial S,$$

$$\begin{aligned}w|_{x \in \partial S} &= f_0(x), \\ \Delta w|_{x \in \partial S} &= f_1(x),\end{aligned}\quad (3)$$
$$x \in \partial S.$$

Here $\partial/\partial \nu \equiv \nu \cdot \nabla$ is the operator of normal derivative on ∂S , ν is the outward unit normal vector to ∂S , and $f_0(x)$ and $f_1(x)$ are given functions.

Various kinds of Neumann problems for (1) can also be considered [2, 3]. In simplest cases these are the problems with boundary conditions (4), (5), or (6):

$$\begin{aligned} \frac{\partial w}{\partial \nu} \Big|_{x \in \partial S} &= f_0(x), \\ \frac{\partial^2 w}{\partial \nu^2} \Big|_{x \in \partial S} &= f_1(x), \end{aligned} \quad (4)$$

$$x \in \partial S,$$

$$\begin{aligned} \frac{\partial w}{\partial \nu} \Big|_{x \in \partial S} &= f_0(x), \\ \frac{\partial \Delta w}{\partial \nu} \Big|_{x \in \partial S} &= f_1(x), \end{aligned} \quad (5)$$

$$x \in \partial S,$$

$$\begin{aligned} \Delta w \Big|_{x \in \partial S} &= f_0(x), \\ \frac{\partial \Delta w}{\partial \nu} \Big|_{x \in \partial S} &= f_1(x), \end{aligned} \quad (6)$$

$$x \in \partial S.$$

One can distinguish two kinds of biharmonic mixed problems [4, 5]. In the mixed problem of the first kind (1) is considered subject to boundary conditions which are weighted combinations of Dirichlet boundary conditions and Neumann boundary conditions (so-called Robin boundary condition). In another case Dirichlet data are prescribed on one part of the boundary and Neumann data are prescribed on the remainder.

Various methods are used for solving of the biharmonic problems. Among them are iterative methods [6], boundary integral method [7], method of finite differences [8], finite element method [9], and so forth.

Significant interest in biharmonic problems in rectangle arises in 2D theory of elasticity [10]. In this connection we should refer to the so-called method of homogeneous solutions [11–14] used for these problems' solving. An idea of the method consists in representing the solution as a series expansion in some complete system of biharmonic functions being solutions of a homogeneous biharmonic problem on infinite strip [11, 14]. These functions satisfy homogeneous Neumann-type boundary conditions on the strip's sides. As such representation automatically satisfies (1) and homogeneous boundary conditions on two opposite sides of the rectangle, to find the solution it is necessary to determine the expansion coefficients by subordinating the solution to the boundary data prescribed on the other two opposite rectangle's sides. To do that the least squares method was applied in [14]. In such way the problem was reduced to a problem of nonconstrained optimization. The approach was applied to solve Neumann problem and some mixed biharmonic problems on rectangle.

The method of least squares on the boundary was also used in [15] to solve the first Dirichlet problem on rectangle. Here the solution of the biharmonic equation was presented

as a linear combination of finite system of biharmonic polynomials.

In [16] an axisymmetric biharmonic problem for a finite cylindrical domain was considered. The solution was presented there as the Fourier-Bessel expansion. In [17] the method of fundamental solution was applied to solve axisymmetric Dirichlet biharmonic problem (1) and (2).

In this paper we consider the method of least squares on the boundary combined with the method of homogeneous solutions in application to axisymmetric biharmonic problems for a semi-infinite cylindrical domain.

2. Problem Formulation

Problems of elastic equilibrium in axisymmetric case can be reduced to axisymmetric biharmonic equation (1), where $\Delta = \partial^2/\partial r^2 + (1/r)(\partial/\partial r) + \partial^2/\partial z^2$ is axisymmetric Laplace operator in cylindrical coordinate (r and z stand for radial and axial coordinates).

Biharmonic function w in this case has the sense of Love stress function, through which displacement components u_r , u_z and stress components σ_{rr} , σ_{rz} , $\sigma_{\theta\theta}$, σ_{zz} can be expressed as [10]

$$u_r = -\frac{\partial^2 w}{\partial r \partial z}, \quad (7)$$

$$u_z = \frac{\partial^2 w}{\partial z^2} + 2(1-\nu)\nabla^2 w,$$

$$\frac{1}{2\mu}\sigma_{rr} = \frac{\partial}{\partial z} \left(\nu \nabla^2 w - \frac{\partial^2 w}{\partial r^2} \right),$$

$$\frac{1}{2\mu}\sigma_{rz} = \frac{\partial}{\partial r} \left((1-\nu)\nabla^2 w - \frac{\partial^2 w}{\partial z^2} \right), \quad (8)$$

$$\frac{1}{2\mu}\sigma_{zz} = \frac{\partial}{\partial z} \left((2-\nu)\nabla^2 w - \frac{\partial^2 w}{\partial z^2} \right),$$

$$\frac{1}{2\mu}\sigma_{\theta\theta} = \frac{\partial}{\partial z} \left[\nu \nabla^2 w - \frac{1}{r} \frac{\partial w}{\partial r} \right],$$

where $\nu \in [0, 0.5]$ is Poisson ratio and μ stands for shear modulus.

We will consider four biharmonic problems for semi-infinite cylindrical domain $\mathbf{V} = (0 \leq r < 1, 0 < \theta \leq 2\pi, 0 < z < \infty)$ with prescribed stresses σ_{rr} and σ_{rz} on its lateral surface $\mathbf{D} = (r = 1, 0 < \theta \leq 2\pi, 0 < z < \infty)$:

$$\begin{aligned} \sigma_{rr} \Big|_{r=1} &= f_1(z), \\ \sigma_{rz} \Big|_{r=1} &= f_2(z). \end{aligned} \quad (9)$$

Here $f_1(z)$ and $f_2(z)$ are integrable functions which decay when z tends to infinity.

Problems I to IV are distinguished by boundary conditions prescribed on the plane circular area $\mathbf{S} = (0 \leq r < 1, 0 < \theta \leq 2\pi, z = 0)$.

Problem I. Consider the following:

$$\begin{aligned} \sigma_{zz}|_{z=0} &= \varphi_1(r), \\ \sigma_{rz}|_{z=0} &= \varphi_2(r). \end{aligned} \quad (10)$$

Problem II. Consider the following:

$$\begin{aligned} u_z|_{z=0} &= \varphi_3(r), \\ u_r|_{z=0} &= \varphi_4(r). \end{aligned} \quad (11)$$

Problem III. Consider the following:

$$\begin{aligned} \sigma_{zz}|_{z=0} &= \varphi_1(r), \\ u_r|_{z=0} &= \varphi_4(r). \end{aligned} \quad (12)$$

Problem IV. Consider the following:

$$\begin{aligned} u_z|_{z=0} &= \varphi_3(r), \\ \sigma_{rz}|_{z=0} &= \varphi_2(r), \end{aligned} \quad (13)$$

where $\varphi_1(r)$, $\varphi_2(r)$, $\varphi_3(r)$, and $\varphi_4(r)$ are given function.

With the use of relations (7) and (8) we can express the boundary conditions (9)–(13) in terms of function $w(r, z)$. We can see that problem I is of Neumann type. It is solvable only if the functions $\varphi_1(r)$ and $f_2(z)$ satisfy the condition

$$\int_0^1 r\varphi(r) dr - 2\pi \int_0^\infty f_2(z) dz = 0. \quad (14)$$

Problems III and IV should be classified as mixed ones.

To use the method of homogeneous solutions we reduce the problems to corresponding problems with homogeneous boundary conditions on \mathbf{D} . To do that we consider an auxiliary biharmonic problem for infinite cylindrical domain $\mathbf{V}^0 = (0 \leq r < 1, 0 < \theta \leq 2\pi, -\infty < z < \infty)$ with boundary conditions

$$\begin{aligned} \sigma_{rr}^0|_{r=1} &= f_1^0(z), \\ \sigma_{rz}^0|_{r=1} &= f_2^0(z), \end{aligned} \quad (15)$$

where $f_1^0(z)$ and $f_2^0(z)$ are defined on the line $z \in (-\infty, \infty)$ integrable functions that satisfy conditions $f_1^0(z) = f_1(z)$, $f_2^0(z) = f_2(z)$, for $z \geq 0$, and both decay when $z \rightarrow -\infty$. For instance, we can choose $f_1^0(z)$ and $f_2^0(z)$ as

$$\begin{aligned} f_1^0(z) &= \begin{cases} f_1(z), & z \geq 0, \\ f_1(-z), & z < 0, \end{cases} \\ f_2^0(z) &= \begin{cases} f_2(z), & z \geq 0, \\ -f_2(-z), & z < 0, \end{cases} \end{aligned} \quad (16)$$

or as

$$\begin{aligned} f_1^0(z) &= \begin{cases} f_1(z), & z \geq 0, \\ -f_1(-z), & z < 0, \end{cases} \\ f_2^0(z) &= \begin{cases} f_2(z), & z \geq 0, \\ f_2(-z), & z < 0. \end{cases} \end{aligned} \quad (17)$$

Problem (1) and (15) was solved with the use of the Fourier integral transform. One can find the solution in [18].

Let $v^0(r, z)$ be the solution of problem (1) and (15) and u_r^0, u_z^0 and $\sigma_{rr}^0, \sigma_{rz}^0, \sigma_{\theta\theta}^0, \sigma_{zz}^0$ the functions, calculated due to formulas (7) and (8) correspondingly for solution $v^0(r, z)$. We introduce the functions

$$\begin{aligned} \varphi_1^0(r) &\equiv \sigma_{zz}^0|_{z=0}, \\ \varphi_2^0(r) &\equiv \sigma_{rz}^0|_{z=0}, \\ \varphi_3^0(r) &\equiv u_z^0|_{z=0}, \\ \varphi_4^0(r) &\equiv u_r^0|_{z=0}. \end{aligned} \quad (18)$$

Now the solutions of the biharmonic problems I to IV can be presented as $w = v^0 + v$, where $v(r, z)$ is the solution of the biharmonic problems for domain \mathbf{V} on the lateral surface $\mathbf{D} \subset \partial\mathbf{V}$ of which Neumann's homogeneous conditions are prescribed:

$$\begin{aligned} \frac{\partial}{\partial z} \left(\nu \Delta v - \frac{\partial^2 v}{\partial r^2} \right) \Big|_{r=1} &= 0, \\ \frac{\partial}{\partial r} \left((1 - \nu) \Delta v - \frac{\partial^2 v}{\partial z^2} \right) \Big|_{r=1} &= 0. \end{aligned} \quad (19)$$

On the surface $\mathbf{S} \subset \partial\mathbf{V}$ the function $v(r, z)$ obeys one pair of conditions (20)–(23):

$$\frac{\partial}{\partial z} \left((2 - \nu) \Delta v - \frac{\partial^2 v}{\partial z^2} \right) \Big|_{z=0} = \sigma(r), \quad (20)$$

$$\frac{\partial}{\partial r} \left((1 - \nu) \Delta v - \frac{\partial^2 v}{\partial z^2} \right) \Big|_{z=0} = \tau(r),$$

$$\left(\frac{\partial^2 v}{\partial z^2} + 2(1 - \nu) \Delta v \right) \Big|_{z=0} = n(r), \quad (21)$$

$$-\frac{\partial^2 v}{\partial r \partial z} \Big|_{z=0} = t(r),$$

$$\left. \frac{\partial}{\partial z} \left((2-\nu) \Delta v - \frac{\partial^2 v}{\partial z^2} \right) \right|_{z=0} = \sigma(r),$$

$$\left. - \frac{\partial^2 v}{\partial r \partial z} \right|_{z=0} = t(r),$$

$$\left. \left(\frac{\partial^2 v}{\partial z^2} + 2(1-\nu) \Delta v \right) \right|_{z=0} = n(r),$$

$$\left. \frac{\partial}{\partial r} \left((1-\nu) \Delta v - \frac{\partial^2 v}{\partial z^2} \right) \right|_{z=0} = \tau(r).$$

Here

$$\begin{aligned} \sigma(r) &= \varphi_1(r) - \varphi_1^0(r), \\ \tau(r) &= \varphi_2(r) - \varphi_2^0(r), \\ n(r) &= \varphi_3(r) - \varphi_3^0(r), \\ t(r) &= \varphi_4(r) - \varphi_4^0(r). \end{aligned}$$

So, biharmonic problems I to IV reduced to biharmonic problems (problems I' to IV') with homogeneous conditions (19) on the cylinder lateral surface and corresponding non-homogeneous conditions (20)–(23) on the circular area S . We will solve these problems using the method of homogeneous solution.

3. Systems of Homogeneous Solutions in Cylindrical Coordinates

We look for a solution of biharmonic equation (1) in the form

$$v(r, z) = \exp(-\gamma z) f(r). \quad (25)$$

Substituting (25) into (1) brings the next ordinary differential equation for the radial function $f(r)$:

$$\begin{aligned} f^{IV}(r) + \frac{2}{r} f'''(r) + \left(2\gamma^2 - \frac{1}{r^2} \right) f''(r) \\ + \left(\frac{1}{r^3} + \frac{2}{r} \gamma^2 \right) f'(r) + \gamma^4 f(r) = 0. \end{aligned} \quad (26)$$

Due to relations (19) and (25) the radial function $f(r)$ obeys at $r = 1$ the boundary conditions:

$$\begin{aligned} \left((\nu-1) \frac{\partial^2 f(r)}{\partial r^2} + \nu \left(\frac{1}{r} \frac{\partial f(r)}{\partial r} + \gamma^2 f(r) \right) \right) \Big|_{r=1} = 0, \\ \left((1-\nu) \left(\frac{\partial^3 f(r)}{\partial r^3} + \frac{1}{r} \frac{\partial^2 f(r)}{\partial r^2} \right) \right. \\ \left. + \left(\frac{\nu-1}{r^2} - \nu \gamma^2 \right) \frac{\partial f(r)}{\partial r} \right) \Big|_{r=1} = 0. \end{aligned} \quad (27)$$

The function $f(r)$ and its derivative should be finite at $r = 0$.

The general solution of (26) is

$$\begin{aligned} f(r) &= ArJ_1(\gamma r) + BrY_1(\gamma r) + CrY_0(\gamma r) \\ &\cdot (-J_1(\gamma r)Y_0(\gamma r) + Y_1(\gamma r)J_0(\gamma r)) \\ &+ Dr(-J_1(\gamma r)J_0(\gamma r)Y_0(\gamma r) - Y_1(\gamma r) \\ &+ Y_1(\gamma r)(J_0(\gamma r))^2). \end{aligned} \quad (28)$$

Here A , B , C , and D stand for arbitrary constants, J_0 , J_1 and Y_0 , Y_1 are Bessel and Hankel functions of orders zero and one correspondingly.

To provide finiteness of solution (28) at the point $r = 0$ we put $C = 0$, $D = B$. Then, with accounting of the property of Bessel functions

$$J_0(\gamma)Y_1(\gamma) - J_1(\gamma)Y_0(\gamma) = -\frac{2}{\pi\gamma}, \quad (29)$$

the radial function $f(r)$ takes the form

$$f(r) = rJ_1(\gamma r)A - \frac{2}{\pi\gamma}J_0(\gamma r)B. \quad (30)$$

Substitution of (30) into boundary conditions (27) brings the linear homogeneous system regarding the constants A and B :

$$\begin{aligned} \pi\gamma((1-2\nu)J_0(\gamma) - \gamma J_1(\gamma))A \\ + 2(\gamma J_0(\gamma) - J_1(\gamma))B = 0, \end{aligned} \quad (31)$$

$$\pi(\gamma J_0(\gamma) + 2(1-\nu)J_1(\gamma))A + 2J_1(\gamma)B = 0.$$

Nontrivial solutions of system (31) exist under the condition

$$\gamma^2(J_0^2(\gamma) + J_1^2(\gamma)) + (2\nu-2)J_1^2(\gamma) = 0. \quad (32)$$

Transcendental equation (32) does not have any real roots except the doubly degenerate root $\gamma = 0$. It does not have imaginary roots too. Hence complex roots should be considered. The set of roots of (32) contains four infinite sequences of complex roots [10]:

$$\begin{aligned} \gamma_k^{(1)} &= \alpha_k + i\beta_k, \\ \gamma_k^{(2)} &= \alpha_k - i\beta_k, \\ \gamma_k^{(3)} &= -\alpha_k + i\beta_k, \\ \gamma_k^{(4)} &= -\alpha_k - i\beta_k, \end{aligned} \quad (33)$$

$k = 1, 2, \dots$

The values of first 15 roots of (32) are presented in Table 1: $\alpha_k = |\operatorname{Re}(\gamma_k^{(\lambda)})|$; $\beta_k = |\operatorname{Im}(\gamma_k^{(\lambda)})|$ $\lambda = \overline{1, 4}$. The data were obtained by numerical solving of (32) at $\nu = 0.25$.

Further we will use the sequences $G^{(1)} = \{\gamma_k^{(1)}, k = 1, 2, \dots\}$ and $G^{(2)} = \{\gamma_k^{(2)}, k = 1, 2, \dots\}$, the members of which

TABLE 1: Real and imaginary parts of roots $\gamma_k^{(\lambda)}$.

k	α_k	β_k	k	α_k	β_k	k	α_k	β_k
1	2.69765	1.36735	6	18.75905	2.16604	11	34.50379	2.46622
2	6.05122	1.63814	7	21.91184	2.24211	12	37.64928	2.50949
3	9.26127	1.82853	8	25.06203	2.30817	13	40.79422	2.54932
4	12.43844	1.96742	9	28.21044	2.36656	14	43.93871	2.58623
5	15.60220	2.07642	10	31.35758	2.41886	15	47.08284	2.62059

have positive real parts. That provides finiteness of solution (25) at infinity $z \rightarrow \infty$.

The set of solutions of linear system (31) is

$$A_k = \kappa_k B_k, \quad (34)$$

$$\kappa_k = \frac{2J_1(\gamma_k)}{\pi((2\nu - 2)J_1(\gamma_k) - \gamma_k J_0(\gamma_k))},$$

where B_k are indefinite complex constants. The notations $\kappa_k^{(1)} = \kappa, \kappa_k^{(2)} = \bar{\kappa}$ are used in (34) (the overline means complex conjugation).

With this in view we obtain two infinite sequences $\mathbf{R}^{(1)} = \{f_k^{(1)}, k = 1, 2, \dots\}$ and $\mathbf{R}^{(2)} = \{f_k^{(2)}, k = 1, 2, \dots\}$ of radial functions

$$f_k^{(1)}(r) = \left(rJ_1(\gamma_k^{(1)}r) \kappa_k^{(1)} - \frac{2}{\pi\gamma_k} J_0(\gamma_k^{(1)}r) \right), \quad (35)$$

$$f_k^{(2)}(r) = \left(rJ_1(\gamma_k^{(2)}r) \kappa_k^{(2)} - \frac{2}{\pi\gamma_k} J_0(\gamma_k^{(2)}r) \right)$$

and two infinite sequences $V^{(1)} = \{v_k^{(1)}, k = 1, 2, \dots\}$ and $V^{(2)} = \{v_k^{(2)}, k = 1, 2, \dots\}$ homogeneous solutions

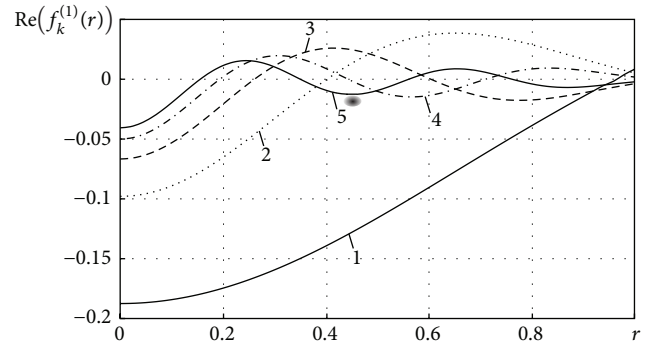
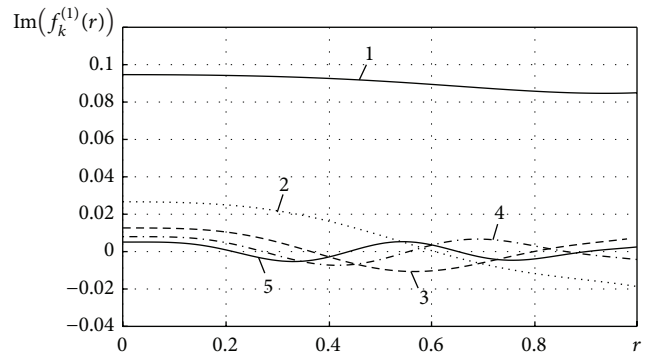
$$v_k^{(1)}(r, z) = f_k^{(1)}(r) \exp(-\gamma_k^{(1)}z), \quad (36)$$

$$v_k^{(2)}(r, z) = f_k^{(2)}(r) \exp(-\gamma_k^{(2)}z).$$

In Figures 1 and 2 the real and imaginary parts of functions $f_k^{(1)}(r)$ are shown for $k = 1, 2, 3, 4, 5$ (curves 1, 2, 3, 4, and 5 correspondingly).

As the functions $f_k^{(1)}(r)$ and $f_k^{(2)}(r)$ are solutions of homogeneous boundary value problem (26) and (27) both sequences $\mathbf{R}^{(1)}$ and $\mathbf{R}^{(2)}$ form independent functional bases on the segment $r \in [0, 1]$ in complex domain. Their real $\text{Re}(f_k^{(1)}(r))$ and $\text{Im}(f_k^{(1)}(r))$ parts form independent functional bases on the same segment in real domain.

We will use the two sequences $V^{(1)}$ and $V^{(2)}$ of complex valued functions (36) to construct the real solutions for four biharmonic problems in \mathbf{V} (problems I' to IV') prescribed on $\mathbf{S} \subset \partial\mathbf{V}$ boundary conditions given by formulas (20) to (23) correspondingly. On the remaining part \mathbf{D} of $\partial\mathbf{V}$ homogeneous conditions (19) are prescribed for all problems.


 FIGURE 1: Real parts of function $f_k^{(1)}(r)$.

 FIGURE 2: Imaginary parts of function $f_k^{(1)}(r)$.

As the sequences $v_k^{(1)}(r, z)$ and $v_k^{(2)}(r, z)$ are mutually complex-conjugated we present the solution $v(r, z)$ in the form

$$v(r, z) = \frac{1}{2} \sum_{k=1}^{\infty} \sum_{p=1}^2 B_k^{(p)} v_k^{(p)}(r, z), \quad (37)$$

where $B_k^{(1)}, B_k^{(2)} \equiv \overline{B_k^{(1)}}$ are indefinite complex constants.

As all functions $v_k^{(p)}(r, z)$, $p = 1, 2$ satisfy (1) and boundary conditions (19) to solve the problems it is necessary to determine the constants $B_k^{(1)}, B_k^{(2)}$ by subordinating the solution (37) to the boundary conditions (20)–(23).

4. A Variational Method

Substitution of solution (37) into boundary conditions (20)–(23) brings two functional relations for each problem:

$$\begin{aligned} \frac{1}{2} \sum_{k=1}^{\infty} \sum_{p=1}^2 B_k^{(p)} \sigma_k^{(p)} &= \sigma(r), \\ \frac{1}{2} \sum_{k=1}^{\infty} \sum_{p=1}^2 B_k^{(p)} \tau_k^{(p)} &= \tau(r), \end{aligned} \quad (38)$$

$$\begin{aligned} \frac{1}{2} \sum_{k=1}^{\infty} \sum_{p=1}^2 B_k^{(p)} n_k^{(p)} &= n(r), \\ \frac{1}{2} \sum_{k=1}^{\infty} \sum_{p=1}^2 B_k^{(p)} t_k^{(p)} &= t(r), \end{aligned} \quad (39)$$

$$\begin{aligned} \frac{1}{2} \sum_{k=1}^{\infty} \sum_{p=1}^2 B_k^{(p)} \sigma_k^{(p)} &= \sigma(r), \\ \frac{1}{2} \sum_{k=1}^{\infty} \sum_{p=1}^2 B_k^{(p)} t_k^{(p)} &= t(r), \end{aligned} \quad (40)$$

$$\begin{aligned} \frac{1}{2} \sum_{k=1}^{\infty} \sum_{p=1}^2 B_k^{(p)} t_k^{(p)} &= t(r), \\ \frac{1}{2} \sum_{k=1}^{\infty} \sum_{p=1}^2 B_k^{(p)} n_k^{(p)} &= n(r), \end{aligned} \quad (41)$$

$$\frac{1}{2} \sum_{k=1}^{\infty} \sum_{p=1}^2 B_k^{(p)} \tau_k^{(p)} = \tau(r),$$

where the following notations are used:

$$\begin{aligned} \sigma_k^{(p)}(r) &= (\nu - 2) \gamma_k^{(p)} \left(\frac{\partial^2 f_k^{(p)}(r)}{\partial r^2} + \frac{1}{r} \frac{\partial f_k^{(p)}(r)}{\partial r} \right) \\ &\quad + (\nu - 1) \left(\gamma_k^{(p)} \right)^3 f_k^{(p)}(r), \\ \tau_k^{(p)}(r) &= (1 - \nu) \left(\frac{\partial^3 f_k^{(p)}(r)}{\partial r^3} + \frac{1}{r} \frac{\partial^2 f_k^{(p)}(r)}{\partial r^2} \right) \\ &\quad + \left(\frac{\nu - 1}{r^2} - \nu \left(\gamma_k^{(p)} \right)^2 \right) \frac{\partial f_k^{(p)}(r)}{\partial r}, \\ n_k^{(p)}(r) &= 2(1 - \nu) \left(\frac{\partial^2 f_k^{(p)}(r)}{\partial r^2} + \frac{1}{r} \frac{\partial f_k^{(p)}(r)}{\partial r} \right) \\ &\quad + (3 - 2\nu) \left(\gamma_k^{(p)} \right)^2 f_k^{(p)}(r), \\ t_k^{(p)}(r) &= -\gamma_k^{(p)} \frac{\partial f_k^{(p)}(r)}{\partial r}. \end{aligned} \quad (42)$$

Hence, to solve any of problems I' to IV' we should find the infinite sequences $\mathbf{B}^{(1)} = \{B_k^{(1)}, k = 1, 2, \dots\}$ and $\mathbf{B}^{(2)} = \{\overline{B_k^{(1)}}, k = 1, 2, \dots\}$ of complex numbers the members $B_k^{(1)} \in \mathbf{B}^{(1)}$ and $\overline{B_k^{(1)}} \in \mathbf{B}^{(2)}$ of which transform the corresponding

pair of functional equations (38) to (41) into identities. We solve the problem of determination of the sequences $\mathbf{B}^{(1)}$ and $\mathbf{B}^{(2)}$ in quadratic norm L^2 exploiting the least squares method. To do that we define the functional for each problem

$$\begin{aligned} F_I &= \int_0^1 \left[\left(\frac{1}{2} \sum_{k=1}^{\infty} \sum_{p=1}^2 B_k^{(p)} \sigma_k^{(p)} - \sigma(r) \right)^2 \right. \\ &\quad \left. + \left(\frac{1}{2} \sum_{k=1}^{\infty} \sum_{p=1}^2 B_k^{(p)} \tau_k^{(p)} - \tau(r) \right)^2 \right] r dr, \end{aligned} \quad (43)$$

$$\begin{aligned} F_{II} &= \int_0^1 \left[\left(\frac{1}{2} \sum_{k=1}^{\infty} \sum_{p=1}^2 B_k^{(p)} n_k^{(p)} - n(r) \right)^2 \right. \\ &\quad \left. + \left(\frac{1}{2} \sum_{k=1}^{\infty} \sum_{p=1}^2 B_k^{(p)} t_k^{(p)} - t(r) \right)^2 \right] r dr, \end{aligned} \quad (44)$$

$$\begin{aligned} F_{III} &= \int_0^1 \left[\left(\frac{1}{2} \sum_{k=1}^{\infty} \sum_{p=1}^2 B_k^{(p)} \sigma_k^{(p)} - \sigma(r) \right)^2 \right. \\ &\quad \left. + \left(\frac{1}{2} \sum_{k=1}^{\infty} \sum_{p=1}^2 B_k^{(p)} t_k^{(p)} - t(r) \right)^2 \right] r dr, \end{aligned} \quad (45)$$

$$\begin{aligned} F_{IV} &= \int_0^1 \left[\left(\frac{1}{2} \sum_{k=1}^{\infty} \sum_{p=1}^2 B_k^{(p)} n_k^{(p)} - n(r) \right)^2 \right. \\ &\quad \left. + \left(\frac{1}{2} \sum_{k=1}^{\infty} \sum_{p=1}^2 B_k^{(p)} \tau_k^{(p)} - \tau(r) \right)^2 \right] r dr. \end{aligned} \quad (46)$$

That reduces the problems to corresponding problems of unconstrained optimization.

Applying the necessary minimum conditions to the functionals (43) to (46)

$$\begin{aligned} \frac{\partial F_j}{\partial B_m^{(1)}} &= 0, \\ \frac{\partial F_j}{\partial B_m^{(2)}} &= 0, \end{aligned} \quad (47)$$

$j = I, II, III, IV, m = 1, 2, \dots$

we come to the infinite system of linear algebraic equations

$$\sum_{k=1}^{\infty} \sum_{p=1}^2 M_{mk}^{(sp)} B_k^{(p)} = K_m^{(s)}. \quad (48)$$

The coefficients $M_{mk}^{(sp)}$ ($s, p = 1, 2, m = 1, 2, \dots$), $K_m^{(s)}$ of system (48) for problems I' to IV' are defined by formulas (49)–(52) correspondingly:

$$M_{mk}^{(sp)} = \frac{1}{2} \int_0^1 (\sigma_k^{(p)} \sigma_m^{(s)} + \tau_k^{(p)} \tau_m^{(s)}) r dr, \quad (49)$$

$$K_m^{(s)} = \int_0^1 (\sigma(r) \sigma_m^{(s)} + \tau(r) \tau_m^{(s)}) r dr,$$

$$M_{mk}^{(sp)} = \frac{1}{2} \int_0^1 (n_k^{(p)} n_m^{(s)} + t_k^{(p)} t_m^{(s)}) r dr - \int_0^1 n_m^{(s)} r dr \int_0^1 n_k^{(p)} r dr, \quad (50)$$

$$K_m^{(s)} = \int_0^1 (n(r) n_m^{(s)} + t(r) t_m^{(s)}) r dr - 2 \int_0^1 n(r) r dr \int_0^1 n_m^{(s)} r dr,$$

$$M_{mk}^{(sp)} = \frac{1}{2} \int_0^1 (\sigma_k^{(p)} \sigma_m^{(s)} + t_k^{(p)} t_m^{(s)}) r dr, \quad (51)$$

$$K_m^{(s)} = \int_0^1 (\sigma(r) \sigma_m^{(s)} + t(r) t_m^{(s)}) r dr,$$

$$M_{mk}^{(sp)} = \frac{1}{2} \int_0^1 (n_k^{(p)} n_m^{(s)} + \tau_k^{(p)} \tau_m^{(s)}) r dr - \int_0^1 n_m^{(s)} r dr \int_0^1 n_k^{(p)} r dr, \quad (52)$$

$$K_m^{(s)} = \int_0^1 (n(r) n_m^{(s)} + \tau(r) \tau_m^{(s)}) r dr - 2 \int_0^1 n(r) r dr \int_0^1 n_m^{(s)} r dr.$$

So, the problems are reduced to solving the infinite system of linear algebraic equations (48).

5. Numerical Experiments

We solved the problems with the use of the reduction method considering the finite system of dimension $2N$ [19]:

$$\sum_{k=1}^N \sum_{p=1}^2 M_{mk}^{(sp)} B_k^{(p)} = K_m^{(s)}. \quad (53)$$

To evaluate the convergence of the solutions for problems I' to IV' depending on dimension of the reduced system we considered some characteristic examples, taking the

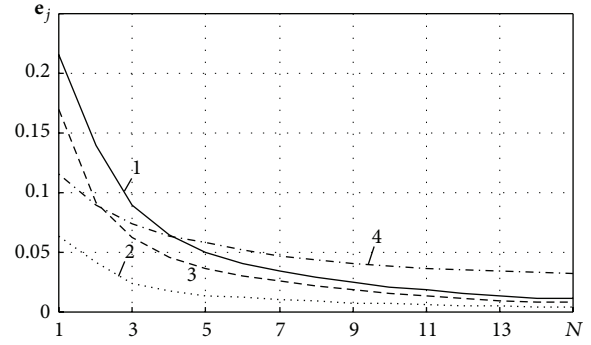


FIGURE 3: Solution error for problems I' to IV'.

functions of right-hand sides of boundary conditions (38)–(41) in the forms

$$\begin{aligned} \sigma(r) &= \sigma_0 \arctan(d(r - r_0)), \\ \tau(r) &= 0, \\ r_0 &= 0.5, \\ d &= 40, \\ n(r) &= 0, \\ t(t) &= t_0 r, \\ \sigma(r) &= \sigma_0 \arctan(d(r - r_0)), \\ t(r) &= 0, \\ n(r) &= 0, \\ \tau(r) &= \tau_0 r. \end{aligned} \quad (54)$$

The solution errors for problems I' to IV' were calculated due to values of the corresponding functional as

$$\begin{aligned} \varepsilon_I &= \frac{1}{\sigma_0} \left(\frac{F_I}{2\pi} \right)^{1/2}, \\ \varepsilon_{II} &= \frac{1}{t_0} \left(\frac{F_{II}}{2\pi} \right)^{1/2}, \\ \varepsilon_{III} &= \frac{1}{\sigma_0} \left(\frac{F_{III}}{2\pi} \right)^{1/2}, \\ \varepsilon_{IV} &= \frac{1}{\tau_0} \left(\frac{F_{IV}}{2\pi} \right)^{1/2}. \end{aligned} \quad (55)$$

Plots in Figure 3 demonstrate how the errors $e_j \in \{\varepsilon_I, \varepsilon_{II}, \varepsilon_{III}, \varepsilon_{IV}\}$ decay with increasing N (curves 1, 2, 3, and 4, resp.). As we can see convergence of the solutions depends on the type of boundary conditions and features of the prescribed boundary data. On the basis of conducted numerical experiments we can conclude that accuracy sufficient for practical goals can be achieved at $N \geq 10$.

In Figures 4–7 some results obtained by solving problems I' and II' are presented. Figure 4 displays the radial

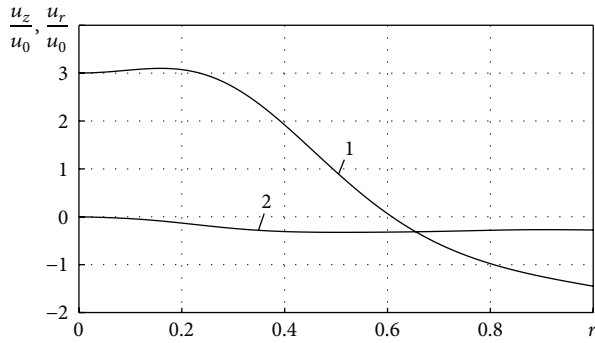


FIGURE 4: The radial dependencies of displacement for problem I'.

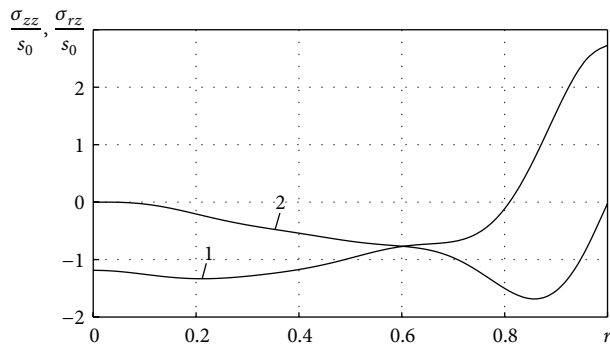


FIGURE 5: The radial dependencies of stresses for problem II'.

dependencies of dimensionless normal u_z/u_0 (curve 1) and tangential u_r/u_0 (curve 2) displacements on the surface $\mathbf{S} \subset \partial\mathbf{V}$ for problem I'. Figure 5 shows the radial dependencies of dimensionless normal σ_{zz}/s_0 (curve 1) and tangential σ_{rz}/s_0 (curve 2) stresses on this surface for problem II'.

Here u_0 and s_0 are parameters defined as $u_0 = \sigma_0 r_0 / (2\mu)$, $s_0 = 2\mu t_0 / r_0$, where $r_0 = 1$ is the cylinder radius.

Figures 6 and 7 illustrate axial dependencies of dimensionless stress components for problems I' and II' correspondingly.

Curves 1 and 2 in both figures correspond to the stress components σ_{zz} calculated at constant radial coordinates $r = 0$ and $r = 1$, respectively, whereas curves 3 and 4 correspond to the stress components $\sigma_{\theta\theta}$ calculated at the same radial coordinates $r = 0$ and $r = 1$.

As we can see the solutions are quickly decayed with axial coordinate. So, developed approach can be applied to finite cylinders the heights of which equal two or more of their radii.

6. Conclusion

In this paper we proposed an approach for solving of the axisymmetric biharmonic boundary value problems for semi-infinite cylindrical domain, on the lateral surface of which homogeneous Neumann boundary conditions are prescribed. On the remaining part of the domain's boundary four different biharmonic boundary pieces of data are considered. The approach is based on presentation of the

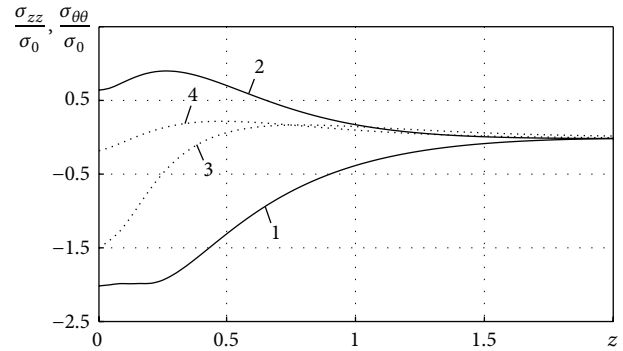


FIGURE 6: The axial dependencies of stress components for problem I'.

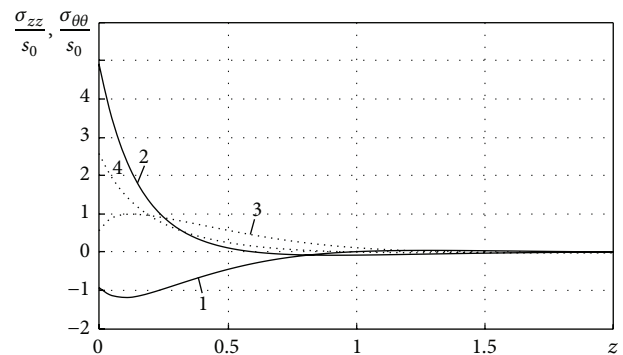


FIGURE 7: The axial dependencies of stress components for problem II'.

solution as a series expansion in two consequences of complex valued biharmonic functions, so-called homogeneous solutions, which obey the Neumann homogeneous boundary conditions on the lateral surface. Application of the method of least squares for subordinating the solution to nonhomogeneous boundary conditions prescribed on the part of the boundary reduces the problems to corresponding problems of unconstrained optimization. These problems, in turn, were reduced to infinite systems of linear algebraic equations regarding the expansion coefficients. Solutions of the systems were obtained for various boundary data given on the part of the boundary with nonhomogeneous conditions exploiting the reduction method. Conducted numerical experiments confirm high convergence of the method: a sufficient accuracy is reached at N equal to about 10.

The approach can be used to solve axisymmetric elasticity problems for cylindrical bodies, the heights of which are equal to or exceed their diameters, when on their lateral surface normal and tangential tractions are prescribed and on the cylinder's end faces one of four possible boundary pieces of data is given: (1) normal and tangential tractions, (2) normal and tangential displacements, (3) normal traction and tangential displacement, and (4) normal displacement and tangential traction.

Similar approach can be developed for the case when on the cylinder's lateral surface boundary conditions in displacements are given.

To expand the developed approach for a short cylindrical body, the height of which is less than its diameter, the interactions of strain-stressed states, caused by boundary data prescribed on the opposite end faces, should be accounted. To do that one can use four sequences $V^{(1)}$, $V^{(2)}$, $V^{(3)}$, and $V^{(4)}$ of homogeneous solutions to construct the solution. Here $V^{(3)} = \{v_k^{(3)}, k = 1, 2, \dots\}$, $V^{(4)} = \{v_k^{(4)}, k = 1, 2, \dots\}$, $v_k^{(3)}(r, z)$, and $v_k^{(4)}(r, z)$ are biharmonic functions corresponding transcendental equation (32) roots $\{\gamma_k^{(3)}, k = 1, 2, \dots\}$ and $\{\gamma_k^{(4)}, k = 1, 2, \dots\}$.

Competing Interests

The authors declare that they have no competing interests.

References

- [1] H. Begehr, "Dirichlet problems for the biharmonic equation," *General Mathematics*, vol. 13, no. 2, pp. 65–72, 2005.
- [2] Q. A. Dang and N. Van Thien, "Iterative method for solving the second boundary value problem for biharmonic-type equation," *Journal of Applied Mathematics*, vol. 2012, Article ID 891519, 18 pages, 2012.
- [3] B. Turmetov and R. Ashurov, "On solvability of the Neumann boundary value problem for non-homogeneous biharmonic equation," *British Journal of Mathematics & Computer Science*, no. 4, pp. 557–571, 2014.
- [4] V. Moises, *Mixed problems and layer potentials for harmonic and biharmonic functions [thesis]*, Syracuse University, Syracuse, NY, USA, paper 66, 2011.
- [5] O. A. Matevosyan, "Solution of a mixed boundary value problem for the biharmonic equation with finite weighted Dirichlet integral," *Differential Equations*, vol. 51, no. 4, pp. 487–501, 2015.
- [6] Q. A. Dang, "Iterative method for solving the Neumann boundary value problem for biharmonic type equation," *Journal of Computational and Applied Mathematics*, vol. 196, no. 2, pp. 634–643, 2006.
- [7] S. Jiang, B. Ren, P. Tsuji, and L. Ying, "Second kind integral equations for the first kind Dirichlet problem of the biharmonic equation in three dimensions," *Journal of Computational Physics*, vol. 230, no. 19, pp. 7488–7501, 2011.
- [8] M. Ben-Artzi, I. Chorev, J.-P. Croisille, and D. Fishelov, "A compact difference scheme for the biharmonic equation in planar irregular domains," *SIAM Journal on Numerical Analysis*, vol. 47, no. 4, pp. 3087–3108, 2009.
- [9] J. Pestana, R. Muddle, M. Heil, F. Tisseur, and M. Mihajlović, "Efficient block preconditioning for a C^1 finite element discretization of the Dirichlet biharmonic problem," *SIAM Journal on Scientific Computing*, vol. 38, no. 1, pp. A325–A345, 2016.
- [10] A. I. Lurie, *Theory of Elasticity*, Springer, Berlin, Germany, 2005.
- [11] S. A. Lurie and V. V. Vasiliev, *The Biharmonic Problem in The Theory of Elasticity*, Gordon and Breach Publishers, Amsterdam, The Netherlands, 1995.
- [12] V. V. Meleshko, "Biharmonic problem in a rectangle," *Applied Scientific Research*, vol. 58, no. 1–4, pp. 217–249, 1997.
- [13] V. T. Grinchenko, "The biharmonic problem and progress in the development of analytical methods for the solution of boundary-value problems," *Journal of Engineering Mathematics*, vol. 46, no. 3–4, pp. 281–297, 2003.
- [14] F. Chekurin and L. I. Postolaki, "A variational method for the solution of biharmonic problems for a rectangular domain," *Journal of Mathematical Sciences*, vol. 160, no. 3, pp. 386–399, 2009.
- [15] K. Rektorys and V. Zahradník, "Solution of the first biharmonic problem by the method of least squares on the boundary," *Aplikace Matematiky*, vol. 19, no. 2, pp. 101–131, 1974.
- [16] R. Sburlati, "Three-dimensional analytical solution for an axisymmetric biharmonic problem," *Journal of Elasticity*, vol. 95, no. 1, pp. 79–97, 2009.
- [17] G. Fairweather, A. Karageorghis, and Y.-S. Smyrlis, "A matrix decomposition MFS algorithm for axisymmetric biharmonic problems," *Advances in Computational Mathematics*, vol. 23, no. 1–2, pp. 55–71, 2005.
- [18] W. Nowacki, *The Theory of Elasticity*, Mir, Moscow, Russia, 1975 (Russian).
- [19] I. V. Kantorovich and V. I. Krylov, *Approximate Methods of Higher Analysis*, Phys.-Mat. Publ., Moscow, Russia, 1962 (Russian), Translated from the 3rd Russian edition by C. D. Benster, Interscience Publishers, New York, NY, USA; P. Noordhoff, Groningen, The Netherlands, 1958.

Research Article

Explicit Determinantal Representation Formulas of W -Weighted Drazin Inverse Solutions of Some Matrix Equations over the Quaternion Skew Field

Ivan I. Kyrchei

Pidstrygach Institute for Applied Problems of Mechanics and Mathematics, NAS of Ukraine, Lviv 79060, Ukraine

Correspondence should be addressed to Ivan I. Kyrchei; kyrchei@online.ua

Received 25 January 2016; Accepted 24 April 2016

Academic Editor: Romain Aubry

Copyright © 2016 Ivan I. Kyrchei. This is an open access article distributed under the Creative Commons Attribution License, which permits unrestricted use, distribution, and reproduction in any medium, provided the original work is properly cited.

By using determinantal representations of the W -weighted Drazin inverse previously obtained by the author within the framework of the theory of the column-row determinants, we get explicit formulas for determinantal representations of the W -weighted Drazin inverse solutions (analogs of Cramer's rule) of the quaternion matrix equations $\mathbf{WAWX} = \mathbf{D}$, $\mathbf{XWBW} = \mathbf{D}$, and $\mathbf{W}_1\mathbf{AW}_1\mathbf{XW}_2\mathbf{BW}_2 = \mathbf{D}$.

1. Introduction

Throughout the paper, we denote the real number field by \mathbb{R} , the set of all $m \times n$ matrices over the quaternion algebra

$$\begin{aligned} \mathbb{H} &= \{a_0 + a_1i + a_2j + a_3k \mid i^2 = j^2 = k^2 \\ &= -1, a_0, a_1, a_2, a_3 \in \mathbb{R}\} \end{aligned} \quad (1)$$

by $\mathbb{H}^{m \times n}$, and the set of all $m \times n$ matrices over \mathbb{H} with a rank r by $\mathbb{H}_r^{m \times n}$. Let $M(n, \mathbb{H})$ be the ring of $n \times n$ quaternion matrices. For $\mathbf{A} \in \mathbb{H}^{n \times m}$, the symbol \mathbf{A}^* stands for the conjugate transpose (Hermitian adjoint) matrix of \mathbf{A} . The matrix $\mathbf{A} = (a_{ij}) \in \mathbb{H}^{n \times n}$ is Hermitian if $\mathbf{A}^* = \mathbf{A}$.

For $\mathbf{A} \in \mathbb{H}^{m \times n}$, we denote by

$\mathcal{R}_r(\mathbf{A}) = \{\mathbf{y} \in \mathbb{H}^m : \mathbf{y} = \mathbf{Ax}, \mathbf{x} \in \mathbb{H}^n\}$ the column right space of \mathbf{A} ;

$\mathcal{N}_r(\mathbf{A}) = \{\mathbf{y} \in \mathbb{H}^n : \mathbf{Ax} = 0\}$ the right null space of \mathbf{A} ;

$\mathcal{R}_l(\mathbf{A}) = \{\mathbf{y} \in \mathbb{H}^m : \mathbf{y} = \mathbf{xA}, \mathbf{x} \in \mathbb{H}^m\}$ the column left space of \mathbf{A} ;

$\mathcal{N}_l(\mathbf{A}) = \{\mathbf{y} \in \mathbb{H}^m : \mathbf{xA} = 0\}$ the left null space of \mathbf{A} .

In the past, researches into the quaternion skew field had a more theoretical importance, but now a growing

number of investigations give wide practical applications of quaternions. In particular through their attitude orientation, the quaternions arise in various fields such as quaternionic quantum theory [1], fluid mechanics and particle dynamics [2, 3], computer graphics [4], aircraft orientation [5], robotic systems [6], and life science [7, 8].

Research on quaternion matrix equations and generalized inverses, which are usefulness tools used to solve matrix equations, has been actively ongoing for more recent years. We mention only some recent papers. Yuan et al. [9] derived solutions of the quaternion matrix equation $\mathbf{AX} = \mathbf{B}$ and their applications in color image restoration. Wang et al. [10] studied extreme ranks of real matrices in solution of the quaternion matrix equation $\mathbf{AXB} = \mathbf{C}$. Yuan et al. [11] obtained the expressions of least squares Hermitian solution with minimum norm of the quaternion matrix equation $(\mathbf{AXB}, \mathbf{CXD}) = (\mathbf{E}, \mathbf{F})$. Feng and Cheng [12] gave a clear description of the solution set to the quaternion matrix equation $\mathbf{AX} - \bar{\mathbf{X}}\mathbf{B} = 0$. Jiang and Wei [13] derived the explicit solution of the quaternion matrix equation $\mathbf{X} - \mathbf{A}\bar{\mathbf{X}}\mathbf{B} = \mathbf{C}$. Caiqin et al. [14] obtained the expressions of the explicit solutions of quaternion matrix equations $\mathbf{XF} - \mathbf{AX} = \mathbf{BY}$ and $\mathbf{XF} - \mathbf{A}\bar{\mathbf{X}} = \mathbf{BY}$. Yuan and Wang [15] gave the expressions of the least squares η -Hermitian solution with the least norm of the quaternion matrix equation $\mathbf{AXB} + \mathbf{CXD} = \mathbf{E}$. Zhang

et al. derived [16] the expressions of the minimal norm least squares solution, the pure imaginary least squares solution, and the real least squares solution for the quaternion matrix equation $AX = B$.

The definitions of the generalized inverse matrices have been extended to quaternion matrices as follows.

The Moore-Penrose inverse of $\mathbf{A} \in \mathbb{H}^{m \times n}$, denoted by \mathbf{A}^\dagger , is the unique matrix $\mathbf{X} \in \mathbb{H}^{n \times m}$ satisfying the following equations:

$$\mathbf{AXA} = \mathbf{A}; \quad (2)$$

$$\mathbf{XAX} = \mathbf{X}; \quad (3)$$

$$(\mathbf{AX})^* = \mathbf{AX}; \quad (4)$$

$$(\mathbf{XA})^* = \mathbf{XA}. \quad (5)$$

For $\mathbf{A} \in \mathbb{H}^{n \times n}$ with $k = \text{Ind } \mathbf{A}$ being the smallest positive number such that $\text{rank } \mathbf{A}^{k+1} = \text{rank } \mathbf{A}^k$, the Drazin inverse of \mathbf{A} , denoted by \mathbf{A}^D , is defined to be the unique matrix \mathbf{X} that satisfies (3) and the equations

$$\mathbf{AX} = \mathbf{XA}; \quad (6)$$

$$\mathbf{A}^{k+1}\mathbf{X} = \mathbf{A}^k.$$

In particular, when $\text{Ind } \mathbf{A} = 1$, then \mathbf{X} is called the group inverse of \mathbf{A} and is denoted by $\mathbf{X} = \mathbf{A}^g$. If $\text{Ind } \mathbf{A} = 0$, then \mathbf{A} is nonsingular, and $\mathbf{A}^D \equiv \mathbf{A}^\dagger = \mathbf{A}^{-1}$.

Cline and Greville [17] extended the Drazin inverse of square matrix to rectangular matrix that has been generalized to the quaternion algebra as follows.

For $\mathbf{A} \in \mathbb{H}^{m \times n}$ and $\mathbf{W} \in \mathbb{H}^{n \times m}$, the W -weighted Drazin inverse of \mathbf{A} with respect to \mathbf{W} is the unique solution to the following equations:

$$\begin{aligned} (\mathbf{AW})^{k+1}\mathbf{XW} &= (\mathbf{AW})^k; \\ \mathbf{XWAWX} &= \mathbf{X}; \end{aligned} \quad (7)$$

$$\mathbf{AWX} = \mathbf{XWA},$$

where $k = \max\{\text{Ind}(\mathbf{AW}), \text{Ind}(\mathbf{WA})\}$.

The Drazin inverse and weighted Drazin inverse have several important applications such as applications in singular differential and difference equations [18], signal processing [19], Markov chains and statistic problems [20, 21], descriptor continuous-time systems [22], numerical analysis and Kronecker product systems [23], solving singular fuzzy linear system [24, 25], constrained linear systems [26], and so forth.

Cramer's rule for the W -weighted Drazin inverse solutions, in particular, has been derived in [27] for singular linear equations and in [26] for a class of restricted matrix equations. Recently, within the framework of the theory of the column-row determinants, Song [28] has first obtained a determinantal representation of the W -weighted Drazin inverse and Cramer's rule of a class of restricted matrix equations over the quaternion algebra. But in obtaining, he has used auxiliary matrices other than that are given. In [29], we have obtained new determinantal representations of the

W -weighted Drazin inverse over the quaternion skew field without any auxiliary matrices.

An important application of determinantal representations of generalized inverses is the Cramer rule for generalized inverse solutions of matrix equations.

But when is there a need for a W -weighted Drazin inverse solution? Consider, for example, the following matrix equation: $\mathbf{A}_1\mathbf{X} = \mathbf{D}$. Let \mathbf{A}_1 be rectangular and we can represent it as $\mathbf{A}_1 = \mathbf{WAW}$, where \mathbf{WA} and \mathbf{AW} are quadratic and singular. Furthermore, we have the following restrictions: $\mathcal{R}_r(\mathbf{X}) \subset \mathcal{R}_r((\mathbf{AW})^k)$, $\mathcal{N}_l(\mathbf{X}) \supset \mathcal{N}_l((\mathbf{WA})^k)$. Then its W -weighted Drazin inverse solution is needed.

In the paper we investigate analogs of Cramer's rule for W -weighted Drazin inverse solutions of the following quaternion matrix equations:

$$\mathbf{WAWX} = \mathbf{D}, \quad (8)$$

$$\mathbf{XWBW} = \mathbf{D}, \quad (9)$$

$$\mathbf{W}_1\mathbf{AW}_1\mathbf{XW}_2\mathbf{BW}_2 = \mathbf{D}. \quad (10)$$

The paper is organized as follows. We start with introducing of the row-column determinants and determinantal representations of the Moore-Penrose and Drazin inverses for a quaternion matrix obtained by them in Section 2.1. Determinantal representations of the W -weighted Drazin inverse and its properties were considered in Section 2.2. In Section 3.1, we give the background of the problem of Cramer's rule for the W -weighted Drazin inverse solution. In Section 3.2 we obtain explicit representation formulas of the W -weighted Drazin inverse solutions (analog of Cramer's rule) of the quaternion matrix equation (10). Consequently, we get both similar and special determinantal representation formulas of the W -weighted Drazin inverse solutions of (8) and (9). In Section 4, we give numerical examples to illustrate the main result.

2. Preliminaries

2.1. Determinantal Representations of the Moore-Penrose and Drazin Inverses by the Column and Row Determinants. The theory of the row-column determinants over the quaternion skew field has been introduced in [30–32], and later it has been applied to research generalized inverses and generalized inverse solutions of matrix equations. In particular, determinantal representations of the Moore-Penrose [33, 34] and explicit representation formulas for the minimum norm least squares solutions of some quaternion matrix equations [35] and determinantal representations of the Drazin [36] and W -weighted Drazin inverses [29] have been obtained by the author. Song derived determinantal representation of the generalized inverse $A_{T,S}^2$ [37], the Bott-Duffin inverse [38], the Cramer rule for the solutions of restricted matrix equations [39], the generalized Stein quaternion matrix equation [40], and so forth.

For $\mathbf{A} = (a_{ij}) \in M(n, \mathbb{H})$ we define n row determinants and n column determinants as follows.

Suppose that S_n is the symmetric group on the set $I_n = \{1, \dots, n\}$.

Definition 1. The i th row determinant of $\mathbf{A} = (a_{ij}) \in M(n, \mathbb{H})$ is defined for all $i = \overline{1, n}$ by putting

$$\begin{aligned} \text{rdet}_i \mathbf{A} &= \sum_{\sigma \in S_n} (-1)^{n-r} \\ &\cdot a_{i i_{k_1}} a_{i i_{k_1+1}} \cdots a_{i i_{k_1+l_1}} \cdots a_{i i_{k_r}} \cdots a_{i i_{k_r+l_r}}, \\ \sigma &= (i i_{k_1} i_{k_1+1} \cdots i_{k_1+l_1}) \\ &\cdot (i_{k_2} i_{k_2+1} \cdots i_{k_2+l_2}) \cdots (i_{k_r} i_{k_r+1} \cdots i_{k_r+l_r}), \end{aligned} \quad (11)$$

with conditions $i_{k_2} < i_{k_3} < \cdots < i_{k_r}$ and $i_{k_t} < i_{k_t+s}$ for $t = \overline{2, r}$ and $s = \overline{1, l_t}$.

Definition 2. The j th column determinant of $\mathbf{A} = (a_{ij}) \in M(n, \mathbb{H})$ is defined for all $j = \overline{1, n}$ by putting

$$\begin{aligned} \text{cdet}_j \mathbf{A} &= \sum_{\tau \in S_n} (-1)^{n-r} \\ &\cdot a_{j k_r} a_{j k_r+l_r} \cdots a_{j k_r+1} a_{j k_r+1+l_r} \cdots a_{j j_{k_1+1}} \cdots a_{j k_1+1} a_{j k_1} a_{j k_1} j, \\ \tau &= (j k_r+l_r \cdots j k_r+1 j k_r) \cdots (j k_2+l_2 \cdots j k_2+1 j k_2) \\ &\cdot (j k_1+l_1 \cdots j k_1+1 j k_1 j), \end{aligned} \quad (12)$$

with conditions $j_{k_2} < j_{k_3} < \cdots < j_{k_r}$ and $j_{k_t} < j_{k_t+s}$ for $t = \overline{2, r}$ and $s = \overline{1, l_t}$.

Suppose that \mathbf{A}^{ij} denotes the submatrix of \mathbf{A} obtained by deleting both the i th row and the j th column. Let \mathbf{a}_j be the j th column and let \mathbf{a}_i be the i th row of \mathbf{A} . Suppose that $\mathbf{A}_{\cdot j}(\mathbf{b})$ denotes the matrix obtained from \mathbf{A} by replacing its j th column with the column \mathbf{b} and that $\mathbf{A}_i(\mathbf{b})$ denotes the matrix obtained from \mathbf{A} by replacing its i th row with the row \mathbf{b} .

The following theorem has a key value in the theory of the column and row determinants.

Theorem 3 (see [30]). *If $\mathbf{A} = (a_{ij}) \in M(n, \mathbb{H})$ is Hermitian, then $\text{rdet}_1 \mathbf{A} = \cdots = \text{rdet}_n \mathbf{A} = \text{cdet}_1 \mathbf{A} = \cdots = \text{cdet}_n \mathbf{A} \in \mathbb{R}$.*

Since all column and row determinants of a Hermitian matrix over \mathbb{H} are equal, we can define the determinant of a Hermitian matrix $\mathbf{A} \in M(n, \mathbb{H})$. By definition, we put $\det \mathbf{A} := \text{rdet}_i \mathbf{A} = \text{cdet}_i \mathbf{A}$, for all $i = \overline{1, n}$. The determinant of a Hermitian matrix has properties similar to a usual determinant. They are completely explored in [30, 31] by its row and column determinants. In particular, within the framework of the theory of the column-row determinants, we have the determinantal representation of the inverse matrix over \mathbb{H} by analogs of classical adjoint matrix. Further, we consider determinantal representations of generalized inverses obtained by the column-row determinants.

We will use the following notations. Let $\alpha := \{\alpha_1, \dots, \alpha_k\} \subseteq \{1, \dots, m\}$ and $\beta := \{\beta_1, \dots, \beta_k\} \subseteq \{1, \dots, n\}$ be subsets of the order $1 \leq k \leq \min\{m, n\}$. By \mathbf{A}_β^α denote the submatrix of \mathbf{A} determined by the rows indexed by α and the columns indexed by β . Then \mathbf{A}_α^α denotes the

principal submatrix determined by the rows and columns indexed by α . If $\mathbf{A} \in M(n, \mathbb{H})$ is Hermitian, then by $|\mathbf{A}_\alpha^\alpha|$ denote the corresponding principal minor of $\det \mathbf{A}$. For $1 \leq k \leq n$, the collection of strictly increasing sequences of k integers chosen from $\{1, \dots, n\}$ is denoted by $L_{k,n} := \{\alpha : \alpha = (\alpha_1, \dots, \alpha_k), 1 \leq \alpha_1 \leq \cdots \leq \alpha_k \leq n\}$. For fixed $i \in \alpha$ and $j \in \beta$, let $I_{r,m}\{i\} := \{\alpha : \alpha \in L_{r,m}, i \in \alpha\}$, $J_{r,n}\{j\} := \{\beta : \beta \in L_{r,n}, j \in \beta\}$.

Denote by \mathbf{a}_j^* and \mathbf{a}_i^* the j th column and the i th row of \mathbf{A}^* and by $\mathbf{a}_j^{(m)}$ and $\mathbf{a}_i^{(m)}$ the j th column and the i th row of \mathbf{A}^m , respectively.

The following theorem gives determinantal representations of the Moore-Penrose inverse over the quaternion skew field \mathbb{H} .

Theorem 4 (see [32]). *If $\mathbf{A} \in \mathbb{H}_r^{m \times n}$, then the Moore-Penrose inverse $\mathbf{A}^+ = (a_{ij}^+) \in \mathbb{H}^{n \times m}$ possesses the following determinantal representations:*

$$a_{ij}^+ = \frac{\sum_{\beta \in J_{r,n}\{i\}} \text{cdet}_i((\mathbf{A}^* \mathbf{A})_{\cdot i}(\mathbf{a}_j^*))_\beta^\beta}{\sum_{\beta \in J_{r,n}} |(\mathbf{A}^* \mathbf{A})_\beta^\beta|} \quad (13)$$

or

$$a_{ij}^+ = \frac{\sum_{\alpha \in I_{r,m}\{j\}} \text{rdet}_j((\mathbf{A} \mathbf{A}^*)_{\cdot j}(\mathbf{a}_i^*))_\alpha^\alpha}{\sum_{\alpha \in I_{r,m}} |(\mathbf{A} \mathbf{A}^*)_\alpha^\alpha|} \quad (14)$$

for all $i = \overline{1, n}$ and $j = \overline{1, m}$.

Proposition 5 (see [20]). *If $\text{Ind}(\mathbf{A}) = k$, then $\mathbf{A}^D = \mathbf{A}^k (\mathbf{A}^{2k+1})^+ \mathbf{A}^k$.*

Denote by $\hat{\mathbf{a}}_s$ and $\check{\mathbf{a}}_t$ the s th column and the t th row of $(\mathbf{A}^{2k+1})^* \mathbf{A}^k := \hat{\mathbf{A}} = (\hat{a}_{ij}) \in \mathbb{H}^{n \times n}$ and the t th row of $\mathbf{A}^k (\mathbf{A}^{2k+1})^* := \check{\mathbf{A}} = (\check{a}_{ij}) \in \mathbb{H}^{n \times n}$, respectively, for all $s, t = \overline{1, n}$. Using the determinantal representations of the Moore-Penrose inverse (13) and (14) and Proposition 5, the following determinantal representations of the Drazin inverse for an arbitrary square matrix over \mathbb{H} have been obtained in [33].

Theorem 6 (see [33]). *If $\mathbf{A} \in M(n, \mathbb{H})$ with $\text{Ind} \mathbf{A} = k$ and $\text{rank} \mathbf{A}^{k+1} = \text{rank} \mathbf{A}^k = r$, then the Drazin inverse \mathbf{A}^D possesses the following determinantal representations:*

$$\begin{aligned} a_{ij}^D &= \frac{\sum_{t=1}^n a_{it}^{(k)} \sum_{\beta \in J_{r,n}\{t\}} \text{cdet}_t((\mathbf{A}^{2k+1})^* (\mathbf{A}^{2k+1})_{\cdot t}(\hat{\mathbf{a}}_j))_\beta^\beta}{\sum_{\beta \in J_{r,n}} |(\mathbf{A}^{2k+1})^* (\mathbf{A}^{2k+1})_\beta^\beta|}, \\ a_{ij}^D &= \frac{\sum_{s=1}^n \left(\sum_{\alpha \in I_{r,n}\{s\}} \text{rdet}_s((\mathbf{A}^{2k+1} (\mathbf{A}^{2k+1})^*)_{\cdot s}(\check{\mathbf{a}}_i))_\alpha^\alpha \right) a_{sj}^{(k)}}{\sum_{\alpha \in I_{r,n}} |(\mathbf{A}^{2k+1} (\mathbf{A}^{2k+1})^*)_\alpha^\alpha|}. \end{aligned} \quad (15)$$

In the special case, when $\mathbf{A} \in M(n, \mathbb{H})$ is Hermitian, we can obtain simpler determinantal representations of the Drazin inverse.

Theorem 7 (see [33]). *If $\mathbf{A} \in M(n, \mathbb{H})$ is Hermitian with $\text{Ind } \mathbf{A} = k$ and $\text{rank } \mathbf{A}^{k+1} = \text{rank } \mathbf{A}^k = r$, then the Drazin inverse $\mathbf{A}^D = (a_{ij}^D) \in \mathbb{H}^{n \times n}$ possesses the following determinantal representations:*

$$a_{ij}^D = \frac{\sum_{\beta \in J_{r,n}\{i\}} \text{cdet}_i \left((\mathbf{A}^{k+1})_{\cdot i} (\mathbf{a}_{\cdot j}^{(k)})_{\beta} \right)_{\beta}}{\sum_{\beta \in J_{r,n}} \left| (\mathbf{A}^{k+1})_{\beta} \right|} \quad (16)$$

or

$$a_{ij}^D = \frac{\sum_{\alpha \in I_{r,n}\{j\}} \text{rdet}_j \left((\mathbf{A}^{k+1})_{\cdot j} (\mathbf{a}_{\cdot i}^{(k)})_{\alpha} \right)_{\alpha}}{\sum_{\alpha \in I_{r,n}} \left| (\mathbf{A}^{k+1})_{\alpha} \right|}. \quad (17)$$

2.2. Determinantal Representations of the W -Weighted Drazin Inverse. We introduce some mathematical background from the theory of the W -weighted Drazin inverse [27, 41, 42] that can be generalized to \mathbb{H} .

Lemma 8. *Let $\mathbf{A} \in \mathbb{H}^{m \times n}$ and $\mathbf{W} \in \mathbb{H}^{n \times m}$ with $k = \max\{\text{Ind}(\mathbf{AW}), \text{Ind}(\mathbf{WA})\}$. Then one has*

- (a) $\mathbf{A}_{d,W} = \mathbf{A}((\mathbf{WA})^D)^2 = ((\mathbf{AW})^D)^2 \mathbf{A}$;
- (b) $\mathbf{A}_{d,W} \mathbf{W} = (\mathbf{AW})^D$; $\mathbf{WA}_{d,W} = (\mathbf{WA})^D$;
- (c) $\mathbf{A}_{d,W} = \{(\mathbf{AW})^k [(\mathbf{AW})^{2k+1}]^+ (\mathbf{AW})^k\} \mathbf{W}^+$; $\mathbf{A}_{d,W} = \mathbf{W}^+ \{(\mathbf{WA})^k [(\mathbf{WA})^{2k+1}]^+ (\mathbf{WA})^k\}$;
- (d) $\mathbf{WAWA}_{d,W} = \mathbf{P}_{\mathcal{R}_r((\mathbf{WA})^k), \mathcal{N}_r((\mathbf{WA})^k)}$; $\mathbf{A}_{d,W} \mathbf{WAW} = \mathbf{P}_{\mathcal{R}_l((\mathbf{AW})^k), \mathcal{N}_l((\mathbf{AW})^k)}$

where $\mathbf{P}_{\mathcal{R}_r((\mathbf{WA})^k), \mathcal{N}_r((\mathbf{WA})^k)}$ is the projector on $\mathcal{R}_r((\mathbf{WA})^k)$ along $\mathcal{N}_r((\mathbf{WA})^k)$ and $\mathbf{P}_{\mathcal{R}_l((\mathbf{AW})^k), \mathcal{N}_l((\mathbf{AW})^k)}$ is the projector on $\mathcal{R}_l((\mathbf{AW})^k)$ along $\mathcal{N}_l((\mathbf{AW})^k)$.

In particular, the point (a) of Lemma 8 due to Cline and Greville [17] is generalized [28] to \mathbb{H} . Using this proposition, we have obtained [29] the following determinantal representations of W -weighted Drazin inverse.

Denote $\mathbf{WA} =: \mathbf{U} = (u_{ij}) \in \mathbb{H}^{m \times n}$ and $\mathbf{AW} =: \mathbf{V} = (v_{ij}) \in \mathbb{H}^{n \times m}$.

Due to Theorem 6, we denote an entry of the Drazin inverse \mathbf{U}^D by

$$u_{ij}^{D,1} = \frac{\sum_{t=1}^n u_{it}^{(k)} \sum_{\beta \in J_{r,n}\{t\}} \text{cdet}_t \left((\mathbf{U}^{2k+1})^* (\mathbf{U}^{2k+1})_{\cdot t} (\hat{\mathbf{u}}_{\cdot j})_{\beta} \right)_{\beta}}{\sum_{\beta \in J_{r,n}} \left| (\mathbf{U}^{2k+1})^* (\mathbf{U}^{2k+1})_{\beta} \right|} \quad (18)$$

or

$$u_{ij}^{D,2} = \frac{\sum_{s=1}^n \left(\sum_{\alpha \in I_{r,n}\{s\}} \text{rdet}_s \left((\mathbf{U}^{2k+1} (\mathbf{U}^{2k+1})^*)_{\cdot s} (\check{\mathbf{u}}_{\cdot i})_{\alpha} \right)_{\alpha} \right) u_{sj}^{(k)}}{\sum_{\alpha \in I_{r,n}} \left| (\mathbf{U}^{2k+1} (\mathbf{U}^{2k+1})^*)_{\alpha} \right|}, \quad (19)$$

where $\hat{\mathbf{u}}_{\cdot s}$ and $\check{\mathbf{u}}_{\cdot t}$ are the s th column of $(\mathbf{U}^{2k+1})^* \mathbf{U}^k =: \hat{\mathbf{U}} = (\hat{u}_{ij}) \in \mathbb{H}^{n \times n}$ and the t th row of $\mathbf{U}^k (\mathbf{U}^{2k+1})^* =: \check{\mathbf{U}} = (\check{u}_{ij}) \in \mathbb{H}^{n \times n}$, respectively, for all $s, t = \overline{1, n}$, and $r = \text{rank } \mathbf{U}^{k+1} = \text{rank } \mathbf{U}^k$.

Then we have the following determinantal representations of $\mathbf{A}_{d,W} = (a_{ij}^{d,W}) \in \mathbb{H}^{m \times n}$:

$$a_{ij}^{d,W} = \sum_{q=1}^n a_{iq} (u_{qj}^D)^{(2)}, \quad (20)$$

where

$$(u_{qj}^D)^{(2)} = \sum_{p=1}^n u_{qp}^{D,l} u_{pj}^{D,f} \quad (21)$$

for all $l, f = \overline{1, 2}$ and $u_{ij}^{D,1}$ from (18) and $u_{ij}^{D,2}$ from (19).

Similarly using $\mathbf{V} = (v_{ij}) \in \mathbb{H}^{n \times m}$,

$$a_{ij}^{d,W} = \sum_{q=1}^m (v_{iq}^D)^{(2)} a_{qj}, \quad (22)$$

where the first factor is one of the following four possible equations:

$$(v_{iq}^D)^{(2)} = \sum_{p=1}^m v_{ip}^{D,l} v_{pq}^{D,f} \quad (23)$$

for all $l, f = \overline{1, 2}$, and an entry of the Drazin inverse \mathbf{V}^D is denoted by

$$v_{ij}^{D,1} = \frac{\sum_{t=1}^m v_{it}^{(k)} \sum_{\beta \in J_{r,m}\{t\}} \text{cdet}_t \left((\mathbf{V}^{2k+1})^* (\mathbf{V}^{2k+1})_{\cdot t} (\hat{\mathbf{v}}_{\cdot j})_{\beta} \right)_{\beta}}{\sum_{\beta \in J_{r,m}} \left| (\mathbf{V}^{2k+1})^* (\mathbf{V}^{2k+1})_{\beta} \right|} \quad (24)$$

or

$$v_{ij}^{D,2} = \frac{\sum_{s=1}^m \left(\sum_{\alpha \in I_{r,m}\{s\}} \text{rdet}_s \left((\mathbf{V}^{2k+1} (\mathbf{V}^{2k+1})^*)_{\cdot s} (\check{\mathbf{v}}_{\cdot i})_{\alpha} \right)_{\alpha} \right) v_{sj}^{(k)}}{\sum_{\alpha \in I_{r,m}} \left| (\mathbf{V}^{2k+1} (\mathbf{V}^{2k+1})^*)_{\alpha} \right|}, \quad (25)$$

where $\hat{\mathbf{v}}_{\cdot s}$ and $\check{\mathbf{v}}_{\cdot t}$ are the s th column of $(\mathbf{V}^{2k+1})^* \mathbf{V}^k =: \hat{\mathbf{V}} = (\hat{v}_{ij}) \in \mathbb{H}^{m \times m}$ and the t th row of $\mathbf{V}^k (\mathbf{V}^{2k+1})^* =: \check{\mathbf{V}} = (\check{v}_{ij}) \in \mathbb{H}^{m \times m}$, respectively, for all $s, t = \overline{1, m}$; $r = \text{rank } \mathbf{V}^{k+1} = \text{rank } \mathbf{V}^k$.

The point (c) of Lemma 8 due to [23] has been generalized to \mathbb{H} in [33]. Using this proposition, we have obtained the following two determinantal representations of the W -weighted Drazin inverse.

Theorem 9 (see [29]). *Let $\mathbf{A} \in \mathbb{H}^{m \times n}$ and $\mathbf{W} \in \mathbb{H}^{n \times m}$ with $k = \text{Ind}(\mathbf{AW})$ and $r = \text{rank}(\mathbf{AW})^{k+1} = \text{rank}(\mathbf{AW})^k$. Then the W -weighted Drazin inverse of \mathbf{A} with respect to \mathbf{W} possesses the following determinantal representations:*

$$a_{ij}^{d,W} = \frac{\sum_{t=1}^m \sum_{\alpha \in I_{r,m}\{t\}} \text{rdet}_t \left(\left(\mathbf{V}^{2k+1} (\mathbf{V}^{2k+1})^* \right)_t (\check{\mathbf{v}}_i) \right)_\alpha^\alpha \sum_{\alpha \in I_{r_1,n}\{j\}} \text{rdet}_j \left((\mathbf{W}\mathbf{W}^*)_j (\check{\mathbf{w}}_t) \right)_\alpha^\alpha}{\sum_{\alpha \in I_{r,m}} \left| \left(\mathbf{V}^{2k+1} (\mathbf{V}^{2k+1})^* \right)_\alpha^\alpha \right| \sum_{\alpha \in I_{r_1,n}} \left| (\mathbf{W}\mathbf{W}^*)_\alpha^\alpha \right|}, \quad (26)$$

$$a_{ij}^{d,W} = \frac{\sum_{t=1}^n \sum_{\beta \in J_{r_1,m}\{i\}} \text{cdet}_i \left((\mathbf{W}^*\mathbf{W})_t (\widehat{\mathbf{w}}_t) \right)_\beta^\beta \sum_{\beta \in J_{r,n}\{t\}} \text{cdet}_t \left(\left((\mathbf{U}^{2k+1})^* \mathbf{U}^{2k+1} \right)_t (\widehat{\mathbf{u}}_j) \right)_\beta^\beta}{\sum_{\beta \in J_{r_1,m}} \left| (\mathbf{W}^*\mathbf{W})_\beta^\beta \right| \sum_{\beta \in J_{r,n}} \left| \left((\mathbf{U}^{2k+1})^* \mathbf{U}^{2k+1} \right)_\beta^\beta \right|}, \quad (27)$$

where $\check{\mathbf{V}} = \mathbf{V}^k (\mathbf{V}^{2k+1})^*$, $\check{\mathbf{W}} = \mathbf{V}^k \mathbf{W}^*$ and $\widehat{\mathbf{U}} = (\mathbf{U}^{2k+1})^* \mathbf{U}^k$, $\widehat{\mathbf{W}} = \mathbf{W}^* \mathbf{U}^k$.

In the special cases, when $\mathbf{A}\mathbf{W} \in \mathbb{H}^{m \times m}$ and $\mathbf{W}\mathbf{A} \in \mathbb{H}^{n \times n}$ are Hermitian, we can obtain simpler determinantal representations of the W -weighted Drazin inverse.

Theorem 10 (see [29]). *If $\mathbf{A} \in \mathbb{H}^{m \times n}$, $\mathbf{W} \in \mathbb{H}^{n \times m}$, and $\mathbf{A}\mathbf{W} \in \mathbb{H}^{m \times m}$ are Hermitian with $k = \max\{\text{Ind}(\mathbf{A}\mathbf{W}), \text{Ind}(\mathbf{W}\mathbf{A})\}$ and $\text{rank}(\mathbf{A}\mathbf{W})^{k+1} = \text{rank}(\mathbf{A}\mathbf{W})^k = r$, then the W -weighted Drazin inverse $\mathbf{A}_{d,W} = (a_{ij}^{d,W}) \in \mathbb{H}^{m \times n}$ with respect to \mathbf{W} possesses the following determinantal representations:*

$$a_{ij}^{d,W} = \frac{\sum_{\beta \in J_{r,m}\{i\}} \text{cdet}_i \left((\mathbf{A}\mathbf{W})_i^{k+2} (\bar{\mathbf{v}}_j) \right)_\beta^\beta}{\sum_{\beta \in J_{r,m}} \left| \left((\mathbf{A}\mathbf{W})_i^{k+2} \right)_\beta^\beta \right|}, \quad (28)$$

where $\bar{\mathbf{v}}_j$ is the j th column of $\bar{\mathbf{V}} = (\mathbf{A}\mathbf{W})^k \mathbf{A}$ for all $j = \overline{1, m}$.

Theorem 11 (see [29]). *If $\mathbf{A} \in \mathbb{H}^{m \times n}$, $\mathbf{W} \in \mathbb{H}^{n \times m}$, and $\mathbf{W}\mathbf{A} \in \mathbb{H}^{n \times n}$ are Hermitian with $k = \max\{\text{Ind}(\mathbf{A}\mathbf{W}), \text{Ind}(\mathbf{W}\mathbf{A})\}$ and $\text{rank}(\mathbf{W}\mathbf{A})^{k+1} = \text{rank}(\mathbf{W}\mathbf{A})^k = r$, then the W -weighted Drazin inverse $\mathbf{A}_{d,W} = (a_{ij}^{d,W}) \in \mathbb{H}^{m \times n}$ with respect to \mathbf{W} possesses the following determinantal representations:*

$$a_{ij}^{d,W} = \frac{\sum_{\alpha \in I_{r,n}\{j\}} \text{rdet}_j \left((\mathbf{W}\mathbf{A})_j^{k+2} (\bar{\mathbf{u}}_i^{(k)}) \right)_\alpha^\alpha}{\sum_{\alpha \in I_{r,n}} \left| \left((\mathbf{W}\mathbf{A})_j^{k+2} \right)_\alpha^\alpha \right|}, \quad (29)$$

where $\bar{\mathbf{u}}_i$ is the i th row of $\bar{\mathbf{U}} = \mathbf{A}(\mathbf{W}\mathbf{A})^k$ for all $i = \overline{1, n}$.

3. Cramer's Rule for the W -Weighted Drazin Inverse Solution

3.1. Background of the Problem. In [27] Wei has established Cramer's rule for solving of a general restricted equation:

$$\mathbf{W}\mathbf{A}\mathbf{W}\mathbf{x} = \mathbf{b}, \quad \mathbf{x} \in \mathcal{R} \left[(\mathbf{A}\mathbf{W})^{k_1} \right], \quad (30)$$

where $\mathbf{A} \in \mathbb{C}^{m \times n}$ and $\mathbf{W} \in \mathbb{C}^{n \times m}$ with $\text{Ind}(\mathbf{A}\mathbf{W}) = k_1$, $\text{Ind}(\mathbf{W}\mathbf{A}) = k_2$ and $\text{rank}(\mathbf{A}\mathbf{W})^{k_1} = r_1$, $\text{rank}(\mathbf{W}\mathbf{A})^{k_2} = r_2$. He proved if $\mathbf{b} \in \mathcal{R}[(\mathbf{W}\mathbf{A})^{k_2} \mathbf{A}]$ and $r_1 = r_2$, then (30) has a

unique solution, $\mathbf{x} = \mathbf{A}_{d,W} \mathbf{b}$, which can be presented by the following Cramer rule:

$$x_j = \frac{\det \begin{pmatrix} \mathbf{W}\mathbf{A}\mathbf{W}(j-\mathbf{b}) & \mathbf{U}_1 \\ \mathbf{V}_1(j \rightarrow 0) & 0 \end{pmatrix}}{\det \begin{pmatrix} \mathbf{W}\mathbf{A}\mathbf{W} & \mathbf{U}_1 \\ \mathbf{V}_1 & 0 \end{pmatrix}}, \quad (31)$$

where $\mathbf{U}_1 \in \mathbb{C}^{n \times n - r_2}$ and $\mathbf{V}_1^* \in \mathbb{C}^{m \times m - r_1}$ are matrices whose columns form bases for $\mathcal{N}((\mathbf{W}\mathbf{A})^{k_2})$ and $\mathcal{N}((\mathbf{A}\mathbf{W})^{k_1})$, respectively.

Recently, within the framework of a theory of the column and row determinants, Song [28] has considered the characterization of the W -weighted Drazin inverse over the quaternion skew and presented a Cramer rule of the restricted matrix equation:

$$\mathbf{W}_1 \mathbf{A} \mathbf{W}_1 \mathbf{X} \mathbf{W}_2 \mathbf{B} \mathbf{W}_2 = \mathbf{D}, \quad (32)$$

$$\begin{aligned} \mathcal{R}_r(\mathbf{X}) &\subset \mathcal{R}_r \left((\mathbf{A}\mathbf{W}_1)^{k_1} \right), \\ \mathcal{N}_r(\mathbf{X}) &\supset \mathcal{N}_r \left((\mathbf{W}_2 \mathbf{B})^{k_2} \right), \\ \mathcal{R}_l(\mathbf{X}) &\subset \mathcal{R}_l \left((\mathbf{B}\mathbf{W}_2)^{k_2} \right), \\ \mathcal{N}_l(\mathbf{X}) &\supset \mathcal{N}_l \left((\mathbf{W}_1 \mathbf{A})^{k_1} \right), \end{aligned} \quad (33)$$

where $\mathbf{A} \in \mathbb{H}^{m \times n}$, $\mathbf{W}_1 \in \mathbb{H}^{n \times m}$, $\mathbf{B} \in \mathbb{H}^{p \times q}$, $\mathbf{W}_2 \in \mathbb{H}^{q \times p}$, and $\mathbf{D} \in \mathbb{H}^{n \times p}$ with $k_1 = \max\{\text{Ind}(\mathbf{A}\mathbf{W}_1), \text{Ind}(\mathbf{W}_1 \mathbf{A})\}$, $k_2 = \max\{\text{Ind}(\mathbf{B}\mathbf{W}_2), \text{Ind}(\mathbf{W}_2 \mathbf{B})\}$, and $\text{rank}(\mathbf{A}\mathbf{W}_1)^{k_1} = s_1$, $\text{rank}(\mathbf{B}\mathbf{W}_2)^{k_2} = s_2$.

He proved that if

$$\begin{aligned} \mathcal{R}_r(\mathbf{D}) &\in \mathcal{R}_r \left((\mathbf{W}_1 \mathbf{A})^{k_1}, (\mathbf{W}_2 \mathbf{B})^{k_2} \right), \\ \mathcal{R}_l(\mathbf{D}) &\in \mathcal{R}_l \left((\mathbf{A}\mathbf{W}_1)^{k_1}, (\mathbf{B}\mathbf{W}_2)^{k_2} \right) \end{aligned} \quad (34)$$

and there exist auxiliary matrices of full column rank, $\mathbf{L}_1 \in \mathbb{H}_{n-s_1}^{n \times n - s_1}$, $\mathbf{M}_1^* \in \mathbb{H}_{m-s_1}^{m \times m - s_1}$, $\mathbf{L}_2 \in \mathbb{H}_{q-s_2}^{q \times q - s_2}$, and $\mathbf{M}_2^* \in \mathbb{H}_{p-s_2}^{p \times p - s_2}$ with additional terms of their ranges and null spaces, then the restricted matrix equation (32) has a unique solution:

$$\mathbf{X} = \mathbf{A}_{d,W_1} \mathbf{D} \mathbf{B}_{d,W_2}. \quad (35)$$

Using auxiliary matrices, \mathbf{L}_1 , \mathbf{M}_1 , \mathbf{L}_2 , and \mathbf{M}_2 , Song presented its Cramer's rule by analogy to (31).

In this paper we have avoided such approach and have obtained explicit formulas for determinantal representations of the W -weighted Drazin inverse solutions of matrix equations by using only given matrices.

3.2. Cramer's Rules for the W -Weighted Drazin Inverse Solutions of Some Matrix Equations. Consider the matrix equation (32) with constraints (33). Denote $\mathbf{ADB} =: \bar{\mathbf{D}} = (\bar{d}_{lf}) \in \mathbb{H}^{m \times q}$ and $\bar{\mathbf{V}}\mathbf{D}\bar{\mathbf{U}} =: \bar{\mathbf{D}} = (\bar{d}_{lf}) \in \mathbb{H}^{m \times q}$, where $\bar{\mathbf{V}} := (\mathbf{AW}_1)^{k_1} \mathbf{A}$ and $\bar{\mathbf{U}} := \mathbf{B}(\mathbf{W}_2\mathbf{B})^{k_2}$.

Theorem 12. Suppose that $\mathbf{D} \in \mathbb{H}^{n \times p}$, $\mathbf{A} \in \mathbb{H}^{m \times n}$, and $\mathbf{W}_1 \in \mathbb{H}^{n \times m}$ with $k_1 = \max\{\text{Ind}(\mathbf{AW}_1), \text{Ind}(\mathbf{W}_1\mathbf{A})\}$, where $\text{rank}(\mathbf{AW}_1)^{k_1} = s_1$, and $\mathbf{B} \in \mathbb{H}^{p \times q}$, $\mathbf{W}_2 \in \mathbb{H}^{q \times p}$ with $k_2 = \max\{\text{Ind}(\mathbf{BW}_2), \text{Ind}(\mathbf{W}_2\mathbf{B})\}$, $\text{rank}(\mathbf{BW}_2)^{k_2} = s_2$. If $\mathcal{R}_r(\mathbf{D}) \in \mathcal{R}_r((\mathbf{W}_1\mathbf{A})^{k_1}, (\mathbf{W}_2\mathbf{B})^{k_2})$, $\mathcal{R}_l(\mathbf{D}) \in \mathcal{R}_l((\mathbf{AW}_1)^{k_1}, (\mathbf{BW}_2)^{k_2})$, then the restricted matrix equation (32) has a unique solution:

$$\mathbf{X} = \mathbf{A}_{d, \mathbf{W}_1} \mathbf{D} \mathbf{B}_{d, \mathbf{W}_2}, \quad (36)$$

which possesses the following determinantal representations for all $i = \overline{1, m}$ and $j = \overline{1, q}$.

(i) Consider

$$x_{ij} = \sum_{l=1}^m \sum_{f=1}^q (v_{il}^D)^{(2)} \tilde{d}_{lf} (u_{fj}^D)^{(2)}, \quad (37)$$

where $(v_{il}^D) = \mathbf{V}^D$ is the Drazin inverse of $\mathbf{V} = \mathbf{AW}_1$ and $(v_{il}^D)^{(2)}$ can be obtained by (23) and $(u_{fj}^D) = \mathbf{U}^D$ is the Drazin inverse of $\mathbf{U} = \mathbf{W}_2\mathbf{B}$ and $(u_{fj}^D)^{(2)}$ can be obtained by (21).

(ii) If $\mathbf{AW}_1 \in \mathbb{H}^{m \times m}$ and $\mathbf{W}_2\mathbf{B} \in \mathbb{H}^{q \times q}$ are Hermitian, then

$$x_{ij} = \frac{\sum_{\beta \in J_{s_1, m\{i\}}} \text{cdet}_i \left((\mathbf{AW}_1)_{\cdot i}^{k_1+2} (\mathbf{d}_j^{\mathbf{B}})_{\beta}^{\beta} \right)}{\sum_{\beta \in J_{s_1, m}} \left| \left((\mathbf{AW}_1)_{\cdot i}^{k_1+2} \right)_{\beta}^{\beta} \right| \sum_{\alpha \in I_{s_2, q}} \left| \left((\mathbf{W}_2\mathbf{B})^{k_2+2} \right)_{\alpha}^{\alpha} \right|} \quad (38)$$

or

$$x_{ij} = \frac{\sum_{\alpha \in I_{s_2, q\{j\}}} \text{rdet}_j \left((\mathbf{W}_2\mathbf{B})_{j \cdot}^{k_2+2} (\mathbf{d}_i^{\mathbf{A}})_{\alpha}^{\alpha} \right)}{\sum_{\beta \in J_{s_1, m}} \left| \left((\mathbf{AW}_1)_{\cdot i}^{k_1+2} \right)_{\beta}^{\beta} \right| \sum_{\alpha \in I_{s_2, q}} \left| \left((\mathbf{W}_2\mathbf{B})_{j \cdot}^{k_2+2} \right)_{\alpha}^{\alpha} \right|}, \quad (39)$$

where

$$\mathbf{d}_j^{\mathbf{B}} = \left(\sum_{\alpha \in I_{s_2, q\{j\}}} \text{rdet}_j \left((\mathbf{W}_2\mathbf{B})_{j \cdot}^{k_2+2} (\bar{\mathbf{d}}_t)_{\alpha}^{\alpha} \right) \right) \in \mathbb{H}^{n \times 1}, \quad (40)$$

$$t = \overline{1, n}$$

$$\mathbf{d}_i^{\mathbf{A}} = \left(\sum_{\beta \in J_{s_1, m\{i\}}} \text{cdet}_i \left((\mathbf{AW}_1)_{\cdot i}^{k_1+2} (\bar{\mathbf{d}}_l)_{\beta}^{\beta} \right) \right) \in \mathbb{H}^{1 \times q}, \quad (41)$$

$$l = \overline{1, q}$$

are the column vector and the row vector, respectively. $\bar{\mathbf{d}}_i$ and $\bar{\mathbf{d}}_j$ are the i th row and the j th column of $\bar{\mathbf{D}}$ for all $i = \overline{1, n}$ and $j = \overline{1, p}$.

Proof. The existence and uniqueness of solution (36) can be proved similarly as in [28], Theorem 5.2.

(i) To derive a Cramer rule (37) we use the point (a) from Lemma 8. Then we obtain

$$\mathbf{X} = \left((\mathbf{AW}_1)^D \right)^2 \mathbf{ADB} \left((\mathbf{W}_2\mathbf{B})^D \right)^2. \quad (42)$$

Denote $\mathbf{ADB} =: \bar{\mathbf{D}} = (\bar{d}_{lf}) \in \mathbb{H}^{m \times q}$, $\mathbf{V} := \mathbf{AW}_1$, and $\mathbf{U} := \mathbf{W}_2\mathbf{B}$. Then (42) will be written componentwise as follows:

$$x_{ij} = \sum_{s=1}^p \sum_{t=1}^n (a_{it}^{d, \mathbf{W}_1}) d_{ts} (b_{sj}^{d, \mathbf{W}_2})$$

$$= \sum_{s=1}^p \sum_{t=1}^n \left(\sum_{l=1}^m (v_{il}^D)^{(2)} a_{lt} \right) d_{ts} \left(\sum_{f=1}^q b_{sf} (u_{fj}^D)^{(2)} \right). \quad (43)$$

By changing the order of summation, from here it follows (37).

(ii) If $\mathbf{A} \in \mathbb{H}^{m \times n}$ and $\mathbf{B} \in \mathbb{H}^{p \times q}$ and $\mathbf{AW}_1 \in \mathbb{H}^{m \times m}$ and $\mathbf{W}_2\mathbf{B} \in \mathbb{H}^{q \times q}$ are Hermitian, then by Theorems 10 and 11 the W -weighted Drazin inverses $\mathbf{A}_{d, \mathbf{W}_1} = (a_{ij}^{d, \mathbf{W}_1}) \in \mathbb{H}^{m \times n}$ and $\mathbf{B}_{d, \mathbf{W}_2} = (b_{ij}^{d, \mathbf{W}_2}) \in \mathbb{H}^{q \times p}$ possess the following determinantal representations, respectively:

$$a_{ij}^{d, \mathbf{W}_1} = \frac{\sum_{\beta \in J_{s_1, m\{i\}}} \text{cdet}_i \left((\mathbf{AW}_1)_{\cdot i}^{k_1+2} (\bar{\mathbf{v}}_j)_{\beta}^{\beta} \right)}{\sum_{\beta \in J_{r, m}} \left| \left((\mathbf{AW}_1)_{\cdot i}^{k_1+2} \right)_{\beta}^{\beta} \right|}, \quad (44)$$

where $\bar{\mathbf{v}}_j$ is the j th column of $\bar{\mathbf{V}} = (\mathbf{AW}_1)^{k_1} \mathbf{A}$ for all $j = \overline{1, m}$ and

$$b_{ij}^{d, \mathbf{W}_2} = \frac{\sum_{\alpha \in I_{s_2, q\{j\}}} \text{rdet}_j \left((\mathbf{W}_2\mathbf{B})_{j \cdot}^{k_2+2} (\bar{\mathbf{u}}_i)_{\alpha}^{\alpha} \right)}{\sum_{\alpha \in I_{s_2, q}} \left| \left((\mathbf{W}_2\mathbf{B})_{j \cdot}^{k_2+2} \right)_{\alpha}^{\alpha} \right|}, \quad (45)$$

where $\bar{\mathbf{u}}_i$ is the i th row of $\bar{\mathbf{U}} = \mathbf{B}(\mathbf{W}_2\mathbf{B})^{k_2}$ for all $i = \overline{1, p}$.

By componentwise writing of (36) we obtain

$$x_{ij} = \sum_{s=1}^p \left(\sum_{t=1}^n a_{it}^{d, \mathbf{W}_1} d_{ts} \right) \cdot b_{sj}^{d, \mathbf{W}_2}. \quad (46)$$

Denote by $\widehat{\mathbf{d}}_s$ the s th column of $\overline{\mathbf{V}}\mathbf{D} = (\mathbf{A}\mathbf{W}_1)^{k_1}\mathbf{A}\mathbf{D} =: \widehat{\mathbf{D}} = (\widehat{d}_{ij}) \in \mathbb{H}^{m \times p}$ for all $s = \overline{1, p}$. It follows from $\sum_t \overline{\mathbf{v}}_t d_{ts} = \widehat{\mathbf{d}}_s$ that

$$\sum_{t=1}^n a_{it}^{d, W_1} d_{ts}$$

$$= \sum_{t=1}^n \frac{\sum_{\beta \in J_{s_1, m} \{i\}} \text{cdet}_i \left((\mathbf{A}\mathbf{W}_1)_i^{k_1+2} (\overline{\mathbf{v}}_t) \right)_\beta}{\sum_{\beta \in J_{s_1, m}} \left| \left((\mathbf{A}\mathbf{W}_1)^{k_1+2} \right)_\beta \right|} \cdot d_{ts}$$

$$\begin{aligned} &= \frac{\sum_{\beta \in J_{s_1, m} \{i\}} \sum_{t=1}^n \text{cdet}_i \left((\mathbf{A}\mathbf{W}_1)_i^{k_1+2} (\overline{\mathbf{v}}_t) \right)_\beta \cdot d_{ts}}{\sum_{\beta \in J_{s_1, m}} \left| \left((\mathbf{A}\mathbf{W}_1)^{k_1+2} \right)_\beta \right|} \\ &= \frac{\sum_{\beta \in J_{s_1, m} \{i\}} \text{cdet}_i \left((\mathbf{A}\mathbf{W}_1)_i^{k_1+2} (\widehat{\mathbf{d}}_s) \right)_\beta}{\sum_{\beta \in J_{s_1, m}} \left| \left((\mathbf{A}\mathbf{W}_1)^{k_1+2} \right)_\beta \right|}. \end{aligned}$$

(47)

Suppose that \mathbf{e}_s and \mathbf{e}_s are, respectively, the unit row vector and the unit column vector whose components are 0, except the s th components, which are 1. Substituting (47) and (45) into (46), we obtain

$$x_{ij} = \sum_{s=1}^p \frac{\sum_{\beta \in J_{s_1, m} \{i\}} \text{cdet}_i \left((\mathbf{A}\mathbf{W}_1)_i^{k_1+2} (\widehat{\mathbf{d}}_s) \right)_\beta}{\sum_{\beta \in J_{s_1, m}} \left| \left((\mathbf{A}\mathbf{W}_1)^{k_1+2} \right)_\beta \right|} \frac{\sum_{\alpha \in I_{s_2, q} \{j\}} \text{rdet}_j \left((\mathbf{W}_2 \mathbf{B})_j^{k_2+2} (\overline{\mathbf{u}}_s) \right)_\alpha}{\sum_{\alpha \in I_{s_2, q}} \left| \left((\mathbf{W}_2 \mathbf{B})^{k_2+2} \right)_\alpha \right|}. \quad (48)$$

Since

$$\begin{aligned} \widehat{\mathbf{d}}_s &= \sum_{t=1}^n \mathbf{e}_t \widehat{d}_{ts}, \\ \overline{\mathbf{u}}_s &= \sum_{l=1}^q \overline{u}_{sl} \mathbf{e}_l, \\ \sum_{s=1}^p \widehat{d}_{ts} \overline{u}_{sl} &= \overline{d}_{tl}, \end{aligned} \quad (49)$$

then we have

$$\begin{aligned} x_{ij} &= \frac{\sum_{s=1}^p \sum_{t=1}^n \sum_{l=1}^q \sum_{\beta \in J_{s_1, m} \{i\}} \text{cdet}_i \left((\mathbf{A}\mathbf{W}_1)_i^{k_1+2} (\mathbf{e}_t) \right)_\beta \widehat{d}_{ts} \overline{u}_{sl} \sum_{\alpha \in I_{s_2, q} \{j\}} \text{rdet}_j \left((\mathbf{W}_2 \mathbf{B})_j^{k_2+2} (\mathbf{e}_l) \right)_\alpha}{\sum_{\beta \in J_{s_1, m}} \left| \left((\mathbf{A}\mathbf{W}_1)^{k_1+2} \right)_\beta \right| \sum_{\alpha \in I_{s_2, q}} \left| \left((\mathbf{W}_2 \mathbf{B})^{k_2+2} \right)_\alpha \right|} \\ &= \frac{\sum_{t=1}^n \sum_{l=1}^q \sum_{\beta \in J_{s_1, m} \{i\}} \text{cdet}_i \left((\mathbf{A}\mathbf{W}_1)_i^{k_1+2} (\mathbf{e}_t) \right)_\beta \overline{d}_{tl} \sum_{\alpha \in I_{s_2, q} \{j\}} \text{rdet}_j \left((\mathbf{W}_2 \mathbf{B})_j^{k_2+2} (\mathbf{e}_l) \right)_\alpha}{\sum_{\beta \in J_{s_1, m}} \left| \left((\mathbf{A}\mathbf{W}_1)^{k_1+2} \right)_\beta \right| \sum_{\alpha \in I_{s_2, q}} \left| \left((\mathbf{W}_2 \mathbf{B})^{k_2+2} \right)_\alpha \right|}. \end{aligned} \quad (50)$$

Denote by

$$\begin{aligned} d_{il}^{\mathbf{A}} &:= \sum_{\beta \in J_{s_1, m} \{i\}} \text{cdet}_i \left((\mathbf{A}\mathbf{W}_1)_i^{k_1+2} (\overline{\mathbf{d}}_l) \right)_\beta \\ &= \sum_{t=1}^n \sum_{\beta \in J_{s_1, m} \{i\}} \text{cdet}_i \left((\mathbf{A}\mathbf{W}_1)_i^{k_1+2} (\mathbf{e}_t) \right)_\beta \overline{d}_{tl} \end{aligned} \quad (51)$$

the l th component of a row vector $\mathbf{d}_l^{\mathbf{A}} = (d_{i1}^{\mathbf{A}}, \dots, d_{iq}^{\mathbf{A}})$ for all $l = \overline{1, q}$. Substituting it into (50), we have

 x_{ij}

$$= \frac{\sum_{l=1}^q d_{il}^{\mathbf{A}} \sum_{\alpha \in I_{s_2, q} \{j\}} \text{rdet}_j \left((\mathbf{W}_2 \mathbf{B})_j^{k_2+2} (\mathbf{e}_l) \right)_\alpha}{\sum_{\beta \in J_{s_1, m}} \left| \left((\mathbf{A}\mathbf{W}_1)^{k_1+2} \right)_\beta \right| \sum_{\alpha \in I_{s_2, q}} \left| \left((\mathbf{W}_2 \mathbf{B})^{k_2+2} \right)_\alpha \right|}. \quad (52)$$

Since $\sum_{l=1}^q d_{il}^{\mathbf{A}} \mathbf{e}_l = \mathbf{d}_i^{\mathbf{A}}$, then it follows (39).

If we denote by

$$\begin{aligned} d_{tj}^{\mathbf{B}} &:= \sum_{l=1}^q \bar{d}_{tl} \sum_{\alpha \in I_{s_2, q} \{j\}} \text{rdet}_j \left((\mathbf{W}_2 \mathbf{B})_j^{k_2+2} (\mathbf{e}_l) \right)_{\alpha}^{\alpha} \\ &= \sum_{\alpha \in I_{s_2, q} \{j\}} \text{rdet}_j \left((\mathbf{W}_2 \mathbf{B})_j^{k_2+2} (\bar{\mathbf{d}}_t) \right)_{\alpha}^{\alpha} \end{aligned} \quad (53)$$

the t th component of a column vector $\mathbf{d}_j^{\mathbf{B}} = (d_{1j}^{\mathbf{B}}, \dots, d_{nj}^{\mathbf{B}})^T$ for all $t = \overline{1, n}$ and substituting it into (50), we obtain

$$x_{ij} = \frac{\sum_{t=1}^n \sum_{\beta \in J_{s_1, m} \{i\}} \text{cdet}_i \left((\mathbf{A} \mathbf{W}_1)_{i, i}^{k_1+2} (\mathbf{e}_t) \right)_{\beta}^{\beta} d_{tj}^{\mathbf{B}}}{\sum_{\beta \in J_{r_1, n}} \left| (\mathbf{A}^* \mathbf{A})_{\beta}^{\beta} \right| \sum_{\alpha \in I_{r_2, p}} \left| (\mathbf{B} \mathbf{B}^*)_{\alpha}^{\alpha} \right|}. \quad (54)$$

Since $\sum_{t=1}^n \mathbf{e}_t d_{tj}^{\mathbf{B}} = \mathbf{d}_j^{\mathbf{B}}$, then it follows (38). \square

Remark 13. To establish a Cramer rule of (32) we will not use the determinantal representations (28) and (28) for (36) because the corresponding determinantal representations of

its solution will be too cumbersome. But they are suitable in the following corollaries.

Corollary 14. Suppose that the following restricted matrix equation is given:

$$\mathbf{W} \mathbf{A} \mathbf{W} \mathbf{X} = \mathbf{D}, \quad (55)$$

$$\mathcal{R}_r(\mathbf{X}) \subset \mathcal{R}_r((\mathbf{A} \mathbf{W})^k), \quad (56)$$

$$\mathcal{N}_l(\mathbf{X}) \supset \mathcal{N}_l((\mathbf{W} \mathbf{A})^k),$$

where $\mathbf{A} \in \mathbb{H}^{m \times n}$ and $\mathbf{W} \in \mathbb{H}_{r_1}^{n \times m}$ with $k = \max\{\text{Ind}(\mathbf{A} \mathbf{W}), \text{Ind}(\mathbf{W} \mathbf{A})\}$ and $\mathbf{D} \in \mathbb{H}^{n \times p}$. If $\mathcal{R}_r(\mathbf{D}) \subset \mathcal{R}_r((\mathbf{A} \mathbf{W})^k)$ and $\mathcal{N}_l(\mathbf{D}) \supset \mathcal{N}_l((\mathbf{W} \mathbf{A})^k)$, then the restricted matrix equation (55)-(56) has a unique solution:

$$\mathbf{X} = \mathbf{A}_{d, \mathbf{W}} \mathbf{D}, \quad (57)$$

which possess the following determinantal representations for all $i = \overline{1, m}$ and $j = \overline{1, p}$.

(i) Consider

$$x_{ij} = \frac{\sum_{t=1}^n \sum_{\beta \in J_{r_1, m} \{i\}} \text{cdet}_i \left((\mathbf{W}^* \mathbf{W})_{i, i} (\widehat{\mathbf{w}}_t) \right)_{\beta}^{\beta} \sum_{\beta \in J_{r, n} \{t\}} \text{cdet}_t \left(((\mathbf{U}^{2k+1})^* \mathbf{U}^{2k+1})_{i, i} (\widehat{\mathbf{d}}_j) \right)_{\beta}^{\beta}}{\sum_{\beta \in J_{r_1, m}} \left| (\mathbf{W}^* \mathbf{W})_{\beta}^{\beta} \right| \sum_{\beta \in J_{r, n}} \left| ((\mathbf{U}^{2k+1})^* \mathbf{U}^{2k+1})_{\beta}^{\beta} \right|}, \quad (58)$$

where $\mathbf{U} = \mathbf{W} \mathbf{A}$, $\widehat{\mathbf{d}}_j$ is the j th column of $\widehat{\mathbf{D}} = \widehat{\mathbf{U}} \mathbf{D} = (\mathbf{U}^{2k+1})^* \mathbf{U}^k \mathbf{D}$, $\widehat{\mathbf{W}} = \mathbf{W}^* \mathbf{U}^k$, and $r = \text{rank}(\mathbf{W} \mathbf{A})^{k+1} = \text{rank}(\mathbf{W} \mathbf{A})^k$.

(ii) Consider

$$x_{ij} = \sum_{q=1}^m (v_{iq}^D)^{(2)} r_{qj}, \quad (59)$$

where $(v_{iq}^D)^{(2)}$ can be obtained by (23) and $\mathbf{A} \mathbf{D} = \mathbf{R} = (r_{qj}) \in \mathbb{H}^{m \times p}$.

(iii) If $\mathbf{A} \mathbf{W} \in \mathbb{H}^{m \times m}$ is Hermitian, then

$$x_{ij} = \frac{\sum_{\beta \in J_{r, m} \{i\}} \text{cdet}_i \left((\mathbf{A} \mathbf{W})_{i, i}^{k+2} (\mathbf{f}_j) \right)_{\beta}^{\beta}}{\sum_{\beta \in J_{r, m}} \left| ((\mathbf{A} \mathbf{W})^{k+2})_{\beta}^{\beta} \right|}, \quad (60)$$

where \mathbf{f}_j is the j th column of $\mathbf{F} = \overline{\mathbf{V}} \mathbf{D} = (\mathbf{A} \mathbf{W})^k \mathbf{A} \mathbf{D}$.

Proof. To derive a Cramer rule (58), we use the determinantal representation (27) for $\mathbf{A}_{d, \mathbf{W}}$. Then

$$x_{ij} = \sum_{s=1}^p a_{is}^{d, \mathbf{W}} d_{sj} = \sum_{s=1}^p \left[\frac{\sum_{t=1}^n \sum_{\beta \in J_{r_1, m} \{i\}} \text{cdet}_i \left((\mathbf{W}^* \mathbf{W})_{i, i} (\widehat{\mathbf{w}}_t) \right)_{\beta}^{\beta} \sum_{\beta \in J_{r, n} \{t\}} \text{cdet}_t \left((\mathbf{U}^{2k+1})^* \mathbf{U}^{2k+1} \right)_{i, i} (\widehat{\mathbf{u}}_s)_{\beta}^{\beta}}{\sum_{\beta \in J_{r_1, m}} \left| (\mathbf{W}^* \mathbf{W})_{\beta}^{\beta} \right| \sum_{\beta \in J_{r, n}} \left| ((\mathbf{U}^{2k+1})^* \mathbf{U}^{2k+1})_{\beta}^{\beta} \right|} \right] d_{sj}. \quad (61)$$

Denote $\widehat{\mathbf{D}} = \widehat{\mathbf{U}} \mathbf{D} = (\mathbf{U}^{2k+1})^* \mathbf{U}^k \mathbf{D}$, where $\widehat{\mathbf{D}} = (\widehat{\mathbf{d}}_{sj}) \in \mathbb{H}^{n \times p}$. Since

$$\sum_{s=1}^p \widehat{\mathbf{u}}_s d_{sj} = \widehat{\mathbf{d}}_j, \quad (62)$$

where $\widehat{\mathbf{d}}_j$ is the j th column of $\widehat{\mathbf{D}}$, then (58) follows from (61).

Cramer's rule (59) and (60) immediately follows from Theorem 12 by putting $\mathbf{W}_1 = \mathbf{W}$ and $\mathbf{W}_2 \mathbf{B} = \mathbf{I}$. \square

Remark 15. In the complex case, that is, $\mathbf{A} \in \mathbb{C}^{m \times n}$, $\mathbf{W} \in \mathbb{C}_{r_1}^{n \times m}$, and $\mathbf{D} \in \mathbb{C}^{n \times p}$, we substitute usual determinants for

all corresponding row and column determinants in (58), (59), and (60).

Note that in case (iii), the condition $\mathbf{A} \mathbf{W} \in \mathbb{C}^{m \times m}$ being Hermitian is not necessary; then in the complex case (60) will have the form

$$x_{ij} = \frac{\sum_{\beta \in J_{r, m} \{i\}} \left| ((\mathbf{A} \mathbf{W})_{i, i}^{k+2} (\mathbf{f}_j))_{\beta}^{\beta} \right|}{\sum_{\beta \in J_{r, m}} \left| ((\mathbf{A} \mathbf{W})^{k+2})_{\beta}^{\beta} \right|}, \quad (63)$$

where \mathbf{f}_j is the j th column of $\mathbf{F} = \overline{\mathbf{V}} \mathbf{D} = (\mathbf{A} \mathbf{W})^k \mathbf{A} \mathbf{D}$.

Corollary 16. Suppose that the following restricted matrix equation is given:

$$\begin{aligned} \mathbf{XWBW} &= \mathbf{D}, \\ \mathcal{R}_l(\mathbf{X}) &\subset \mathcal{R}_l((\mathbf{BW})^k), \\ \mathcal{N}_r(\mathbf{X}) &\supset \mathcal{N}_r((\mathbf{BA})^k), \end{aligned} \quad (64)$$

where $\mathbf{B} \in \mathbb{H}^{p \times q}$ and $\mathbf{W} \in \mathbb{H}_{r_1}^{q \times p}$ with $k = \max\{\text{Ind}(\mathbf{AW}), \text{Ind}(\mathbf{WB})\}$ and $\mathbf{D} \in \mathbb{H}^{n \times p}$. If $\mathcal{R}_l(\mathbf{D}) \subset \mathcal{R}_l((\mathbf{BW})^k)$ and

$\mathcal{N}_r(\mathbf{D}) \supset \mathcal{N}_r((\mathbf{WB})^k)$, then the restricted matrix equation (64) has a unique solution:

$$\mathbf{X} = \mathbf{DB}_{d,W}, \quad (65)$$

which possesses the following determinantal representations for $i = \overline{1, n}$ and $j = \overline{1, q}$.

(i) Consider

$$x_{ij} = \frac{\sum_{l=1}^p \sum_{\alpha \in I_{r,p}\{l\}} \text{rdet}_l \left(\left(\mathbf{V}^{2k+1} (\mathbf{V}^{2k+1})^* \right)_l, (\check{\mathbf{d}}_i)_\alpha \right) \sum_{\alpha \in I_{r_1,q}\{j\}} \text{rdet}_j \left((\mathbf{WW}^*)_{j \cdot} (\check{\mathbf{w}}_l)_\alpha \right)}{\sum_{\alpha \in I_{r,m}} \left| \left(\mathbf{V}^{2k+1} (\mathbf{V}^{2k+1})^* \right)_\alpha \right| \sum_{\alpha \in I_{r_1,n}} \left| (\mathbf{WW}^*)_\alpha \right|}, \quad (66)$$

where $\mathbf{V} = \mathbf{BW}$, $\check{\mathbf{d}}_i$ is the i th row of $\check{\mathbf{D}} = \mathbf{D}\check{\mathbf{V}} = \mathbf{D}\mathbf{V}^k(\mathbf{V}^{2k+1})^*$, $\check{\mathbf{w}}_l$ is the l th row of $\check{\mathbf{W}} = \mathbf{V}^k\mathbf{W}^*$, and $r = \text{rank}(\mathbf{BW})^{k+1} = \text{rank}(\mathbf{BW})^k$.

(ii) Consider

$$x_{ij} = \sum_{t=1}^q l_{it} (u_{ij}^D)^{(2)}, \quad (67)$$

where $(u_{ij}^D)^{(2)}$ can be obtained by (21) and $\mathbf{DB} = \mathbf{L} = (l_{it}) \in \mathbb{H}^{n \times q}$.

(iii) If $\mathbf{WB} \in \mathbb{H}^{q \times q}$ is Hermitian, then

$$x_{ij} = \frac{\sum_{\alpha \in I_{r,q}\{j\}} \text{rdet}_j \left((\mathbf{WB})_{j \cdot}^{k+2} (\mathbf{g}_i)_\alpha \right)}{\sum_{\alpha \in I_{r,q}} \left| \left((\mathbf{WB})^{k+2} \right)_\alpha \right|}, \quad (68)$$

where \mathbf{g}_i is the i th row of $\mathbf{G} = \mathbf{DB}(\mathbf{WB})^k$ for all $i = \overline{1, n}$.

Proof. The proof is similar to the proof of Corollary 14 in the point (i) and follows from Theorem 12 by putting $\mathbf{W}_2 = \mathbf{W}$ and $\mathbf{AW}_1 = \mathbf{I}$. \square

Remark 17. In the complex case, that is, $\mathbf{B} \in \mathbb{C}^{p \times q}$, $\mathbf{W} \in \mathbb{C}_{r_1}^{q \times p}$, and $\mathbf{D} \in \mathbb{C}^{n \times p}$, we substitute usual determinants for all corresponding row and column determinants in (66), (67), and (68). Herein the condition $\mathbf{WB} \in \mathbb{C}^{n \times n}$ being Hermitian is not necessary; then in the complex case (68) can be represented as follows:

$$x_{ij} = \frac{\sum_{\alpha \in I_{r,q}\{j\}} \left| \left((\mathbf{WB})_{j \cdot}^{k+2} (\mathbf{g}_i)_\alpha \right) \right|}{\sum_{\alpha \in I_{r,q}} \left| \left((\mathbf{WB})^{k+2} \right)_\alpha \right|}, \quad (69)$$

where \mathbf{g}_i is the i th row of $\mathbf{G} = \mathbf{DB}(\mathbf{WB})^k$ for all $i = \overline{1, n}$.

4. Examples

In this section, we give examples to illustrate our results.

(1) Let us consider the matrix equation

$$\mathbf{WAWX} = \mathbf{D} \quad (70)$$

with the restricted conditions (56), where

$$\begin{aligned} \mathbf{A} &= \begin{pmatrix} 0 & i & 0 \\ k & 1 & i \\ 1 & 0 & 0 \\ 1 & -k & -j \end{pmatrix}, \\ \mathbf{W} &= \begin{pmatrix} k & 0 & i & 0 \\ -j & k & 0 & 1 \\ 0 & 1 & 0 & -k \end{pmatrix}, \\ \mathbf{D} &= \begin{pmatrix} k & i \\ i & -j \\ 1 & -i \end{pmatrix}. \end{aligned} \quad (71)$$

Then

$$\begin{aligned} \mathbf{V} = \mathbf{AW} &= \begin{pmatrix} -k & -j & 0 & i \\ -1-j & i+k & j & 1+j \\ k & 0 & i & 0 \\ -i+k & 1-j & i & i-k \end{pmatrix}, \\ \mathbf{U} = \mathbf{WA} &= \begin{pmatrix} i & j & 0 \\ 0 & k & 0 \\ 0 & 0 & 0 \end{pmatrix}, \end{aligned} \quad (72)$$

and $\text{rank } \mathbf{W} = 3$, $\text{rank } \mathbf{V} = 3$, $\text{rank } \mathbf{V}^3 = \text{rank } \mathbf{V}^2 = 2$, and $\text{rank } \mathbf{U}^2 = \text{rank } \mathbf{U} = 2$. So, $\text{Ind } \mathbf{V} = 2$, $\text{Ind } \mathbf{U} = 1$, and $k = \max\{\text{Ind}(\mathbf{AW}), \text{Ind}(\mathbf{WA})\} = 2$.

We will find the W -weighted Drazin inverse solution of (70) by its determinantal representation (58). We have

$$\mathbf{U}^2 = \begin{pmatrix} -1 & i+k & 0 \\ 0 & -1 & \\ 0 & 0 & 0 \end{pmatrix},$$

$$\begin{aligned}
\mathbf{U}^5 &= \begin{pmatrix} i & 2+3j & 0 \\ 0 & k & \\ 0 & 0 & 0 \end{pmatrix}, & \mathbf{W}^* &= \begin{pmatrix} -k & j & 0 \\ 0 & -k & 1 \\ -i & 0 & 0 \\ 0 & 1 & k \end{pmatrix}, \\
(\mathbf{U}^5)^* &= \begin{pmatrix} -i & 0 & 0 \\ 2-3j & -k & \\ 0 & 0 & 0 \end{pmatrix}, & \mathbf{W}^*\mathbf{W} &= \begin{pmatrix} 2 & i & -j & j \\ -i & 2 & 0 & -2k \\ j & 0 & 1 & 0 \\ -j & 2k & 0 & 2 \end{pmatrix}, \\
(\mathbf{U}^5)^* \mathbf{U}^5 &= \begin{pmatrix} 1 & -2i-3k & 0 \\ 2i+3k & 14 & \\ 0 & 0 & 0 \end{pmatrix}, & \widehat{\mathbf{W}} = \mathbf{W}^* \mathbf{U}^2 &= \begin{pmatrix} -k & 1-2j & 0 \\ 0 & i+k & 0 \\ i & 1+j & 0 \\ 0 & -1 & 0 \end{pmatrix}. \\
\widehat{\mathbf{D}} = (\mathbf{U}^5)^* \mathbf{U}^2 \mathbf{D} & & & & & & & & & (73) \\
&= \begin{pmatrix} i-j-k & -j & \\ 1+3i+6j-2k & 4i-2k & \\ 0 & 0 & 0 \end{pmatrix},
\end{aligned}$$

Since by (58)

$$x_{11} = \frac{\sum_{t=1}^3 \sum_{\beta \in I_{3,4}\{1\}} \text{cdet}_1((\mathbf{W}^*\mathbf{W})_{\cdot 1}(\widehat{\mathbf{w}}_{\cdot t}))_{\beta}^{\beta} \sum_{\beta \in J_{2,3}\{t\}} \text{cdet}_t(((\mathbf{U}^5)^* \mathbf{U}^5)_{\cdot t}(\widehat{\mathbf{d}}_{\cdot 1}))_{\beta}^{\beta}}{\sum_{\beta \in J_{3,4}} |(\mathbf{W}^*\mathbf{W})_{\beta}^{\beta}| \sum_{\beta \in J_{2,3}} |((\mathbf{U}^5)^* \mathbf{U}^5)_{\beta}^{\beta}|}, \quad (74)$$

where

$$\begin{aligned}
&\sum_{\beta \in I_{3,4}\{1\}} \text{cdet}_1((\mathbf{W}^*\mathbf{W})_{\cdot 1}(\widehat{\mathbf{w}}_{\cdot 1}))_{\beta}^{\beta} \\
&= \text{cdet}_1 \begin{pmatrix} k & i & -j \\ 0 & 2 & 0 \\ i & 0 & 1 \end{pmatrix} + \text{cdet}_1 \begin{pmatrix} k & i & j \\ 0 & 2 & -2k \\ 0 & 2k & 1 \end{pmatrix} \\
&+ \text{cdet}_1 \begin{pmatrix} k & -j & j \\ i & 1 & 0 \\ 0 & 0 & 2 \end{pmatrix} = 0,
\end{aligned}$$

$$\sum_{\beta \in I_{3,4}\{1\}} \text{cdet}_1((\mathbf{W}^*\mathbf{W})_{\cdot 1}(\widehat{\mathbf{w}}_{\cdot 2}))_{\beta}^{\beta} = -2j,$$

$$\sum_{\beta \in I_{3,4}\{1\}} \text{cdet}_1((\mathbf{W}^*\mathbf{W})_{\cdot 1}(\widehat{\mathbf{w}}_{\cdot 3}))_{\beta}^{\beta} = 0,$$

$$\sum_{\beta \in J_{3,4}} |(\mathbf{W}^*\mathbf{W})_{\beta}^{\beta}| = 2,$$

$$\sum_{\beta \in J_{2,3}\{1\}} \text{cdet}_1(((\mathbf{U}^5)^* \mathbf{U}^5)_{\cdot 1}(\widehat{\mathbf{d}}_{\cdot 1}))_{\beta}^{\beta}$$

$$= \text{cdet}_1 \begin{pmatrix} i-j-k & -2i-3k \\ 1+3i+6j-2k & 14 \end{pmatrix}$$

$$+ \text{cdet}_1 \begin{pmatrix} i-j-k & 0 \\ 0 & 0 \end{pmatrix} = -2i-j-k,$$

$$\sum_{\beta \in J_{2,3}\{2\}} \text{cdet}_2(((\mathbf{U}^5)^* \mathbf{U}^5)_{\cdot 2}(\widehat{\mathbf{d}}_{\cdot 1}))_{\beta}^{\beta} = j,$$

$$\sum_{\beta \in J_{2,3}\{3\}} \text{cdet}_3(((\mathbf{U}^5)^* \mathbf{U}^5)_{\cdot 3}(\widehat{\mathbf{d}}_{\cdot 1}))_{\beta}^{\beta} = 0,$$

$$\sum_{\beta \in J_{2,3}} |((\mathbf{U}^5)^* \mathbf{U}^5)_{\beta}^{\beta}| = 1,$$

(75)

then

$$x_{11} = \frac{0 \cdot (-2i-j-k) + (-2j) \cdot j + 0 \cdot 0}{2 \cdot 1} = 1.$$

$$x_{12} = \frac{0 \cdot (-2+2j) + (-2j) \cdot i + 0 \cdot 0}{2 \cdot 1} = k,$$

$$\begin{aligned}
x_{21} &= \frac{2j \cdot (-2i-j-k) + (10i-4k) \cdot j + 0 \cdot 0}{2 \cdot 1} \\
&= 1 + i + 7k,
\end{aligned}$$

$$x_{22} = \frac{2j \cdot (-2+2j) + (10i-4k) \cdot i + 0 \cdot 0}{2 \cdot 1}$$

$$= -7 - 4j,$$

$$x_{31} = \frac{10i \cdot (-2i-j-k) + j \cdot j + 0 \cdot 0}{2 \cdot 1}$$

$$\begin{aligned}
 &= 9.5 + 5j - 5k, \\
 x_{32} &= \frac{10i \cdot (-2 + 2j) + j \cdot i + 0 \cdot 0}{2 \cdot 1} = -10i + 9.5k,
 \end{aligned} \tag{76}$$

We finally get

$$\mathbf{X} = \begin{pmatrix} 1 & k \\ 1 + i + 7k & -7 - 4j \\ 9.5 + 5j - 5k & -10i + 9.5k \end{pmatrix}. \tag{77}$$

(2) Let now us consider the matrix equation

$$\mathbf{W}_1 \mathbf{A} \mathbf{W}_1 \mathbf{X} \mathbf{W}_2 \mathbf{B} \mathbf{W}_2 = \mathbf{D}, \tag{78}$$

with constraints (33), where

$$\begin{aligned}
 \mathbf{A} &= \begin{pmatrix} k & 0 & i & 0 \\ -j & k & 0 & 1 \\ 0 & 1 & 0 & -k \end{pmatrix}, \\
 \mathbf{W}_1 &= \begin{pmatrix} k & -j & 0 \\ 0 & k & 1 \\ i & 0 & 0 \\ 0 & 1 & -k \end{pmatrix}, \\
 \mathbf{W}_2 &= \begin{pmatrix} k & -i \\ j & 0 \\ 0 & 1 \end{pmatrix}, \\
 \mathbf{B} &= \begin{pmatrix} k & j & 0 \\ j & 0 & 1 \end{pmatrix}, \\
 \mathbf{D} &= \begin{pmatrix} i & -1 \\ k & 0 \\ 0 & j \\ -1 & 0 \end{pmatrix}.
 \end{aligned} \tag{79}$$

Since the following matrices are Hermitian:

$$\begin{aligned}
 \mathbf{V} = \mathbf{A} \mathbf{W}_1 &= \begin{pmatrix} -2 & i & 0 \\ -i & -1 & 0 \\ 0 & 0 & 0 \end{pmatrix}, \\
 \mathbf{U} = \mathbf{W}_2 \mathbf{B} &= \begin{pmatrix} 0 & -i & -i \\ i & -1 & 0 \\ i & 0 & -1 \end{pmatrix},
 \end{aligned} \tag{80}$$

then we can find the W -weighted Drazin inverse solution of (78) by its determinantal representation (38).

We have

$$\begin{aligned}
 k_1 &= \max \{ \text{Ind}(\mathbf{A} \mathbf{W}_1), \text{Ind}(\mathbf{W}_1 \mathbf{A}) \} = 1, \\
 k_2 &= \max \{ \text{Ind}(\mathbf{B} \mathbf{W}_2), \text{Ind}(\mathbf{W}_2 \mathbf{B}) \} = 1,
 \end{aligned} \tag{81}$$

and $s_1 = \text{rank}(\mathbf{A} \mathbf{W}_1) = 2$ and $s_2 = \text{rank}(\mathbf{W}_2 \mathbf{B}) = 2$. Since

$$(\mathbf{A} \mathbf{W}_1)^3 = \begin{pmatrix} -13 & 8i & 0 \\ -8i & -5 & 0 \\ 0 & 0 & 0 \end{pmatrix}, \tag{82}$$

$$(\mathbf{W}_2 \mathbf{B})^3 = \begin{pmatrix} 0 & -3i & -3i \\ 3i & -3 & 0 \\ 3i & 0 & 3 \end{pmatrix},$$

then

$$\begin{aligned}
 \sum_{\beta \in J_{2,3}} |((\mathbf{A} \mathbf{W}_1)^3)_\beta^\beta| &= 1, \\
 \sum_{\alpha \in I_{2,3}} |((\mathbf{W}_2 \mathbf{B})^3)_\alpha^\alpha| &= -27.
 \end{aligned} \tag{83}$$

We have

$$\begin{aligned}
 \bar{\mathbf{D}} &= \mathbf{A} \mathbf{W}_1 \mathbf{A} \mathbf{D} \mathbf{B} \mathbf{W}_2 \mathbf{B} \\
 &= \begin{pmatrix} 2i + j & -7 + k & -5 + 2k \\ -1 + k & -5i - j & -4i - 2j \\ 0 & 0 & 0 \end{pmatrix}.
 \end{aligned} \tag{84}$$

By (40), we can get

$$\begin{aligned}
 \mathbf{d}_1^{\mathbf{B}} &= \begin{pmatrix} 36i - 9j \\ -27 - 9k \\ 0 \end{pmatrix}, \\
 \mathbf{d}_2^{\mathbf{B}} &= \begin{pmatrix} -27 \\ -18i \\ 0 \end{pmatrix}, \\
 \mathbf{d}_3^{\mathbf{B}} &= \begin{pmatrix} 9 - 9k \\ 9i + 3j \\ 0 \end{pmatrix}.
 \end{aligned} \tag{85}$$

Since

$$(\mathbf{A} \mathbf{W}_1)_1^3 (\mathbf{d}_1^{\mathbf{B}}) = \begin{pmatrix} 36i - 9j & 8i & 0 \\ -27 - 9k & -5 & 0 \\ 0 & 0 & 4 \end{pmatrix}, \tag{86}$$

then finally we obtain

$$\begin{aligned}
 x_{11} &= \frac{\sum_{\beta \in J_{2,3}\{1\}} \text{cdet}_1((\mathbf{A} \mathbf{W}_1)_1^3 (\mathbf{d}_1^{\mathbf{B}}))_\beta^\beta}{\sum_{\beta \in J_{2,3}} |((\mathbf{A} \mathbf{W}_1)^3)_\beta^\beta| \sum_{\alpha \in I_{2,3}} |((\mathbf{W}_2 \mathbf{B})^3)_\alpha^\alpha|} \\
 &= \frac{36i - 27j}{-27} = \frac{-4i + 3j}{3}.
 \end{aligned} \tag{87}$$

Similarly,

$$\begin{aligned}
 x_{12} &= \frac{\text{cdet}_1 \begin{pmatrix} -27 & 8i \\ -18i & -5 \end{pmatrix}}{-27} = \frac{1}{3}, \\
 x_{13} &= \frac{\text{cdet}_1 \begin{pmatrix} 9-9k & 8i \\ 9i-3j & -5 \end{pmatrix}}{-27} = \frac{-9-7k}{9}, \\
 x_{21} &= \frac{\text{cdet}_2 \begin{pmatrix} -13 & 36i-9j \\ -8i & -27-9k \end{pmatrix}}{-27} = \frac{-7-5k}{3}, \\
 x_{22} &= \frac{\text{cdet}_2 \begin{pmatrix} -13 & -27 \\ -8i & -18i \end{pmatrix}}{-27} = \frac{-2i}{3}, \\
 x_{23} &= \frac{\text{cdet}_2 \begin{pmatrix} -13 & -9-9k \\ -8i & 9i+3j \end{pmatrix}}{-27} = \frac{15i-11j}{9}, \\
 x_{31} &= x_{32} = x_{33} = 0.
 \end{aligned} \tag{88}$$

So, the W -weighted Drazin inverse solution of (78) is

$$\mathbf{X} = \frac{1}{9} \begin{pmatrix} -12i + 9j & 3 & -9 - 7k \\ -21 - 15k & -6i & 15i - 11j \\ 0 & 0 & 0 \end{pmatrix}. \tag{89}$$

Note that we used Maple with the package CLIFFORD in the calculations.

Competing Interests

The author declares that there are no competing interests.

References

- [1] S. L. Adler, *Quaternionic Quantum Mechanics and Quantum Fields*, Oxford University Press, New York, NY, USA, 1995.
- [2] J. D. Gibbon, "A quaternionic structure in the three-dimensional Euler and ideal magneto-hydrodynamics equations," *Physica D*, vol. 166, no. 1-2, pp. 17-28, 2002.
- [3] J. D. Gibbon, D. D. Holm, R. M. Kerr, and I. Roulstone, "Quaternions and particle dynamics in the Euler fluid equations," *Nonlinearity*, vol. 19, no. 8, pp. 1969-1983, 2006.
- [4] A. J. Hanson and H. Ma, "Quaternion frame approach to streamline visualization," *IEEE Transactions on Visualization and Computer Graphics*, vol. 1, no. 2, pp. 164-174, 1995.
- [5] B. L. Stevens, F. L. Lewis, and E. N. Johnson, *Aircraft Control and Simulation: Dynamics, Controls Design, and Autonomous Systems*, John Wiley & Sons, 3rd edition, 2015.
- [6] A. Perez and J. M. McCarthy, "Dual quaternion synthesis of constrained robotic systems," *Journal of Mechanical Design*, vol. 126, no. 3, pp. 425-435, 2004.
- [7] T. Isokawa, T. Kusakabe, N. Matsui, and F. Peper, "Quaternion neural network and its application," in *Knowledge-Based Intelligent Information and Engineering Systems: 7th International Conference, KES 2003, Oxford, UK, September 2003. Proceedings, Part II*, vol. 2774 of *Lecture Notes in Computer Science*, pp. 318-324, Springer, Berlin, Germany, 2003.
- [8] J. Prošková, "Description of protein secondary structure using dual quaternions," *Journal of Molecular Structure*, vol. 1076, pp. 89-93, 2014.
- [9] S. F. Yuan, Q. W. Wang, and X. F. Duan, "On solutions of the quaternion matrix equation $AX = B$ and their applications in color image restoration," *Applied Mathematics and Computation*, vol. 221, pp. 10-20, 2013.
- [10] Q. Wang, S. Yu, and W. Xie, "Extreme ranks of real matrices in solution of the quaternion matrix equation $AXB = C$ with applications," *Algebra Colloquium*, vol. 17, no. 2, pp. 345-360, 2010.
- [11] S. Yuan, A. Liao, and Y. Lei, "Least squares Hermitian solution of the matrix equation $(AXB; CXD) = (E; F)$ with the least norm over the skew field of quaternions," *Mathematical and Computer Modelling*, vol. 48, pp. 91-100, 2008.
- [12] L. G. Feng and W. Cheng, "The solution set to the quaternion matrix equation $AX - XB = 0$," *Algebra Colloquium*, vol. 19, no. 1, pp. 175-180, 2012.
- [13] T. S. Jiang and M. S. Wei, "On a solution of the quaternion matrix equation $X - A\bar{X}B = C$," *Acta Mathematica Sinica*, vol. 21, no. 3, pp. 483-490, 2005.
- [14] S. Caiqin, C. Guoliang, and W. Xiaodong, "On solutions of quaternion matrix equations $XF \# AX = BY$ and $XF \# A\bar{X} = BY$," *Acta Mathematica Scientia*, vol. 32, no. 5, pp. 1967-1982, 2012.
- [15] S.-F. Yuan and Q.-W. Wang, "Two special kinds of least squares solutions for the quaternion matrix equation $AXB + CXD = E$," *Electronic Journal of Linear Algebra*, vol. 23, pp. 257-274, 2012.
- [16] F. Zhang, M. Wei, Y. Lia, and J. Zhao, "Special least squares solutions of the quaternion matrix equation $AX = B$ with applications," *Applied Mathematics and Computation*, vol. 270, pp. 425-433, 2015.
- [17] R. E. Cline and T. N. E. Greville, "A Drazin inverse for rectangular matrices," *Linear Algebra and Its Applications*, vol. 29, pp. 53-62, 1980.
- [18] S. L. Campbell, C. D. Meyer Jr., and N. J. Rose, "Applications of the Drazin inverse to linear systems of differential equations with singular constant coefficients," *SIAM Journal on Applied Mathematics*, vol. 31, no. 3, pp. 411-425, 1976.
- [19] S. L. Campbell, "Comments on 2-D descriptor systems," *Automatica*, vol. 27, no. 1, pp. 189-192, 1991.
- [20] S. L. Campbell and C. D. Meyer, *Generalized Inverse of Linear Transformations. Corrected Reprint of the 1979 Original*, Dover, New York, NY, USA, 1991.
- [21] D. J. Spitzner and T. R. Boucher, "Asymptotic variance of functionals of discrete-time Markov chains via the Drazin inverse," *Electronic Communications in Probability*, vol. 12, pp. 120-133, 2007.
- [22] T. Kaczorek, "Application of the Drazin inverse to the analysis of descriptor fractional discrete-time linear systems with regular pencils," *International Journal of Applied Mathematics and Computer Science*, vol. 23, no. 1, pp. 29-33, 2013.
- [23] Z. Al-Zhour, A. Kılıçman, and M. H. Abu Hassa, "New representations for weighted Drazin inverse of matrices," *International Journal of Mathematical Analysis*, vol. 1, no. 15, pp. 697-708, 2007.
- [24] M. Nikuie and M. Z. Ahmad, "New results on the W -weighted drazin inverse," in *Proceedings of the 3rd International Conference on Mathematical Sciences*, vol. 1602 of *AIP Conference Proceedings*, p. 157, Kuala Lumpur, Malaysia, June 2014.
- [25] M. Nikuie, "Singular fuzzy linear systems," *Applied Mathematics and Computational Intelligence*, vol. 2, no. 2, pp. 157-168, 2013.
- [26] G. Wang and J. Sun, "A Cramer rule for solution of the general restricted matrix equation," *Applied Mathematics and Computation*, vol. 154, no. 2, pp. 415-422, 2004.

- [27] Y. Wei, "A characterization for the W -weighted Drazin inverse and a Cramer rule for the W -weighted Drazin inverse solution," *Applied Mathematics and Computation*, vol. 125, no. 2-3, pp. 303–310, 2002.
- [28] G. J. Song, "Characterization of the W -weighted Drazin inverse over the quaternion skew field with applications," *Electronic Journal of Linear Algebra*, vol. 26, pp. 1–14, 2013.
- [29] I. Kyrchei, "Determinantal representations of the W -weighted Drazin inverse over the quaternion skew field," *Applied Mathematics and Computation*, vol. 264, Article ID 21118, pp. 453–465, 2015.
- [30] I. Kyrchei, "Cramer's rule for quaternion systems of linear equations," *Journal of Mathematical Sciences*, vol. 155, no. 6, pp. 839–858, 2008.
- [31] I. Kyrchei, "The theory of the column and row determinants in a quaternion linear algebra," in *Advances in Mathematics Research*, A. R. Baswell, Ed., vol. 15, pp. 301–359, Nova Science, New York, NY, USA, 2012.
- [32] I. I. Kyrchei, "Cramer's rule for some quaternion matrix equations," *Applied Mathematics and Computation*, vol. 217, no. 5, pp. 2024–2030, 2010.
- [33] I. I. Kyrchei, "Determinantal representations of the Moore-Penrose inverse over the quaternion skew field and corresponding Cramer's rules," *Linear and Multilinear Algebra*, vol. 59, no. 4, pp. 413–431, 2011.
- [34] I. Kyrchei, "Determinantal representation of the Moore-Penrose inverse matrix over the quaternion skew field," *Journal of Mathematical Sciences*, vol. 180, no. 1, pp. 23–33, 2012.
- [35] I. Kyrchei, "Explicit representation formulas for the minimum norm least squares solutions of some quaternion matrix equations," *Linear Algebra and Its Applications*, vol. 438, no. 1, pp. 136–152, 2013.
- [36] I. Kyrchei, "Determinantal representations of the Drazin inverse over the quaternion skew field with applications to some matrix equations," *Applied Mathematics and Computation*, vol. 238, pp. 193–207, 2014.
- [37] G.-J. Song, "Determinantal representation of the generalized inverses over the quaternion skew field with applications," *Applied Mathematics and Computation*, vol. 219, no. 2, pp. 656–667, 2012.
- [38] G.-J. Song, "Bott-Duffin inverse over the quaternion skew field with applications," *Journal of Applied Mathematics and Computing*, vol. 41, no. 1-2, pp. 377–392, 2013.
- [39] G.-J. Song, Q.-W. Wang, and H.-X. Chang, "Cramer rule for the unique solution of restricted matrix equations over the quaternion skew field," *Computers & Mathematics with Applications*, vol. 61, no. 6, pp. 1576–1589, 2011.
- [40] C. Song, X. Wang, and X. Zhang, "On solutions of the generalized Stein quaternion matrix equation," *Journal of Applied Mathematics and Computing*, vol. 43, no. 1-2, pp. 115–131, 2013.
- [41] V. Rakočević and Y. Wei, "A weighted Drazin inverse and applications," *Linear Algebra and Its Applications*, vol. 350, pp. 25–39, 2002.
- [42] Y. Wei, "Integral representation of the W -weighted Drazin inverse," *Applied Mathematics and Computation*, vol. 144, pp. 3–10, 2003.

Research Article

A General Solution to Least Squares Problems with Box Constraints and Its Applications

Yueyang Teng, Shouliang Qi, Dayu Xiao, Lisheng Xu, Jianhua Li, and Yan Kang

Sino-Dutch Biomedical and Information Engineering School, Northeastern University, Shenyang 110004, China

Correspondence should be addressed to Yan Kang; kangyan@bmie.neu.edu.cn

Received 15 November 2015; Revised 4 March 2016; Accepted 18 April 2016

Academic Editor: Masoud Hajarian

Copyright © 2016 Yueyang Teng et al. This is an open access article distributed under the Creative Commons Attribution License, which permits unrestricted use, distribution, and reproduction in any medium, provided the original work is properly cited.

The main contribution of this paper is presenting a flexible solution to the box-constrained least squares problems. This solution is applicable to many existing problems, such as nonnegative matrix factorization, support vector machine, signal deconvolution, and computed tomography reconstruction. The key concept of the proposed algorithm is to replace the minimization of the cost function at each iteration by the minimization of a surrogate, leading to a guaranteed decrease in the cost function. In addition to the monotonicity, the proposed algorithm also owns a few good features including the self-constraint in the feasible region and the absence of a predetermined step size. This paper theoretically proves the global convergence for a special case of below-bounded constraints. Using the proposed mechanism, some valuable algorithms can be derived. The simulation results demonstrate that the proposed algorithm provides performance that is comparable to that of other commonly used methods in numerical experiment and computed tomography reconstruction.

1. Introduction

Solving the linear system $Y = AX$ is a classic inverse problem, where $X \in R^N$ and $Y \in R^M$ are vectors and $A \in R^{M \times N}$ is a matrix. This problem is applicable in many fields, including nonnegative matrix factorization (NMF), support vector machine (SVM), signal deconvolution, and medical image reconstruction (e.g., computed tomography (CT)) [1–5]. In many cases, we need to impose a box constraint on the problem. A classical approach to choosing X is to minimize the least squares (LS) error between Y and AX :

$$\min_{C_1 \leq X \leq C_2} F(X) = \|AX - Y\|^2, \quad (1)$$

where C_1 and C_2 are given constant vectors and $\|\cdot\|$ denotes the Euclidean distance.

In fact, (1) can be easily converted into an equivalent form by a linear transformation $\xi = X - C_1$, which is convenient to study. In the following, we only focus on such LS problems and still denote variables with X for simple

notation; subsequently, the readers may generalize all the results of this paper to the generic form by themselves:

$$\min_{0 \leq X \leq C} F(X) = \|AX - Y\|^2, \quad (2)$$

where C is a constant vector.

If we denote $C = +\infty$, then it is the widely used case, that is, the nonnegativity constrained LS problem:

$$\min_{X \geq 0} F(X) = \|AX - Y\|^2. \quad (3)$$

There are many methods for solving nonnegativity constrained problems. A simple method for solving such problems is by using

$$X = (A^T A)^{-1} A^T Y, \quad (4)$$

$$X = \max\{X, 0\}.$$

Of course, we must truncate the negative pixel values to satisfy the nonnegativity constraint. However, we will encounter two difficulties: perhaps $A^T A$ is not invertible or $A^T A$ is too large. A viable example for the minimization of (3) is

the gradient-based method. The steepest descent method is perhaps the simplest technique to implement, which takes the negative gradient as the descent direction:

$$\begin{aligned} X^{t+1} &= X^t - \alpha(t) \nabla F(X^t), \\ X^{t+1} &= \max\{X^{t+1}, 0\}, \end{aligned} \quad (5)$$

where the superscript (t) denotes the t th iteration and $\alpha(t)$ is the step size.

Let $\alpha(t) = \alpha$ be a constant, where $0 < \alpha < 2/\|\nabla^2 F(X^t)\|_E$, and $\|\cdot\|_E$ denotes the maximum eigenvalue for a matrix; then, (5) becomes the projected Landweber (PL) method [6]:

$$\begin{aligned} X^{t+1} &= X^t - \alpha \nabla F(X^t), \\ X^{t+1} &= \max\{X^{t+1}, 0\}. \end{aligned} \quad (6)$$

In addition, Lantéri et al. [7, 8] provided a general multiplicative algorithm, which was also a gradient-based method. Let $a_j(X^t)$ be a positive function with positive values for any $X_j^t > 0$; then, $-\text{diag}[X_j^t a_j(X^t)] \nabla F(X^t)$ is also a descent direction. Therefore, the algorithm in a modified gradient form can be written as

$$X_j^{t+1} = X_j^t - X_j^t a_j(X^t) \nabla_j F(X^t). \quad (7)$$

Again, let $U_j(X^t)$ and $V_j(X^t)$ be two positive functions for any $X_j^t > 0$, which satisfy $-\nabla_j F(X^t) = U_j(X^t) - V_j(X^t)$. Taking $a_j(X^t) = 1/V_j(X^t)$, Lantéri et al. obtained a multiplicative update

$$X_j^{t+1} = X_j^t \frac{U_j(X^t)}{V_j(X^t)}. \quad (8)$$

The conjugate gradient (CG) method is also a popular method, and it is often implemented as an iterative algorithm, applicable to sparse systems that are too large to be handled by a direct implementation.

The above approaches are not effective for processing the upper-bounded constraints, and, generally, a truncation is imposed to the update rule, which may lead to a divergent modification.

In this paper, we consider a specific application of the surrogate-based methods [9] to a specific type of LS problem with box constraints. We derive a multiplicative update rule to iteratively and monotonically (in the sense of decreasing the cost function) solve the problem, similar to the EM algorithm [10]. The nonnegativity constraints will be satisfied automatically, and the upper-bounded constraints are performed by an upper truncation. Meanwhile, the algorithm still has the monotonicity and does not require an adjustable step size. We provide a rigorous global convergence proof for the case of only nonnegativity constraints, which can be easily generalized to the below-constrained case. We demonstrate the power of this mechanism by deriving many existing and new algorithms. We also present some computer simulation results to show the desirable behavior of the proposed algorithm with respect to the convergence rate and the stability compared with existing methods.

2. Methodology

A note about our notation: all vectors will be column vectors unless transposed to a row vector by a prime superscript T . For a matrix or vector X , $X \geq 0$ means that any component of X is equal to or greater than 0. For a matrix A , A_{i*} and A_{*i} represent the i th row and i th column of A , respectively.

As mentioned in many articles [1, 2, 9, 11], a surrogate as defined below is useful in algorithm derivations and convergence proofs.

Definition 1 (surrogate). Denote $\psi(X | X^t)$ as a surrogate for $\Psi(X)$ at X^t (fixed) if $\psi(X^t | X^t) = \Psi(X^t)$ and $\psi(X | X^t) \geq \Psi(X)$.

Clearly, $\Psi(X)$ is decreasing under the update $X^{t+1} = \min_X \psi(X | X^t)$ because

$$\Psi(X^{t+1}) \leq \psi(X^{t+1} | X^t) \leq \psi(X^t | X^t) = \Psi(X^t). \quad (9)$$

There are two obvious and important properties for a surrogate: additivity and transitivity. For the former, the sum of two surrogates is a surrogate of the sum of the two original functions. For the latter, the surrogate of a surrogate of a function is a surrogate of this function.

In the following, we proceed step by step: firstly, assume that $A \geq 0$ and $C = +\infty$; secondly, remove the restriction of $A \geq 0$; and thirdly, remove the restriction of $C = +\infty$.

2.1. $A \geq 0$ and $C = +\infty$. Let $-Y = Y^+ - Y^-$, where Y^+ and Y^- are nonnegative vectors; then, $F(X) = \|AX + Y^+ - Y^-\|^2$. Note that we decompose $-Y$ instead of Y for convenient derivation, which can be seen below. We construct a surrogate $f(X | X^t)$ by the convexity of $F(X)$. Denote

$$\begin{aligned} \lambda_{i*} &= \frac{Y_i^+}{(AX^t + Y^+)_i}, \\ \lambda_{ij} &= \frac{A_{ij} X_j^t}{(AX^t + Y^+)_i} \end{aligned} \quad (10)$$

that satisfy $\lambda_{i*}, \lambda_{ij} \geq 0$ and $\lambda_{i*} + \sum_{j=1}^N \lambda_{ij} = 1$. They can be the convex combination coefficients such that

$$\begin{aligned} f(X | X^t) &= \sum_{i=1}^M \left[\lambda_{i*} \left(\frac{Y_i^+}{\lambda_{i*}} - Y_i^- \right)^2 + \sum_{j=1}^N \lambda_{ij} \left(\frac{A_{ij} X_j}{\lambda_{ij}} - Y_i^- \right)^2 \right]. \end{aligned} \quad (11)$$

It is easy to verify that $f(X^t | X^t) = F(X^t)$. If considering Jensen's inequality and the convex combination coefficients λ_{ij} , then $f(X | X^t) \geq F(X)$ is proven by the following inequality:

$$\begin{aligned} \lambda_{i*} \left(\frac{Y_i^+}{\lambda_{i*}} - Y_i^- \right)^2 + \sum_{j=1}^N \lambda_{ij} \left(\frac{A_{ij} X_j}{\lambda_{ij}} - Y_i^- \right)^2 &\geq [(AX)_i + Y_i^+ - Y_i^-]^2. \end{aligned} \quad (12)$$

Take the partial derivatives of $f(X | X^t)$; then, we can solve the one-dimensional equations $\partial f(X | X^t)/\partial X_j = 0$ to obtain a multiplicative update rule:

$$X_j^{t+1} = X_j^t \frac{(A^T Y^-)_j}{[A^T (AX^t + Y^+)]_j}. \quad (13)$$

2.2. *Any A but C = +∞.* Let $A = A^+ - A^-$, $w_1 + w_2 = 1$, and $w_1, w_2 > 0$, where A^+ and A^- are two nonnegative matrices; then, we can construct the surrogate $f_{\text{mid}}(X | X^t)$ for $F(X)$ as follows:

$$f_{\text{mid}}(X | X^t) = \bar{f}(X | X^t) + \hat{f}(X | X^t), \quad (14)$$

where

$$\begin{aligned} \bar{f}(X | X^t) &= w_1 \left\| \frac{1}{w_1} [A^+ X + Y^+] \right. \\ &\quad \left. - \left(\frac{1}{w_1} - 1 \right) [A^+ X^t + Y^+] - [A^- X^t + Y^-] \right\|^2, \end{aligned} \quad (15)$$

$$\begin{aligned} \hat{f}(X | X^t) &= w_2 \left\| \frac{1}{w_2} [A^- X + Y^-] - [A^+ X^t + Y^+] \right. \\ &\quad \left. - \left(\frac{1}{w_2} - 1 \right) [A^- X^t + Y^-] \right\|^2. \end{aligned}$$

It is easy to verify that $f_{\text{mid}}(X^t | X^t) = F(X^t)$. By the convexity of $F(X)$, it is clear that

$$\begin{aligned} f_{\text{mid}}(X | X^t) &= w_1 \left\| \frac{1}{w_1} [A^+ X + Y^+] \right. \\ &\quad \left. - \left(\frac{1}{w_1} - 1 \right) [A^+ X^t + Y^+] - [A^- X^t + Y^-] \right\|^2 \\ &\quad + w_2 \left\| -\frac{1}{w_2} [A^- X + Y^-] + [A^+ X^t + Y^+] \right. \\ &\quad \left. + \left(\frac{1}{w_2} - 1 \right) [A^- X^t + Y^-] \right\|^2 \geq F(X) \end{aligned} \quad (16)$$

(note that $w_1 + w_2 = 1$).

Following the same process as in Section 2.1, we can construct surrogates for $\bar{f}(X | X^t)$ and $\hat{f}(X | X^t)$. Let

$$\lambda_{ij}^+ = \frac{A_{ij}^+ X_j^t}{(A^+ X^t + Y^+)_i},$$

$$\lambda_{i*}^+ = \frac{Y_i^+}{(A^+ X^t + Y^+)_i},$$

$$\lambda_{i*}^- = \frac{Y_i^-}{(A^- X^t + Y^-)_i},$$

$$\lambda_{ij}^- = \frac{A_{ij}^- X_j^t}{(A^- X^t + Y^-)_i},$$

$$\bar{B} = \left(\frac{1}{w_1} - 1 \right) [A^+ X^t + Y^+] + [A^- X^t + Y^-],$$

$$\hat{B} = [A^+ X^t + Y^+] + \left(\frac{1}{w_2} - 1 \right) [A^- X^t + Y^-]; \quad (17)$$

then,

$$\bar{\bar{f}}(X | X^t) = w_1 \sum_{i=1}^M \sum_{j=1}^N \lambda_{ij}^+ \left[\frac{1}{w_1} \frac{A_{ij}^+ X_j}{\lambda_{ij}^+} - \bar{B}_i \right]^2 + \text{const}, \quad (18)$$

$$\hat{\hat{f}}(X | X^t) = w_2 \sum_{i=1}^M \sum_{j=1}^N \lambda_{ij}^- \left[\frac{1}{w_2} \frac{A_{ij}^- X_j}{\lambda_{ij}^-} - \hat{B}_i \right]^2 + \text{const}.$$

Note that λ_{i*}^+ and λ_{i*}^- are relative to the constant terms, which do not work for the optimization problems; thus, we ignore them. We can now obtain a surrogate for $F(X)$ at X^t :

$$f(X | X^t) = \bar{\bar{f}}(X | X^t) + \hat{\hat{f}}(X | X^t). \quad (19)$$

Take the partial derivatives of $\bar{\bar{f}}(X | X^t)$ and $\hat{\hat{f}}(X | X^t)$:

$$\begin{aligned} \frac{\partial \bar{\bar{f}}(X | X^t)}{\partial X_j} &= \frac{2X_j}{w_1 X_j^t} \left[(A^+)^T (A^+ X^t + Y^+) \right]_j \\ &\quad - 2 \left[(A^+)^T \bar{B} \right]_j, \end{aligned} \quad (20)$$

$$\begin{aligned} \frac{\partial \hat{\hat{f}}(X | X^t)}{\partial X_j} &= \frac{2X_j}{w_2 X_j^t} \left[(A^-)^T (A^- X^t + Y^-) \right]_j \\ &\quad - 2 \left[(A^-)^T \hat{B} \right]_j. \end{aligned}$$

Then, we solve the one-dimensional equations $\partial f(X | X^t)/\partial X_j = 0$ to obtain a multiplicative update rule:

$$\begin{aligned} X_j^{t+1} &= X_j^t \\ &\quad \cdot \frac{w_1 w_2 \left[(A^+)^T \bar{B} + (A^-)^T \hat{B} \right]_j}{\left[w_2 \left[(A^+)^T (A^+ X^t + Y^+) \right]_j + w_1 \left[(A^-)^T (A^- X^t + Y^-) \right]_j \right.} \\ &= X_j^t \\ &\quad \cdot \frac{\left\{ (w_2 A^+ + w_1 A^-)^T \left[w_2 (A^+ X^t + Y^+) + w_1 (A^- X^t + Y^-) \right] \right\}_j}{\left[w_2 \left[(A^+)^T (A^+ X^t + Y^+) \right]_j + w_1 \left[(A^-)^T (A^- X^t + Y^-) \right]_j \right.} \end{aligned} \quad (21)$$

2.3. *Any A and C.* As shown, (21) will ensure the monotonic decrease of the cost function and satisfy the nonnegativity constraints. In the following, it will be modified by a truncation at the end of each iteration to satisfy the box constraints:

$$X = \min \{X, C\}. \quad (22)$$

We will show that the truncation still ensures the monotonic decrease of the cost function.

It is easy to see the separability of the variables of (19); that is, $f(X, X^t) = \sum_{j=1}^N f_j(X_j, X^t)$, and every separated function $f_j(X_j, X^t)$ has a quadratic form:

$$f_j(X_j, X^t) = w_1 \sum_{i=1}^M \lambda_{ij}^+ \left[\frac{1}{w_1} \frac{A_{ij}^+ X_j}{\lambda_{ij}^+} - \bar{B}_i \right]^2 + w_2 \sum_{i=1}^M \lambda_{ij}^- \left[\frac{1}{w_2} \frac{A_{ij}^- X_j}{\lambda_{ij}^-} - \hat{B}_i \right]^2 + \text{const.} \quad (23)$$

We further simplify it into a general form:

$$g(X_j) = a(X_j - b)^2 + \text{const.} \quad (24)$$

where $a > 0$, $b > 0$, and $X_j^t \in (0, C]$. It is clear that $X_j = b$ minimizes the quadratic function. If $b \leq C$, we change nothing. If $b > C$, then it is easy to obtain that $g(X_j^t) \geq g(C)$ because $g'(X_j) = 2a(X_j - b) < 0$ on the open interval (X_j^t, b) such that $g(X_j)$ strictly monotonously decreases on that open interval. Thus, the proof is established.

In fact, we know that $X = \min\{X, +\infty\}$; therefore, we may provide a generic solution to (2), which is the main result of this paper.

Algorithm 2. Start from an initial point $X^0 > 0$; then,

- (1) update X by (21);
- (2) truncate X by (22).

It is easy to generalize the constraints from $0 \leq X \leq C$ to $C_1 \leq X \leq C_2$ by the transformation $\xi = X - C_1$, which is left for readers to complete by themselves.

3. Convergence

The convergence proof with box constraints is very difficult; thus, we only focus on the below-bounded constraints, which can be viewed as a special case of box constraints with $C = +\infty$. Additionally, we consider the equivalence between the general below-constrained form and the nonnegative constrained one by a linear transformation $\xi = X - C_1$; then, we will theoretically prove the global convergence of the latter case for simplification, which is easy to extend to that of the former. In theory, the Kuhn-Tucker (KT) point will be a global solution if the cost function is convex. It is easy to see the convexity of $F(X)$. By Theorem 2.19 in [12], the KT conditions of (3) ($X \geq 0$) are as follows:

$$\frac{\partial F(X)}{\partial X_j} = 0 \quad \text{if } X_j > 0, \quad (25)$$

$$\frac{\partial F(X)}{\partial X_j} \geq 0 \quad \text{if } X_j = 0. \quad (26)$$

We entertain several important and reasonable assumptions.

Assumption 3. For the iteration sequence $\{X^t\}$, we assume that

- (1) the algorithm starts from a positive image;
- (2) $(A^T A)_{jj} > 0$ for all j ;
- (3) F is a strictly convex function.

The first assumption forces the iterations to be positive, but the limit may be zero. The second condition is reasonable because $(A^T A)_{jj} = 0$ suggests $A_{ij} = 0$ for any i . Thus, the equation $Y = AX$ is irrelevant to X_j , and, then, X_j in X is removable. The third one is indeed restrictive; however, it is important for the following derivation.

We will prove the global convergence along the lines of [13–17]. First, we provide several useful lemmas.

Lemma 4. *The set of accumulation points of a bounded sequence $\{Z^t\}$ with $\{\|Z^{t+1} - Z^t\|\} \rightarrow 0$ is connected and compact.*

Proof. This is Theorem 28.1 from Ostrowski [18]. The reader is kindly referred to this paper for the proof. \square

Lemma 5. *The iteration sequence $\{X^t\}$ is bounded.*

Proof. Because F is a strictly convex function, $A^T A$ is a positive definite symmetric matrix, and, thus, it can be factorized into $A^T A = U^T U$ by Cholesky's method, where U is an invertible matrix. We assume that X^* is the sole minimum, and, then, we expand F on X^* using a Taylor series:

$$F(X) - F(X^*) = (X - X^*)^T (A^T A) (X - X^*) = (X - X^*)^T U^T U (X - X^*) \geq 0. \quad (27)$$

Let $\xi = U(X - X^*)$; then, for any constant L , it is easy to know the boundedness of $S = \{\xi : \xi^T \xi < L\}$ such that $\{X : X = U^{-1}\xi + X^*, \xi \in S\}$ is bounded, which is equivalent to $\{X : F(X) - F(X^*) < L\}$ being bounded. Let $L_0 = F(X^0) - F(X^*)$; then, $\{X^t\} \subset \{X : F(X) - F(X^*) < L_0\}$ because $\{F(X^t)\}$ monotonically decreases. Therefore, $\{X^t\}$ is bounded. \square

Lemma 6. *The sequence $\{\|X^t - X^{t+1}\|\} \rightarrow 0$.*

Proof. Take into account that

$$\begin{aligned} \nabla_{jj}^2 f(X | X^t) &= \frac{2}{w_1 X_j^t} \left[(A^+)^T (A^+ X^t + Y^+) \right]_j \\ &\quad + \frac{2}{w_2 X_j^t} \left[(A^-)^T (A^- X^t + Y^-) \right]_j \\ &\geq \frac{2}{w_1 X_j^t} \left[(A^+)^T A^+ X^t \right]_j \\ &\quad + \frac{2}{w_2 X_j^t} \left[(A^-)^T A^- X^t \right]_j \end{aligned}$$

$$\begin{aligned}
 &\geq \frac{2}{w_1} \sum_{i=1}^M (A_{ij}^+)^2 + \frac{2}{w_2} \sum_{i=1}^M (A_{ij}^-)^2 = \gamma_j \\
 &> 0 \\
 &\text{(see the second one of Assumption 3)}.
 \end{aligned} \tag{28}$$

Let $\gamma = \min_j \{\gamma_j\}$. Because $\nabla f(X^{t+1} | X^t) = 0$,

$$\begin{aligned}
 F(X^t) - F(X^{t+1}) &\geq f(X^t | X^t) - f(X^{t+1} | X^t) \\
 &= \frac{1}{2} (X^t - X^{t+1})^T \nabla^2 f(X^{t+1} | X^t) (X^t - X^{t+1}) \\
 &\geq \frac{\gamma}{2} \|X^t - X^{t+1}\|^2.
 \end{aligned} \tag{29}$$

Because $\{F(X^t)\}$ monotonically decreases and is bounded from below, $\{F(X^t) - F(X^{t+1})\} \rightarrow 0$; therefore, $\{\|X^t - X^{t+1}\|\} \rightarrow 0$. \square

Lemma 7. *If a subsequence $\{X^{t_s}\} \rightarrow X^*$, then $\{X^{t_s+1}\} \rightarrow X^*$ as well.*

Proof. By contradiction, if $\{X^{t_s+1}\}$ diverges, then it must have a convergent subsequence $\{X^{t_{ss}+1}\} \rightarrow X^{**} \neq X^*$ because of the boundness by Lemma 5. Let $\epsilon_0 = \|X^* - X^{**}\| > 0$, and if we consider the two convergent subsequences $\{X^{t_{ss}}\}$ and $\{X^{t_{ss}+1}\}$, then there must be a positive integer \mathcal{T} to make $\|X^{t_{ss}} - X^*\| < \epsilon_0/4$ and $\|X^{t_{ss}+1} - X^{**}\| < \epsilon_0/4$ when $t_{ss} > \mathcal{T}$. By the triangle inequality, we can obtain the contradictive result to $\{\|X^t - X^{t+1}\|\} \rightarrow 0$ as

$$\begin{aligned}
 &\|X^{t_{ss}} - X^{t_{ss}+1}\| + \|X^{t_{ss}} - X^*\| + \|X^{t_{ss}+1} - X^{**}\| \\
 &\geq \|X^* - X^{**}\| \implies \|X^{t_{ss}} - X^{t_{ss}+1}\| > \frac{\epsilon_0}{2}.
 \end{aligned} \tag{30}$$

\square

Lemma 8. *At each iteration, one knows that*

$$\begin{aligned}
 X_j^{t+1} &= X_j^t - \alpha_j [\nabla F(X^t)]_j, \\
 \alpha_j &= \frac{w_1 w_2 X_j^t}{2 [w_2 [(A^+)^T (A^+ X^t + Y^+)]_j + w_1 [(A^-)^T (A^- X^t + Y^-)]_j].}
 \end{aligned} \tag{31}$$

Proof. We consider that

$$\begin{aligned}
 \nabla F(X^t) &= 2(A^+ - A^-)^T [(A^+ X^t + Y^+) \\
 &\quad - (A^- X^t + Y^-)] = 2(A^+)^T (A^+ X^t + Y^+) \\
 &\quad + 2(A^-)^T (A^- X^t + Y^-) - 2(A^+)^T (A^- X^t + Y^-) \\
 &\quad - 2(A^-)^T (A^+ X^t + Y^+) = \frac{2}{w_1} [(A^+)^T \\
 &\quad \cdot (A^+ X^t + Y^+)] + \frac{2}{w_2} [(A^-)^T (A^- X^t + Y^-)]
 \end{aligned}$$

$$\begin{aligned}
 &- 2(A^+)^T \left[\left(\frac{1}{w_1} - 1 \right) (A^+ X^t + Y^+) \right. \\
 &\quad \left. + (A^- X^t + Y^-) \right] - 2(A^-)^T \left[(A^+ X^t + Y^+) \right. \\
 &\quad \left. + \left(\frac{1}{w_2} - 1 \right) (A^- X^t + Y^-) \right] \\
 &= \frac{2}{w_1 w_2} \left\{ w_2 [(A^+)^T (A^+ X^t + Y^+)] \right. \\
 &\quad \left. + w_1 [(A^-)^T (A^- X^t + Y^-)] \right\} \\
 &\quad - \frac{2}{w_1 w_2} \left\{ (w_2 A^+ + w_1 A^-)^T \right. \\
 &\quad \left. \cdot [w_2 (A^+ X^t + Y^+) + w_1 (A^- X^t + Y^-)] \right\}
 \end{aligned} \tag{32}$$

$$= \nabla f(X^t | X^t) \quad (\text{compare (32) with (20)}). \tag{33}$$

It is easy to verify the correctness of (31) if replacing $\nabla F(X^t)$ by (32). \square

The global convergence will be proven from the three theorems below.

Theorem 9. *Let $\{X^{t_s}\} \rightarrow X^*$ be any convergent subsequence; then, X^* meets the first KT condition (25).*

Proof. When $X_j^* > 0$, it is easy to obtain that $[\nabla F(X^*)]_j = [\nabla f(X^* | X^*)]_j$ by (33). In addition, $\partial F(X | X^{t_s}) / \partial X_j |_{X^{t_s+1}} = 0$ and $\{X^{t_s}\} \rightarrow X^*$ such that $\{X^{t_s+1}\} \rightarrow X^*$ (Lemma 7); thus,

$$\left. \frac{\partial F(X | X^*)}{\partial X_j} \right|_{X^*} = \lim_{t_s \rightarrow +\infty} \left. \frac{\partial F(X | X^{t_s})}{\partial X_j} \right|_{X^{t_s+1}} = 0. \tag{34}$$

\square

Theorem 10. *The entire sequence $\{X^t\}$ converges.*

Proof. According to Lemmas 4, 5, and 6, the set of accumulation points of $\{X^t\}$ is connected and compact. If we can prove that the number of accumulation points is finite, then the desired result follows because a finite set can be connected only if it consists of a single point [16].

To prove the existence of a finite number of accumulation points, we consider any accumulation point X^* . Given an integer set $\Omega = \{1, 2, \dots, \mathcal{T}\}$, where \mathcal{T} is the total number of components of X , $\Omega^* = \{j : X_j^* = 0\}$ is a subset of Ω . Let F_{Ω^*} be the restrictions of F to the set $\{X : X_j = 0, j \in \Omega^*\}$, which is a strictly convex function of the reduced variables. It follows that F_{Ω^*} has a unique minimum (Theorem 9: $\partial F(X^*) / \partial X_j = 0$ if $X_j^* > 0$). This means that an accumulation point must correspond to a subset of Ω . The number of subsets of Ω is finite, and, thus, the number of accumulation points is also finite. \square

In Theorem 9, we prove that every accumulation point meets the first KT condition, by which the full sequence convergence is provided in Theorem 10. Naturally, the limit of $\{X^t\}$ satisfies the first KT condition. In the following, we will show that the second KT condition is satisfied.

Theorem 11. *The limit X^* of $\{X^t\}$ satisfies the second KT condition (26).*

Proof. When $X_j^* = 0$, by contradiction, we assume that there is an $X_j^* = 0$ that satisfies $[\nabla F(X^*)]_j < 0$. Because $\{X^t\} \rightarrow X^*$, there exists an $\epsilon < 0$ and a positive integer \mathcal{T} such that $[\nabla F(X^t)]_j < \epsilon$ for $t > \mathcal{T}$; then,

$$X_j^{t+1} - X_j^t = -\alpha_j [\nabla F(X^t)]_j > -\alpha_j \epsilon > 0 \quad (35)$$

(by Lemma 8).

Thus, we can obtain that $X_j^{t+1} > X_j^t$, which is a contradiction to $\{X_j^t\} \rightarrow 0$. \square

4. Solutions to Some Existing and New Examples

4.1. NMF. NMF has been widely used in pattern recognition, machine learning, and data mining. It decomposes the non-negative matrix Y by the product of two other nonnegative matrices A and X . Lee and Seung [1] have proposed using the square of the Euclidean distance to measure the similarity between Y and AX :

$$\min_{A \geq 0, X \geq 0} F(A, X) = \|Y - AX\|^2. \quad (36)$$

Minimizing them under the constraints $A \geq 0$ and $X \geq 0$, Lee and Seung [1] alternated between solving an optimization problem in the variables A and then solving another one in the variables X . As can be seen, A and X have the same roles.

To take X , for instance, with $X^t > 0$ and $A > 0$ given, denote $\lambda_{ijk} = A_{ik}^t X_{kj}^t / (AX^t)_{ij}$ such that the surrogate function can be constructed:

$$f(X | X^t) = \sum_{ijk} \left[\lambda_{ijk} \left(\frac{A_{ik} X_{kj}}{\lambda_{ijk}} - Y_{ij} \right)^2 \right]. \quad (37)$$

The update rule can be obtained by solving $\partial f(X, X^t) / \partial X_{kj} = 0$. Reversing the roles of A and X , we can similarly construct the surrogate for A and acquire the update rule:

$$X_{kj}^{t+1} = X_{kj}^t \frac{(A^T Y)_{kj}}{(A^T A X^t)_{kj}}, \quad (38)$$

$$A_{ik}^{t+1} = A_{ik}^t \frac{(Y X^T)_{ik}}{(A^T X X^T)_{ik}}.$$

4.2. Variation of Linearized SVM. SVM attempts to separate points belonging to two given sets in real Euclidean space

R^n by a surface. Several practical applications of SVMs use nonlinear kernels, such as the polynomial and radial basis function kernels. However, in applications such as text classification, linear SVMs are still used because it has been observed that many text classification problems are linearly separable [19]. Most literature on large-scale SVM training have targeted the linear SVM problem, citing this fact. A dual form of linear SVM is usually used because of the simple structure, which can be formulated as [20]

$$\begin{aligned} \min \quad & \frac{1}{2} X^T D A^T A D X - 1^T X \\ \text{s.t.} \quad & 0 \leq X \leq C, \\ & D^T X = 0, \end{aligned} \quad (39)$$

where A is the input data, D is the class label, C is the penalty parameter, and X represents the Lagrangian multiplier that needs to be optimized. Hsieh et al. [21] handled the constraint $D^T X = 0$ by removing it, which corresponded to removing the ‘‘intercept’’ from the classifier. For a simplified expression, we denote $B = AD$, and, then, we obtain the following simple formula:

$$\begin{aligned} \min \quad & \frac{1}{2} X^T B^T B X - 1^T X \\ \text{s.t.} \quad & 0 \leq X \leq C. \end{aligned} \quad (40)$$

We can solve this optimization problem using the proposed method. Let $w_1 = w_2 = 1/2$ and $B = B^+ - B^-$, where B^+ and B^- are two nonnegative matrices; then,

$$f_{\text{mid}}(X | X^t) = \bar{f}(X | X^t) + \hat{f}(X | X^t) - 1^T X, \quad (41)$$

where

$$\begin{aligned} \bar{f}(X | X^t) &= \frac{1}{4} \|2B^+ X - B^+ X^t - B^- X^t\|^2, \\ \hat{f}(X | X^t) &= \frac{1}{4} \|2B^- X - B^+ X^t - B^- X^t\|^2. \end{aligned} \quad (42)$$

We, respectively, construct surrogates for $\bar{f}(X | X^t)$ and $\hat{f}(X | X^t)$. Let

$$\begin{aligned} \lambda_{ij}^+ &= \frac{B_{ij}^+ X_j^t}{(B^+ X^t)_i}, \\ \lambda_{ij}^- &= \frac{B_{ij}^- X_j^t}{(B^- X^t)_i} \end{aligned} \quad (43)$$

then,

$$\begin{aligned} \bar{f}(X | X^t) &= \frac{1}{4} \sum_{i=1}^M \sum_{j=1}^N \lambda_{ij}^+ \left[2 \frac{B_{ij}^+ X_j}{\lambda_{ij}^+} - (B^+ X^t + B^- X^t)_i \right]^2, \\ \hat{f}(X | X^t) &= \frac{1}{4} \sum_{i=1}^M \sum_{j=1}^N \lambda_{ij}^- \left[2 \frac{B_{ij}^- X_j}{\lambda_{ij}^-} - (B^+ X^t + B^- X^t)_i \right]^2. \end{aligned} \quad (44)$$

We now obtain a surrogate for $F(X)$ at X^t :

$$f(X | X^t) = \bar{f}(X | X^t) + \hat{f}(X | X^t). \quad (45)$$

We solve the one-dimensional equation $\partial f(X | X^t) / \partial X_j = 0$ and truncate it to obtain an update:

$$X_j^{t+1} = X_j^t \frac{1 + \left[(B^+ + B^-)^T (B^+ + B^-) X^t \right]_j}{2 \left\{ \left[(B^+)^T B^+ + (B^-)^T B^- \right] X^t \right\}_j}, \quad (46)$$

$$X_j^{t+1} = \min \{ X_j^{t+1}, C \}.$$

4.3. Nonnegative Image Deblurring. In many optical devices, the process of image blurring can be considered to be the result of convolution by a point spread function (PSF) [22, 23]. It is assumed that the degraded image Y is in the form $Y = AX$, where X is the true image and A is the PSF matrix consisting of PSFs at every pixel. As noted in [24, 25], a simple way to approach the deconvolution problem is to find the least squares (LS) estimation between Y and AX . It is well known that the problem of restoring the original image from the noisy and degraded version is an ill-posed inverse problem: small perturbations in the data may result in an unacceptable result [26]. The Tikhonov regularization method [27, 28] is a popular method that generally leads to a unique solution, which is formulated as

$$\min_{X \geq 0} F(X) = \|AX - Y\|^2 + \beta \|RX\|^2. \quad (47)$$

Note that we must approve negative values existing in the matrix R .

In [17], we assume that A and Y are a nonnegative matrix and vector and that there is no restriction on R ; then, we, respectively, construct surrogate functions for $\|AX - Y\|^2$ and $\|RX\|^2$ using the method proposed in this paper such that we obtain a multiplicative update rule as follows:

$$\begin{aligned} X_j^{t+1} &= X_j^t \frac{(A^T Y)_j + \beta \left[(R^+ + R^-)^T (R^+ + R^-) X^t \right]_j}{(A^T A X^t)_j + 2\beta \left[((R^+)^T R^+ + (R^-)^T R^-) X^t \right]_j}. \end{aligned} \quad (48)$$

If $\beta = 0$, it is De Pierro's ISRT (Image Space Reconstruction Technique) [4]:

$$X_j^{t+1} = X_j^t \frac{(A^T Y)_j}{(A^T A X^t)_j}. \quad (49)$$

4.4. CT Reconstruction with L_1 Regularization. In CT reconstruction, let A be the system probability matrix, Y projections, and R a predetermined matrix. Then, a classical approach is to choose an X (X -ray attenuation image) such that the LS error [5] between Y and AX is minimized:

$$\min_{X \geq 0} F(X) = \|AX - Y\|^2 + \beta \|RX\|_1, \quad (50)$$

where $\beta \geq 0$ serves as a penalty parameter. Many R matrices have been used, such as the first- or second-order derivative matrix or wavelet basis matrix. Note that both A and Y are a nonnegative matrix and vector; however, we must accept negative values existing in the matrix R .

The alternating direction method of multipliers (ADMM) [29, 30] has been developed for solving optimization problems. This method decomposes the original problem into three subproblems and then sequentially solves them at each iteration.

Introducing the additional variable $V = RX$, a fixed penalty parameter ρ , and the Lagrangian multiplier μ , a unified framework can then be given to solve the L_1 -norm regularized LS reconstruction problem [29].

Algorithm 12 (ADMM general framework). (1) $V_i^{t+1} = (|(RX^t + \mu^t)_i| - \beta/\rho)_+ \text{sgn}[(RX^t + \mu^t)_i]$, $i = 1, \dots, M$.
 (2) $X^{t+1} = \arg \min_{X \geq 0} L(X, V^{t+1}, \mu^t) = \|AX - Y\|^2 + (\rho/2) \|RX - V^{t+1} + \mu^t\|_2^2$.
 (3) $\mu^{t+1} = \mu^t + RX^{t+1} - V^{t+1}$.

The X -update is the most difficult problem that minimizes $L(X, V^{t+1}, \mu^t)$ with nonnegativity constraints. We can, respectively, construct surrogate functions for $\|AX - Y\|^2$ and $\|RX - V^{t+1} + \mu^t\|_2^2$, then minimize the sum of the surrogates to update X ; however, there is a high overlap ratio with the above, so we leave them to the readers.

5. Experimental Results

We compare the performance of the proposed surrogate method, with those of the PL method (6) and the CG method on simulated data and CT projection data. For the PL method, we use $\alpha = 1/(\|A\|_1 \|A\|_\infty)$ [31], where $\|\cdot\|_1$ and $\|\cdot\|_\infty$ denote the 1- and ∞ -norm of a matrix. The code for the CG method comes from [32], which is slightly modified to meet our criteria.

The experiments are performed on a HP Compaq PC with a 3.00 GHz Core i5 CPU and 4 GB memory. The algorithms are implemented in MATLAB 7.0. All of the algorithms are initiated by the same uniform image for a fair comparison.

TABLE 1: Performance comparison of the three algorithms.

Iteration		1	50	150	200	250	300
MSE	Proposed	0.2860	0.2226	0.1961	0.1822	0.1737	0.1682
	CG	0.3441	0.2240	0.3183	0.3183	0.3183	0.3183
	PL	0.3441	0.2398	0.2136	0.2033	0.1978	0.1943
χ	Proposed	0.0031	0.0016	0.0009	0.0006	0.0004	0.0003
	CG	1.0000	0.0001	0	0	0	0
	PL	1.0000	0.0117	0.0037	0.0018	0.0010	0.0007

TABLE 2: Total running time of the three algorithms with 300 iterations and 50 random start points.

Algorithm	Proposed	CG	PL
Time (second)	2.22	2.13	1.95

The mean square error (MSE) is used to measure the similarity to the true solution, as given below:

$$\text{MSE}(t) = \frac{1}{N} \|X^t - X^{\text{True}}\|^2. \quad (51)$$

The following criterion is applied to stop the iterative process:

$$\chi(t) = \frac{\|X^{t+1} - X^t\|}{\|X^t\|} < \epsilon, \quad (52)$$

where ϵ is a difference tolerance.

5.1. Numerical Simulation. Here, we randomly generate $X \in R^{500}$ and $A \in R^{100 \times 500}$, where the former are uniformly distributed on $[0 \ 1]$ and the latter are on $[-1 \ 1]$. Then we obtain Y by $Y = AX$. We will minimize $F(X) = \|Y - AX\|^2$ under the box constraints $0 \leq X \leq 1$. In the experiment, we generate X, Y , and A once, but we randomly generate start points (uniformly distributed on $[0 \ 1]$) 50 times to obtain a reliable averaged result.

Figure 1 presents a comparison of MSE and χ versus iteration number. As shown, CG rapidly finishes iteration to a static solution, so that $\chi(t) = 0$ after that, which can not be shown with a log-scaled y -axis. However, such a phenomenon does not mean a good result. Instead, it is the worst result among the three algorithms by observing the MSE curve. We can conclude that CG is not suitable to the box-constrained LS problem. PL and the proposed method always decrease the curves of MSE and χ . However, the proposed method shows a superior performance than the PL method.

Table 1 shows the quantitative comparison of the three algorithms; then we can draw the same conclusion as above. This table further proves that the proposed method is rapid and stable, and CG is not suitable to the box-constrained LS problem.

Table 2 shows the computational time of the algorithms. As can be seen, they have similar computational complexity;

however, the proposed algorithm requires only a little more time because of the nonnegative decomposition of Y and A . In fact, from the above theoretical analysis, we can observe that the proposed algorithm is also some gradient-based method; thus, it has a similar computational complexity with the CG and PL methods.

5.2. CT Reconstruction. CT reconstruction is a medical imaging technique for creating a meaningful diagnostic image. A computer can take the input from the CT machine, run it through the formula, and return a set of images for a physician to examine. Here, we only consider the simplest mathematical model $\min_{X \geq 0} \|Y - AX\|^2$ to pursue the structural image. A simulated thorax phantom with 128×128 grids and 0.5 mm pixels, as shown in Figure 2, is used in the following experiments. There are many advantages to using simulated phantoms, including prior knowledge of the pixel values and the ability to control noise. The total attenuation value is approximately 5×10^7 . For this case, the proposed algorithm is called ISRT, which is widely used in the field of CT reconstruction [4].

The system matrix is obtained using the ‘‘angle of view’’ method [10]. From the system matrix, we forward project the phantom on the sinogram with 128 radial bins (bin size of 0.5 mm) and 128 angular views evenly spaced over π . The noisy projections are obtained by the Poisson-random formula $y_i = \text{Poisson}(y_i^*)$, where y_i^* is the noise-free projection.

Figure 3 shows the reconstructions with 50 iterations for every algorithm. As shown, the CG’s image suffers from serious noise artifacts. The PL algorithm provides a reconstructed image that is slightly blurred compared with that of ISRT. The proposed ISRT provides the sharpest edge and clearest interior region.

Figure 4 quantitatively compares the histograms of the reconstructed images. The CG’s result still shows a clear turbulence around the true value. PL and ISRT provide two comparable curves, and neither is significantly better than the other.

We also present a comparison of the MSE curves and χ with increasing iteration number in Figure 5. As shown, CG exhibits an unsteady reconstruction property in which more iterations may lead to a worse result. Both PL and ISRT overcome this shortcoming so that more iterations always provide considerably better results. In addition, ISRT will provide a more rapid convergence than PL.

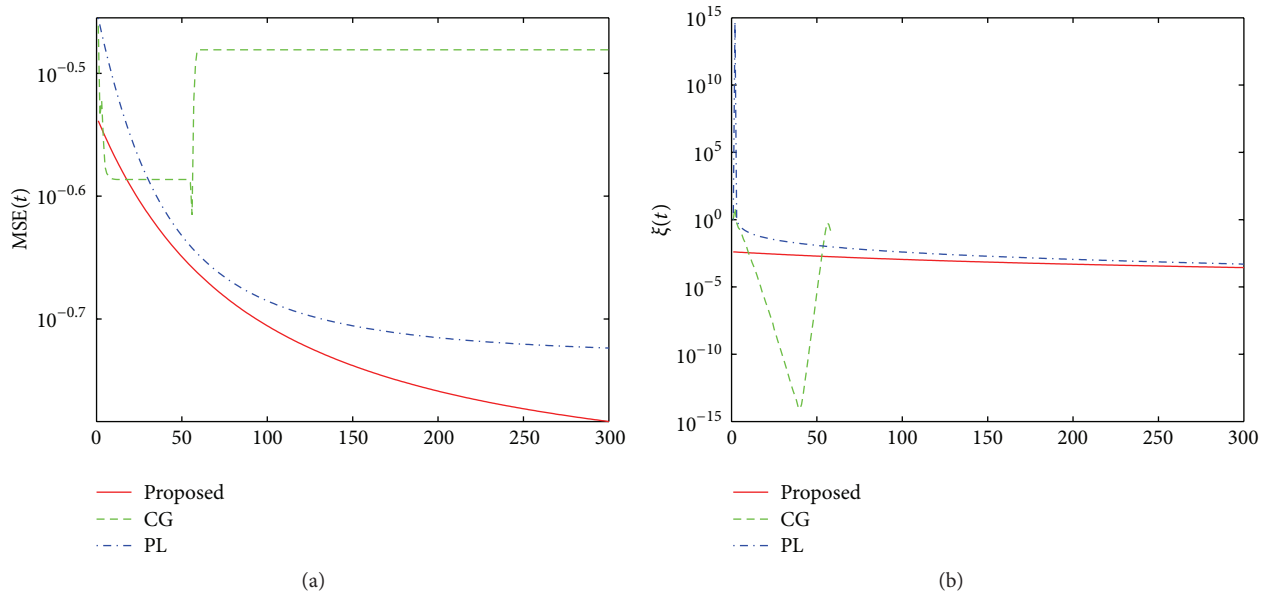


FIGURE 1: Simulated data: MSE and χ versus iteration number: (a) MSE and (b) χ .

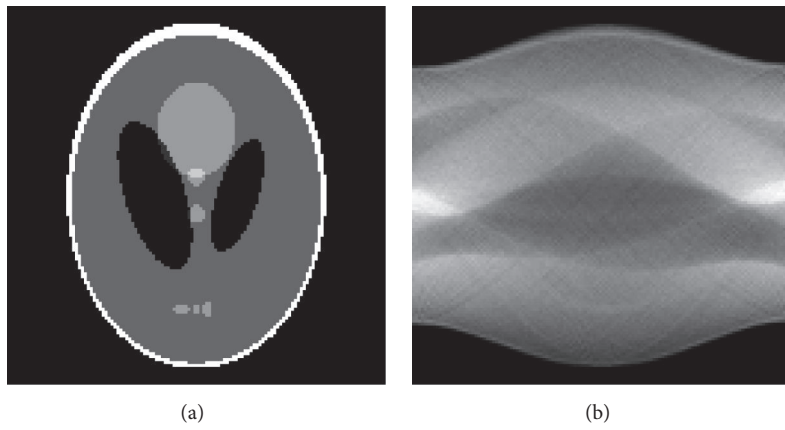


FIGURE 2: Shepp-Logan phantom with 128×128 grids: (a) true phantom and (b) noisy projections.

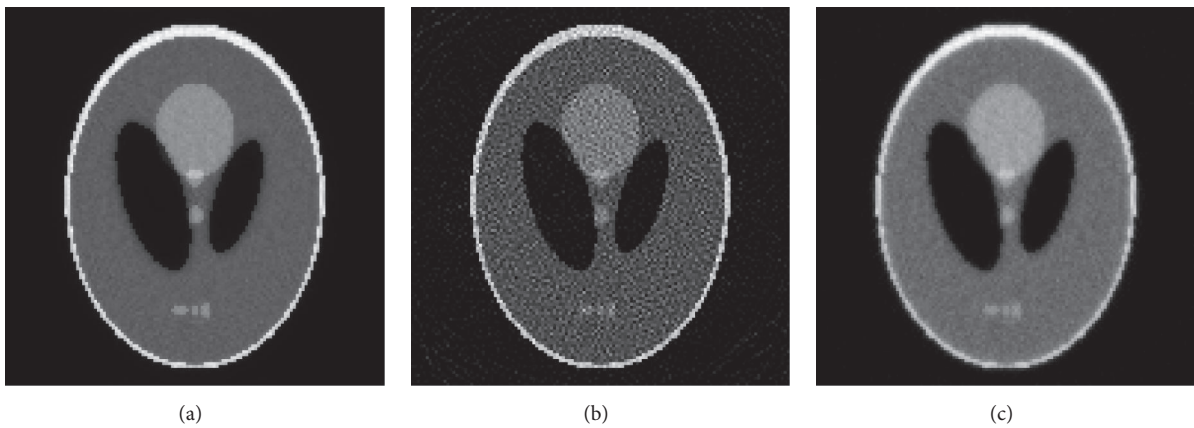


FIGURE 3: Reconstructed images with 50 iterations by (a) the proposed ISRT, (b) CG, and (c) PL.

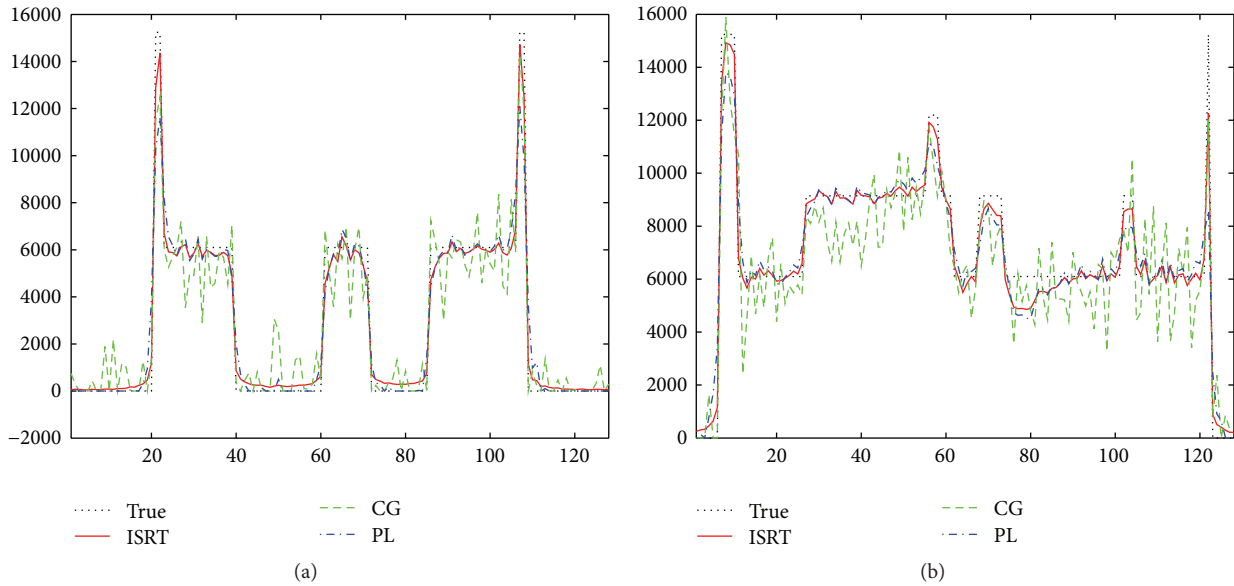


FIGURE 4: Intensity of the true and reconstructed images: (a) horizontal central line and (b) vertical central line.

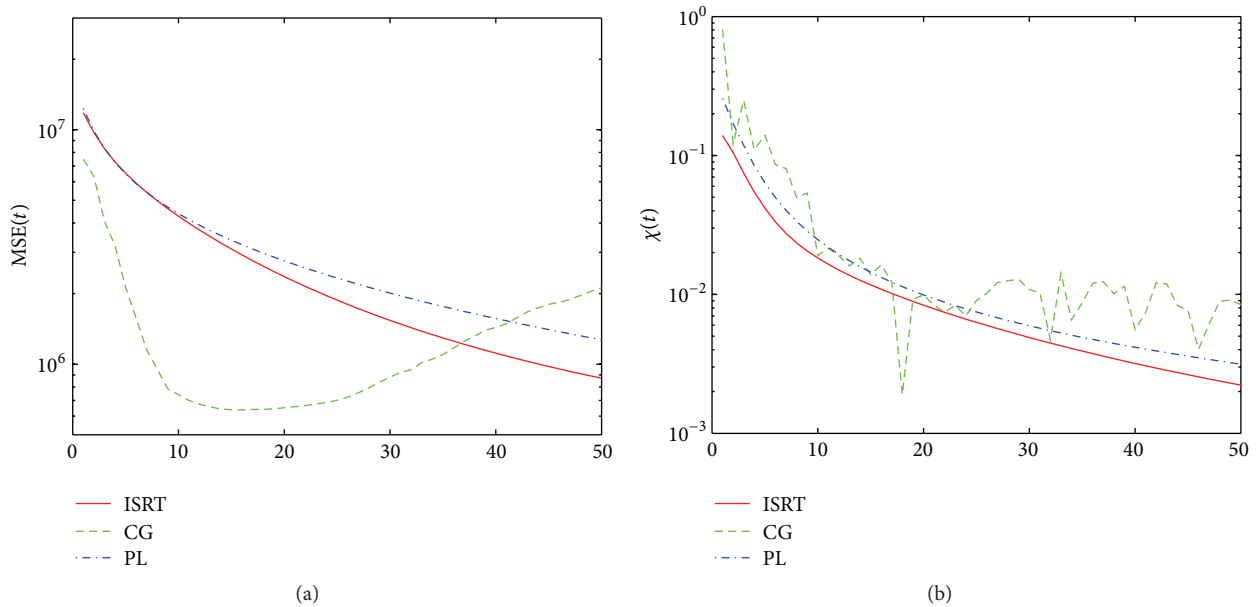


FIGURE 5: MSE and χ versus iteration number: (a) MSE and (b) χ .

6. Conclusion

We present a special application of a surrogate-based method for solving box-constrained LS problems. A new update rule is developed to iteratively update variables, and this rule exhibits desirable properties, including monotonic decrease of the cost function, self-constraining in the feasible region, and no need to impose a step size. This algorithm covers many existing algorithms, as well as new ones, as the special examples. Targeting the special case of only below-bounded constraints, we provide a rigorous theoretical global convergence proof. We use the simulated data to evaluate

the performance of the algorithm, demonstrating that the proposed algorithm provides a stabler and faster convergence than the PL and CG approaches.

In this paper, we only provide a global convergence proof for the below-bounded case, not the box-constrained case; thus, proving the convergence for the latter case will be the focus of future work.

Competing Interests

The authors declare that they have no competing interests.

Acknowledgments

This work was supported by the National Natural Science Foundations of China (61302013 and 61372014), Science and Technology Plan of Liaoning Province of China (2014305001), and Fundamental Research Funds for the Central Universities of China (N130219001 and N141008001).

References

- [1] D. D. Lee and H. S. Seung, "Algorithms for non-negative matrix factorization," in *Proceedings of the Advances in Neural Information Processing Systems 13 (NIPS '00)*, pp. 556–562, Breckenridge, Colo, USA, 2000.
- [2] Y. Lin and D. D. Lee, "Bayesian regularization and nonnegative deconvolution for room impulse response estimation," *IEEE Transactions on Signal Processing*, vol. 54, no. 3, pp. 839–847, 2006.
- [3] O. L. Mangasarian and D. R. Musicant, "Lagrangian support vector machines," *Journal of Machine Learning Research*, vol. 1, no. 3, pp. 161–177, 2001.
- [4] A. R. De Pierro, "On the relation between the ISRA and the EM algorithm for positron emission tomography," *IEEE Transactions on Medical Imaging*, vol. 12, no. 2, pp. 328–333, 1993.
- [5] J. A. Fessler, "Penalized weighted least-squares image reconstruction for positron emission tomography," *IEEE Transactions on Medical Imaging*, vol. 13, no. 2, pp. 290–300, 1994.
- [6] M. Piana and M. Bertero, "Projected Landweber method and preconditioning," *Inverse Problems*, vol. 13, no. 2, pp. 441–463, 1997.
- [7] H. Lantéri, M. Roche, O. Cuevas, and C. Aime, "A general method to devise maximum-likelihood signal restoration multiplicative algorithms with non-negativity constraints," *Signal Processing*, vol. 81, no. 5, pp. 945–974, 2001.
- [8] H. Lanteri, M. Roche, and C. Aime, "Penalized maximum likelihood image restoration with positivity constraints: multiplicative algorithms," *Inverse Problems*, vol. 18, no. 5, pp. 1397–1419, 2002.
- [9] K. Lange, D. R. Hunter, and I. Yang, "Optimization transfer using surrogate objective functions," *Journal of Computational and Graphical Statistics*, vol. 9, no. 1, pp. 1–20, 2000.
- [10] L. A. Shepp and Y. Vardi, "Maximum likelihood reconstruction for emission tomography," *IEEE Transactions on Medical Imaging*, vol. 1, no. 2, pp. 113–122, 1982.
- [11] A. Cichocki, H. Lee, Y.-D. Kim, and S. Choi, "Non-negative matrix factorization with α -divergence," *Pattern Recognition Letters*, vol. 29, no. 9, pp. 1433–1440, 2008.
- [12] W. I. Zangwill, *Nonlinear Programming: A Unified Approach*, Prentice-Hall, New York, NY, USA, 1969.
- [13] A. R. De Pierro, "A modified expectation maximization algorithm for penalized likelihood estimation in emission tomography," *IEEE Transactions on Medical Imaging*, vol. 14, no. 1, pp. 132–137, 1995.
- [14] A. R. De Pierro, "On the convergence of an EM-type algorithm for penalized likelihood estimation in emission tomography," *IEEE Transactions on Medical Imaging*, vol. 14, pp. 762–765, 1995.
- [15] C. F. J. Wu, "On the convergence properties of the EM algorithm," *The Annals of Statistics*, vol. 11, no. 1, pp. 95–103, 1983.
- [16] K. Lange and R. Carson, "EM reconstruction algorithms for emission and transmission tomography," *Journal of Computer Assisted Tomography*, vol. 8, no. 2, pp. 306–316, 1984.
- [17] Y. Teng, Y. Zhang, H. Li, and Y. Kang, "A convergent non-negative deconvolution algorithm with Tikhonov regularization," *Inverse Problems*, vol. 31, no. 3, Article ID 035002, 2015.
- [18] A. M. Ostrowski, *Solution of Equations in Euclidean and Banach Spaces*, Academic Press, New York, NY, USA, 1973.
- [19] B. Scholkopf, C. Burges, and A. Smola, "Making large-scale SVM learning practical," in *Advances in Kernel Methods*, pp. 169–184, MIT Press, Cambridge, Mass, USA, 1998.
- [20] J. C. Platt, "Fast training of support vector machines using sequential minimal optimization," in *Advances in Kernel Methods Support Vector Learning*, B. Schölkopf, C. J. C. Burges, and A. J. Smola, Eds., pp. 185–208, MIT Press, Cambridge, Mass, USA, 1999.
- [21] C.-J. Hsieh, K.-W. Chang, C.-J. Lin, S. S. Keerthi, and S. Sundararajan, "A dual coordinate descent method for large-scale linear SVM," in *Proceedings of the 25th International Conference on Machine Learning (ICML '08)*, pp. 408–415, Helsinki, Finland, July 2008.
- [22] H. Andrews and B. Hunt, *Digital Image Restoration*, Prentice-Hall, Englewood Cliffs, NJ, USA, 1977.
- [23] M. Bertero and P. Boccacci, *Introduction to Inverse Problems in Imaging*, IOP Publishing, London, UK, 1998.
- [24] S. Walrand, F. Jamar, and S. Pauwels, "Improved solution for ill-posed linear systems using a constrained optimization ruled by a penalty: evaluation in nuclear medicine tomography," *Inverse Problems*, vol. 25, no. 11, Article ID 115004, 2009.
- [25] A. Beck and M. Teboulle, "A fast iterative shrinkage-thresholding algorithm for linear inverse problems," *SIAM Journal on Imaging Sciences*, vol. 2, no. 1, pp. 183–202, 2009.
- [26] H. Liu, L. Yan, Y. Chang, H. Fang, and T. Zhang, "Spectral deconvolution and feature extraction with robust adaptive Tikhonov regularization," *IEEE Transactions on Instrumentation and Measurement*, vol. 62, no. 2, pp. 315–327, 2013.
- [27] A. N. Tikhonov, A. V. Goncharsky, V. V. Stepanov, and A. G. Yagola, *Numerical Methods for the Solution of Ill-Posed Problems*, Kluwer Academic Publishers, Boston, Mass, USA, 1995.
- [28] A. N. Tikhonov and V. Y. Arsenin, *Solution of Ill-Posed Problems*, Winston & Sons, Washington, DC, USA, 1977.
- [29] S. Boyd, N. Parikh, E. Chu, and J. Eckstein, "Distributed optimization and statistical learning via the alternating direction method of multipliers," *Foundations and Trends in Machine Learning*, vol. 3, no. 1, pp. 1–122, 2011.
- [30] J. F. C. Mota, J. M. F. Xavier, P. M. Q. Aguiar, and M. Püschel, "D-ADMM: a communication-efficient distributed algorithm for separable optimization," *IEEE Transactions on Signal Processing*, vol. 61, no. 10, pp. 2718–2723, 2013.
- [31] G. H. Golub and C. F. Van Loan, *Matrix Computations*, Johns Hopkins University Press, Baltimore, Md, USA, 1996.
- [32] <http://web.stanford.edu/group/SOL/index.html>.

Research Article

A Novel Control Strategy of DFIG Based on the Optimization of Transfer Trajectory at Operation Points in the Islanded Power System

Zengqiang Mi,¹ Liqing Liu,¹ He Yuan,¹ Ping Du,² and Yuliang Wan²

¹State Key Laboratory of Alternate Electrical Power System with Renewable Energy Sources, Baoding 071003, China

²Power Dispatching Control Center, State Grid East Inner Mongolia Electric Power Company Limited, Hohhot 010020, China

Correspondence should be addressed to Liqing Liu; liuliqing328@163.com

Received 16 October 2015; Revised 28 December 2015; Accepted 6 January 2016

Academic Editor: Ivan Kyrchei

Copyright © 2016 Zengqiang Mi et al. This is an open access article distributed under the Creative Commons Attribution License, which permits unrestricted use, distribution, and reproduction in any medium, provided the original work is properly cited.

A novel control strategy based on the optimization of transfer trajectory at operation points for DFIG is proposed. Aim of this control strategy is to reduce the mechanical fatigue of DFIG caused by the frequent adjustment of rotating speed and pitch angle when operating in the islanded power system. Firstly, the stability of DFIG at different operation points is analyzed. Then an optimization model of transfer trajectory at operation points is established, with the minimum synthetic adjustment amount of rotating speed and pitch angle as the objective function and with the balance of active power and the stability of operation points as the constraint conditions. Secondly, the wind speed estimator is designed, and the control strategy of pitch system is improved to cooperate with the indirect stator flux orientation control technology for rotor-side inverter control. Then by the coordination control of its rotating speed and pitch angle, an operation trajectory controller is established to ensure the islanded operation of DFIG along the optimal transfer trajectory. Finally, the simulation results show that the proposed control strategy is technical feasibility with good performance.

1. Introduction

The islanded operation is a significant operation mode of wind turbine, and this can widen the applied range of wind turbine [1]. It can improve the service ability, reduce the cost of power supply, and protect the environment by composing an islanded power system with wind turbine in some remote regions or islands [2, 3]. And for some areas that lack emergency power supply, their economic losses caused by the power grid failure can be reduced when the important local load is supplied by the wind turbine [4, 5]. So it is significant to make an intensive study of the control strategy for wind turbine to operate in the islanded operation mode.

The doubly fed induction generator based wind turbine (DFIG) is currently the most widely used type of unit [6], and some researches about the islanded operation control strategy of DFIG have been carried out at home and abroad. In [7], the battery energy storage system (BESS) is connected in parallel

with the DC link of DFIG inverter, and the hybrid system can operate in different modes and has the ability to supply power for the load independently. The coordinate control strategies of wind turbines and energy storage systems for stabilizing the islanded power system are proposed in [8, 9]. In [10–12], with the droop control strategy introduced, the DFIG can respond to the frequency and voltage changes of the isolated power system and keep its voltage and frequency to be stable, so the DFIG can continue to supply the load around in the case of disconnection from power grid. Through applying the control strategies proposed in [7–12], the DFIG can operate in the islanded mode. However, the strategies only make the DFIG to be similar with a current source essentially, so that a large power source is needed to sustain the voltage of islanded power system. An indirect stator flux orientation (ISFO) control strategy which is suitable for the doubly fed induction generator is proposed in [13, 14]; it can enable the doubly fed induction generator with voltage source characteristics

to control the frequency and amplitude of its stator voltage independently. The DFIG can obtain the ability to supply the load independently with the application of ISFO control strategy [15, 16]. Operating in the islanded mode, the frequent adjustment of rotating speed and pitch angle may produce mechanical fatigue on the DFIG and affect its service life seriously.

In this paper, a control strategy based on the optimization of transfer trajectory at operation points for a stand-alone DFIG is proposed. Through applying this control strategy to coordinately regulate the rotating speed and pitch angle, the DFIG can autonomously operate along the transfer trajectory with the minimum synthetic adjustment amount of rotating speed and pitch angle. This paper is structured as follows. In Section 2, the mathematical model of DFIG is outlined, and the optimization model of transfer trajectory at operation points is established by the stability analysis of operation points. In Section 3, the designed control strategy is described. It mainly contains the wind speed estimator, the control unit of rotor-side converter and variable pitch system, and the operation trajectory controller. Simulation results are given and discussed in Section 4. Finally, conclusions are presented in Section 5.

2. Transfer Trajectory Optimization of DFIG Operation Point

2.1. Mathematical Model of DFIG. The aerodynamic power captured by the turbine is as follows:

$$P_a = \frac{1}{2} \rho \pi R^2 C_p(\lambda, \beta) V_W^3 = T_a \omega_r, \quad (1)$$

where P_a is the aerodynamic power, ρ is the air density, R is the rotor radius, C_p is the aerodynamic power performance coefficient which is the function of tip speed ratio λ and pitch angle β , V_W is the wind speed, T_a is the aerodynamic torque, and ω_r is the rotating speed of the turbine.

The aerodynamic power performance coefficient C_p is calculated according to the following equation:

$$C_p = c_1 \left(c_6 \lambda + \frac{(-c_4 - c_3 a_1 + c_2 a_2)}{\exp(c_5 a_2)} \right),$$

$$\lambda = \frac{\omega_r R}{V_W}, \quad (2)$$

$$a_1 = 2.5 + \beta,$$

$$a_2 = \frac{1}{(\lambda + c_7 a_1)} - \frac{c_8}{(1 + a_1^3)},$$

where c_1 – c_8 are constants related to the aerodynamic characteristics of the wind wheel.

The dynamic behavior of the drive train can be described with a two-mass model [17]:

$$J_t \dot{\omega}_r = T_a - D_m \left(\omega_r - \frac{\omega_g}{n} \right) - K_m \theta,$$

$$J_g \dot{\omega}_g = \frac{1}{n} \left[D_m \left(\omega_r - \frac{\omega_g}{n} \right) + K_m \theta \right] - F_g \omega_g - T_e, \quad (3)$$

$$\dot{\theta} = \omega_r - \frac{\omega_g}{n},$$

where J_t and J_g are the turbine and generator inertia, respectively, D_m is damping coefficient, K_m is the shaft elastic coefficient, F_g is the friction coefficient of generator, T_e is the electromagnetic torque of generator, ω_g is the generator speed, n is the gearbox ratio, and θ is the shaft deformation angle.

The equations of doubly fed induction generator written in a synchronously rotating d - q reference frame are expressed as follows [13]:

$$u_{sd} = R_s i_{sd} + \frac{d\psi_{sd}}{dt} - \omega_1 \psi_{sq},$$

$$u_{sq} = R_s i_{sq} + \frac{d\psi_{sq}}{dt} + \omega_1 \psi_{sd},$$

$$u_{rd} = R_r i_{rd} + \frac{d\psi_{rd}}{dt} - (\omega_1 - \omega_r) \psi_{rq},$$

$$u_{rq} = R_r i_{rq} + \frac{d\psi_{rq}}{dt} + (\omega_1 - \omega_r) \psi_{rd}, \quad (4)$$

$$\psi_{sd} = L_s i_{sd} + L_m i_{rd} = L_m i_{ms},$$

$$\psi_{sq} = L_s i_{sq} + L_m i_{rq},$$

$$\psi_{rd} = L_m i_{sd} + L_r i_{rd},$$

$$\psi_{rq} = L_m i_{sq} + L_r i_{rq},$$

where u_{sd} , u_{sq} , u_{rd} , u_{rq} are the dq components of stator voltage and rotor voltage, respectively, ψ_{sd} , ψ_{sq} , ψ_{rd} , ψ_{rq} are the dq components of stator flux and rotor flux, respectively, i_{sd} , i_{sq} , i_{rd} , i_{rq} are the dq components of stator current and rotor current, respectively, R_s and R_r are the stator resistance and rotor resistance, L_s , L_r , and L_m are the stator inductance, rotor inductance, and the mutual inductance, ω_1 is the synchronous speed, and i_{ms} is the equivalent stator magnetizing current.

2.2. Stability Analysis of DFIG Operation Points. Based on the historical statistics data of wind speed and load in the islanded power system, if the capacity of DFIG is configured reasonably, the DFIG can satisfy the reactive power demand of load. On this basis, the specific active power can be output by adjusting the rotating speed and pitch angle of DFIG. It is

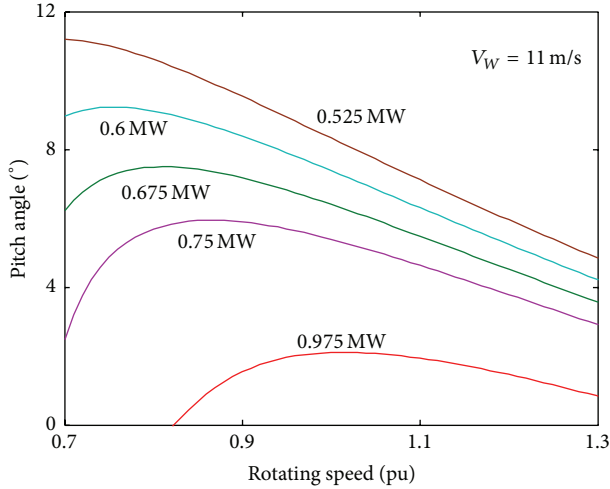


FIGURE 1: The relationship between rotating speed and pitch angle for different aerodynamic power.

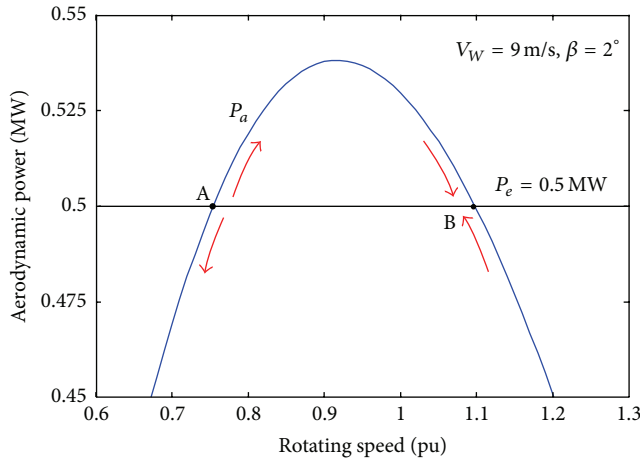


FIGURE 2: The stability analysis of operation points.

known from (1) and (2) that, for a certain wind speed, the aerodynamic power captured by the turbine is a nonlinear function of the rotating speed ω_r and pitch angle β and this is shown in Figure 1.

For specific wind speed and captured aerodynamic power, DFIG can operate with different rotating speeds and pitch angles, namely, different operating points. However, the DFIG is not able to operate at some operation points stably (shown in Figure 1), and the following analysis is made. As shown in Figure 2, when the wind speed is 9 m/s, there are two operation points called A and B where DFIG can absorb 0.5 MW power from the wind. For operation point A,

$$\left. \frac{\partial P_a}{\partial \omega_r} \right|_{(\omega_{r,A}, \beta)} > 0. \quad (5)$$

And for operation point B,

$$\left. \frac{\partial P_a}{\partial \omega_r} \right|_{(\omega_{r,B}, \beta)} \leq 0. \quad (6)$$

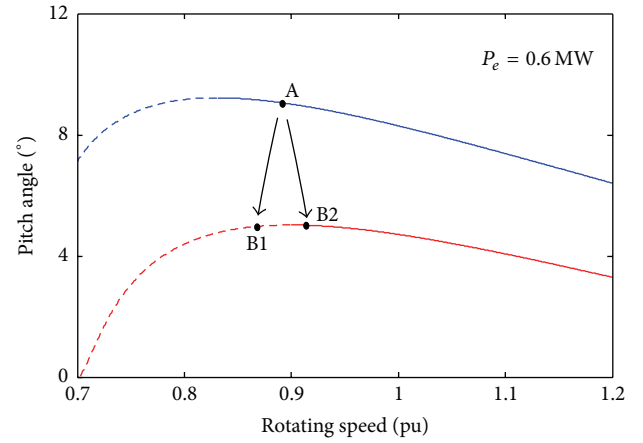


FIGURE 3: The transfer trajectories of operation point for DFIG.

When DFIG operates at point A, the captured aerodynamic power and the rotating speed would rise following the increasing wind speed. As shown in (5), the increasing rotating speed will drive DFIG to capture more aerodynamic power, and then the rotating speed will be further increased, which makes the turbine gradually deviate from operation point A. When the wind turbine operates at point B, the increase of wind speed will also result in the rise of rotating speed. But as shown in (6), the rise of rotating speed would decrease the aerodynamic power absorbed by DFIG, and this may force DFIG to return to operation point B. The operation condition is similar to the one above when wind speed is reduced. Thus operation point A is not the stable one while operation point B is. Through analysis, to ensure that DFIG stably operate at a certain point, (6) is necessary.

2.3. Transfer Trajectory Optimization of DFIG Operation Point. The operation point will be adjusted according to the fluctuation of wind speed and load when DFIG operates in the islanded mode. As shown in Figure 3, the wind speed is 10 m/s at t_0 , and DFIG operates stably at point A with the output power 0.6 MW. The wind speed reduces to 10 m/s at t_1 , so the wind turbine operation point needs to be transferred from point A to another operation point on the red line in order to keep its output power unchanged. The red dotted line is the set of unstable operation points, while the solid line presents the stable ones. The synthetic adjustment amount of rotating speed and pitch angle will be minimized if the operation point is transferred from point A to B1 or B2. But B1 is not the stable one, so transferring operation point to B2 can keep the output power unchanged and minimize the synthetic adjustment of rotating speed and pitch angle.

Therefore the optimization model of transfer trajectory at operation points is established to obtain the optimal transfer trajectory that DFIG operates along, and the objective function of which is the minimum of the synthetic adjustment amount of rotating speed and pitch angle between two adjacent times. The constraint conditions include the balance of active power and the stability of operation points. The model is shown from (7) to (12). Equation (7) is the objective

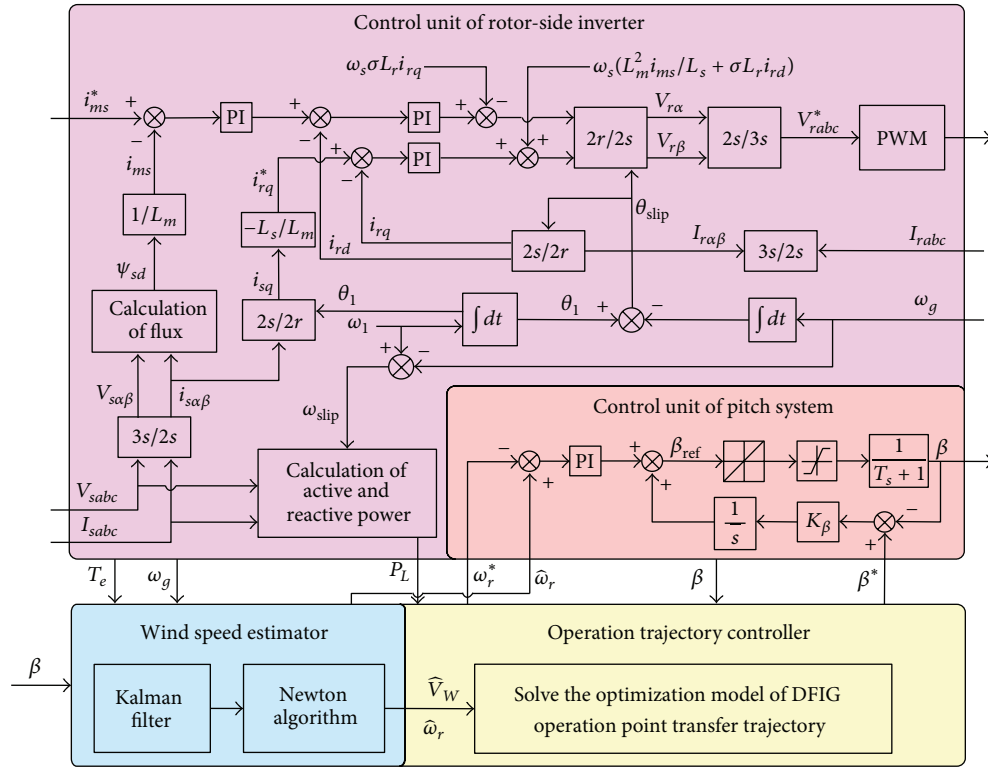


FIGURE 4: Schematic of the islanded operation control strategy of DFIG.

function, in which two terms present the rotating speed and pitch angle adjustment amount between two adjacent times, respectively. Equations (8) and (9) are the restrictions of pitch angle and rotating speed, respectively. The restriction described in (10) can ensure the stable operation of DFIG at the selected operation point. Equations (11) and (12) are the active power balance constraints

$$J_1 = \min \left(a_\omega \frac{|\omega_{r,k}^* - \omega_{r,k-1}|}{\omega_{r,\max}} + a_\beta \frac{|\beta_k^* - \beta_{k-1}|}{\beta_{\max}} \right), \quad (7)$$

$$\beta_{\min} \leq \beta_k^* \leq \beta_{\max}, \quad (8)$$

$$\omega_{r,\min} \leq \omega_{r,k}^* \leq \omega_{r,\max}, \quad (9)$$

$$\left. \frac{\partial P_{a,k}^*}{\partial \omega_{r,k}^*} \right|_{(\omega_{r,k}^*, \beta_k^*)} \leq 0, \quad (10)$$

$$P_{a,k}^* = \frac{1}{2} \rho \pi R^2 C_p (\omega_{r,k}^*, \beta_k^*) V_{W,k}^3, \quad (11)$$

$$P_{a,k}^* - (1 + L_x) P_{L,k}^* = 0, \quad (12)$$

where $\omega_{r,k}^*$, β_k^* are the control commands of rotating speed and pitch angle at next moment, respectively, $\omega_{r,k-1}$, β_{k-1} are

the rotating speed and pitch angle at the present moment, respectively, and $\omega_{r,\max}$, $\omega_{r,\min}$, β_{\max} , β_{\min} are the maximum and minimum of rotor speed and pitch angle, respectively. a_ω , a_β are weight values of rotating speed and pitch angle, respectively, and set to be 0.1 and 0.9 according to experimental comparison. L_x is the internal power loss coefficient, which is between 0.03 and 0.05. $P_{L,k}^*$ is the active power requirement of load at next moment and $P_{a,k}^*$ is the captured aerodynamic power of DFIG at next moment. $V_{W,k}^*$ is the wind speed at next moment, which can be estimated by establishing a state observer [17].

3. Islanded Operation Control Strategy of DFIG

A control strategy for DFIG which operates in the islanded mode, based on the optimization of transfer trajectory at operation points, is proposed in this paper (shown in Figure 4). A wind speed estimator using Kalman filter (KF) and Newton-Raphson (NR) algorithms is established to estimate the wind speed and rotating speed. The ISFO control technology is applied to control the rotor-side inverter of DFIG, and the traditional control strategy of pitch system is modified. Then by the coordination control of rotating speed and pitch angle, an operation trajectory controller is established to ensure the islanded operation of DFIG along the optimal transfer trajectory.

3.1. Wind Speed Estimator. Wind turbines are usually equipped with anemometers which can measure the wind speed. However, the measurement data are not accurate enough because of the aerodynamic turbulent phenomena caused by the rotating blades of wind turbine. Moreover, the wind measured by anemometers is not exactly equal to the component that transfer power to the turbine rotor. Therefore, in order to obtain a good performance in the overall control loop, it is necessary to exploit the indirect information to precisely estimate the wind speed. KF is adopted in the wind speed estimator to estimate the aerodynamic torque \hat{T}_a and rotating speed $\hat{\omega}_r$, and then the effective wind speed could be derived from \hat{T}_a and $\hat{\omega}_r$ with NR method [17].

For the estimator design, it is assumed that the rotating speed and electromagnetic torque of generator are available through measurements, and only the generator rotating speed is a noisy measurement. With the aerodynamic torque T_a as an additional state, the augmented state-space model is given as follows:

$$\begin{bmatrix} \dot{\omega}_r \\ \dot{\omega}_g \\ \dot{\theta} \\ \dot{T}_a \end{bmatrix} = \begin{bmatrix} -\frac{D_m}{J_t} & \frac{D_m}{nJ_t} & -\frac{K_m}{J_t} & \frac{1}{J_t} \\ \frac{D_m}{nJ_g} & -\frac{D_m + n^2 F_g}{n^2 J_g} & \frac{K_m}{nJ_g} & 0 \\ 1 & -1 & 0 & 0 \\ 0 & 0 & 0 & 0 \end{bmatrix} \begin{bmatrix} \omega_r \\ \omega_g \\ \theta \\ T_a \end{bmatrix} + \begin{bmatrix} 0 \\ -\frac{1}{J_g} \\ 0 \\ 0 \end{bmatrix} T_e + \begin{bmatrix} 0 \\ 0 \\ 0 \\ \zeta \end{bmatrix}, \quad (13)$$

$$y = [0 \ 1 \ 0 \ 0] \begin{bmatrix} \omega_r \\ \omega_g \\ \theta \\ T_a \end{bmatrix} + v,$$

where ζ , v are the process noisy and measurement noisy, respectively.

Equation (13) can be discretized by zero-holding method with sampling time T_s , and then the discretized model can be used in an estimation algorithm by applying the KF. Finally, the wind speed estimation \hat{V}_W can be obtained by resolving (14) with NR method:

$$\hat{T}_a \hat{\omega}_r - \frac{1}{2} \rho \pi R^2 C_p(\lambda, \beta) \hat{V}_W^3 = 0. \quad (14)$$

3.2. Rotor-Side Inverter Control. When ISFO control technology is adopted in the control unit of rotor-side inverter, the amplitude and frequency of DFIG stator voltage can be controlled by regulating its i_{ms} and i_{rq} . The d -axis in synchronous rotating reference frame is orientated in stator flux vector of generator, and the following equations are established:

$$i_{sd} = \frac{L_m}{L_s} (i_{ms} - i_{rd}), \quad (15)$$

$$i_{rq} = -\frac{L_s}{L_m} i_{sq}. \quad (16)$$

Replacing i_{sd} in stator voltage equation with (15), then (17) can be obtained:

$$\frac{L_s}{R_s} \frac{di_{ms}}{dt} + i_{ms} = i_{rd} + \frac{L_s}{R_s L_m} u_{sd}. \quad (17)$$

Neglecting the voltage drop on the stator resistance, then the stator voltage equations can be expressed as follows:

$$\begin{aligned} u_{sd} &\approx 0, \\ u_{sq} &\approx \omega_1 \psi_{sd} = \omega_1 L_m i_{ms}. \end{aligned} \quad (18)$$

Neglecting the differential term of i_{ms} , the rotor voltage equations can be expressed as follows:

$$\begin{aligned} u_{rd} &= R_r i_{rd} + \sigma L_r \frac{di_{rd}}{dt} - \omega_s \sigma L_r i_{rq}, \\ u_{rq} &= R_r i_{rq} + \sigma L_r \frac{di_{rq}}{dt} + \omega_s \left(\frac{L_m^2}{L_s} i_{ms} + \sigma L_r i_{rd} \right), \end{aligned} \quad (19)$$

where $\omega_s = \omega_1 - \omega_g$, which presents the slip angular speed.

The rotor current i_{rd} can be controlled by adjusting u_{rd} , and then the stator voltage amplitude can be controlled by regulating u_{rd} to make i_{ms} track the reference value i_{ms}^* . The rotor current i_{rq} can be controlled by adjusting u_{rq} . Regulating i_{rq} to track the reference value i_{rq}^* calculated via (16) will force the orientation of the reference frame along the stator flux vector position, and then the control of stator voltage frequency is achieved indirectly. This means that the stator flux angle does not have to be derived from integration of the stator voltages; instead, it can be derived directly from a free running integral of the stator voltage frequency demand ω_1 (50 Hz). The control strategy is shown in Figure 4. In addition, the traditional control strategy is adopted in the grid-side inverter control to stabilize the DC link voltage.

3.3. Pitch System Control. As shown in (1) and (2), for specific wind speed and aerodynamic power captured by the turbine, its pitch angle could be controlled indirectly by regulating the rotating speed. Therefore the DFIG can operate along the selected transfer trajectory by regulating ω_r and β to track the reference value ω_r^* and β^* calculated from the operation trajectory controller. In this paper, ω_r^* is used as the reference value of the pitch control unit and β is regulated to make the rotating speed estimation value $\hat{\omega}_r$ track the reference value ω_r^* . However, there will always exist a little slight error between the real pitch angle β and reference value β^* because of some reasons such as the inertia of the pitch system actuator. In order to reduce the tracking error, a compensation term is introduced into the pitch control, and the integration coefficient K_β is set to be 0.01.

3.4. Operation Trajectory Controller of DFIG. In order to obtain the optimal transfer trajectory of DFIG, the operation trajectory controller based on the optimization model of transfer trajectory at operation points is established. As shown in Figure 4, the input of the operation trajectory

controller contains \widehat{V}_W and $\widehat{\omega}_r$, sampled from the wind speed estimator and P_L and β sampled from the control unit of rotor-side converter and pitch system, respectively. The optimization model of transfer trajectory at operation points is solved in real time, and the optimization results, namely, the control commands of ω_r^* and β^* , are sent to the control unit of pitch system. Then the coordinate control of rotating speed and pitch angle could be achieved through the control unit of rotor-side inverter and pitch system, and this would make the wind turbine track the selected operation transfer trajectory.

The interior point method has the characteristics of fast calculation, strong robustness, and global convergence [18, 19]. It is widely used in solving the large nonlinear optimization model, such as the optimal power flow model of power system [20], the optimal coordinated voltage control model [21], and the restoring power flow model of power system [22]. Therefore, in order to obtain the optimal transfer trajectory of DFIG, the interior point method is applied to get the global optimal solution of the transfer trajectory optimization model.

In this paper, the Ipopt toolbox [23] in MATLAB is used in the operation trajectory controller to solve the optimization model of transfer trajectory at operation points. The Ipopt toolbox is based on the interior point method. Through a large number of simulations, it shows that solving the model generally takes 0.02–0.05 s once. Therefore, 0.1 s is taken as the sampling time of the operation trajectory controller, which can ensure obtaining the solution of the optimization model within one sample cycle. In addition, it is rational to assume that the use of lower level software suitable for control system practical implementation would further decrease the calculation time.

4. Simulation Results

The islanded power system shown in Figure 5 is simulated to verify the feasibility of the control strategy of DFIG proposed in this paper. In Figure 5, the DFIG whose rated power is 1.55 MVA can supply the controllable load L1 through the 0.69/10 kv box-type transformer T1, the 0.1 km transmission line, and the 10/0.4 kv transformer T2. The controllable load L1 has been simulated by the inverter and the DC source. The simulation results are shown in Figure 6.

An actual measured time series of wind speed is used in this paper, and its sample period is 1 s. The wind speed data between two sample points is obtained by linear interpolation. As shown in Figures 6(a) and 6(b), the actual wind speed and rotating speed of DFIG can be precisely estimated by the wind speed estimator designed in this paper. It is obvious that the error of the designed wind speed estimator is adequately small to ensure better performance of the overall control loop. The control strategy of pitch system was switched to the proposed one in this paper from the one mentioned in [10]. Figures 6(h) and 6(i) show that, with ISFO control technology adopted in the control unit of DFIG rotor-side inverter, the actual values of the equivalent stator magnetizing current and the q -axis component of rotor current could be regulated to track their reference values, respectively. Then the amplitude

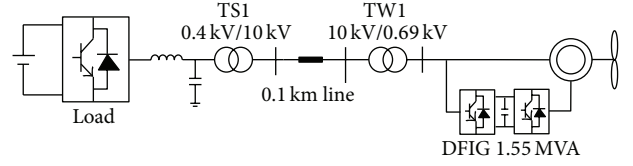


FIGURE 5: Diagram of the islanded power system.

and frequency of DFIG stator voltage could be stabilized as shown in Figures 6(f) and 6(g), and the active power and reactive power demand of load can be satisfied as shown in Figures 6(d) and 6(e).

Due to the wind speed in Figure 6(a) and active power demand of load in Figure 6(d) changing over time, the rotating speed and pitch angle of DFIG need to be adjusted to keep the balance between the captured aerodynamic power and active power output of DFIG. As shown in Figures 6(b)–6(d), on the basis of the active power requirement of load satisfied, the rotating speed and pitch angle of DFIG can track the reference values offered by the operation trajectory controller. Figures 6(k) and 6(l) show that the operation trajectory controller could always obtain the global optimal solution of the optimization model within 0.1 s, and it ensures the selected operation transfer trajectory to be the optimal one that has the minimum synthetic adjustment amount of rotating speed and pitch angle. Figure 6(j) shows that the DC link voltage can be stabilized by the control of the grid-side inverter, and it could provide slip power for the rotor-side inverter. Therefore, DFIG could autonomously operate in the islanded mode along the optimal trajectory by adopting the control strategy proposed in this paper.

In order to evaluate the performance of the proposed control strategy, with the same simulation conditions employed, the control strategies of pitch system proposed in [10, 16] (shown in Figure 7) are also simulated. Figure 8 shows that the control strategy proposed in this paper could make the rotating speed and pitch angle track their reference values more quickly and accurately. Moreover, three evaluation indexes are defined as follows to quantitatively compare the adjustment amount of the rotating speed and pitch angle, including the adjustment amount of rotating speed $\Delta\omega_r$, the adjustment amount of pitch angle $\Delta\beta$, and the synthetic adjustment amount Δz . It is obvious that when DFIG operates in the islanded mode, its synthetic adjustment amount of the rotating speed and pitch angle could be reduced with the application of the control strategy proposed in this paper as shown in Table 1:

$$\Delta\omega_r = \sum_{i=1}^K \frac{|\omega_{r,k} - \omega_{r,k-1}|}{\omega_{r,\max}},$$

$$\Delta\beta = \sum_{i=1}^K \frac{|\beta_k - \beta_{k-1}|}{\beta_{\max}}, \quad (20)$$

$$\Delta z = \Delta\omega_r + \Delta\beta.$$

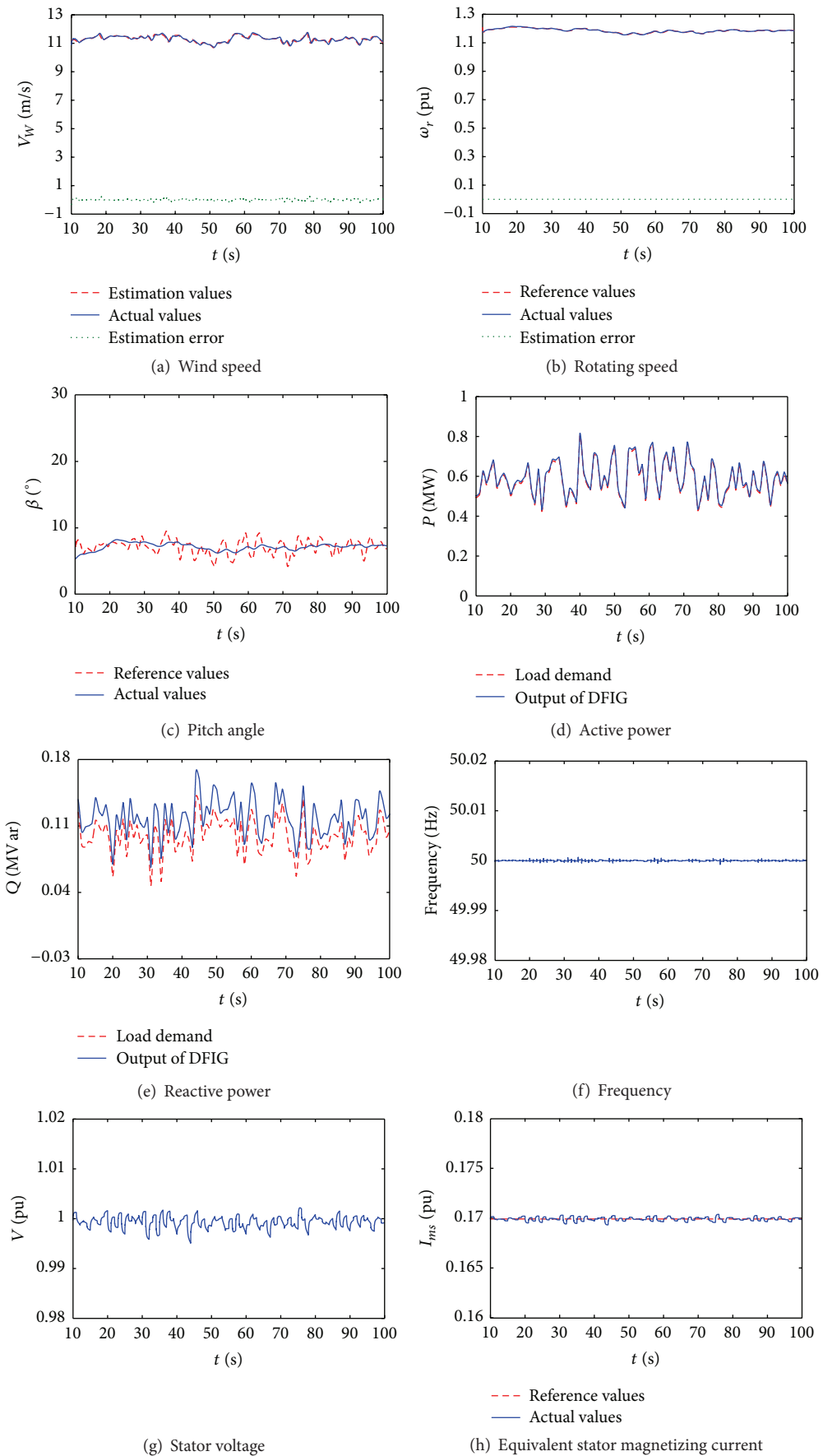


FIGURE 6: Continued.

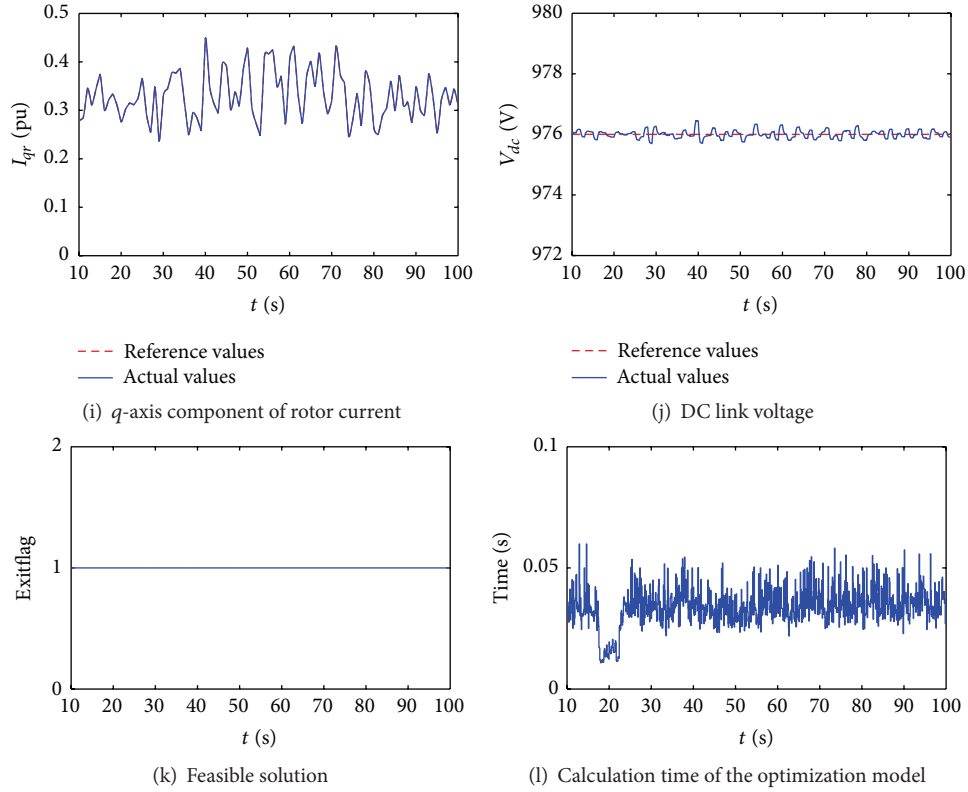


FIGURE 6: Simulation results of the proposed control strategy.

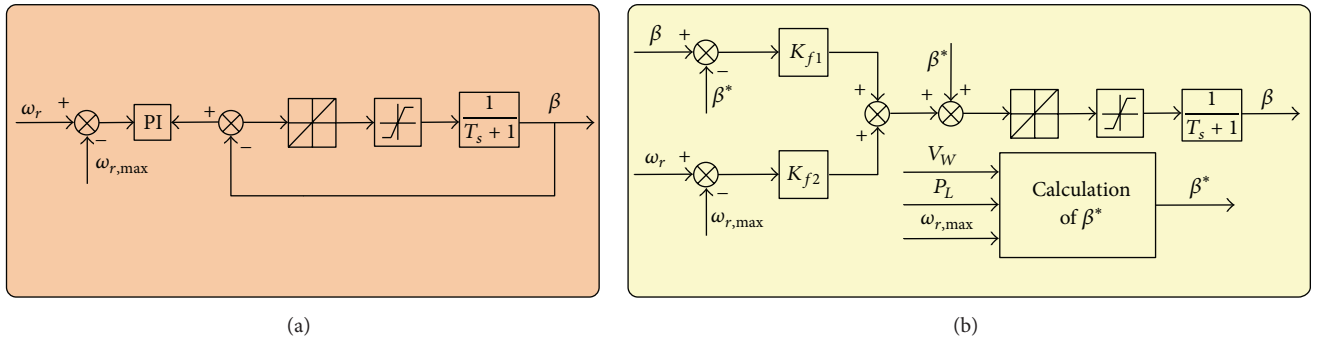


FIGURE 7: Schematic of the pitch system control strategy: (a) the strategy proposed in [10] and (b) the strategy proposed in [16].

TABLE 1: Comparison of the adjustment amount of rotating speed and pitch angle for different control strategies.

	$\Delta\omega_r$	$\Delta\beta$	Δz
This paper	5.041	0.724	5.765
Reference [10]	5.325	1.105	6.43
Reference [16]	4.961	2.171	7.132

5. Conclusion

This paper presents a novel control strategy to enable the DFIG to operate in the islanded mode. The control strategy is based on the optimal control of rotating speed and pitch angle of DFIG. Simulation results of the operation of a DFIG

supplying a varying power load are given. Assuming that the capacity of DFIG is enough to satisfy the requirement of the active and reactive power of load simultaneously, the proposed control strategy presents several advantages as follows.

- (1) The control strategy enables DFIG to control the frequency and amplitude of the stator voltage independently which is similar to a voltage source, and then it is not needed to equip a large power source to sustain the voltage of islanded power system.
- (2) The improved control strategy of pitch system can make the rotating speed and pitch angle of DFIG track their reference values more quickly and accurately compared with other methods.

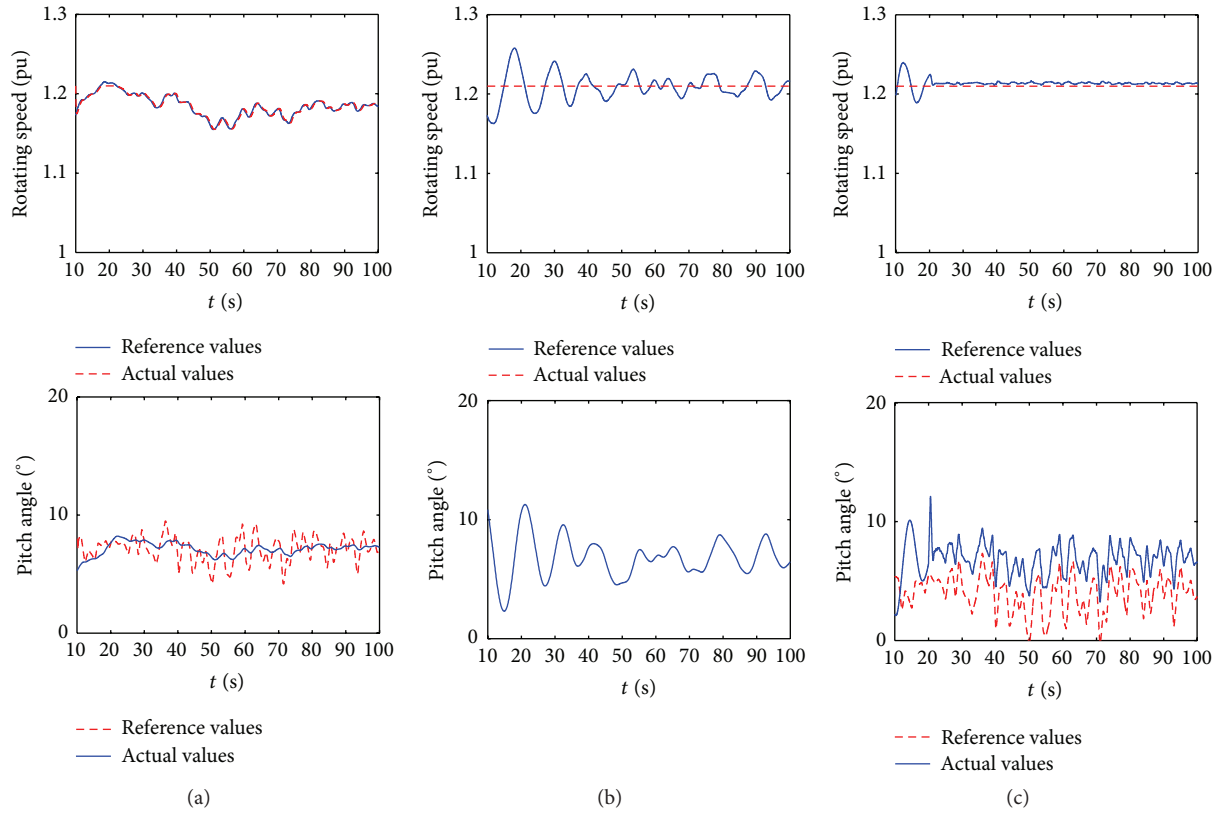


FIGURE 8: Rotating speed and pitch angle using the different pitch system control strategy: (a) the strategy proposed in this paper, (b) the strategy proposed in [10], and (c) the strategy proposed in [16].

- (3) The application of this control strategy can ensure the DFIG to operate along the optimal transfer trajectory in islanded mode, with minimized adjustment amount of rotating speed and pitch angle.

Even if the DFIG may not track the maximum wind power, it is not necessarily a disadvantage for the islanded power systems in remote regions. The utilization efficiency of DFIG can be improved by equipping an energy storage system with appropriate capacity in the islanded power system. When the demand power of load is less than the extractable wind power of DFIG, the extra power can be absorbed by the energy storage system. Otherwise, the energy storage system can supply the load together with DFIG through releasing power. The coordinate control strategy of the DFIG and energy storage system will be fully addressed in the future publication.

Conflict of Interests

The authors declare that there is no conflict of interests regarding the publication of this paper.

Acknowledgment

This work was supported by the Science and Technology Project of State Grid Corporation of China under Grant SGMD0000DDJS1500096.

References

- [1] G. Weidong, “Development and application of large-scale non-grid-connected wind power system,” *Automation of Electric Power Systems*, vol. 32, no. 19, pp. 1–9, 2008.
- [2] H. Yang, R. Zhao, H. Xin, Z. Wang, and D. Gan, “Development and research status of island power systems,” *Transactions of China Electrotechnical Society*, vol. 28, no. 11, pp. 95–105, 2013.
- [3] E. Guizzo, “Wind power in paradise,” *IEEE Spectrum*, vol. 45, no. 3, pp. 38–45, 2008.
- [4] G. Iwanski and W. Koczara, “DFIG-based power generation system with UPS function for variable-speed applications,” *IEEE Transactions on Industrial Electronics*, vol. 55, no. 8, pp. 3047–3054, 2008.
- [5] C. L. Moreira, F. O. Resende, and J. A. P. Lopes, “Using low voltage MicroGrids for service restoration,” *IEEE Transactions on Power Systems*, vol. 22, no. 1, pp. 395–403, 2007.
- [6] S. Müller, M. Deicke, and R. W. De Doncker, “Doubly fed induction generator systems for wind turbines,” *IEEE Industry Applications Magazine*, vol. 8, no. 3, pp. 26–33, 2002.
- [7] F. A. Bhuiyan and A. Yazdani, “Multimode control of a DFIG-based wind-power unit for remote applications,” *IEEE Transactions on Power Delivery*, vol. 24, no. 4, pp. 2079–2089, 2009.
- [8] S. Lin, L. Yi, and S. Nian, “A control strategy of isolated grid with high penetration of wind and energy storage systems,” *Proceedings of the CSEE*, vol. 33, no. 16, pp. 78–85, 2013.

- [9] J.-Y. Kim, J.-H. Jeon, S.-K. Kim et al., "Cooperative control strategy of energy storage system and microsourses for stabilizing the microgrid during islanded operation," *IEEE Transactions on Power Electronics*, vol. 25, no. 12, pp. 3037–3048, 2010.
- [10] L.-R. Chang-Chien and Y.-C. Yin, "Strategies for operating wind power in a similar manner of conventional power plant," *IEEE Transactions on Energy Conversion*, vol. 24, no. 4, pp. 926–934, 2009.
- [11] F. D. Kanellos and N. D. Hatzargyriou, "Optimal control of variable speed wind turbines in islanded mode of operation," *IEEE Transactions on Energy Conversion*, vol. 25, no. 4, pp. 1142–1151, 2010.
- [12] Y. Zhang and B. T. Ooi, "Stand-Alone doubly-fed induction generators (DFIGs) with autonomous frequency control," *IEEE Transactions on Power Delivery*, vol. 28, no. 2, pp. 752–760, 2013.
- [13] R. Cárdenas, R. Peña, J. Proboste, G. Asher, and J. Clare, "MRAS observer for sensorless control of standalone doubly fed induction generators," *IEEE Transactions on Energy Conversion*, vol. 20, no. 4, pp. 710–718, 2005.
- [14] R. Pena, J. C. Clare, and G. M. Asher, "A doubly fed induction generator using back-to-back PWM converters supplying an isolated load from a variable speed wind turbine," *IEE Proceedings-Electric Power Applications*, vol. 143, no. 5, pp. 380–387, 1996.
- [15] R. D. Shukla and R. K. Tripathi, "A novel voltage and frequency controller for standalone DFIG based wind energy conversion system," *Renewable and Sustainable Energy Reviews*, vol. 37, pp. 69–89, 2014.
- [16] M. Fazeli, G. M. Asher, C. Klumpner, and L. Yao, "Novel integration of DFIG-based wind generators within microgrids," *IEEE Transactions on Energy Conversion*, vol. 26, no. 3, pp. 840–850, 2011.
- [17] B. Boukhezzer and H. Siguerdidjane, "Nonlinear control of a variable-speed wind turbine using a two-mass model," *IEEE Transactions on Energy Conversion*, vol. 26, no. 1, pp. 149–162, 2011.
- [18] A. Wächter and L. T. Biegler, "On the implementation of an interior-point filter line-search algorithm for large-scale nonlinear programming," *Mathematical Programming*, vol. 106, no. 1, pp. 25–57, 2006.
- [19] A. Forsgren, P. E. Gill, and M. H. Wright, "Interior methods for nonlinear optimization," *SIAM Review*, vol. 44, no. 4, pp. 525–597, 2002.
- [20] R. A. Jabr, A. H. Coonick, and B. J. Cory, "A primal-dual interior point method for optimal power flow dispatching," *IEEE Transactions on Power Systems*, vol. 17, no. 3, pp. 654–662, 2002.
- [21] W. Zheng and M. Liu, "Solution of optimal coordinated voltage control using line search filter interior point method," *Transactions of China Electrotechnical Society*, vol. 27, no. 9, pp. 70–77, 2012.
- [22] T. Xianghong, B. Guangquan, and W. Hongfu, "An optimization method based on weighted least absolute value to restore power flow solvability of bulk power system," *Automation of Electric Power Systems*, vol. 38, no. 23, pp. 60–64, 2014.
- [23] A. Wächter and L. T. Biegler, "Line search filter methods for nonlinear programming: motivation and global convergence," *SIAM Journal on Optimization*, vol. 16, no. 1, pp. 1–31, 2005.

Research Article

A Joint Scheduling Optimization Model for Wind Power and Energy Storage Systems considering Carbon Emissions Trading and Demand Response

Yin Aiwei,¹ Xu Congwei,¹ and Ju Liwei²

¹School of Economics and Management, Beijing University of Aeronautics and Astronautics, Beijing 100191, China

²School of Economics and Management, North China Electric Power University, Beijing 102206, China

Correspondence should be addressed to Ju Liwei; 183758841@qq.com

Received 16 November 2015; Revised 11 January 2016; Accepted 27 January 2016

Academic Editor: Jinyun Yuan

Copyright © 2016 Yin Aiwei et al. This is an open access article distributed under the Creative Commons Attribution License, which permits unrestricted use, distribution, and reproduction in any medium, provided the original work is properly cited.

To reduce the influence of wind power random on system operation, energy storage systems (ESSs) and demand response (DR) are introduced to the traditional scheduling model of wind power and thermal power with carbon emission trading (CET). Firstly, a joint optimization scheduling model for wind power, thermal power, and ESSs is constructed. Secondly, DR and CET are integrated into the joint scheduling model. Finally, 10 thermal power units, a wind farm with 2800 MW of installed capacity, and 3×80 MW ESSs are taken as the simulation system for verifying the proposed models. The results show backup service for integrating wind power into the grid is provided by ESSs based on their charge-discharge characteristics. However, system profit reduces due to ESSs' high cost. Demand responses smooth the load curve, increase profit from power generation, and expand the wind power integration space. After introducing CET, the generation cost of thermal power units and the generation of wind power are both increased; however, the positive effect of DR on the system profit is also weakened. The simulation results reach the optimum when both DR and CET are introduced.

1. Introduction

The implementation of China's energy-saving and pollutant emission reduction strategies has prompted large-scale wind power development. In 2014, the installed capacity of wind power reached 115 million kW, ranking first in the world. However, influenced by the intermittency that is characteristic of wind power, the growth rate of wind power grid integration is smaller than the growth rate of the installed capacity. This phenomenon leads to a high rate of curtailed wind power in China. The average rate of curtailed wind power is approximately 12.8%. Especially in the "three north areas," the rate of curtailed wind power has already reached 15.4%. In order to solve the problem of curtailed wind power, suitable backup service should be provided on the generation site for wind power connected to the grid. Energy storage systems (ESSs) could flexibly provide backup service by charging and discharging. This property gives ESSs the most potential as a means to provide backup service for

wind power integration. Additionally, demand response (DR) could optimize customers' power consumption behavior and incentivize customers to participate in system scheduling for wind power consumption.

Currently, China is implementing carbon emission trading (CET) pilot projects and plans to establish a CET market to prompt energy-saving and emissions reduction in the "thirteenth five-year plan" period. CET could affect the generation cost of thermal power units and make clean energy generation more advantageous. Hetzer et al. [1] regard carbon emission as a virtual network flow to subsequently build a theoretical framework for carbon emissions from the power system based on analyses of carbon emission trading and developing trends in the power industry. References [2–4] study carbon emission right definition problems in cross-regional power trading and build a fair allocation principle based on the construction of a mathematical model that tracks carbon flow. The above research shows that CET can affect the cost of thermal power generation and make grid

integration of clean energy more advantageous. Therefore, a study of how to integrate ESSs, DR, and CET into the traditional generation scheduling of a power system with wind power has important practical significance.

Selecting a better backup method is the most effective way to overcome the random nature of wind power. Currently, backup service for wind power grid integration consists of three main parts: thermal power, pumped storage power plants, and ESSs. Jiang et al. [5] develop a wind-thermal economic emission scheduling model considering coordination of the power allocation of thermal units and wind turbines. Yuan et al. [6] establish a multiobjective economic scheduling model for the hydrothermal-wind problem, considering the uncertainty cost of wind power. Wang et al. [7] propose a novel stochastic constraint model to solve for the uncertainty cost of wind power and present an improved particle swarm optimization (PSO) algorithm to solve the proposed model. Thermal power units can provide backup service for wind power by adjusting their start-stop condition, but their fuel consumption and pollution emission are not environmentally friendly. Therefore, pumped storage power stations are a better way to provide backup service. Papaefthymiou et al. [8] achieve high penetration levels of renewable energy in power systems by combining wind power and pumped storage power plants. Papaefthymiou and Papathanassiou [9] propose a novel unit commitment problem model and binary PSO algorithm to find the optimal schedule scheme. Ming et al. [10] calculate the effect of pumped storage power stations on wind power regulation and develop an economic evaluation model for combined wind power and pumped storage systems. Pumped storage power plants have the advantages of saving energy and reducing pollutant emission, but they are not suitable for large-scale application because they are restricted by geographic location and conditions.

The operational theory of ESSs is similar to that of pumped storage power plants, but ESSs have more flexible installation requirements with better prospects for large-scale application. Wu et al. [11] take constraints on power generation units and energy storage units into consideration and build a static model for joint operation of wind power and energy storage. Hu et al. [12] combine opportunity and constraint theory and build a joint scheduling model for wind power and energy storage systems considering the uncertainty in wind power output, which is applied with good results. Ding et al. [13] build a wind-storage joint scheduling model considering risk constraints and use a Monte Carlo simulation method to simulate wind power output. García-González et al. [14] improve the power ramp mathematic expression for wind power and build a joint scheduling optimization model for the control of curtailed wind power and energy storage systems.

The researchers cited above have achieved good results in actual applications; however, the high initial investment cost limits the scale of application of energy storage systems. Therefore, other routes are needed to optimize the application of ESSs. DR can optimize customers' power consumption behavior, smooth the demand load curve, and increase the consumption of wind power. Greening [15] puts forward the basic concept of demand response. Niu et al. [16] classify DR

into price-based demand response (PBDR) and incentive-based demand response (IBDR). López et al. [17] propose an optimization model for performing load shifting in the context of a smart grid. Nwulu and Xia [18] integrate game theory into dynamic economic emission scheduling considering DR. A framework for optimizing the bidding strategy of a smart distribution company that contains wind farms and responsive loads in the day-ahead energy market is proposed by Ghasemi et al. [19]. Wang et al. [20] construct a modeling framework for an integrated electricity system in which loads become an additional resource.

CET can highlight the environmental friendliness of wind power and increase the advantages of wind power generation [21]. Zhu et al. [22] developed a full-infinite fuzzy stochastic programming method for planning municipal electric power systems associated with greenhouse gas control under uncertainty. Khalid and Savkin [23] developed and tested a methodology for controlling the emissions from a group of microgenerators aggregated in a virtual power plant with wind power. The above papers discussed the impact of CET on system scheduling; the effects of collaborative optimization of CET, ESSs, and DR should be analyzed.

The rest of this paper is organized as follows. Section 2 puts forward a demand response mathematical model. Section 3 presents a model for charging and discharging ESSs. Section 4 establishes the joint scheduling optimization model for wind power and ESSs with and without CET. Section 5 takes 10 thermal units, a wind farm with 2800 MW of installed capacity, and 3×80 MW ESSs as the simulation system and comparatively analyzes the influence of ESSs, DR, and CET on system operation. Section 6 presents the primary conclusions.

2. Demand Response Model

Power demand response refers to a situation in which customers dynamically adjust their power consumption behavior according to price, which should guarantee a balance between power supply and demand. From an economic point of view, when electricity price increases, the demand for power should decrease. Part of the power demand during the peak load period will be transferred to other periods, while the other part will be reduced. Thus, for the peak load period, the load reduction consists of three parts: one is load transfer due to an increased electricity price, the second is load reduction, and the third is load transfer due to a reduced electricity price during the valley load period. For the float load period, the load change consists of two parts: one part comes from the peak load period and the other part goes to the valley load period. For the valley load period, the load increase consists of three parts: one is load transfer due to a decreased electricity price, the second part comes from the peak load period, and the third part is new power demand due to the price reduction.

This study defines the power demand during the peak load period, float load period, and valley load period before

implementing time-of-use (TOU) price as G_{peak} , G_{flat} , and G_{valley} . Power demand at period t is G_t ; therefore,

$$\begin{aligned} G_{\text{peak}} &= \sum_{t \in \text{peak}} G_t, \\ G_{\text{flat}} &= \sum_{t \in \text{flat}} G_t, \\ G_{\text{valley}} &= \sum_{t \in \text{valley}} G_t. \end{aligned} \quad (1)$$

The proportion of power demand reduction during the peak load period is given by α , the proportion of the load that transfers to other periods is α_1 and the load loss proportion is $1 - \alpha_1$, and the proportion of the load that transfers to the float load period is α_2 and the proportion that transfers to the valley load period is $1 - \alpha_2$. The proportion of power demand increase during the valley load period is β , the proportion of the load transferred to the valley load period is β_2 , and the new demand proportion is $1 - \beta_2$. The proportion of the load that comes from the valley load period is β_2 , and the proportion from the float load period is $1 - \beta_2$. Thus, the demand during the peak, float, and valley load periods is calculated as follows:

$$\begin{aligned} G'_{\text{peak}} &= G_{\text{peak}} - G_{\text{peak}} \cdot \alpha - G_{\text{valley}} \beta \cdot \beta_1 \cdot \beta_2, \\ G'_{\text{flat}} &= G_{\text{flat}} + G_{\text{peak}} \cdot \alpha \cdot \alpha_1 \cdot \alpha_2 - G_{\text{valley}} \cdot \beta \cdot \beta_1 \\ &\quad \cdot (1 - \beta_2), \\ G'_{\text{valley}} &= G_{\text{valley}} + G_{\text{valley}} \cdot \beta + G_{\text{peak}} \cdot \alpha \cdot \alpha_1 \cdot (1 - \alpha_2). \end{aligned} \quad (2)$$

If the proportion of load change is the same at each point in time in the same period, the load at each time point is

$$\begin{aligned} G'_t &= \frac{G_t}{G_{\text{peak}}} G'_{\text{peak}} \quad t \in \text{peak}, \\ G'_t &= \frac{G_t}{G_{\text{flat}}} G'_{\text{flat}} \quad t \in \text{flat}, \\ G'_t &= \frac{G_t}{G_{\text{valley}}} G'_{\text{valley}} \quad t \in \text{valley}. \end{aligned} \quad (3)$$

The system load period will change from G_t to G'_t with the introduction of DR; load demand reduces during the peak load period and increases during the valley load period. The demand load curve becomes smoother after peak load shifting.

3. Charging and Discharging Model for ESSs

ESSs can be regarded as both power resources and load demand. When wind power output is high at night, ESSs are regarded as load demand. In the daytime, they are regarded as power resources to meet load demand. Charge and discharge of ESSs are limited by the system capacity. Assuming

the storage energy of ESSs at time t is $Q_{s,t}$, the charging and discharging power balance should obey

$$Q_{s,t} = Q_{s,t-1} + Q_{s,t}^+ - \frac{Q_{s,t}^-}{(1 - \theta_s)}, \quad (4)$$

where $Q_{s,t}^+$ is the charging power at time t , $Q_{s,t}^-$ is the discharging power at time t , and θ_s is the loss coefficient for charging and discharging power.

Charging and discharging power from ESSs is limited as follows:

$$\begin{aligned} Q_{s,t}^+ &\leq \overline{Q}_s, \\ Q_{s,t}^- &\leq \overline{Q}_s, \end{aligned} \quad (5)$$

where \overline{Q}_s is the upper limit for charging and discharging power.

In addition, the energy storage capacity of ESSs is limited:

$$Q_{s,t} < Q_s^{\text{max}}, \quad (6)$$

where Q_s^{max} is the maximum storage capacity of the ESSs.

4. Scheduling Model for Wind Power and ESSs

4.1. Mathematical Model without CET

4.1.1. Objective Function. Wind farm operators hope for higher consumption of wind power to gain more profits; however, this will cause more frequent adjustment of thermal power units for peak regulation, improving wind power grid integration but also increasing system coal consumption. To achieve the optimum energy efficiency, a joint optimization scheduling model for wind power and thermal power is built. The maximum total profit of ESSs, wind power, and thermal power is taken as the optimization objective:

$$\max z_1 = \pi_c + \pi_w + \pi_s, \quad (7)$$

where π_w , π_c , and π_s are the profits of wind farms, thermal power units, and ESSs, respectively.

The wind farm profit is calculated as follows:

$$\pi_w = p_w \sum_{t=1}^T Q_{w,t} (1 - \theta_w) - \text{OM}_w - D_w. \quad (8)$$

The profit of thermal power units is calculated as follows:

$$\pi_c = p_c \sum_{i=1}^I \sum_{t=1}^T Q_{i,t} (1 - \theta_{c,i}) - C_{\text{fuel}} - \sum_{i=1}^I \text{OM}_{c,i} - \sum_{i=1}^I D_{c,i}, \quad (9)$$

where p_c is the benchmark price of thermal power, $Q_{i,t}$ is the real-time power generation of unit i at time t , $\theta_{c,i}$ is the power consumption rate of unit i , C_{fuel} is the fuel cost for power generation, $\text{OM}_{c,i}$ is the operation and maintenance cost of unit i , and $D_{c,i}$ is the depreciation cost of unit i .

The fuel cost of a thermal power unit is calculated by

$$\begin{aligned} C_{\text{fuel}} &= \sum_{i=1}^I \sum_{t=1}^T [p_{\text{coal}} u_{i,t} f_i(Q_{i,t}) + u_{i,t} (1 - u_{i,t-1}) \text{SU}_i \\ &\quad + u_{i,t-1} (1 - u_{i,t}) \text{SD}_i], \end{aligned} \quad (10)$$

where p_{coal} is the standard coal purchase price, $u_{i,t}f_i(Q_{i,t})$ is the standard coal consumption, and $u_{i,t}$ is a binary variable. When a thermal power unit is shut down, coal consumption is zero, when the thermal power unit is operating, coal consumption is determined by the consumption characteristics function $f_i(\cdot)$ and the real-time power output $Q_{i,t}$:

$$f_i(Q_{i,t}) = a_i + b_i Q_{i,t} + c_i Q_{i,t}^2, \quad (11)$$

where a_i , b_i , and c_i are coal consumption parameters of unit i , $u_{i,t}(1 - u_{i,t-1})\text{SU}_i$ is the start-up cost of unit i at time t , SU_i is the start-up cost of unit i , $u_{i,t-1}(1 - u_{i,t})\text{SD}_i$ is the shutdown cost of unit i at time t , and SD_i is the shutdown cost of unit i :

$$\pi_s = p_{s,\text{char}} \sum_{t=1}^T Q_{s,t}^+ - p_{s,\text{disc}} \sum_{t=1}^T Q_{s,t}^- - F_s, \quad (12)$$

where $p_{s,\text{char}}$ is the electricity price when charging ESSs, $p_{s,\text{disc}}$ is the electricity price when discharging, and F_s is the fixed cost of the ESSs.

4.1.2. Constraint Conditions. In the joint optimization model, the constraints of demand and supply balance, thermal power unit operation, wind power operation, and ESS operation should be comprehensively considered.

(1) System Demand and Supply Balance Constraint. Before DR, the system demand and supply balance constraint is described by

$$\begin{aligned} & \sum_{i=1}^I u_{i,t} Q_{i,t} (1 - \theta_i) + Q_{w,t} (1 - \theta_w) + Q_{s,t}^- \\ & = \frac{G_t}{(1 - l)} + Q_{s,t}^+. \end{aligned} \quad (13)$$

After DR, the constraint is described by

$$\begin{aligned} & \sum_{i=1}^I u_{i,t} Q_{i,t} (1 - \theta_i) + Q_{w,t} (1 - \theta_w) + Q_{s,t}^- \\ & = \frac{G'_t}{(1 - l)} + Q_{s,t}^+. \end{aligned} \quad (14)$$

(2) Thermal Power Unit Power Generation Constraint. Real-time generation output is limited by the installed capacity and the minimum generation output:

$$u_{i,t} \underline{Q}_i \leq Q_{i,t} \leq u_{i,t} \overline{Q}_i. \quad (15)$$

(3) Unit Ramp Rate Constraint. Depending on the technology level, unit generation output change is constrained by the adjacent period. The real-time output increment and decrement should obey

$$\Delta Q_i^- \leq Q_{i,t} - Q_{i,t-1} \leq \Delta Q_i^+. \quad (16)$$

(4) Unit Start-Stop Time Constraints. Frequent start-stop affects the performance of a thermal unit. The continuous unit start-stop constraint is shown as follows:

$$(T_{i,t-1}^{\text{on}} - M_i^{\text{on}})(u_{i,t-1} - u_{i,t}) \geq 0, \quad (17)$$

$$(T_{i,t-1}^{\text{off}} - M_i^{\text{off}})(u_{i,t} - u_{i,t-1}) \geq 0. \quad (18)$$

Equation (17) is the shortest time constraint on unit i . $T_{i,t-1}^{\text{on}}$ is the continuous running time of unit i at time $t - 1$. M_i^{on} is the shortest running time of unit i . Equation (18) is the shortest shutdown time constraint on unit i . $T_{i,t-1}^{\text{off}}$ is the continuous shutdown time of unit i at time $t - 1$. M_i^{off} is the unit shortest shutdown time.

(5) Wind Power Output Constraint. The real-time wind power output is constrained by the wind farm capacity:

$$Q_{w,t} \leq \delta_t P_w, \quad (19)$$

where δ_t is the equivalent utilization efficiency and P_w is the total installed capacity of wind farm w .

(6) Charging and Discharging Power Constraint on ESSs. For ESSs, the cumulative charging and discharging power should obey

$$\sum_{t=1}^T Q_{s,t}^+ (1 - \theta_s) = \sum_{t=1}^T Q_{s,t}^-. \quad (20)$$

Therefore, if ESS operators hope to profit, the charging and discharging prices should obey

$$p_{s,\text{char}} > \frac{p_{s,\text{disc}}}{(1 - \theta_s)}. \quad (21)$$

(7) System Generation Reserve Constraints. When the power system is in operation, fluctuations may happen on both the generation side and the demand side. To ensure real-time balance, the supply of power should be adjusted to fall within a certain margin by increasing or reducing the power output:

$$\sum_{i=1}^I u_{i,t} (Q_{i,t}^{\text{max}} - Q_{i,t}) (1 - \theta_i) \geq R_t^{\text{usr}}, \quad (22)$$

$$Q_{i,t}^{\text{max}} = \min(u_{i,t-1} \overline{Q}_i, Q_{i,t-1} + \Delta Q_i^+) \cdot u_{i,t-1}, \quad (23)$$

$$R_t^{\text{usr}} = \beta_c \sum_{i=1}^I Q_{i,t} + \beta_w Q_{w,t}. \quad (24)$$

Equations (22)–(24) are the system upward spinning reserve constraints. $Q_{i,t}^{\text{max}}$ is the maximum possible output of unit i at time t . R_t^{usr} is the upward spinning reserve demand, depending on thermal and wind generation power in the corresponding period. \overline{Q}_i is the maximum possible energy generation by unit i at time t , adjusted for the installed capacity. ΔQ_i^+ is the upward ramp rate, namely, the maximum

power generation in the adjacent period. β_c is the thermal power unit reserve coefficient. β_w is the power reserve coefficient for wind turbines:

$$\sum_{i=1}^I Q_{i,t} (Q_{i,t} - Q_{i,t}^{\min}) (1 - \theta_i) \geq R_t^{\text{dsr}}, \quad (25)$$

$$Q_{i,t+1}^{\min} = \max(u_{i,t} Q_i, Q_{i,t} - \Delta Q_i^-) \cdot u_{i,t}, \quad (26)$$

$$R_t^{\text{dsr}} = \beta_w Q_{w,t}. \quad (27)$$

Equations (25)–(27) are the system downward spinning reserve constraints. $Q_{i,t}^{\min}$ is the minimum possible output of unit i at time t , restricted by two factors, namely, the minimum possible generation capacity under operation and the unit downward ramp rate constraint. R_t^{dsr} is the system downward spinning reserve demand, depending on wind power in the corresponding period. Q_i is the minimum possible generation capacity of unit i , adjusted for the real-time minimum power output. ΔQ_i^- is the unit downward ramp rate, that is, the maximum power reduction generation unit in the adjacent period.

4.2. Mathematical Model with CET. Currently, China is performing pilot construction and planning to establish a CET market in the “thirteenth five-year plan” period. CO₂ emission from the thermal power industry accounts for approximately 40% of the total. Generation rights displacement and the CET mechanism are both market mechanisms to optimize the thermal industry structure and reduce energy consumption and emission, which are consistent in purpose and results.

The marginal generation cost of thermal power changes under a CET mechanism, and carbon emission parameters are different due to different unit technologies, so the generation scheduling plan also changes. To maximize system profit under a carbon trading mechanism, this study builds an optimization model with the objective of maximizing thermal and wind power profit:

$$\max z_2 = \pi_c + \pi_w + \pi_s. \quad (28)$$

Thermal power profit should meet the following conditions:

$$\pi_c = p_c \sum_{i=1}^I \sum_{t=1}^T Q_{i,t} (1 - \theta_{c,i}) - C_c - \sum_{i=1}^I \text{OM}_{c,i} - \sum_{i=1}^I D_{c,i} \quad (29)$$

$$C_c = C_{\text{fuel}} + C_{\text{CO}_2},$$

where C_{CO_2} is the cost of carbon emission:

$$C_{\text{CO}_2} = (E_{\text{CO}_2} - E_0) p_{\text{CO}_2}, \quad (30)$$

where E_{CO_2} is the actual carbon emission of thermal units during the operation period, E_0 is the total initial carbon emission right, and p_{CO_2} is the carbon trading price, which is related to the carbon trading demand. To simplify the model, this study assumes that the price does not change with the carbon trading demand.

The actual carbon emission of thermal units is related to the power load rate. Generally speaking, the actual carbon emission of units can be expressed as a quadratic function, similar to (22):

$$E_i(Q_{i,t}) = a_{\text{CO}_2,i} + b_{\text{CO}_2,i} Q_{i,t} + c_{\text{CO}_2,i} Q_{i,t}^2, \quad (31)$$

where $a_{\text{CO}_2,i}$, $b_{\text{CO}_2,i}$, and $c_{\text{CO}_2,i}$ are parameters of the carbon emission function.

Then, total system emissions are as follows:

$$E_{\text{CO}_2} = \sum_{t=1}^T \sum_{i=1}^I E_i(Q_{i,t}). \quad (32)$$

Scheduling and operation constraint conditions for wind power and ESSs should be considered comprehensively in carbon emissions trading. The system demand and supply constraints, wind power unit operation constraints, and ESSs operation constraints are shown in (13) to (27).

In the mathematical model without CET, (10), (11), (17), (18), and (31) are nonlinear constraints, which are inconvenient to solve. Therefore, they should be linearized. The details of this process can be found in the literature [24, 25].

5. Example Analysis

5.1. Case Descriptions. To analyze the impact of ESSs, DR, and CET on system operation, four cases are set up as follows.

Case 1 (baseline case). Self-scheduling of the system without DR and CET: DR and CET are not considered, so the impact of ESSs on wind power grid integration is analyzed alone in this case. The ESS capacity is 3×80 MW, the charging and discharging power of a single ESS unit is 20 MW, and the charging and discharging loss coefficient is 15%.

Case 2 (self-scheduling of the system with DR). Demand response is introduced into the joint scheduling. The demand load curve is divided into peak, valley, and float load periods according to the literature [24], which are listed in Table 1. The values of α_1 and α_2 are 0.95 and 0.7, respectively, β_1 and β_2 are 0.90 and 0.40, respectively, and both α and β are 5%.

Case 3 (self-scheduling of the system with CET). 90% of CO₂ emissions from Case 1 are taken as the initial baseline for carbon emission trading, with a carbon emissions trading price of 80 ¥/t.

Case 4 (self-scheduling of the system with DR and CET). Collaborative optimization of CET and DR is analyzed with joint scheduling of wind power and ESSs.

5.2. Basic Data. This study uses 10 thermal power units and a wind farm with an installed capacity of 2800 MW as the simulation system. Coal consumption and carbon emission parameters of the thermal power units are listed in Table 2, and the operation coefficients are listed in Table 3. The grid purchase price of wind power is assumed to be 540 ¥/MW-h, the total operation and depreciation cost is 600 million/year,

TABLE 1: Period division of TOU.

Load	Valley load period	Float load period	Peak load period
Period	0:00–6:00; 22:00–24:00	6:00–9:00; 14:00–19:00	9:00–14:00; 19:00–22:00

TABLE 2: Coal consumption and carbon emission parameters of thermal power units.

Unit	a_j	b_j	c_j	$a_{\text{CO}_2,j}$	$b_{\text{CO}_2,j}$	$c_{\text{CO}_2,j}$
1#	11.6	0.260	$1.88E-05$	29.04	0.680	$1.60E-05$
2#	9.7	0.259	$6.55E-06$	24.77	0.713	$2.04E-05$
3#	8.8	0.268	$9.44E-06$	22.64	0.747	$2.86E-05$
4#	8.4	0.273	$1.65E-05$	21.54	0.754	$4.67E-05$
5#	7.2	0.28	$2.17E-05$	18.97	0.793	$6.26E-05$
6#	6.1	0.285	$3.39E-05$	15.80	0.788	$9.37E-05$
7#	5.2	0.292	$3.42E-05$	13.57	0.818	$9.65E-05$
8#	4.6	0.304	$4.13E-05$	12.18	0.859	$12.03E-05$
9#	3.5	0.306	$3.63E-05$	9.35	0.876	$10.96E-05$
10#	1.4	0.314	$8.35E-05$	3.82	0.900	$24.06E-05$

TABLE 3: Operation coefficients of coal-fired power units.

Unit	\overline{Q}_i (MW)	\underline{Q}_i (MW)	ΔQ_i^+ (MW/h)	ΔQ_i^- (MW/h)	M_i^{on} (h)	M_i^{off} (h)	θ_i (%)
1#	250	600	280	-280	8	8	4.9
2#	200	500	240	-240	8	8	5.3
3#	200	450	210	-210	7	7	5.2
4#	180	400	180	-180	7	7	5.7
5#	150	350	150	-150	6	6	6.1
6#	150	300	150	-150	5	5	6.8
7#	120	300	120	-120	4	4	6.9
8#	100	250	100	-100	4	4	7.3
9#	70	150	70	-70	3	3	8.3
10#	30	100	50	-50	2	2	8.7

the grid purchase price of thermal power is 380 ¥/MW·h, and the price of standard coal is 800 ¥/t. The wind power unit equivalent utilization rate and system load distribution are set according to the literature [22] and listed in Table 4.

5.3. Simulation Results. The simulation was implemented in GAMS optimization software using the CPLEX 11.0 linear solver from ILOG_solver. The CPU time required for solving the problem for different case studies with an idea pad450 series laptop computer powered by a core T6500 processor and 4 GB of RAM was less than 10 s.

5.3.1. Case 1: Self-Scheduling of the System without DR or CET. This case mainly analyzes the impact of ESSs on wind power grid integration. The scheduling result is shown in Figure 1, in which the maximum load is 2860 MW, the minimum load is 1230 MW, and the peak-valley ratio is 2.33. The maximum load for the thermal power equivalent output curve is 2458 MW, the minimum load is 204 MW, and the peak-valley ratio is 12.07. Figure 1 shows the wind and thermal power outputs.

After introducing ESSs, the peak-valley ratio is 2, the coal consumption rate is reduced from 326 kg/MWh to 322.5 kg/MWh, the system profit is enhanced by 160000 yuan, the electricity from wind power delivered to the grid is increased from 16840.5 MWh to 18620.6 MWh, and the curtailed wind power rate is reduced by 8.1%. ESSs can smooth the demand load curve, provide backup service for wind power, and reduce the start-stop cost of thermal power units. The scheduling optimization results for the power system with and without ESSs are listed in Table 5.

If ESS operators hope to maximize their economic benefit in the optimization period, they should discharge all stored energy to gain more economic benefit. However, to reduce the impact of wind power output fluctuation, ESSs make charging and discharging decisions based on wind power output to reduce thermal power peak regulation, as shown in Figure 2. The ESSs charge when wind power output increases and discharge when wind power output decreases.

Total profit declines with addition of ESSs, due to their high investment cost and the lack of large-scale commercial production. China has gradually become concerned with large-scale ESS development; in the long term, it has great

TABLE 4: Equivalent utilization of wind power units.

Period	Load/MW	Utilization rate/%	Period	Load/MW	Utilization rate/%	Period	Load	Utilization rate/%
1	1100	33	9	2300	28	17	1700	32
2	1200	55	10	2500	11	18	1900	29
3	1400	68	11	2600	26	19	2100	17
4	1600	76	12	2500	23	20	2500	13
5	1700	67	13	2400	12	21	2300	23
6	1900	51	14	2300	20	22	1900	38
7	2000	36	15	2100	9	23	1500	33
8	2100	32	16	1800	21	24	1300	38

TABLE 5: Scheduling optimization result of power system in different cases.

	Wind power			Thermal power			System profit (10 ⁴ yuan)
	Generating capacity (MWh)	Grid proportion (%)	Curtailed wind power rate (%)	Generating capacity (MWh)	Grid proportion (%)	Curtailed wind power rate (%)	
Without ESSs	16840.5	31.2	24	37032.6	68.8	326	294
With ESSs	18620.6	34.6	15.9	35252.5	65.4	322.5	290

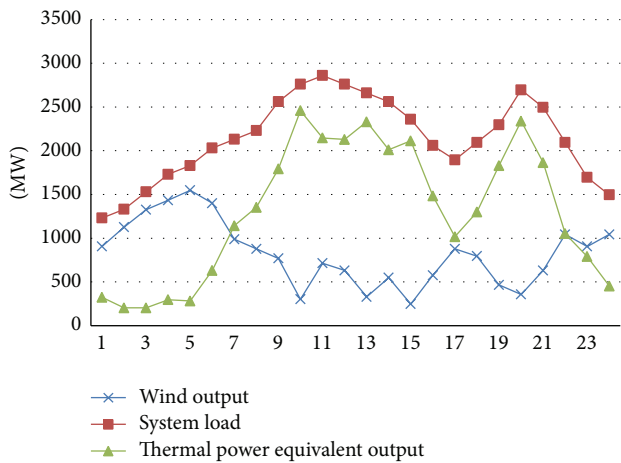


FIGURE 1: Output distribution of wind power and thermal power.

potential with the establishment of price mechanisms and mature technology.

5.3.2. Case 2: Self-Scheduling of the System with DR. The impact of DR on joint scheduling is analyzed in this case. DR can optimize customers' power consumption behavior and smooth the demand load curve. With α and β assumed to equal 3%, the system load curves for the two cases are shown in Figure 3.

According to Figure 3, the peak-valley differences for the two cases are 1400 MW and 1252 MW, respectively. The peak-valley ratios are 2.33 and 2. DR can smooth the demand load curve and reduce the curtailed wind power rate, which is 15.9% in Case 1 and 13.8% in Case 2. The utilization rate of wind power increases. The system scheduling optimization results for Case 2 are outlined in Table 6.

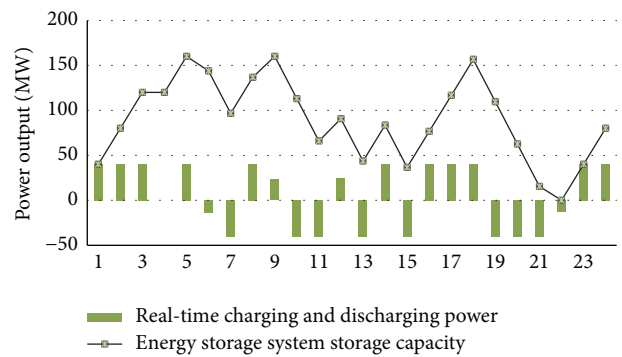


FIGURE 2: Charge and discharge optimization result for ESSs.

5.3.3. Case 3: Self-Scheduling of the System with CET. The impact of CET on the joint scheduling problem is analyzed in this case. The CET price is 100 yuan/t. 98% of total emissions in Case 1 are taken as the initial carbon emission permit, namely, 26171.73. The output of the thermal power units with different carbon trading prices is shown in Figure 4.

With a carbon trading price of 100 ¥/t, the output of wind power increased by 470.21 MWh, and the curtailed wind power rate decreased to 13.78%. CET would increase the cost of thermal power generation and change the system scheduling plan. The output of units with high carbon emission coefficient decreased, for example, unit 2 and unit 3. The output of units with low carbon emission coefficient rose, for example, unit 5. The optimization scheduling result in Case 3 is given in Table 6.

Compared with Cases 1 and 3, CET can increase the cost of thermal power generation and enhance the competitive advantage of wind power. System coal consumption decreased by 3.2072 million yuan, which is lower than that for Case 2. Profit increased to 2.9445 million yuan with increased wind power integration, which is lower than that for Case 2.

TABLE 6: System scheduling optimization results under different cases.

Scenario	Generating capacity (MWh)	Wind power		Generating capacity (MWh)	Thermal power		System profit (10^4 yuan)
		Grid proportion (%)	Curtailed wind power rate (%)		Grid proportion (%)	Curtailed wind power rate (%)	
Case 1	18620.60	35.40	15.90	35252.50	64.60	322.50	290.00
Case 2	19124.70	35.50	15.77	34748.40	64.50	318.72	301.54
Case 3	19090.81	35.44	13.78	34782.29	64.56	320.60	294.45
Case 4	19354.72	35.93	12.58	34518.38	64.07	314.82	312.72

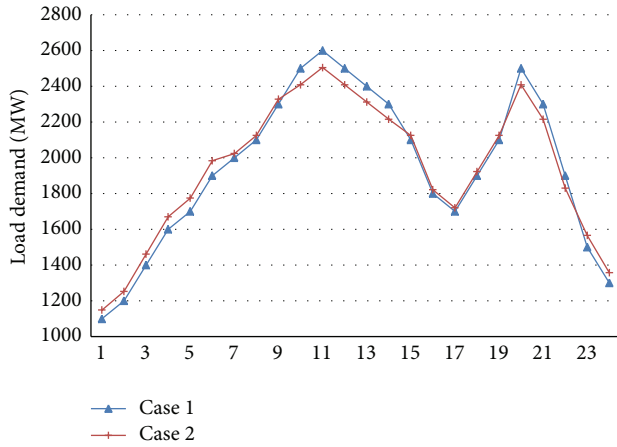


FIGURE 3: System load under different cases.

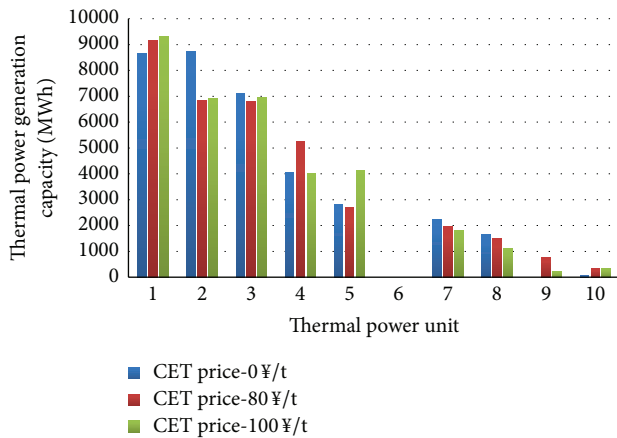


FIGURE 4: Comparison of thermal power generation under different carbon prices.

5.3.4. *Case 4: Self-Scheduling of System with DR and CET.* The synergistic effects of DR and CET on the joint scheduling problem are analyzed in Case 4. The maximum wind power output was 19354.72 MWh. The curtailed wind power rate declined from 19.5% to 12.58%. After introducing DR and CET, system coal consumption decreased to 314.82 kg/MWh. The maximum system profit was 3.1272 million yuan. The system optimization scheduling results under different cases are shown in Table 6.

In summary, DR leads to proper power consumption behavior, while system operation obtains an optimal result when introducing DR and CET at the same time. The comprehensive operation result of Case 4 is better than Cases 2 and 3, which shows that a collaborative optimization effect exists for DR and CET. The curtailed wind power rate and coal consumption reach the minimum when DR and CET are both introduced.

6. Conclusions

The randomness of wind power output has become the primary impediment to wind power grid integration. To improve the system's capability to consume wind power, proper backup service should be provided on the generation side. Demand response should also be introduced to incentivize customers to respond to system scheduling. This paper constructs a joint optimization scheduling model for wind power and energy storage systems with CET and DR. The simulation results show the following:

- (1) ESSs can provide backup service for wind power and increase the system's ability to consume wind power. However, total system generation profits would decrease due to the high fixed cost of ESSs. In the long term, China's large-scale ESS market has great potential with the establishment of a reasonable price mechanism and the development of mature energy storage technology.
- (2) Demand response can optimize customers' power consumption behavior, smooth the demand load curve, and improve wind power grid integration. After introducing DR, wind power grid integration is enhanced, the system power structure becomes reasonable, thermal power costs are reduced, and the total system generation profit increases.
- (3) Carbon emissions trading can increase the generation cost of thermal power units, enhance the advantages of integrating clean energy into the power grid, reduce the curtailed wind power rate, and optimize the system power structure. However, the total system generation profit is reduced due to the increased cost of thermal power generation.
- (4) With the introduction of DR and CET, system operation and scheduling obtained an optimal result. The total system profit increased and the high cost of

ESSs was reduced. In addition, the demand load curve was smoothed and the curtailed wind power rate and system coal consumption were reduced to the minimum. System profit increased to the maximum, which shows that a collaborative effect exists for DR and CET.

- (5) Though the proposed model examined the optimization effect of ESSs, CET, and DR on wind power grid integration, some constraints related to practical applications are ignored for the sake of convenient analysis and reaching a conclusion.

Nomenclature

t :	Time index
i :	Thermal power unit index
w :	Wind farm index
u :	Binary variable: 1 means in operation; 0 means not in operation
$Q_{s,t}^+$:	Charging power at time t
$Q_{s,t}^-$:	Discharging power at time t
θ_s :	Charging and discharging power loss coefficient
\overline{Q}_s :	Upper limit for charging and discharging power
Q_s^{\max} :	Maximum storage capacity of ESS
π_w :	Wind farm profit
π_c :	Thermal power unit profit
π_s :	ESSs profit
p_c :	Benchmark price of thermal power
$Q_{i,t}$:	Real-time generation power of unit i at time t
$\theta_{c,i}$:	Power consumption rate of unit i
C_{fuel} :	Generation fuel cost
$OM_{c,i}$:	Operation and maintenance cost of unit i
$D_{c,i}$:	Depreciation cost of unit i
p_{coal} :	Standard coal purchase price
$f_i(Q_{i,t})$:	Standard coal consumption of unit i at time t
a_i, b_i, c_i :	Coal consumption parameters of unit i
SU_i :	Start-up cost of unit i
SD_i :	Shutdown cost of unit i
$p_{s,\text{char}}$:	Electricity price when charging ESSs
$p_{s,\text{disc}}$:	Electricity price when discharging ESSs
F_s :	Fixed cost of ESSs
$T_{i,t-1}^{\text{on}}$:	Running time of unit i at time $t - 1$
$T_{i,t-1}^{\text{off}}$:	Shutdown time of unit i at time $t - 1$
M_i^{on} :	Shortest running time of unit i
M_i^{off} :	Unit shortest shutdown time of unit i
δ_t :	Equivalent utilization efficiency at time t
P_w :	Total installed capacity of wind farm w
$Q_{i,t}^{\max}$:	Maximum possible output of unit i at time t
R_t^{usr} :	Upward spinning reserve demand at time t
\overline{Q}_i :	Maximum possible energy generated by unit i at time t
ΔQ_i^+ :	Upward ramp rate of unit i

β_c :	Thermal power unit reserve coefficient
β_w :	Power reserve coefficient for wind turbines
$Q_{i,t}^{\min}$:	Minimum possible output of unit i at time t
R_t^{dsr} :	Downward spinning reserve demand at time t
\underline{Q}_i :	Minimum possible generation capacity of unit i
ΔQ_i^- :	Downward ramp rate of unit i
C_{CO_2} :	Carbon emission cost
E_{CO_2} :	Actual carbon emission of thermal unit during operation period
E_0 :	Total initial carbon emission right
p_{CO_2} :	Carbon trading price.

Competing Interests

The authors declare that they have no competing interests.

Acknowledgments

This paper is supported by Beijing Union Cultivate Scientific Research Project and the Fundamental Research Funds of the Central Universities of China (2015XS29). Dr. Pan Ge helped in improving the language of the paper.

References

- [1] J. Hetzer, D. C. Yu, and K. Bhattacharai, "An economic dispatch model incorporating wind power," *IEEE Transactions on Energy Conversion*, vol. 23, no. 2, pp. 603–611, 2008.
- [2] M. Grubb, T. Jamsb, and M. G. Pollitt, *Delivering a Low-Carbon Electricity System*, Cambridge University Press, 2008.
- [3] IPCC, *Climate Change 2007: The Physical Science Basis Contribution of Working Group I to the Fourth Assessment Report of the Intergovernmental Panel on Climate Change*, Intergovernmental Panel on Climate Change, 2007.
- [4] X. Yao, H. C. Zhou, A. Z. Zhang, and A. Li, "Regional energy efficiency, carbon emission performance and technology gaps in China: a meta-frontier non-radial directional distance function analysis," *Energy Policy*, vol. 84, pp. 142–154, 2015.
- [5] S. H. Jiang, Z. C. Ji, and Y. Wang, "A novel gravitational acceleration enhanced particle swarm optimization algorithm for wind-thermal economic emission dispatch problem considering wind power availability," *International Journal of Electrical Power & Energy Systems*, vol. 73, pp. 1035–1050, 2015.
- [6] X. Yuan, H. Tian, Y. Yuan, Y. Huang, and R. M. Ikram, "An extended NSGA-III for solution multi-objective hydro-thermal-wind scheduling considering wind power cost," *Energy Conversion and Management*, vol. 96, pp. 568–578, 2015.
- [7] K. Y. Wang, X. J. Luo, L. Wu, and X. C. Liu, "Optimal coordination of wind-hydro-thermal based on water complementing wind," *Renewable Energy*, vol. 60, pp. 169–178, 2013.
- [8] S. V. Papaefthymiou, V. G. Lakiotis, I. D. Margaritis, and S. A. Papathanassiou, "Dynamic analysis of island systems with wind-pumped-storage hybrid power stations," *Renewable Energy*, vol. 74, pp. 544–554, 2015.

- [9] S. V. Papaefthymiou and S. A. Papathanassiou, "Optimum sizing of wind-pumped-storage hybrid power stations in island systems," *Renewable Energy*, vol. 64, pp. 187–196, 2014.
- [10] Z. Ming, Z. Kun, and W. Liang, "Study on unit commitment problem considering wind power and pumped hydro energy storage," *International Journal of Electrical Power and Energy Systems*, vol. 63, pp. 91–96, 2014.
- [11] X. Wu, X. L. Wang, J. Li, J. Guo, K. Zhang, and J. Chen, "A joint operation model and solution for hybrid wind energy storage systems," *Proceedings of the Chinese Society of Electrical Engineering*, vol. 33, no. 13, pp. 10–17, 2013.
- [12] Z. Hu, H. Ding, and T. Kong, "A joint daily operational optimization model for wind power and pumped-storage plant," *Automation of Electric Power Systems*, vol. 36, no. 2, pp. 36–57, 2012.
- [13] H. J. Ding, Z. C. Hu, and Y. H. Song, "Stochastic optimization of the daily operation of wind farm and pumped-hydro-storage plant," *Renewable Energy*, vol. 48, pp. 571–578, 2012.
- [14] J. García-González, R. M. R. de la Muela, L. M. Santos, and A. M. Gonzalez, "Stochastic joint optimization of wind generation and pumped-storage units in an electricity market," *IEEE Transactions on Power Systems*, vol. 23, no. 2, pp. 460–468, 2008.
- [15] L. A. Greening, "Demand response resources: who is responsible for implementation in a deregulated market?" *Energy*, vol. 35, no. 4, pp. 1518–1525, 2010.
- [16] W. J. Niu, Y. Li, and B. B. Wang, "Demand response based virtual power plant modeling considering uncertainty," *Proceedings of the Chinese Society of Electrical Engineering*, vol. 34, no. 22, pp. 3630–3637, 2014.
- [17] M. A. López, S. D. L. Torre, S. Martín, and J. A. Aguado, "Demand-side management in smart grid operation considering electric vehicles load shifting and vehicle-to-grid support," *International Journal of Electrical Power & Energy Systems*, vol. 64, pp. 689–698, 2015.
- [18] N. I. Nwulu and X. H. Xia, "Multi-objective dynamic economic emission dispatch of electric power generation integrated with game theory based demand response programs," *Energy Conversion and Management*, vol. 89, pp. 963–974, 2015.
- [19] A. Ghasemi, S. S. Mortazavi, and E. Mashhour, "Hourly demand response and battery energy storage for imbalance reduction of smart distribution company embedded with electric vehicles and wind farms," *Renewable Energy*, vol. 85, pp. 124–136, 2016.
- [20] J. H. Wang, C. Liu, D. Ton, Y. Zhou, J. Kim, and A. Vyas, "Impact of plug-in hybrid electric vehicles on power systems with demand response and wind power," *Energy Policy*, vol. 39, no. 7, pp. 4016–4021, 2011.
- [21] L. W. Liu, C. X. Chen, Y. F. Zhao, and E. Zhao, "China's carbon-emissions trading: overview, challenges and future," *Renewable and Sustainable Energy Reviews*, vol. 49, pp. 254–266, 2015.
- [22] Y. Zhu, Y. P. Li, G. H. Huang, Y. R. Fan, and S. Nie, "A dynamic model to optimize municipal electric power systems by considering carbon emission trading under uncertainty," *Energy*, vol. 88, pp. 636–649, 2015.
- [23] M. Khalid and A. V. Savkin, "Minimization and control of battery energy storage for wind power smoothing: aggregated, distributed and semi-distributed storage," *Renewable Energy*, vol. 64, pp. 105–112, 2014.
- [24] L. W. Ju, Z. F. Tan, H. H. Li, X. Yu, and H. Zhang, "Multiobjective synergistic scheduling optimization model for wind power and plug-in hybrid electric vehicles under different grid-connected modes," *Mathematical Problems in Engineering*, vol. 2014, Article ID 179583, 15 pages, 2014.
- [25] Z. F. Tan, L. W. Ju, H. H. Li, C. Qin, and D. Peng, "Multiobjective CVaR optimization model and solving method for hydrothermal system considering uncertain load demand," *Mathematical Problems in Engineering*, vol. 2015, Article ID 741379, 10 pages, 2015.

Research Article

Parallelization of Eigenvalue-Based Dimensional Reductions via Homotopy Continuation

Size Bi, Xiaoyu Han, Jing Tian, Xiao Liang, Yang Wang, and Tinglei Huang

Institute of Electronics, Chinese Academy of Sciences, North Fourth Ring Road West 98, Beijing 100190, China

Correspondence should be addressed to Tinglei Huang; tlhuang@mail.ie.ac.cn

Received 12 December 2015; Accepted 22 February 2016

Academic Editor: Jinyun Yuan

Copyright © 2016 Size Bi et al. This is an open access article distributed under the Creative Commons Attribution License, which permits unrestricted use, distribution, and reproduction in any medium, provided the original work is properly cited.

This paper investigates a homotopy-based method for embedding with hundreds of thousands of data items that yields a parallel algorithm suitable for running on a distributed system. Current eigenvalue-based embedding algorithms attempt to use a sparsification of the distance matrix to approximate a low-dimensional representation when handling large-scale data sets. The main reason of taking approximation is that it is still hindered by the eigendecomposition bottleneck for high-dimensional matrices in the embedding process. In this study, a homotopy continuation algorithm is applied for improving this embedding model by parallelizing the corresponding eigendecomposition. The eigenvalue solution is converted to the operation of ordinary differential equations with initialized values, and all isolated positive eigenvalues and corresponding eigenvectors can be obtained in parallel according to predicting eigenpaths. Experiments on the real data sets show that the homotopy-based approach is potential to be implemented for millions of data sets.

1. Introduction

Dimensional reduction has been an important technology for data visualization and analysis in the age of big data. One of these methods is based on eigendecomposition used widely in observing intrinsic associations between data items by 2D graphic. With this context, the solution of eigenvalues is an essential step regarded as a multidimensional scaling (MDS) problem to establish low-dimensional embedding spaces with a distance matrix. The capacity of an implemented eigendecomposition determines what scale of data can be dealt with. However, there is a bottleneck of eigendecomposition in embedding large-scale data sets directly [1–3]. These eigenvalue-based approaches have been developed to two categories: the direct solution immediately acquires the eigenpairs (eigenvalues and associated eigenvectors) from the distance matrix [4] and the indirect solution selects a small set of landmark points to calculate the eigenvalues; then these estimated eigenpairs are fed to approximate the entire embedding [1]. All of them are operated in a serial computational mode [5], leading to some negative influences in processing massive data sets: firstly the indirect methods need to select

landmark set that will break up embedded space by the error, generated from approximate calculation [1, 3]; secondly they both have low efficiency needing a balance between the representational precision and computational efficiency [4, 5]; thirdly they both are prone to omit some positive eigenvalues that reduces the maximum dimensions available for dimensional reduction [2].

This work investigates the parallelization of eigenvalue-based dimensional reductions in the context of large-scale data sets. It is aiming at providing a paralleled solution for data reduction in practice. The general frameworks are often divided into two categories [4], distance scaling and classical scaling; the methods based on the spring model of distance scaling [6] are prone to local minima and can only be used to embed data in two or three dimensions [7], while classical scaling, the eigenvalue-based approaches, [8] has been considered as a useful replacement for large graphs. To overcome the eigenvalue problem in big processing, several algebraic operations have been conducted. One of the most useful methods is the Nyström matrix approximation [1, 2, 9]. It samples a small matrix from the distance matrix to solve eigenvalues and then approximates objective embedding.

This workflow is closely related between each segment of computation. For matrix sampling, some studies on the selecting strategy [3, 10–12] make the approach worse for parallelization to cut the time consumed consumption. In today's eigencalculation technology, it is well established that eigendecomposition of large and sparse matrix can be resolved by some novel numerical solutions, such as Block Lanczos [13], PCG Lanczos [14], and homotopy [15, 16]. Resorting to these high-performance approaches may expand considerably the applications of dimensional reductions.

As to the homotopy continuation method, it is suggested as an alternative to find all isolated eigenvalues of a large matrix. It is demonstrated that there are n distinct smooth curves connecting trivial solutions to desired eigenvalues [17] and then a proof of the existence of homotopy curves for eigenvalue problems is presented by [18]. Reference [19] reports the numerical experience of the homotopy for computing eigenvalues of real symmetric tridiagonal matrices. It enables eigenvalues to calculate for embedding in parallel. For the recent studies, [16] combines with a divide-and-conquer approach to find all the eigenvalues and eigenvectors of a diagonal-plus-semiseparable matrix. Reference [20] establishes some bounds to justify the Newton method in constructing the homotopy curves.

In this paper, a parallelization of eigenvalue-based dimensional reduction (HC-MDS, Homotopy Continuation Multi-dimensional Scaling) via the homotopy continuation method is proposed. Unlike those Nyström-based approaches, HC-MDS can directly solve most positive eigenvalues in parallel from large distance matrices (transformed from more than 60,000 data items). With the theory, we construct a homotopy continuation function to link a trivial set with the object eigenpairs. In this case, the eigenvalue problem is converted to the solution of ordinary differential equations (ODE). Each eigenpair will be obtained by tracing the ordinary differential function with corresponding initialized values that means the solutions of eigenvalues can be implemented in independent computational threads. This model will bring an advantage that allows scheduling computational resources for each eigenpair calculation, so that it can be enhanced on parallel or distributed systems.

The remainder of this report is organized as follows. Section 2 talks about the review on the eigenvalue-based MDS. Section 3 outlines the methodologies used in this paper. The experiments are presented in Section 4. Finally, we draw a conclusion in Section 5.

2. Background

Most eigenvalue-based dimensional reductions involve a step of spectral decomposition for solving eigenvalues, such as LLE [21], Laplacian Eigenmaps [22], Isomap [23], and L-Isomap [1]. A more fundamental MDS by using the power method for eigenpairs is illustrated in [4]. The aim of eigenvalue calculation in embedding is to obtain eigenpairs of the inner product matrix, which is converted by the distance matrix using a "double-centering." A low-dimensional space is then built by those positive ones among the estimated eigenvalues and corresponding eigenvectors. Without loss of

generality, the general eigenvalue-based dimensional reduction is summarized as follows.

Procedure. Eigenvalues in embedding are shown as follows.

Step 1. Let $\mathbf{D} \in \mathbf{R}^{n \times n}$ denote the distance of square matrix that is symmetric and real valued. An existing inner product matrix \mathbf{B} ($b_{ij} \in \mathbf{B}$) can be derived from \mathbf{D} ($d_{ij} \in \mathbf{D}$) as $b_{ij} = -(1/2)(d_{ij}^2 - (1/n) \sum_{i=1}^n d_{ij}^2 - (1/n) \sum_{j=1}^n d_{ij}^2 + (1/n^2) \sum_{i=1}^n \sum_{j=1}^n d_{ij}^2)$.

Step 2. Implement one of eigendecomposition methods into \mathbf{B} , as $\mathbf{B} = \mathbf{Q}\mathbf{A}\mathbf{Q}^T$; \mathbf{A} is a diagonal matrix of eigenvalues and \mathbf{Q} is a matrix whose columns are corresponding orthonormal eigenvectors.

Step 3. \mathbf{X} is the embedded space that can be generated by $\mathbf{X} = \mathbf{Q}^+ \sqrt{\mathbf{A}^+}$ with $(\mathbf{Q}^+, \mathbf{A}^+) \subseteq (\mathbf{Q}, \mathbf{A})$, where $(\mathbf{Q}^+, \mathbf{A}^+)$ is a combination of the positive eigenpairs among (\mathbf{Q}, \mathbf{A}) . Those negative and zero eigenpairs should be discarded because of the arithmetical rule of extraction of square root.

If the Nyström approximate method is applied for approximating embedding [2], the following steps should be proceeded.

Step 4. Assume that the inner product matrix \mathbf{B} belongs to a partition of the original inner product matrix $\begin{bmatrix} \mathbf{B} & \mathbf{C} \\ \mathbf{C} & \mathbf{D} \end{bmatrix}$. The remainder embedded space \mathbf{X}' is approximated by $\mathbf{X}' = \sqrt{\mathbf{A}^+} \mathbf{Q}^+ \mathbf{C}$ with the error estimation $\|\mathbf{D} - \mathbf{C}^T \mathbf{B}^{-1} \mathbf{C}\|$.

Step 5. Let \mathbf{X}' be incorporated with \mathbf{X} ; we finally obtain the entire embedded space as $\mathbf{X}_{\text{entire}} = (\mathbf{X}, \mathbf{X}')$.

For embedding with eigenpairs, most investigations do not discuss how the eigenpairs are generated but commonly draw a conclusion that eigendecomposing for large symmetric, dense matrices is an expensive calculation. Currently the embedding technologies applied on large-scale data sets are mainly used for data visualization. Since this kind of application only needs two or three eigenvalues, the largest one and the second largest one are solved by the existing eigenvalue methods, for example, the power iteration method [4]. However, this eigenvalue approach operates in a serial way and its computation is considerably inefficient [4]. To capture more positive eigenvalues for embedding, QR has been justified in small to medium matrices [24] and all eigenvalues will be solved including negative ones and zero ones that are useless and consuming CPU time; Lanczos, a family of eigenpair solutions based on the Lanczos process, has demonstrated that it is available for millions of data items in actual engineering applications [14], but they may have the problem to complete computing procedure once related errors accumulated to a certain range [24]. Therefore, we investigate an alternative, the homotopy continuation method, for parallelization of embedding. Compared to the presented works, we employ a Runge-Kutta (R-K) method with step estimation to control tracking procedures of homotopy curves that can omit the constraints for eigenpairs tracking [20].

3. Methodology

The homotopy continuation method consists of two parts: how to convert the eigendecomposition of embedding to the solution of ODE with initialized values (Section 3.1) and how to calculate each ODE of eigenpair using numerical methods (Section 3.2).

3.1. Homotopy for Eigenpairs. Before constructing the homotopy function, the symmetric square matrix \mathbf{B} should be transformed to the symmetric tridiagonal matrix \mathbf{A} by the Householder transformation [20]. The eigenvalues of \mathbf{A} are equal to the eigenvalues of \mathbf{B} . We obtain the eigenvalues of \mathbf{B} through the approximate eigendecomposition to \mathbf{A} , and then the corresponding eigenvectors of \mathbf{B} can be reversed out by their eigenvalues. For eigendecomposing to the transformed matrix \mathbf{A} , we consider the eigenvalue problem as

$$\mathbf{A}\mathbf{x} = \lambda\mathbf{x}, \quad (1)$$

where \mathbf{x} is the corresponding eigenvector of the eigenvalue λ by $\mathbf{x} = (x_1, \dots, x_n)^T \in \mathbf{R}^n$. The orthogonality of eigenvectors is expressed by $\mathbf{x}^T \mathbf{x} = 1$.

Associating (1) with the orthogonality of eigenvectors, we convert the eigenvalue problem to an optimal problem as

$$f(\mathbf{x}, \lambda) = \begin{bmatrix} \mathbf{A}\mathbf{x} - \lambda\mathbf{x} \\ \frac{1}{2}(1 - \mathbf{x}^T \mathbf{x}) \end{bmatrix} = \mathbf{O} \quad (\mathbf{x}, \lambda) \in \mathbf{R}^n \times \mathbf{R}, \quad (2)$$

where \mathbf{O} is the corresponding zero vector by $\mathbf{O} \in \mathbf{R}^n$.

To find the optimum set of such object function, the homotopy method has been recommended. We thus construct a homotopy function to link the object function with an auxiliary function by the Newton method [20]:

$$\begin{aligned} H(\mathbf{x}(t), \lambda(t), t) &= t \begin{bmatrix} \mathbf{A}\mathbf{x}(t) - \lambda(t)\mathbf{x}(t) \\ \frac{1}{2}(1 - \mathbf{x}^T(t)\mathbf{x}(t)) \end{bmatrix} \\ &+ (1-t) \begin{bmatrix} \mathbf{A}_0\mathbf{x}(t) - \lambda(t)\mathbf{x}(t) \\ \frac{1}{2}(1 - \mathbf{x}^T(t)\mathbf{x}(t)) \end{bmatrix} \\ &= \begin{bmatrix} \mathbf{A}(t)\mathbf{x}(t) - \lambda(t)\mathbf{x}(t) \\ \frac{1}{2}(1 - \mathbf{x}^T(t)\mathbf{x}(t)) \end{bmatrix} = \mathbf{O}, \end{aligned} \quad (3)$$

where $\mathbf{x}(t) \in \mathbf{R}^n$, $\lambda(t) \in \mathbf{R}$, $\{t \in \mathbf{R} \mid 0 \leq t \leq 1\}$, and $\mathbf{A}(t) = \mathbf{A}_0 + t(\mathbf{A} - \mathbf{A}_0)$. The constant matrix \mathbf{A}_0 needs to be user-defined, where its eigenpairs are apparently captured; for example, if $\mathbf{A} \in \mathbf{R}^{3 \times 3}$, we often set \mathbf{A}_0 as $\begin{bmatrix} 1 & 0 & 0 \\ 0 & 2 & 0 \\ 0 & 0 & 3 \end{bmatrix}$. Obviously, the diagonal elements 1, 2, and 3 are exactly the eigenvalues of \mathbf{A}_0 and $\begin{bmatrix} 1 \\ 0 \\ 0 \end{bmatrix}$, $\begin{bmatrix} 0 \\ 1 \\ 0 \end{bmatrix}$, $\begin{bmatrix} 0 \\ 0 \\ 1 \end{bmatrix}$ are the corresponding eigenvectors, respectively.

Since there are n distinct smooth curves called eigenpaths connecting the trivial solution of \mathbf{A}_0 to the desired eigenpairs

of \mathbf{A} [17], each eigenpath is expressed by an ODE with a pair of initial values as

$$\begin{bmatrix} \frac{d\mathbf{x}}{dt} \\ \frac{d\lambda}{dt} \end{bmatrix} = \begin{bmatrix} \lambda(t)\mathbf{I} - \mathbf{A}(t) & \mathbf{x}(t) \\ \mathbf{x}^T(t) & 0 \end{bmatrix}^{-1} \begin{bmatrix} (\mathbf{A} - \mathbf{A}_0)\mathbf{x}(t) \\ 0 \end{bmatrix} \quad (4)$$

$$(\mathbf{x}(0), \lambda(0))^T = (\mathbf{y}_i, r_i)^T,$$

where the interval of t is $[0, 1]$ and the initial values $(\mathbf{x}(0), \lambda(0))^T$ are given by $(\mathbf{y}_i, r_i)^T$ obtained from one eigenpair of \mathbf{A}_0 . Solving (4) with all initial values given by \mathbf{A}_0 , the eigendecomposition of \mathbf{B} can be implemented in parallel. We show the derivation of (4) from (3) as follows.

We take the derivative of (3):

$$\begin{aligned} \frac{d(H)}{d(t)} &= \mathbf{O}, \\ \begin{bmatrix} (\mathbf{A} - \mathbf{A}_0)\mathbf{x}(t) + \mathbf{A}(t)\frac{d\mathbf{x}}{dt} - \frac{d\lambda}{dt}\mathbf{x}(t) - \lambda(t)\frac{d\mathbf{x}}{dt} \\ -\mathbf{x}^T(t)\frac{d\mathbf{x}}{dt} \end{bmatrix} \\ &= \mathbf{O}, \end{aligned} \quad (5)$$

$$\begin{bmatrix} \lambda(t)\mathbf{I} - \mathbf{A}(t) & \mathbf{x}(t) \\ \mathbf{x}(t) & \mathbf{0} \end{bmatrix} \begin{bmatrix} \frac{d\mathbf{x}}{dt} \\ \frac{d\lambda}{dt} \end{bmatrix} = \begin{bmatrix} (\mathbf{A} - \mathbf{A}_0)\mathbf{x}(t) \\ \mathbf{0} \end{bmatrix},$$

$$\begin{bmatrix} \frac{d\mathbf{x}}{dt} \\ \frac{d\lambda}{dt} \end{bmatrix} = \begin{bmatrix} \lambda(t)\mathbf{I} - \mathbf{A}(t) & \mathbf{x}(t) \\ \mathbf{x}(t) & \mathbf{0} \end{bmatrix}^{-1} \begin{bmatrix} (\mathbf{A} - \mathbf{A}_0)\mathbf{x}(t) \\ \mathbf{0} \end{bmatrix}.$$

Adding the initialized values, we obtain the ODE of homotopy curve as (4). The solving procedure of (4) is the solution of ODE within $0 \leq t \leq 1$. When t increases to 1, each eigenpair of \mathbf{A} is obtained as $(\mathbf{x}|_{t=1}, \lambda|_{t=1})^T$.

We need to transform the calculated eigenvector because the eigenvector from the homotopy method cannot be applied to build an embedded space directly. The transforming formula is described as

$$\mathbf{x}_{\text{real}} = (\mathbf{B} - \lambda\mathbf{I})^{-1} (\mathbf{A} - \lambda\mathbf{I})\mathbf{x}, \quad (6)$$

where \mathbf{x}_{real} is the eigenvector of \mathbf{B} corresponding to λ .

Since it is proved that the eigenpaths of homotopy function are continuous and monotonous [17, 18], this brings an advantage for forecasting the trend of eigenpaths: the negative eigenvalues and undersize positive eigenvalues can be estimated by the tracking of homotopy function curves, for example, Figure 1. Specifically, each trace of eigenvalues evolution is implemented in an independent computational thread. When the trend of an ODE is predicted to be negative (red tracks), the associated computation is regarded as not effective and shut down. With this feature, it enables dynamical allocation of computing resource.

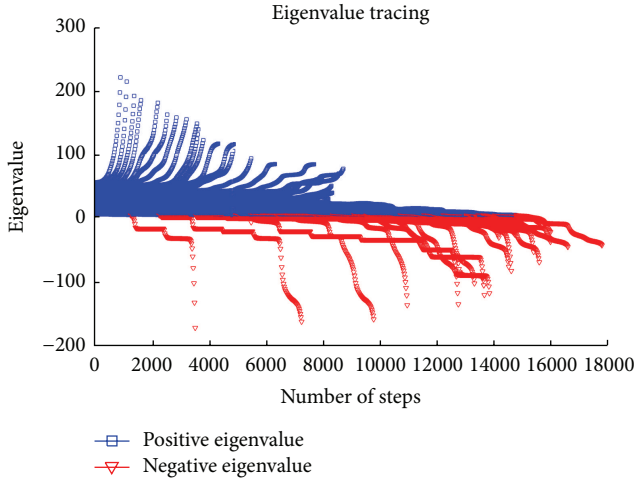


FIGURE 1: A 50×50 distance matrix by the prediction of positive eigenvalues.

```

Input  $f(t, y), t_0, y_0, \text{tol}, \alpha$ 
Output  $y_n$ 
(1)  $\mathbf{k}_1 = f(t_0, y_0)$ 
(2)  $h = \text{initialize step}$ 
(3)  $t = 0$ 
While  $t \leq 1$  do
  (4)  $\mathbf{k}_2 = f\left(t_n + \frac{h}{2}, y_n + \frac{h}{2}\mathbf{k}_1\right)$ 
  (5)  $\mathbf{k}_3 = f\left(t_n + \frac{3h}{4}, y_n + \frac{3h}{4}\mathbf{k}_2\right)$ 
  (6)  $y_{n+1} = y_n + \frac{h}{24}(7\mathbf{k}_1 + 6\mathbf{k}_2 + 8\mathbf{k}_3 + 3\mathbf{k}_4)$ 
  (7)  $\mathbf{k}_4 = f\left(t_n + h, y_n + \frac{h}{9}(2\mathbf{k}_1 + 3\mathbf{k}_2 + 4\mathbf{k}_3)\right)$ 
  (8)  $e = \left|\frac{h}{72}(-5\mathbf{k}_1 + 6\mathbf{k}_2 + 8\mathbf{k}_3 - 9\mathbf{k}_4)\right|$ 
  If  $e \leq \text{tol}$  then
     $\mathbf{k}_1 = \mathbf{k}_4$ 
     $t = t + h$ 
  End
   $h = \alpha \left(\frac{\text{tol}}{e}\right)^{1/3} h$ 
End

```

ALGORITHM 1: R-K method for automatic step.

3.2. *Numerical Calculation of ODE.* For avoiding overflow during calculating a massive matrix, we normalize the matrix \mathbf{B} in Section 3.1 as

$$d'_{ij} = \frac{d_{ij} - \min(\mathbf{B})}{\max(\mathbf{B}) - \min(\mathbf{B})}, \quad (7)$$

where $\max(\mathbf{B})$ and $\min(\mathbf{B})$ are the maximum and minimum, respectively.

The specific steps are as shown in Algorithm 1.

For solving the ODE problem in (4), we adopt an automatic step method based error estimation [25, 26]. Let

$\mathbf{y} = (\mathbf{x}, \lambda)^T$; the \mathbf{y} is iterative to calculate each homotopy curve by

$$\begin{aligned}
 y_{n+1} &= y_n + \frac{h}{24}(7\mathbf{k}_1 + 6\mathbf{k}_2 + 8\mathbf{k}_3 + 3\mathbf{k}_4), \\
 \mathbf{k}_1 &= f(t_n, y_n), \\
 \mathbf{k}_2 &= f\left(t_n + \frac{h}{2}, y_n + \frac{h}{2}\mathbf{k}_1\right), \\
 \mathbf{k}_3 &= f\left(t_n + \frac{3h}{4}, y_n + \frac{3h}{4}\mathbf{k}_2\right), \\
 \mathbf{k}_4 &= f\left(t_n + h, y_n + \frac{h}{9}(2\mathbf{k}_1 + 3\mathbf{k}_2 + 4\mathbf{k}_3)\right),
 \end{aligned} \quad (8)$$

where $f(\cdot)$ is the ODE of (4) and the parameter h is calculated by

$$h = \alpha \left(\frac{\text{tol}}{e}\right)^{1/3} h. \quad (9)$$

For estimating the error of each eigenpath tracking, the e is operated by

$$e = \left|\frac{h}{72}(-5\mathbf{k}_1 + 6\mathbf{k}_2 + 8\mathbf{k}_3 - 9\mathbf{k}_4)\right|, \quad (10)$$

where α is customized for h and the tol is an allowable error referring to an empirical value.

4. Simulation

In this section, we experiment on two large data sets to embed a series of low-dimensional spaces (2, 3, 50, and 100 dimensions) for comparison between our parallelized approach and the typical serial mode of dimensional reduction. The assessments are implemented in terms of the scale-independent quality criteria [27], relative distance error [2], and CPU time. The first two tests reflect the precisions of resulting embedded spaces indirectly and directly, respectively. The third part is the empirical evaluation of performance period.

4.1. *Experiments Setup.* Our experiments compare the following embedding methods with the three eigendecompositions modes: QR, Lanczos, and homotopy. Embedding with the first two modes is a typical serial workflow that worked in a single process, while it is operated in parallel in the third mode:

- (i) classical metric multidimensional scaling [4] (CMDS),
- (ii) landmark multidimensional scaling employing the Nyström matrix approximation [2] (LMDS),
- (iii) isometric feature mapping [21] (Isomap),
- (iv) landmark isometric feature mapping [1] (L-Isomap),
- (v) t-distributed stochastic neighbor embedding [7] (t-SNE).

TABLE 1: Scalar quality criteria derived from the curves in Figure 3, for Corel Image Features.

Case	Q_{local}	Q_{global}	dist-err
$\text{LMDS}_{(\text{QR+pivots+Eucl})-2,3}$	0.431/0.606	0.612/0.689	0.682/0.517
$\text{LMDS}_{(\text{QR+pivots+Eucl})-50,100}$	0.661/0.664	0.723/0.749	0.459/0.422
$\text{CMDS}_{(\text{Homotopy+Eucl})-2,3}$	0.389/0.504	0.608/0.649	0.607/0.567
$\text{CMDS}_{(\text{Homotopy+Eucl})-50,100}$	0.565/0.570	0.704/0.743	0.445/0.494
$\text{CMDS}_{(\text{Lanczos+Eucl})-2,3}$	0.409/0.514	0.706/0.751	0.624/0.582
$\text{CMDS}_{(\text{Lanczos+Eucl})-50,100}$	0.558/0.586	0.823/0.834	0.585/0.524
$\text{Isomap}_{(\text{Homotopy+Geod})-2,3}$	0.542/0.569	0.691/0.733	0.654/0.534
$\text{Isomap}_{(\text{Homotopy+Geod})-50,100}$	0.669/0.697	0.785/0.806	0.428/0.453
$\text{Isomap}_{(\text{Lanczos+Geod})-2,3}$	0.567/0.586	0.748/0.772	0.657/0.543
$\text{Isomap}_{(\text{Lanczos+Geod})-50,100}$	0.734/0.753	0.764/0.825	0.436/0.421
$\text{L-Isomap}_{(\text{QR+pivots+Geod})-2,3}$	0.553/0.620	0.606/0.704	0.646/0.615
$\text{L-Isomap}_{(\text{QR+pivots+Geod})-50,100}$	0.601/0.598	0.807/0.813	0.439/0.481
$\text{t-SNE}_{(\text{Geod})-2,3}$	0.427/0.458	0.784/0.818	0.315/0.263
$\text{t-SNE}_{(\text{Eucl})-2,3}$	0.432/0.486	0.758/0.801	0.262/0.207

As the third part testing for performance reference, the t-SNE and its relative variants are well established which are available in massive data [7], based on distance scaling. We randomly initialize the embedding of t-SNE. Both the Euclidean distance and geodesic distance are used. Specifically the geodesic distances are approximated by 6-ary neighborhoods using the Euclidean graph. Parameters of the comparative methods are set to typical values, with no further optimization. All experiments are carried out in a distributed computing environment built by four computers (amount of 20 GB memory).

For the quality criteria, we assess embedding in terms of $(Q_{\text{local}}, Q_{\text{global}}, Q(K))$, a rank-based criteria [27], where Q_{local} indicates the local preservation of neighborhoods, Q_{global} shows a global consensus of the embedding, and $Q(X)$ measures the preservation of K -ary neighborhoods in a straightforward way; relative distance error (dist-err) [2] is computed by average distance value between original distance matrix and reconstructed matrix; CPU time records computing time of the eigendecomposition procedure in embedding.

4.2. Corel Image Features. The Corel Image Features is a UCI KDD data set consisting of features extracted from 68,040 images. Four sets of features are extracted: 32 color histograms, 32 color layout histograms, 9 color moments, and 16 texture features. Images with missing features are ignored, leaving 64,433 images. We computed the Euclidean distance between two image feature vectors from each feature set and combined them to a single distance following [2]. The first 5000 data items are selected as the pivot points used for the Nyström matrix approximation.

For the comparison between local and global preservation and mean distance error, Table 1 summarizes the results. The selection for the serial and parallel computational modes clearly impacts on the embedded results when operated around hundreds of thousands of items. To find an embedding space, the QR-based methods need the Nyström approximation to reduce the scale of matrices in middle

procedure. The results are in the rows of $\text{LMDS}_{(\text{QR+pivots+Eucl})}$ and $\text{L-Isomap}_{(\text{QR+pivots+Geod})}$. These proximate methods, $\text{LMDS}_{(\text{QR+pivots})}$ and $\text{L-Isomap}_{(\text{QR+pivots})}$, have acceptable precisions for 0.422 and 0.481 of the mean distance error to the 100-dimensional spaces, respectively. The homotopy-based and Lanczos-based methods are both successful obtaining sufficient numbers of positive eigenpairs for embedding with all the desired numbers of dimensions. The Lanczos-based approaches outperform the homotopy-based ones in the three criteria. Embedding with the geodesic distance shows better results than the Euclidean ones in the same embedding type. The distance errors in all competitive models decrease with the increase of embedding dimensions. Embedding with the homotopy outperforms slightly compared to those Lanczos-based and QR-based ones in distance error.

For a more intuitive comparison, Figures 2 and 3 show the results of two-dimensional embedding refereed with the pair of scalar values, Q_{local} and Q_{global} . From Figure 2, the local preservation of the homotopy-based embedding with the Euclidean distance is found in the bottom of the others, while its corresponding geodesic version reaches the third place. That implies that the geodesic distance may be more suitable for this kind of eigenvalue-based embedding, and the similar result occurs in the next data set. With the geodesic distance, t-SNE runs the highest result according to the coordinate of Q_{local} and Q_{global} in Figure 3. The homotopy method for embedding the Euclidean distance matrix races the last one that indicates that it may be problematic with the solving accuracy of eigenpairs and its geodesic version with Isomap shows a moderate performance.

For the comparison in CPU time, the items of X -axis in Figure 4 correspond to the first column of Table 1. The homotopy approaches save the most CPU time for 12 min and 58 s and 12 min and 26 s ($\text{CMDS}_{(\text{Homo+Eucl})}$ and $\text{Isomap}_{(\text{Homo+Geod})}$) except the approximation methods in Figure 4 (the red bars) by taking advantage of parallel computational design. The time consuming with embedding approximation of the Nyström is far less than the direct

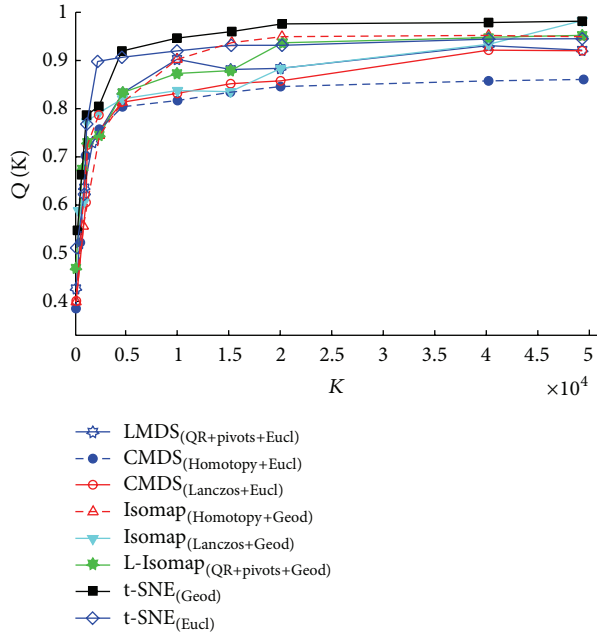


FIGURE 2: Behavior curves for assessing local embedding of Corel Image Features.

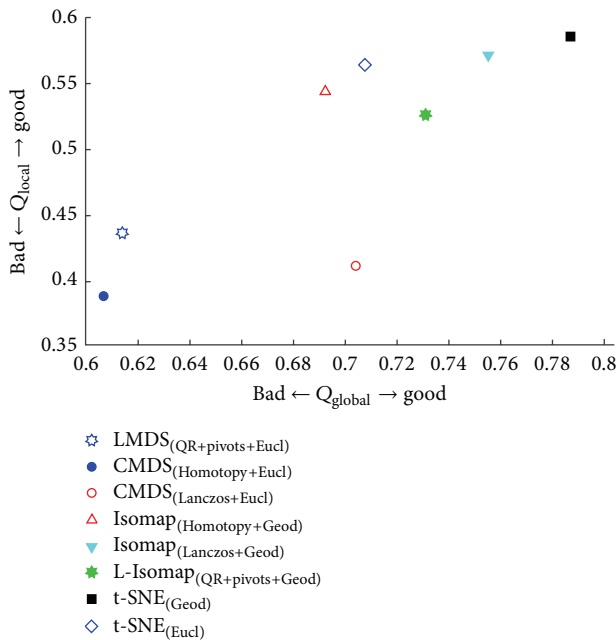


FIGURE 3: Quality for assessing embedding of Corel Image Features.

methods (homotopy and Lanczos), achieving the embedding tasks by 3 min and 52 s and 3 min and 45 s (the first and eighth bars), although the homotopy-based approach is enhanced by the parallel computational environment. The two-version t-SNE (Geodesic and Euclidean distance) runs in the last two of CPU time for 36 min and 53 s and 35 min and 18 s. The CPU times of CMDS_(QR+Eucl) and Isomap_(QR+Geod) are not recorded because the QR method cannot be applied to

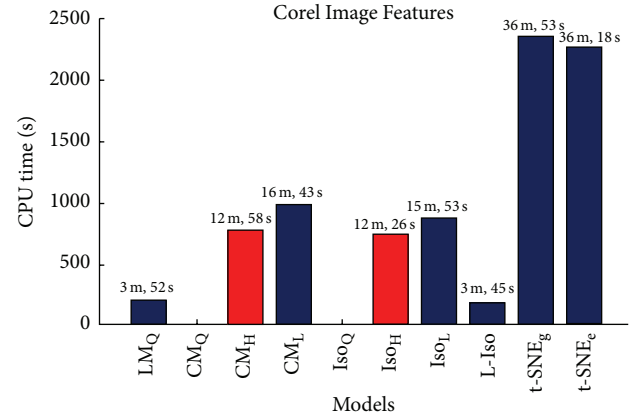


FIGURE 4: CPU time for embedding of Corel Image Features.

the eigendecomposition directly for the large square matrices which exceed 8,000 dimensions.

4.3. *PNAS Titles*. The title data was obtained by crawling the PNAS website and yielded 79,801 long sentences. Each title is represented by the standard tf-idf vector representation. The distance matrix is obtained following the cosine distance measured by all title vectors. We employ the Nyström approximation with the first 5000 pivots of data items.

The results of assessing local and global preservation and mean distance error are given in Table 2. Under experiments on the text data set, we demonstrate once again the fact that the QR eigendecomposition is unable to implement in the large-scale data set. The corresponding results are absent denoted by “-.” Both in the models of CMDS and Isomap, the Lanczos-based methods run ahead of the homotopy-based ones in terms of Q_{local} , Q_{global} , and dist-err, although the advance is slight. The QR-based LMDS with the matrices approximation is better than L-Isomap when the scale of data increases, but they both fall behind the homotopy method in the three criteria. The homotopy-based Isomap outperforms the homotopy-based and Lanczos-based CMDS but slightly runs behind the Lanczos-based Isomap.

From Figures 5 and 6, the results of the text data set also show that the embedding constructed by geodesic distance represents the original matrix better than them with the Euclidean distance. The top three are all based on geodesic distance: Isomap_(Homotopy+Geod), t-SNE_(Geod), and Isomap_(Lanczos+Geod). In this case, the approximation with the landmarks or pivots seems to be not good at representing the global preservation for the entire embedding space. The embedding of t-SNE applying with the Euclidean distance declines slightly both in the local and global parts.

The results of time consuming are shown in Figure 7. The LMDS and L-Isomap are the top two for 3 min and 46 s and 4 min and 01 s, respectively (the first and eighth bars). The homotopy-based methods are in the second echelon (red bars) for 17 min and 23 s and 17 min and 38 s. The Lanczos-based approaches are in the third level for 26 min and 18 s and 32 min and 33 s. The t-SNE based methods consume the most time for 57 min and 32 s and 61 min and 28 s. Regardless of

TABLE 2: Scalar quality criteria derived from the curves in Figure 5, for PNAS Titles.

Case	Q_{local}	Q_{global}	dist-err
$\text{LMDS}_{(\text{QR+pivots+Eucl})-2,3}$	0.502/0.522	0.725/0.755	0.564/0.522
$\text{LMDS}_{(\text{QR+pivots+Eucl})-50,100}$	0.632/0.616	0.783/0.786	0.421/0.404
$\text{CMDS}_{(\text{Homotopy+Eucl})-2,3}$	0.402/0.432	0.721/0.768	0.594/0.542
$\text{CMDS}_{(\text{Homotopy+Eucl})-50,100}$	0.536/0.546	0.714/0.725	0.434/0.426
$\text{CMDS}_{(\text{Lanczos+Eucl})-2,3}$	0.453/0.585	0.743/0.745	0.572/0.482
$\text{CMDS}_{(\text{Lanczos+Eucl})-50,100}$	0.597/0.598	0.723/0.775	0.420/0.397
$\text{Isomap}_{(\text{Homotopy+Geod})-2,3}$	0.434/0.525	0.798/0.799	0.573/0.569
$\text{Isomap}_{(\text{Homotopy+Geod})-50,100}$	0.526/0.525	0.763/0.787	0.405/0.384
$\text{Isomap}_{(\text{Lanczos+Geod})-2,3}$	0.521/0.547	0.782/0.721	0.594/0.527
$\text{Isomap}_{(\text{Lanczos+Geod})-50,100}$	0.584/0.593	0.780/0.805	0.447/0.332
$\text{L-Isomap}_{(\text{QR+pivots+Geod})-2,3}$	0.528/0.578	0.732/0.772	0.602/0.584
$\text{L-Isomap}_{(\text{QR+pivots+Geod})-50,100}$	0.689/0.702	0.813/0.818	0.574/0.486
$\text{t-SNE}_{(\text{Geod})-2,3}$	0.576/0.607	0.782/0.832	0.403/0.342
$\text{t-SNE}_{(\text{Eucl})-2,3}$	0.564/0.615	0.703/0.764	0.378/0.339

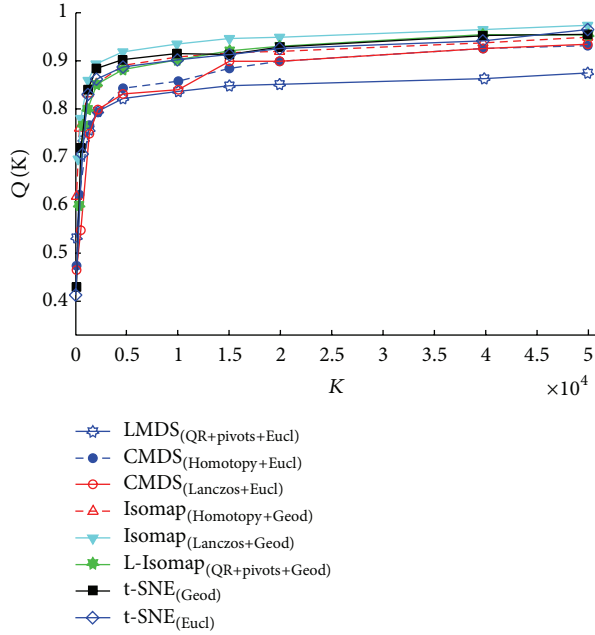


FIGURE 5: Behavior curves for assessing local embedding of PNAS Titles.

the approximation embeddings, a clear superiority brought by the homotopy is the boost from the distributed system.

5. Discussion

5.1. *QR*. Combining the results of the two data sets, the capability of the QR based method is limited within around 10,000 of data scale, even though it improved by both the Nyström approximation and the geodesic measuring approach [23]. Although the QR approach is subject to the small and medium size problem, it is also used widely [2] integrated with matrices reduction which can reach a

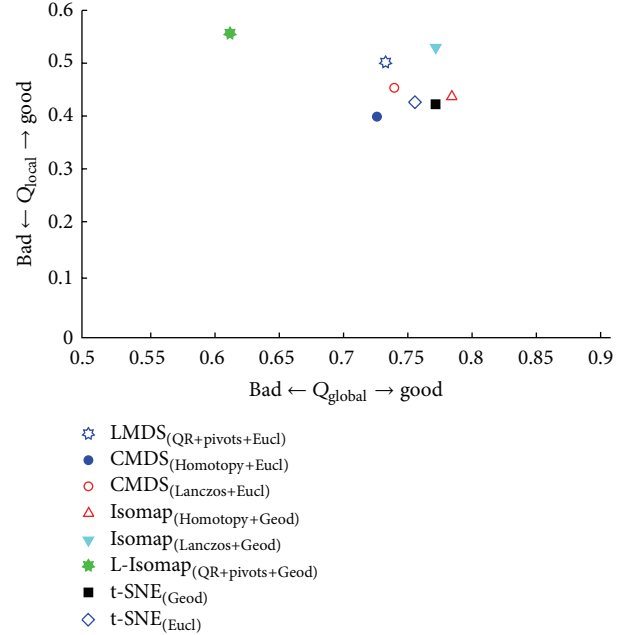


FIGURE 6: Quality for assessing embedding of PNAS Titles.

balance between time consuming, computational resources, and embedding precision. Furthermore, most algorithms of QR are designed for dense square matrices which mean the QR-based models are difficult to expand to distributed systems for decentralized computation and storage compared with sparse matrices.

5.2. *Homotopy versus Lanczos*. For several hundreds of thousands of levels of data scale, we should consider to employ those eigendecompositions technologies which are specific to super large scale matrices. The homotopy continuation method and the Lanczos family will be the feasible options. However, the result in Figure 2 shows that the

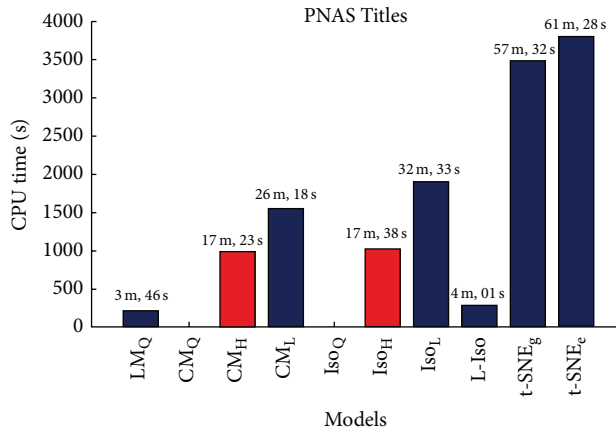


FIGURE 7: CPU time for embedding of PNAS Titles.

homotopy-based method may exist in the problem of numerical instability which decreased the precision of embedded space. The Lanczos also has a similar problem arising on some form of matrices [26]. To overcome this impediment, we need further substantial steps in these fields.

The superiorities of the homotopy approach have three aspects: the calculation of each eigenpairs is a separate process which means that a boost of multiple eigenpairs solution can be realized by the augmentation of computational cells, that is the core idea for parallelizing the eigenvalue-based dimensional reduction; the trend of each eigenpath is predictable that makes those negative eigenpairs can be estimated before it completely calculated, this can be a basis for scheduling computational resources by aborting those meaningless processes; it also provides a way to estimate the maximum available dimensions of embedding space by predicting the number of positive eigenvalues before completing the calculation of eigenpairs.

6. Conclusions and Future Work

This paper focuses on the parallelization of eigenvalue-based dimensional reduction via the homotopy continuation method. A novel embedding method based on the homotopy is presented. It transforms the eigendecomposition process of embedding to an ODE problem with initial values. By tracking eigenpaths separately, all isolated positive eigenpairs can be solved in parallel. The experiments show that the homotopy-based approach is applicable to the embedding task with around hundreds of thousands of data items. This will satisfy to approximate embedding to millions of items.

From the analysis of experiments, there are two problems around the homotopy on eigendecomposition of embedding: the accuracy of eigenpairs is still expected to improve. The numerical instability which may exist during computational procedure needs more works to investigate the convergence of homotopy method.

Competing Interests

The authors declare that they have no competing interests.

Acknowledgments

This paper was supported by the National Natural Science Foundation of China under Grant no. 61302170.

References

- [1] V. De Silva and J. B. Tenenbaum, *Global Versus Local Methods in Nonlinear Dimensionality Reduction*, vol. 15 of *Advances in Neural Information Processing Systems*, 2002.
- [2] J. C. Platt, "Fastmap, metricmap, and landmark mds are all nystrom algorithms," in *Proceedings of the 10th International Workshop on Artificial Intelligence and Statistics*, 2005.
- [3] C. Orsenigo, "An improved set covering problem for isomap supervised landmark selection," *Pattern Recognition Letters*, vol. 49, pp. 131–137, 2014.
- [4] I. Borg and P. J. Groenen, *Modern Multidimensional Scaling, Theory and Applications*, Springer, Mannheim, Germany, 2nd edition, 2005.
- [5] U. Brandes and C. Pich, "Eigensolver methods for progressive multidimensional scaling of large data," in *Graph Drawing: 14th International Symposium, GD 2006, Karlsruhe, Germany, September 18–20, 2006. Revised Papers*, vol. 4372 of *Lecture Notes in Computer Science*, pp. 42–53, Springer, Berlin, Germany, 2007.
- [6] M. Williams, "Steerable, progressive multidimensional scaling," in *Proceedings of the IEEE Symposium on Information Visualization (INFOVIS '04)*, pp. 57–64, Austin, Tex, USA, 2004.
- [7] L. van der Maaten, "Accelerating t-SNE using tree-based algorithms," *Journal of Machine Learning Research*, vol. 15, pp. 3221–3245, 2014.
- [8] A. Civril, M. Magdon-Ismael, and E. Bocek-Rivele, "SDE: graph drawing using spectral distance embedding," in *Graph Drawing: 13th International Symposium, GD 2005, Limerick, Ireland, September 12–14, 2005. Revised Papers*, vol. 3843 of *Lecture Notes in Computer Science*, pp. 512–513, Springer, Berlin, Germany, 2006.
- [9] K.-I. Lin and C. Faloutsos, "FastMap—a fast algorithm for indexing, data-mining and visualization of traditional and multimedia datasets," in *Proceedings of the ACM SIGMOD International Conference on Management of Data*, pp. 163–174, San Jose, Calif, USA, May 1995.
- [10] D. Harel and Y. Koren, "Graph drawing by high-dimensional embedding," in *Proceedings of the Symposium on Graph Drawing*, pp. 207–219, Irvine, Calif, USA, August 2002.
- [11] A. Morrison and M. Chalmers, "Improving hybrid MDS with pivot-based searching," in *Proceedings of the Ninth Annual IEEE Conference on Information Visualization (INFOVIS '03)*, pp. 85–90, 2003.
- [12] J. G. Silva, J. S. Marques, and J. M. Lemos, "Selecting landmark points for sparse manifold learning," in *Neural Information Processing Systems*, 2006.
- [13] C. Campos and J. E. Roman, "Strategies for spectrum slicing based on restarted Lanczos methods," *Numerical Algorithms*, vol. 60, no. 2, pp. 279–295, 2012.
- [14] J. Beisheim, "Introducing the PCG lanczos eigensolver," *ANSYS Advantage*, vol. 1, no. 1, pp. 42–43, 2007.
- [15] S. H. Lui, H. B. Keller, and T. W. C. Kwok, "Homotopy method for the large, sparse, real nonsymmetric eigenvalue problem," *SIAM Journal on Matrix Analysis and Applications*, vol. 18, no. 2, pp. 312–333, 1997.

- [16] A. Chesnokov, M. V. Barel, N. Mastronardi, and R. Vandebril, "Homotopy algorithm for the symmetric diagonal-plus-semiseparable eigenvalue problem," *Numerical Analysis and Applied Mathematics*, 2011.
- [17] M. T. Chu, "A simple application of the homotopy method to symmetric eigenvalue problems," *Linear Algebra and Its Applications*, vol. 59, pp. 85–90, 1984.
- [18] M. T. Chu, "A note on the homotopy method for linear algebraic eigenvalue problems," *Linear Algebra and its Applications*, vol. 105, pp. 225–236, 1988.
- [19] T. Y. Li and N. H. Rhee, "Homotopy algorithm for symmetric eigenvalue problems," *Numerische Mathematik*, vol. 55, no. 3, pp. 265–280, 1989.
- [20] P. Brockman, T. Carson, Y. Cheng et al., "Homotopy method for the eigenvalues of symmetric tridiagonal matrices," *Journal of Computational and Applied Mathematics*, vol. 237, no. 1, pp. 644–653, 2013.
- [21] S. T. Roweis and L. K. Saul, "Nonlinear dimensionality reduction by locally linear embedding," *Science*, vol. 290, no. 5500, pp. 2323–2326, 2000.
- [22] M. Belkin and P. Niyogi, "Laplacian eigenmaps and spectral techniques for embedding and clustering," in *Proceedings of the Advances in Neural Information Processing Systems 14 (NIPS '02)*, MIT Press, December 2002.
- [23] J. B. Tenenbaum, V. de Silva, and J. C. Langford, "A global geometric framework for nonlinear dimensionality reduction," *Science*, vol. 290, no. 5500, pp. 2319–2323, 2000.
- [24] W. Ford, "Implementing the QR decomposition," in *Numerical Linear Algebra with Applications Using MATLAB*, chapter 17, pp. 351–378, Academic Press, 2015.
- [25] P. Bogacki and L. F. Shampine, "A 3(2) pair of runge—kutta formulas," *Applied Mathematics Letters*, vol. 2, no. 4, pp. 321–325, 1989.
- [26] C. B. Moler, *Numerical Computing with MATLAB*, SIAM Press, Philadelphia, Pa, USA, 2004.
- [27] J. A. Lee and M. Verleysen, "Scale-independent quality criteria for dimensionality reduction," *Pattern Recognition Letters*, vol. 31, no. 14, pp. 2248–2257, 2010.